REBOUND AND TOUGHENING MECHANISMS IN STEEL FIBER REINFORCED DRY-MIX SHOTCRETE

by

HUGO SOGAYAR ARMELIN

B.Sc., University of Sao Paulo, 1990
M.A.Sc., University of Sao Paulo, 1992

A THESIS SUBMITTED IN PARTIAL FULFILLMENT OF
THE REQUIREMENTS FOR THE DEGREE OF
DOCTOR OF PHILOSOPHY

in

THE FACULTY OF GRADUATE STUDIES

DEPARTMENT OF CIVIL ENGINEERING

We accept this thesis as conforming
to the required standard

THE UNIVERSITY OF BRITISH COLUMBIA

August 1997

© Hugo Sogayar Armelin, 1997

In presenting this thesis in partial fulfilment of the requirements for an advanced degree at the University of British Columbia, I agree that the Library shall make it freely available for reference and study. I further agree that permission for extensive copying of this thesis for scholarly purposes may be granted by the head of my department or by his or her representatives. It is understood that copying or publication of this thesis for financial gain shall not be allowed without my written permission.

Department of _Civil Engineering_

The University of British Columbia
Vancouver, Canada

Date _October 10th, 1997_

ABSTRACT

Despite its worldwide application, dry-mix shotcrete is characterized by a 30 to 40% material loss due to rebound. For cases in which steel fibers are used, fiber rebound tends to be even greater at approximately 75%. This represents one of the main drawbacks to this technique and is one of the primary challenges facing the shotcrete industry today. Therefore, this work aimed at examining the fundamental mechanisms of aggregate and fiber rebound in dry-mix shotcrete and the parameters influencing them.

In order to deal with aggregate rebound, a high speed camera was used to observe the shooting and rebound processes and an extensive shotcrete experimental program was carried out to investigate the various parameters of mix design and shooting technique that cause rebound. Additionally, using a theory of plasticity approach, a general model of aggregate rebound for shotcrete was developed and shown to be in good agreement with experiments. Shotcrete tests show that proper adjustment of the mix-design and shooting technique can lead to minimized aggregate rebound.

The problem of fiber rebound was investigated using an experimental approach in which various mix designs and fiber geometries were produced and tested in actual dry-mix shotcrete conditions. It was found that steel fiber rebound is linearly related to a fiber aspect ratio given by the fiber length divided by the square root of its diameter.

Special emphasis was given to the development of a steel fiber for dry-mix shotcrete with reduced rebound and optimized toughness performance. In order for this to be possible, a new concept in fiber anchorage was introduced and a computer model, capable of relating the pull-out of single fibers to the post-cracking flexural strength of shotcrete was developed and used to optimize this new fiber geometry for shotcrete conditions. Prototype tests using this new fiber in dry-mix shotcrete show significantly enhanced toughness performance when compared to the most efficient existing commercial fibers.

TABLE OF CONTENTS

Chapter 1 - Introduction

Chapter 2 - Steel Fiber Concrete and Dry-mix Shotcrete (Literature Survey and Presentation)

Chapter 3 - Experimental Evaluation of Aggregate Rebound in Dry-Mix Shotcrete

Chapter 4 - Kinematics of Dry-mix Shotcrete

Chapter 5 - Mechanics of Aggregate Rebound

Chapter 6 - Modeling of Aggregate Rebound in Dry-mix Shotcrete

Chapter 7 - Experimental Evaluation of Steel Fiber Rebound: Influence of Mix Design and Shooting Technique

Chapter 8 - Experimental Evaluation of Steel Fiber Rebound: Influence of Fiber Geometry

Chapter 9 - Predicting the Flexural Post-Cracking Performance of Steel-fiber Reinforced Concrete from the Pull-out of Single Fibers

Chapter 10 - Development of a New Steel Fiber For Dry-Mix Shotcrete

Chapter 11 - General Conclusions and Recommendations for Future Research

LIST OF TABLES

LIST OF FIGURES

LIST OF SYMBOLS

Chapter 2 - Steel Fiber Concrete and Dry-Mix Shotcrete (Literature Survey and Presentation)

R - Percentage shotcrete overall rebound.

R_f - Percentage fiber rebound.

T - Percentage fiber retention (in-situ fiber content divided by the design fiber content).

V_f - Percentage volume fraction of fibers in the design mix.

V'_f - Percentage volume fraction of fibers in the in-situ shotcrete.

Chapter 4 - Kinematics of Dry-mix Shotcrete

A, B - Constants relating the aggregate diameter to its shooting velocity.

$\overline{A_{sp}}$ - Specific projected area (projected area divided by the mass).

I_G - Particle mass moment of inertia.

l - Fiber length.

m - Particle mass.

T, T_t and T_r - Respectively, the total, translational and rotational particle kinetic energy.

V - Translational velocity.

Φ - Aggregate or fiber diameter.

ρ - Aggregate or fiber mass density.

ω - Angular (or rotational) velocity.

Chapter 5 - Mechanics of Aggregate Rebound

a - Radius of the contact area formed between the indenter (or impactor) and the substrate.

α - Radius of the contact area between the indenter and the elastic cavity.

c - Radius of the elastic plastic boundary formed around the hydrostatic core.

δ and δ^* - Depth of penetration of the impactor and maximum depth of penetration.

ΔD - Deformation imposed on the substrate by the impactor.

Δt - Time frame taken for a deformation to be imposed on the substrate by the impactor.

e - Coefficient of restitution.

ε_{pc} - Limit elastic strain of fresh concrete.

f - Contact force between the indenter and the substrate.

F - Maximum contact force between the indenter and the substrate.

h - Displacement of the indenter into the substrate.

K - Constant relating the coefficient of restitution to the impact factor (Ψ).

m - Mass of the impactor.

$\overline{p}$ - Magnitude of the hydrostatic stress acting on the core beneath the contact area.

p and p_d - Static and dynamic contact stress between the impactor and the substrate.

$\sigma_r, \sigma_\theta, \sigma_\phi$ - Radial and tangential components of stress acting on the substrate.

R - Radius of the indenter.

r_1 and r_2 - Radii of the impactor and the elastic cavity before contact.

ρ - Mass density of the impactor.

t_{pen} - Time taken for the impactor to penetrate to full depth.

E^*, E_c, E_i - Composite, concrete and impactor elastic moduli.

V and V' - Velocities of impact and rebound.

V_a - Apparent volume dislocated by the impactor.

W_1 and W_2 - Energy of impact and rebound.

Y - Yield stress of the substrate as determined from uniaxial stress conditions.

Ψ - Impact factor.

z - Distance traveled by the indenter in contact with the cavity under elastic conditions.

Chapter 6 - Modeling of Aggregate Rebound in Dry-mix Shotcrete

a - Radius of the contact area between the aggregate and the substrate.

a^* - Maximum radius of the contact area between the aggregate and the substrate.

A - Mass percentage of aggregates in the mix .

C - Mass percentage of cement in the mix .

δ and δ^* - Depth of penetration of the impactor and maximum depth of penetration.

e - Coefficient of restitution.

ε_{pc} - Limit elastic strain of fresh concrete.

E^*, E_c, E_i - Composite, concrete and impactor elastic moduli.

ϕ - Aggregate diameter.

p and p_d - Static and dynamic contact stress between the particle and the substrate.

p_i - Percentage of aggregates from the combined gradation retained in the sieve size i.

R - Overall rate of rebound by mass (rebounded material/total material shot).

r_i and r_c - Rates of rebound for an individual sieve size i and cement rebound.

σ_o - Adhesive strength of the aggregate to fresh shotcrete contact.

V and V' - Velocities of impact and rebound.

V_a - Apparent volume dislocated (or penetrated) by the aggregate.

W_1, W_2 and W_D - Impact, rebound and debonding energies.

Y - Yield stress of the substrate as determined from uniaxial stress conditions.

Chapter 7 - Experimental Evaluation of Steel Fiber Rebound: Influence of Mix Design and Shooting Technique

M_r - Total mass of rebounded material.

M_s - Total mass of in-situ shotcrete.

FM_r - Fiber mass per kilogram of rebound material collected.

FM_s - Fiber mass per kilogram of in-situ shotcrete collected.

R - Percentage shotcrete overall rebound.

R_f - Percentage fiber rebound.

T - Percentage fiber retention.

V_f - Percentage volume fraction of fibers in the design mix.

V'_f - Percentage volume fraction of fibers in the in-situ shotcrete.

Chapter 8 - Experimental Evaluation of Steel Fiber Rebound: Influence of Fiber Geometry

l_f - Fiber length.

M_r - Total mass of rebounded material.

M_s - Total mass of in situ shotcrete.

FM_r - Fiber mass per kilogram of rebound material collected.

FM_s - Fiber mass per kilogram of in situ shotcrete collected.

ϕ - Fiber diameter.

R - Percentage shotcrete overall rebound.

R_f - Percentage fiber rebound.

T - Percentage fiber retention.

V_f - Percentage volume fraction of fibers in the design mix.

V'_f - Percentage volume fraction of fibers in the in situ shotcrete.

Chapter 9 - Predicting the Flexural Post Cracking Performance of Steel Fiber Reinforced Concrete from the Pull-out of Single Fibers

A, B, C, Ep - Adjustment constants of the Ramberg-Osgood equation.

b - width of the beam.

c - Depth of the neutral axis.

c' - Depth of the beam up to which concrete is able to transfer stresses.

$dCMOD$ - Incremental crack-mouth opening displacement.

E_{ct} - Tangent modulus of elasticity of concrete.

f'_c - Cylinder compressive-strength of concrete.

f_{cr} - Maximum tensile-strength of concrete.

$\bar{f}$ - Average pull-out force of a single fiber contained in a given region.

f_i - Pull-out force of an individual fiber i.

f_α - Pull-out force of an individual fiber with inclination angle α w.r.t. the pull-out direction.

F_t - Total pull-out force generated by the N fibers contained in a given region.

h - Depth of the beam.

L - Total beam span under third-point loading.

l - Distance between loading points under third-point loading.

l_{ei} - Embedment length of an individual fiber i ($0 < l_e < l_f/2$).

l_f - Total fiber length.

M_e - Bending moment necessary to equilibrate the cracked-section.

N - Total number of fibers intercepting a given region.

n - Fiber density distribution (average number of fibers intercepted per unit area).

P - Flexural load under third-point loading.

V_f - Volume fraction of fibers contained in the composite.

$\bar{x}$ and S_d - Mean and standard deviation of a sample.

y_i - Position of an individual fiber i with respect to the neutral-axis.

α_i - Inclination angle of an individual fiber i with respect to the pull-out load.

Δ_o - Total axial shortening of the beam at the top-most fiber, under third-point loading.

$d\delta$ - incremental mid-point deflection of the beam.

$d\theta$ - Incremental rotation of the cracked section of the beam.

ε_x and ε_c - General axial strain and axial strain in the concrete.

ε_o - Axial strain of the top-most fiber of the beam at midspan, under third-point loading.

ε_{cr} - Cracking or limit elastic strain of concrete under tension.

μ and σ - Mean and standard deviation of the population.

σ_c - General concrete stress.

σ_{ct} - Tensile stress in the concrete.

Chapter 10 - Development of a New Steel Fiber for Dry-Mix Shotcrete

ϕ - Fiber diameter.

l_f - Fiber length.

t - Thickness of the "drag" anchor.

t' - Thickness of the "dead" anchor.

w - Width of the "drag" anchor.

ACKNOWLEDGMENT

I would like to acknowledge the full support and independence of thought given to me throughout these four years by my research supervisor, Dr. Nemkumar Banthia, who had the vision and leadership needed to tackle a project that, initially seemed impossible to me. I would also like to extend my appreciation to my co-supervisor, Dr. D. R. Morgan who has dedicated a great deal of his personal time to the development of the shotcrete industry and who, through patient discussions, always steered my work towards an industry applicable research. I would also like to thank Dr. Sidney Mindess for generously allowing me to use his high speed equipment.

From a practical point of view, this work would not have been possible without the support and expertise of the technicians at the UBC Civil Engineering Department, particularly Dick Postgate, Doug Smith and John Wong. I would also like to thank all of those who helped me with shootings, carrying test panels, operating the shotcrete machine etc.: Craig Steeves, Bob Ambardar, Dennis Teo, Hamed Shabazzi, Prabakar Gupta, Kevin Campbell and Jeff Tan.

Finally, these four years spent at UBC would not have been complete had it not been for a group of people with whom I experienced moments of both joy and frustration, doubts, failure, hikes, beer, laughs, rain, sushi, summits and all things that make the difference between a mere technical exercise and a lifetime experience: Isabelle Genois, Jack Genois, Monique Pare, Marc Jolin with Helene and Cedric, "Vince" Latendresse, Nick Lehoux, Natacha Dumais, Wellington Reppette and Mariana, Thomas Horyna with Petra and "Hanza", Antonio Figueiredo and Armando Galassini - stay gold.

a meus pais

Chapter 1 - Introduction

1.1 - Definition of Shotcrete

According to ACI Committee 506 (1990) shotcrete is defined as mortar or concrete that is pneumatically applied at a high speed. To this definition, the Austrian Concrete Society (1990) adds that, in order to be classified as shotcrete, the material should be compacted by its own momentum. The basic form in which it is applied (i.e. by a spray) renders shotcrete especially advantageous in applications such as tunneling, mining, slope and rock stabilization and structural repair, for which the use of formwork and ordinary cast concrete is relatively costlier or more time consuming.

There are basically two distinct forms of shotcrete, depending on whether or not all the mixing water is present in the shotcrete when the concrete is introduced into the spraying machine. For the case in which all the water is present, the technique is named "wet-mix" shotcrete; on the other hand, when the materials are introduced into the spraying machine in the bone-dry state or containing only a part of the mixing water, the technique is named "dry-mix" shotcrete.

Although the definition of the two possible forms of shotcreting (wet or dry-mix) is given only by the form in which water is added, there are several distinctions between the two techniques: dry-mix shotcrete is characterized by a greater stiffness of the mixture and the possibility of a high early age strength; in addition, the small size and lower cost of its equipment and the possibility to shoot as small a volume as desired when using bone-dry materials makes this technique especially attractive for NATM tunnel fronts, mining and overhead structural and cosmetic repair. The main drawbacks of the dry-mix process are the dust that it produces and the high material loss caused by rebound.

The wet-mix technique, on the other hand, is characterized by a lower stiffness of the mix (and thus the possibility of troweling and finishing the surface), lower material loss due to rebound and a higher productivity. The main drawbacks of this process are the higher equipment cost and the need to apply the entire batch of concrete before setting takes place. As a result, the wet-mix

technique tends to be better suited for applications in which a high standard of surface finishing is required (e.g. facades) or for applications of large volumes of shotcrete requiring a high productivity and for which rebound has a major implication on the final cost (e.g. secondary tunnel linings and large underground cavities).

1.2 - Problem Description

As mentioned earlier, one of the main drawbacks of the dry-mix technique is material loss due to rebound, which is usually in the range of 30 to 40%[1] (Austin 1995 and Wolsiefer & Morgan, 1993). In fact, the computation of all the dry-mix shotcrete consumed in the construction of the primary lining of a NATM subway tunnel revealed a 50% loss of shotcrete due to rebound by the time the project was completed (Telles, 1992). This figure is confirmed for extreme cases by both Warner (1995) and Vandevalle (1990).

Besides the obvious cost implications, material loss due to rebound has other consequences: because it is primarily composed of aggregates, rebound causes the in place shotcrete to have a higher cement content than the design mix, with in-situ cement content figures as high as 600 kg/m^3 being reported in the literature (Armelin et. al, 1994 and Cabrera & Woolley, 1996). This leads to a greater heat of hydration and shrinkage cracking, leaving the final structure more vulnerable to the surrounding environment.

For cases in which steel fibers are used in the dry-mix process, fiber loss due to rebound tends to be of the order of 75% for the fibers available in the market today (as will be demonstrated ahead). Considering that steel fibers are the most expensive constituent of the mixture, this represents a significant cost increase to the production of fiber reinforced shotcrete. Moreover, because fiber rebound is greater than the overall shotcrete rebound, the in-situ shotcrete tends to have a fiber content 30 to 50% lower than the design mix, thus representing a significant loss in the reinforcing capacity of the composite.

---

[1] Throughout this thesis, fiber and overall rebound are defined as the mass of rebounded material divided by the total mass of material shot. Overall rebound figures commonly found are reported assuming an ACI No. 2 gradation or coarser (i.e. lower values should be expected for gunite, for which the gradation is finer - not the object of this study).

All aspects considered, it may be said that, although dry-mix shotcrete (with and without fiber reinforcement) is widely used throughout the world, the waste in material and performance caused by rebound represents one of the main problems facing the shotcrete industry today. It is believed that improvements in this aspect of the process can have a significant impact on the overall efficiency of the material as related to both cost and performance.

1.3 - Objectives

The objective of this study was to investigate the fundamental processes involved in aggregate and steel fiber rebound in dry-mix shotcrete, and to characterize the main parameters affecting it using industrial scale shotcrete equipment, under laboratory controlled conditions. It is expected that, by understanding the rebound process, one can rationally act to minimize material loss in shotcrete.

Ultimately, from a fiber rebound point of view, this study aimed at developing a steel fiber geometry possessing minimized rebound and maximized reinforcing capacity for dry-mix shotcrete, and thus allowing for a more efficient composite with respect to flexural toughness performance.

Chapter 2 - Steel Fiber Concrete and Dry-mix Shotcrete
(Literature Survey and Presentation)

2.1 - Steel Fiber Reinforcement of Concrete

The use of short and randomly distributed lengths of steel for reinforcing concrete was first explored from a scientific perspective by Romualdi and Mandel (1964). Using concepts of fracture mechanics, they predicted that the first crack tensile strength of concrete could be significantly improved by the addition of short lengths of steel wire. Although the experimental results obtained by Romualdi and Mandel (1964) were not confirmed by later literature, the fact that the steel fibers pulled out from concrete, thus bridging cracks, demonstrated the possibility of transforming an inherently brittle material into a composite several times tougher.

Since then, due to intensified research, steel fibers for concrete reinforcement have evolved from the straight (undeformed) lengths of wire originally used by Romualdi and Mandel into complex geometries that allow for increased anchorage with concrete and thus result in a greater post-cracking ductility (Fig. 2.1). The developments in the fiber reinforced concrete industry in the past thirty years have made the use of steel fibers commonplace throughout the world, with shotcrete as one of its main applications.

The main reasons for the success of steel fibers as a means of concrete reinforcement are related to the ability of the fibers to transmit forces across a crack, providing therefore greater cracking control for slabs on grade and industrial floors (Nishioka et al., 1980) and dry-mix shotcrete (Campbell, 1997). From a structural point of view, when used along with conventional rebar reinforcement, steel fibers have also been found to produce greater structural ductility and increased shear and flexural capacities in full scale structural elements (Adebar et. al., 1997).

Steel fibers presently being used for concrete reinforcement are usually made of carbon steel with tensile strength in excess of 1000 MPa. Their dimensions are usually 25 to 60 mm in length and

0.4 to 1.0 mm in diameter. For example, the standard hooked ends fibers used today for both cast and sprayed concrete are 0.5 mm in diameter and 28 to 30 mm in length.

Figure 2.1 - Different steel fiber geometries presently available in the market for concrete and shotcrete reinforcement.

Unlike the reinforcement ratio of traditional reinforced concrete (ρ) which is reported in terms of area ratio, the addition rate of steel fibers is usually reported in terms of the volume fraction (V_f)[2]. Therefore, steel fiber concrete for industrial floors or slabs on grade usually requires a volume fraction of approximately 0.5% (35 kg/m^3) while structural applications are usually between 0.5 and 1.0% (35 to 75 kg/m^3). Fiber addition rates in excess of 1.0% can be considered rare not only due to the cost that it represents, but also due to the difficulty in mixing and placing concrete at such high fiber contents.

2.2 - Dry-mix Shotcrete

Although double chamber machines were the first to be developed for sprayed concrete, the most common production method for dry-mix shotcrete today is using a rotating barrel machine. The principle involved is that of a barrel containing, on average, eight pockets rotating about its axis (Fig. 2.2). The dry-mix (1 - mixture of cement and aggregates that may or may not be pre-dampened) is fed to one side of the barrel, thus filling one pocket at a time (2). As the barrel

---

[2] It is shown in Chapter 9 that the fiber volume fraction (V_f) is related to the reinforcement ratio (ρ) by the orientation factor (α). Therefore, for a typical 3-D random fiber distribution the reinforcement ratio (ρ) is one half the fiber volume fraction (V_f - Eq. 9.8).

rotates, the filled pocket reaches a position in which the compressed air (3) forces the dry-mix out of the pocket and into the main line (4). The mix is then accelerated through the hose (38 to 64 mm in diameter, usually more than 20 m in length) towards the nozzle, where the remainder of the mixing water is introduced.
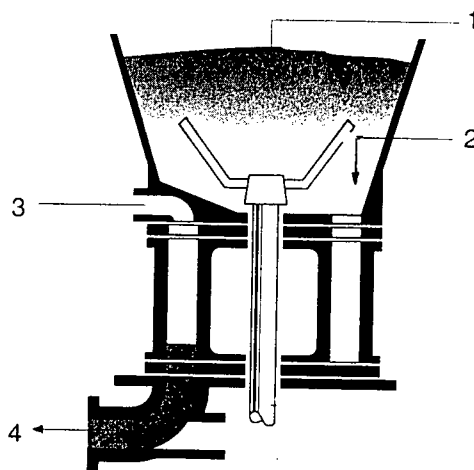
Figure 2.2 - Schematic representation of the mechanism involved in a rotating barrel shotcrete machine (for a description of steps 1 to 4 refer to the text).

When a 0.40 water to cement ratio is assumed, the aggregate to cement composition is such that the designed mix usually results in a cement consumption of 400 to 450 kg/m^3. The dry-mix composition may or may not contain coarse aggregates, for the case when only sand is used the technique is named gunite, which is commonly used for thin linings and repair. When a coarse aggregate[3] is used, the maximum size is usually limited to 9.5 mm with a 35 to 65% coarse to fine aggregate ratio being used for what is commonly referred to as the ACI N° 2 recommended gradation (ACI Committee 506, 1990).

The shooting water is usually controlled by the nozzle operator (or nozzleman) who may add more or less water depending on the shooting consistency desired. When building up thick layers (in excess of 100 mm) and/or shooting overhead, it is common practice to add set accelerators to the mix, thus allowing the shotcrete to quickly gain stiffness, preventing the dangerous and costly

---

[3] Coarse aggregates are defined here as the material retained in the 2.4 mm sieve

fall-out of large shotcrete masses from the overhead. Powder accelerators can be added to the dry mix and liquid accelerators can be added to the shooting water. Accelerator admixtures are also used in NATM tunneling, for which high early age strength is required in order to guarantee the stability of the excavation front. Prudencio et al. (1996) presents a review on the effect of accelerators on strength gain and general properties while Jolin (1996) describes their influence on shotcrete setting time, shrinkage and durability issues under freezing conditions.

Another addition often found in dry-mix shotcrete is silica fume. It is found that, at rates of 8 to 12% in substitution to cement, this fine powder reduces the overall rebound and allows for a greater overhead build up (Wolsiefer & Morgan, 1993) without the need for accelerator admixtures and without the loss in strength and durability that an accelerator may cause.

With respect to design requirements, dry-mix shotcrete is usually specified in terms of its 28 day compressive strength and volume of permeable voids (ASTM C 642). The latter test is considered to assess how well compacted the material is, and thus a maximum limit of 17% voids (8% absorption) is usually considered to characterize sound shotcrete (Morgan 1995). As mentioned earlier, NATM tunnel fronts may include early age strength requirements, in which case the compressive strength as early as 8 hours may also be specified, depending on the excavation conditions.

2.3 - Steel Fiber Reinforced Dry-mix Shotcrete

Historically, steel fiber reinforcement was first used in North America with the dry-mix process in the early 1970's at the Ririe Dam, in the United States (Morgan, 1993). In Europe, intense research and applications using the wet-mix process for rock stabilization in Scandinavian countries date to the early 1980's (Opshal, 1982) with the same occurring in Japan (Nishioka et al., 1980). Since then, applications have been reported throughout the world (for a compilation of projects, refer to Vandevalle, 1990).

When used for dry-mix shotcrete reinforcement, steel fibers are simply mixed and sprayed along with aggregates and cement and therefore do not represent any additional placing difficulties. However, the main benefits in using steel fiber reinforcement are found when conventional steel

mesh reinforcement can be eliminated. In this case, steel fibers are considered to bring advantages with respect to:

- Faster and safer construction due to the elimination of the time consuming and often dangerous mesh installation in rock slopes, tunnels and mines.
- Increased protection against rock bursts in deep mines.
- Reduced shotcrete rebound given that the wire mesh is an obstacle to shotcrete placement.
- Lower shotcrete consumption for irregular rock faces, allowing the lining to contour the natural profile of the rock mass without the need to create a smooth plane to embed the wire mesh (Vandevalle, 1990).
- Elimination of voids and sand pockets behind the steel mesh that can be caused by unskilled nozzle operation.

The possibility of substituting wire mesh with steel fiber reinforcement was demonstrated using large scale tests simulating a shotcrete lining containing rock bolt anchors (Morgan & Mowatt, 1979 ; Little, 1983) as well as for the case of a rock mass in which a large block becomes loose and has to be supported entirely by the shotcrete lining (Opshal, 1982).

As far as design requirements are concerned, steel fiber reinforced shotcrete is usually specified using the same criteria as conventional shotcrete (compressive strength and permeable voids volume) which are intended to guarantee the quality of the matrix. In addition to that, the performance with respect to its reinforcing ability is usually controlled using a standard 100 x 100 x 350 mm prismatic specimen tested using third point flexural loading under a 300 mm span (ASTM C 1018). The test method requires that simultaneous load and mid-point deflections be recorded. Net displacement measurements are taken at midspan using a so called "Japanese Yoke"(Fig 2.3) intended to eliminate extraneous deflections arising from load point crushing and support settlement.

Although the test is widely used as a standard, there is considerable debate on how to report and interpret test results (Chen, 1995). Thus, while ASTM recommends the computation of toughness indices ($I_{10, 20, 30}$) as a ratio between the energy consumed by the material and the theoretical

energy consumption for an ideally elastic-plastic material, JSCE makes use of the total energy consumed up to a deflection of 1/150 of the span. Recently, a template approach, adapted from the Norwegian standard has gained popularity, especially for shotcrete applications in Western Canada (Morgan, 1995).
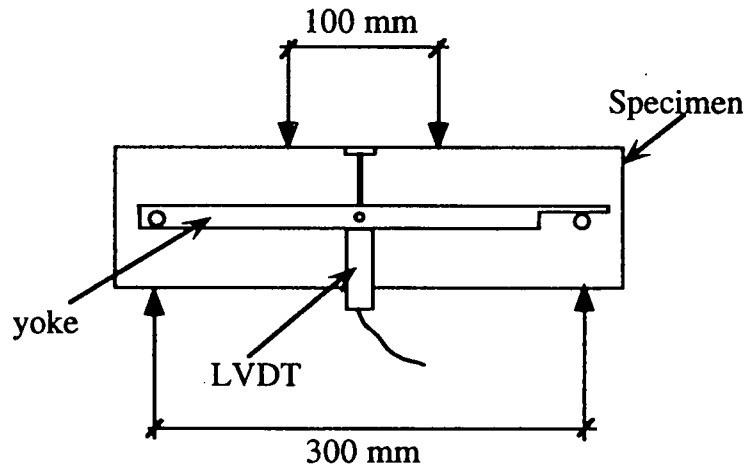
Figure 2.3 - Schematic representation of the ASTM C 1018 flexural toughness test using a "Japanese Yoke" to eliminate extraneous deformations and two LVDTs.

In reality, all the procedures for test interpretation proposed to date have strengths and limitations, a comprehensive review of the various criteria available and their implications is given by Chen (1995). Despite the various forms of interpretation given to the flexural toughness test, it should be kept in mind that all criteria measure essentially the post-cracking load carrying capacity of the composite and therefore, the higher the load bearing capacity past the first crack deflection, the more efficient the material is, regardless of the criterion adopted.

As for the influence that the steel fibers may have on the mechanical properties of dry-mix shotcrete, it has been experimentally demonstrated (Armelin & Helene, 1995) that, due to the relatively low in-situ fiber content, the compressive and tensile strengths, modulus of elasticity and volume of permeable voids of dry-mix shotcrete is not affected by either fiber type or content. The same study also demonstrated that, although there is a tendency for fibers to have a 2-dimensional orientation, no anisotropic behavior is found with respect to compressive strength in directions perpendicular and parallel to the direction of shooting (although the post-peak compressive behavior is affected by fiber orientation).

It should be mentioned that fibers for shotcrete reinforcement have been made of glass, carbon, polypropylene or steel. However, the durability problems related to glass fibers, the cost and difficulty in mixing carbon fibers and the low modulus of fibrillated polypropylene fibers have made steel the material of choice for the vast majority of fiber reinforced shotcrete produced to date. Recently, polymeric fibers, made of polyolefin, have been reported to provide adequate reinforcement to wet-mix shotcrete (Morgan, 1996). These fibers, however, have so far failed to show good toughness results for the dry-mix process due to excessively high fiber rebound.

2.4 - Factors Affecting the Overall rebound in Dry-mix Shotcrete

The causes of rebound in dry-mix shotcrete can be related to both the mix design and the shooting technique. The main parameter related to mix design is the shooting stiffness (or shooting consistency) which is controlled by the amount of water added by the nozzleman. Another parameter that is commonly recognized to influence shotcrete rebound is the cement content, with richer mixes having less rebound. Austin (1995) presented data on eight shotcrete mixes at two different cement contents (aggregate to cement ratios of 1:3 and 1:4) and consistently found that the richer mixes had a 5% lower rate of rebound.

The third aspect of mix design that has a pronounced influence on rebound is the aggregate gradation. Because the coarser aggregates tend to rebound more than fine aggregates (approximately four times more as will be demonstrated in Chapter 6), it is generally recognized that coarser aggregate gradations lead to more rebound. Therefore, ACI Committee 506 (1990) recognizes three distinct gradation curves for blended aggregates (commonly referred to as N°s 1, 2 and 3). Because the gradation N° 3 curve (the coarsest) leads to the highest rate of rebound, gradations N°s 1 and 2 are most often used, with the latter being the most commonly found in North America (Morgan, 1992).

One addition that has gained popularity in dry-mix shotcrete and is known to influence rebound is silica-fume. Austin (1995) reported tests using two different cement contents (A:C = 1:3 and 1:4) showing a linear trend in the variation of overall rebound with silica fume content, resulting in approximately 6 to 7% less rebound per 10% mass of silica fume substitution for cement. Similar

results of a 15% reduction in rebound have been reported for silica fume additions of up to 15% (Morgan, 1988). Silica fume contents typically used in North America are in the range of 7 to 15% by mass of cement (Morgan, 1995).

Although quick set accelerators are known to reduce wet-mix shotcrete rebound, the effect that these admixtures have on dry-mix shotcrete rebound is not clear. Melbye et al. (1995) stated that accelerators tend to reduce rebound. Schultz (1982) presented data on dry-mix shotcrete sprayed with and without accelerators, and concluded that the latter led to a lower aggregate rebound and hence also to a decrease in the in-situ cement content. This, however, is not true for all accelerator compositions, as the data to be presented in this study will show. Results by Jolin (1996) also did not confirm any influence of accelerators on dry-mix shotcrete rebound.

The second category of parameters that are known to influence rebound is related to the shooting technique. Among the parameters included in this category and perhaps the most controversial is the shooting velocity. The controversy on the subject begins with different claims regarding the speed at which particles tend to travel while shooting, with reported particle velocities varying widely from 10 to more than 100 m/s (Glassgold, 1989).

The discussion is further complicated by the fact that the published literature is not clear regarding whether a high or a low velocity leads to minimized rebound. Thus, while Warner (1995) and Maidl & Sommavilla (1995) recommend low shooting velocities, they do not offer a rationale for the recommendation and, furthermore do not quantify this "low velocity".

Although quantifying shooting velocity can be difficult and requires a high-speed camera or an equivalent device, it is generally recognized, and will be experimentally demonstrated in Chapter 4 that, for a given hose and nozzle system, it is the air flow that determines the particle velocities and therefore an air flowmeter is a viable means of controlling the shooting velocity.

Another parameter related to shooting technique that influences rebound is the thickness of application, with thinner layers leading to a greater rebound. Parker (1976) presented data indicating that, in the first 10 mm of application, rebound can be as high as 80%, falling to 20% after a build-up of 100 mm has been established.

The position of shooting is also considered to influence rebound, with overhead shooting being generally recognized to lead to greater losses. Morgan (1990) presented data on five mixes shot on the wall and overhead positions, with an average 6% greater rebound for the latter case. However, Wolsiefer & Morgan (1993) reported that, in three cases out of four, overhead shooting actually led to a lower rebound. In Chapter 3 it is demonstrated that, in effect, when shooting test panels, overhead and wall shooting lead to similar rates of rebound.

2.5 - Fiber Rebound in Dry-mix Shotcrete

Little is known about the factors affecting steel fiber rebound in dry-mix shotcrete. Using high-speed photography, Parker (1976) described fiber rebound as being caused, in part, by fibers being blown away from the shotcrete stream before reaching the plane of shooting. Peaston (1993) showed that fiber rebound is closely related to the overall shotcrete rebound, indicating that fiber rebound could be reduced by proper mix design.

One point of controversy is how to calculate steel fiber rebound. It is commonly accepted that calculations using only the design and in-situ fiber contents (V_f and V'_f) are unrealistic since they do not account for the overall shotcrete rebound. Robins and Austin (1985) first suggested a formula to compute fiber rebound that accounts for the overall shotcrete rebound. However, their calculations require knowledge of the in-situ water to cement ratio and aggregate to cement ratio, quantities that are not only difficult to obtain in practice, but are also bound to significant error.

Armelin and Helene (1995) suggested a simpler formula[4] that only needs as input parameters the design and in-situ fiber contents (V_f and V'_f) and the overall shotcrete rebound (R) to calculate fiber rebound (R_f):

$$R_f(\%) = 100 - T + (T \cdot \frac{R(\%)}{100}) \text{ , where: } T = \textit{Fiber Retention} = \frac{V'_f}{V_f} \cdot 100\% \qquad (2.1)$$

---

[4] The development of this equation is presented in Appendix A..

Conversely, this same formula allows calculating the in-situ fiber content (V'_f), as a function of the design fiber content (V_f), the fiber rebound (R_f) and the overall shotcrete rebound (R):

$$V'_f (\%) = \frac{V_f \cdot \left(100 - R_f (\%)\right)}{\left(100 - R(\%)\right)} \qquad (2.2)$$

As will be shown in Chapter 7 (Fig. 7.1), despite the fact that it does not take into consideration a possible difference in specific gravity between in-situ shotcrete and rebound (as done in Robins and Austin, 1985 and Banthia et al., 1994) Eq. 2.1 provides an accurate assessment of fiber rebound and Eq. 2.2 allows one to predict the expected in-situ fiber content and analyze the effect that the overall rebound has on it.

Considerable evidence is available to support the belief that steel fiber geometry also plays a role in the fiber rebound process. For the dry-mix process, Banthia et al. (1992) described flat fiber geometries as having greater rebound than fibers of a circular cross section, suggesting that fiber rebound should be related to the specific projected area of the fibers. This, however, was not confirmed by Peaston (1993) and Armelin and Helene (1995).

Peaston (1993) further suggested that the fiber mass influenced fiber rebound, although the data presented did not strongly support this hypothesis and the same group (Austin, Peaston and Robins, 1995) later concluded that the fiber mass is *not* a significant factor.

Although no consensus exists on the parameters of fiber geometry that influence fiber rebound, the fact remains that the steel fibers presently being used for shotcrete were designed to perform in conventional cast-in-place concrete and, as a result, are not optimized from a dry-mix shotcrete point of view. This has led to suggestions that there is a 'need to develop fiber types specifically for sprayed concrete ... which will provide the least fiber rebound and maximum toughness" (Morgan, 1995).

2.6 - Presentation

From the literature survey presented above, it appears that, despite the fact that a considerable amount of research has been done on the subject of rebound in dry-mix shotcrete, efforts have been concentrated on empirically characterizing the influence of the various intervening parameters, without an emphasis on the fundamental processes involved. As a result, progress has been limited and several basic questions remain unanswered:

- Why is the dry-mix process characterized by a 30 to 40% rebound while wet-mix shows only 5 to 15% ?
- Why do coarse aggregates rebound up to four times more than fines ?
- What is the mechanism that allows silica fume to reduce rebound ?
- Are there fiber geometries that rebound less ? If so, is it possible to develop a steel fiber for minimized rebound ?

Seeking to answer the above questions, the research program described in the following has been divided into 11 Chapters. Chapters 1 and 2 are dedicated to introduction and literature survey. Chapter 3 describes an experimental study of aggregate rebound in dry-mix shotcrete, aiming at characterizing the main parameters that influence aggregate rebound in practice and determining the rebound composition. Chapter 4 is dedicated to analyzing the aggregate and fiber velocities in the shotcrete stream by means of high speed filming, while Chapter 5 deals with the mechanics of an aggregate particle striking a fresh concrete substrate and rebounding from it.

In Chapter 6, the velocity figures obtained in Chapter 4 are used as input parameters to the rebound model developed in Chapter 5 in order to predict shotcrete overall rebound and rebound composition.

Chapters 7 and 8 are dedicated to the study of fiber rebound. Therefore, in Chapter 7 an experimental study of dry-mix shotcrete is carried out to determine the main parameters of mix design and shooting technique that influence fiber rebound. In Chapter 8 different combinations of fiber length and diameter are tested to examine the influence of fiber geometry.

Appreciating that ultimately it is the flexural toughness that defines the performance of steel fiber reinforced shotcrete, in Chapter 9, the relationship between the pull-out of individual fibers and the toughness of the composite is analyzed and a computer program is developed allowing prediction of the flexural toughness from the pull-out data of a limited amount of steel fibers.

Finally, Chapter 10 takes advantage of the information regarding the relationship between fiber geometry and rebound from Chapter 8 and the toughness model developed in Chapter 9 to develop a steel fiber geometry that conciliates minimized rebound and maximized flexural toughness for dry-mix shotcrete. General conclusions and suggestions for future research are presented in Chapter 11 and Appendix D presents practical guidelines to the design of dry-mix shotcrete compostions for a minimized rebound.

Chapter 3 - Experimental Evaluation of Aggregate Rebound in Dry-Mix Shotcrete

3.1 - Introduction and Objectives

As described in the previous chapter, despite the considerable amount of data on aggregate rebound available in the literature, there is still considerable debate on the influence of several important parameters such as the shooting velocity, the effect of accelerator admixtures, pre-moisturization and others. In great part, this conflict in the results presented in the literature is caused by the fact that a comprehensive experimental program on the subject is still lacking.

Therefore, the objective of this chapter was to use industrial scale dry-mix shotcrete equipment under carefully controlled laboratory conditions of air flow and shooting consistency to characterize aggregate rebound and its variation with parameters of mix design and shooting technique. The information extracted from this chapter will provide a solid basis for quantifying aggregate rebound as well as serve as the experimental data base to test a general theory of aggregate rebound in Chapter 6.

3.2 - Material and Methods

Throughout this research program, shotcrete was produced using a dry-mix rotating barrel equipment (model ALIVA 246 with a 3.6 liter, eight pocket drum) instrumented with a spring-loaded, in-line, air flowmeter (model OMEGA FL8945). Water was added 2 m before the nozzle at a high pressure (between 1 and 5.2 MPa, controlled and read on a manometer[1] by the operator at the nozzle). The high pressure water system[2] enables a better water dispersion in the mix as well as a reduction in the variation in the water feed caused by fluctuations in the air pressure (between 0.5 and 0.8 MPa). Additionally, a 20 m long, 50 mm internal diameter hose and

---

[1] Because, for a given orifice size, the water flow is controlled by the pressure, this apparatus is, in effect, a flowmeter (Appendix B).

[2] The high pressure water ring used was originally developed without a means for water flow measurement and control by the nozzleman under the CBPO/USP/IPT 1990 shotcrete research program at the University of Sao Paulo, S.P., Brazil.

maximum rotor speed were used in order to minimize fluctuations in the feed of material to the nozzle.

Test panels (600 x 400 x 125 mm with tapered sides) were sprayed inside a closed chamber (2.4 x 2.4 x 2.4 m) for both wall[3] (Fig. 3.1) and overhead positions using a 300 cfm air flow (100 cfm = 0.05 m^3/s). In order to take into account the variations in rebound with the thickness of application, all panels were filled in three consecutive layers respectively 25, 50 and 50 mm in thickness. Plastic tarpaulins were laid out inside the shooting chamber before each layer was shot and the panel was weighed after each shooting. After shooting the third layer, the rebound material was collected from each of the three tarpaulins and weighed.

Figure 3.1 - Schematic view of the rebound chamber and the position in which the shotcrete panels were produced.

Immediately after shooting, the shooting consistency was assessed using the electronic penetrometer developed at UBC and described in section 3.3.1.1. The signal from the penetrometer was recorded by an electronic data acquisition system that immediately displayed

---

[3] All panels tested throughout this research program were shot on the wall position with the panel held 1.5 m from the ground at a 90 degree angle with the horizon. It is fairly common that test panels in the field and for research programs be shot at an angle of less than 90 degrees with the horizon by positioning the test panel on the floor and against the wall. This, however, is not considered representative of actual shotcrete conditions and is shown to lead to a 15% lower aggregate and fiber rebound in item 7.3.9.

the complete stress vs depth of penetration curve on a computer screen. Shotcrete mixes that did not comply with the workability range of penetration stresses set for this research program (2 $\pm$ 0.5 MPa using the 9 mm cylindrical needle)[4] were generally discarded and the mixtures re-shot.

These controlled conditions of air flow and shooting consistency yielded an excellent reproducibility of results for the overall rebound. For six consecutive test panels shot using the same conditions, the coefficient of variation of the rebound was found to be only 5% of the average rebound value (rebound between 43 and 46%).

From each test panel shot, a 1 kg sample of fresh shotcrete was collected and heat dried immediately after shooting to determine the in-situ water content of the mix. Also, a 4 kg sample of shotcrete and two 8 kg samples of the rebound material (one from each of the last two layers sprayed) were collected and washed over a 75 μm sieve[5] to obtain the in-situ cementitious content and the aggregate gradation of the in-situ and rebound materials. These gradation curves were later used to calculate the individual rates of rebound for each aggregate size (results for which are presented in Chapter 6).

All shotcrete was produced using pre-bagged, bone dry materials. For the pre-moisturized mixes, water was added in the form of a spray while mixing the materials[6] and the moisture content was determined by heat drying. Unless otherwise specified, all shotcrete mixes were produced using the same ordinary Portland cement added at a rate of 19% by mass of dry-materials (approximately 400 kg/m^3 assuming a 0.40 water to cement ratio). The bulk mass of dry-materials to produce a 1000 kg batch resulted in: cement = 186 kg, sand = 515 kg, 9.5 mm aggregate = 277 kg and steel fibers (when used at 50 kg/m^3) = 22.4 kg.

The aggregates used were concrete sand and river gravel. Unless otherwise stated, the gradation curve used for all mixes was that of an ACI N° 2 gradation - labeled medium-coarse in Fig. 3.2.

---

[4] For comparative purposes, ASTM C 1117 establishes a 3.5 MPa penetration resistance as indicative of initial setting in shotcrete. The 2 MPa consistency used here is shown to lead to a 100 mm overhead build-up in Fig. 3.5.

[5] For the in-situ cementitious content obtained from washout tests, fines from the aggregates passing the 75 μm were accounted for by previous washout tests using only fine and coarse aggregates.

[6] For all pre-moisturized mixes, the material was shot within 5 minutes counting from the time water was added to the dry materials.

Five other aggregate gradation curves were also tested: one fine, one medium and one coarse (all with respect to the ACI N° 2 recommended limits) and two gap-graded gradations, with virtually no material retained on alternate sieves (Fig. 3.2).

SIEVE	Fine	Medium	Med-coarse	Coarse	Discont. I	Discont. II
9.5mm	97%	98%	95%	91%	88%	100%
4.8	85%	83%	73%	63%	88%	78%
2.4	70%	60%	55%	44%	50%	77%
1.2	56%	43%	40%	32%	50%	38%
0.6	37%	27%	23%	18%	44%	38%
0.3	15%	6%	9%	8%	17%	18%
0.2	5%	1%	4%	4%	3%	5%
0.075	1%	0%	1%	1%	0%	0%
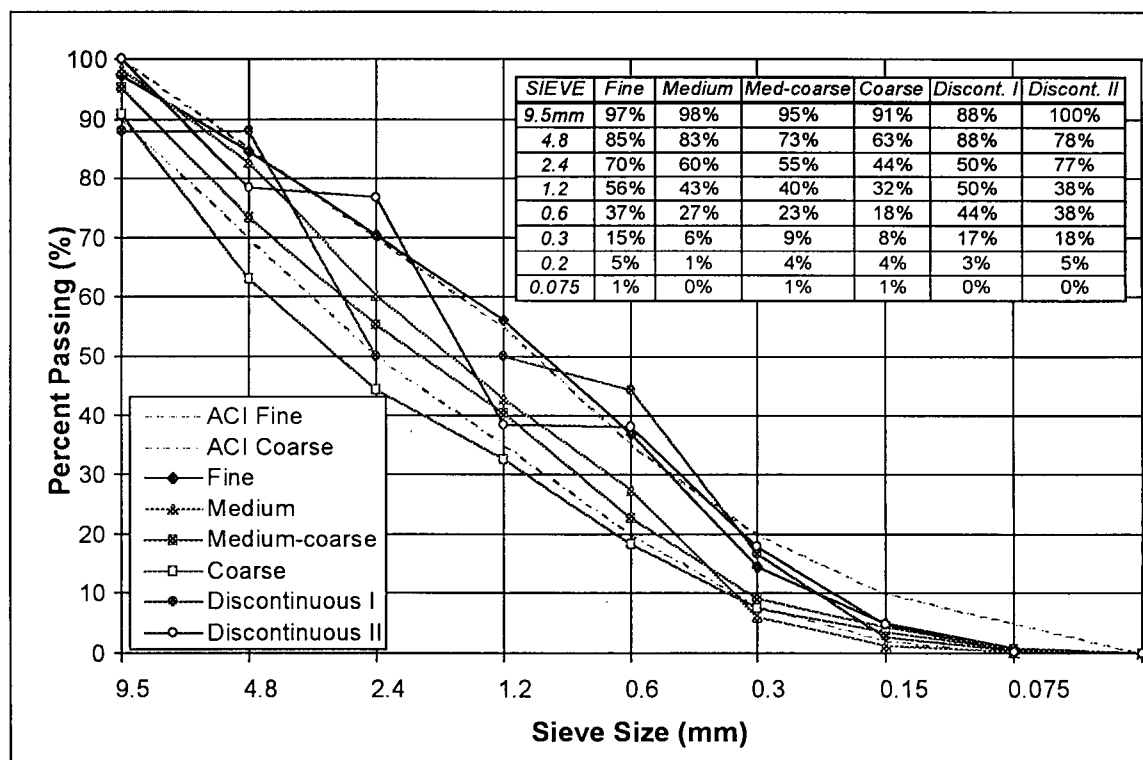
Figure 3.2 - Gradation curves used in this study and the recommended ACI limits for a No. 2 gradation.

The accelerator admixtures used were a caustic powder, a non caustic powder of unknown chemical composition and an aluminate based liquid (named A, B and C, respectively). The powder accelerators were added in the concrete mixer, while the liquid accelerator was added to the shooting water, with the final accelerator content being calculated from the total water content of the in-situ material.

In tests for the maximum overhead build-up thickness, a special test panel was shot overhead with the shooting nozzle kept at a fixed position[7]. This test panel contained 50 mm long wood screws

---

[7] The nozzle was kept at a fixed position in order to build-up a cylindrical shape of shotcrete (approximately constant cross section) as opposed to a conical shape which would not be representative.

which prevented the shotcrete from debonding from the smooth surface of the plywood panel, thus inducing a cohesive failure inside the shotcrete mass.

All test panels were demolded 24 hours after shooting and kept in a moist-room until the age of testing. After 28 days, cores (85 mm in diameter and 100 mm in height)[8] were drilled and tested for compressive strength (3 specimens) and volume of permeable voids (ASTM C 642 - 2 specimens).

3.3 - Results and Analysis

3.3.1 - Parameters of Mix-Design that Influence Rebound

3.3.1.1 - Shooting Consistency and Workability of Dry-mix Shotcrete

When dealing with rebound in dry-mix shotcrete, one of the most important parameters to be considered is the shooting consistency (or shooting stiffness), with rebound increasing for stiffer (i.e. drier) shooting consistencies. It is generally recognized that, although some degree of variation in the amount of water added can be allowed, depending on the position of shooting (overhead or wall), in general, dry-mix shotcrete is a workability controlled material. Thus, if too much water is added, the mix tends to lose cohesiveness and fall-out, while if too little water is used, the rebound tends to increase rapidly.

In practice, control of water addition is left to the experience of the nozzleman, who relies solely on personal judgment. As expected, this leads to a fair amount of variation on rebound measurements between successive shootings by the same operator and an even larger scatter when different operators are compared. This subjectivity in controlling the shooting consistency is one of the first problems encountered when analyzing rebound data from different sources or carrying out research on shotcrete rebound.

However, there are tools available to assess the shooting consistency: ASTM C 1117 (1989) recommends, and some investigators have used (Shchultz, 1982; Prudencio et. al., 1996 and Jolin,

---

[8] Compressive strength values reported here were corrected for the specimen length/diameter ratio by multiplying the maximum laod by 0.90, in accordance with ASTM C 42-87.

1996) penetration tests to measure the consistency of fresh shotcrete. For this research program, a more sophisticated, instrumented version of the penetration test was developed. The device is equipped with one load cell and two LVDTs (Fig. 3.3) and, when using a cylindrical needle, the penetration test results are characterized by an increasing resistance to penetration for the first few millimeters penetrated followed by a plateau, which tends to be reached at a penetration of approximately half the needle diameter (Fig. 3.4).

Because the plateau value in the penetration test is actually a measure of the yield strength of fresh shotcrete (as will be demonstrated in Chapter 5), it is not surprising that it correlates well with the maximum overhead build-up thickness[9] (Fig. 3.5), making this a general test for dry-mix shotcrete *workability* in a broader sense.
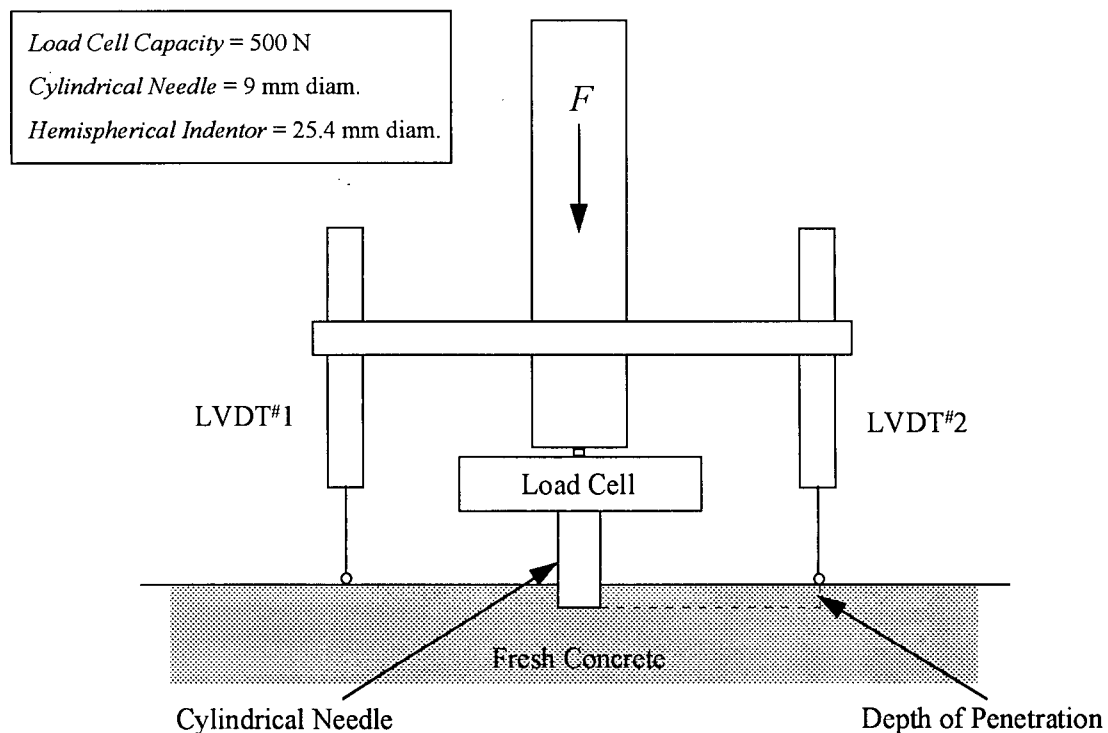
Figure 3.3 - Schematic representation of the electronic penetrometer developed at UBC to measure shotcrete workability. The indentor head can be cylindrical (as recommended by ASTM C 1117) or hemispherical (Chapter 5).

---

[9]In a strict sense, the penetration test is a measure of the yield strength under conditions of compression, while overhead build-up is determined by yield strength under tension. From a rheological point of view, the yield strength under the two conditions can be significantly different for cohesive materials,, but are usually correlated.
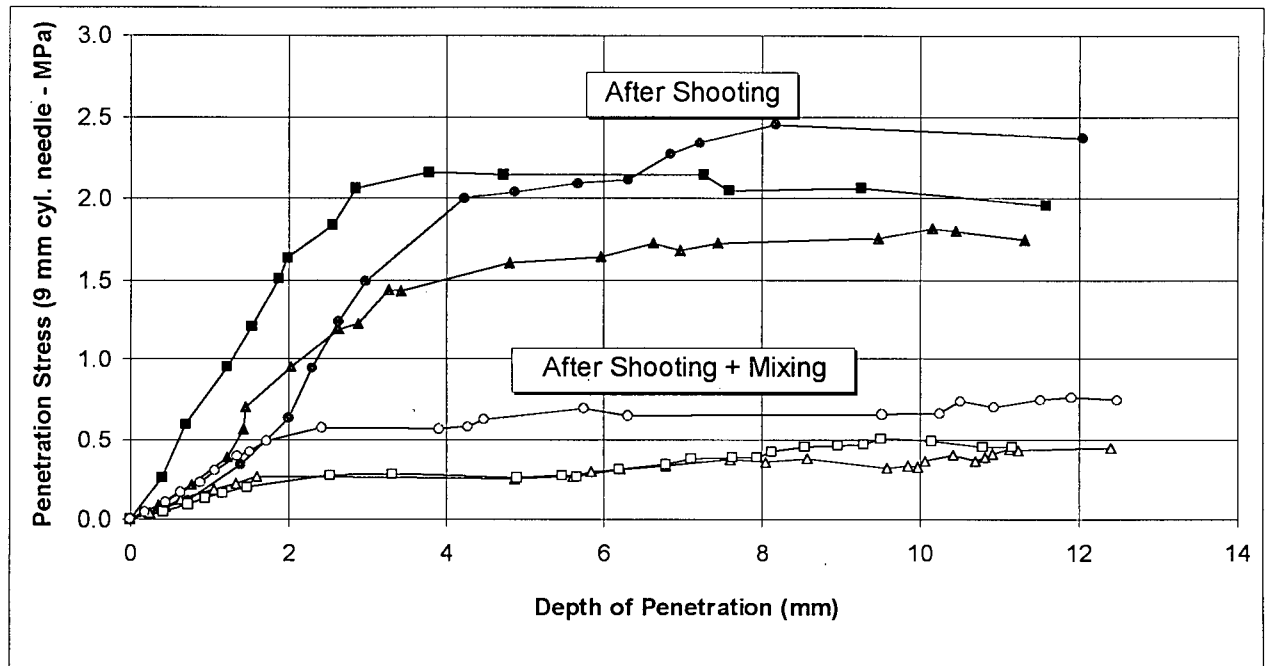
Figure 3.4 - Penetrometer test results showing the yielding plateau and the effect of mixing.
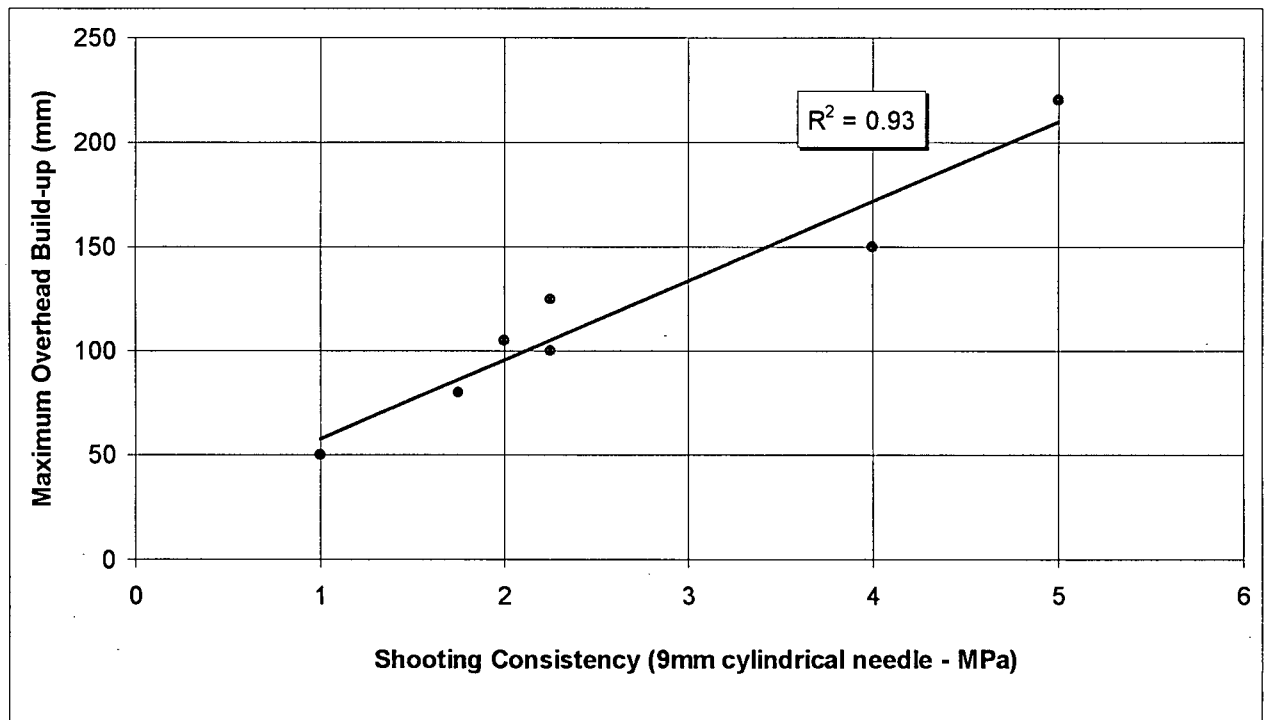
Figure 3.5 - Correlation between the maximum achievable overhead build-up and the shooting consistency measured using the penetrometer.

It is interesting to note that, although the yield strength of fresh dry-mix shotcrete is related to the in-situ water-to-binder ratio by an exponential curve (Fig. 3.6), just as cement paste is known to be (Powers, 1968), the origin and nature of the yield strength of dry-mix shotcrete differs significantly from cast concrete. This can be proven by a simple experiment: If penetration tests are performed on a dry-mix shotcrete test panel immediately after shooting and the *same* shotcrete is then placed in a mixer for four minutes and vibrated back into the panel, the penetration tests systematically reveal a significant reduction in the yield strength due to mixing (Fig. 3.4). Using Fig. 3.5, it can be shown that this drop in the yield strength, caused by mixing, corresponds to an expected loss in overhead build up of more than 50% (from 100 mm for the sprayed situation to less than 50 mm for the sprayed and mixed case).
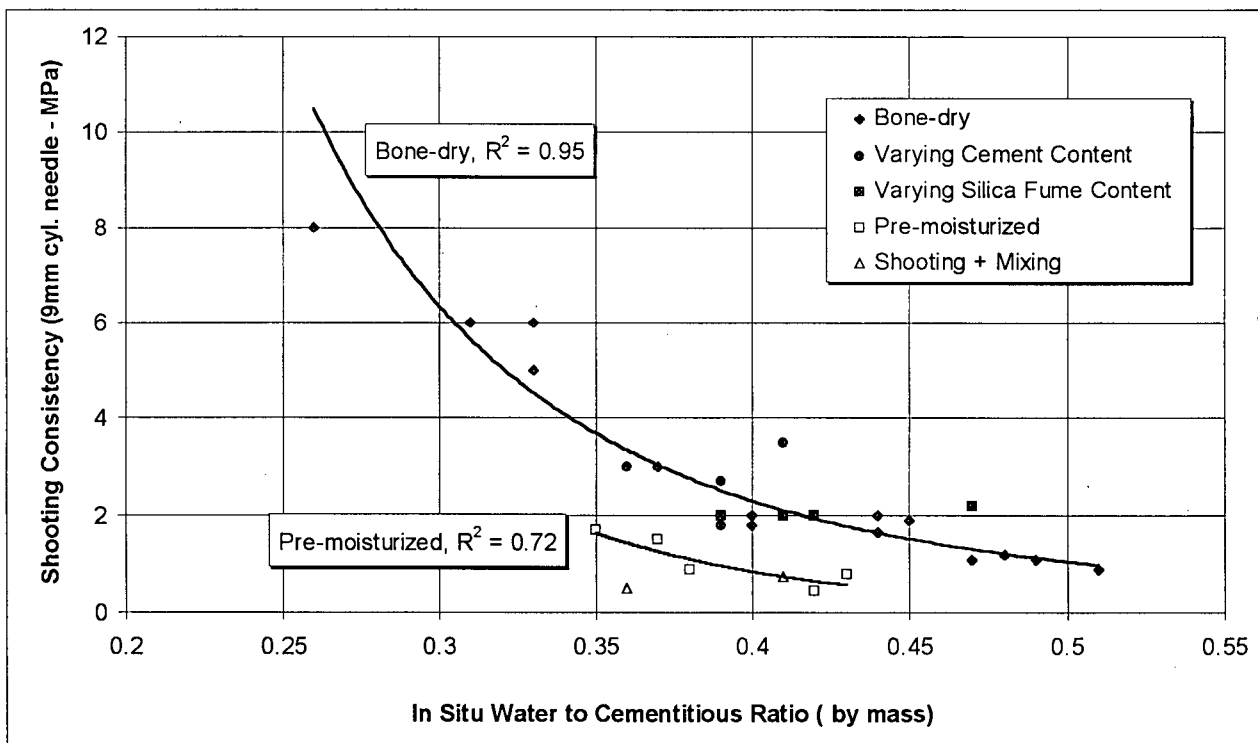
Figure 3.6 - Variation in the shooting consistency as measured by the penetrometer with the in-situ water to binder ratio for pre-moisturized and bone-dry mixes.[+]

While the exact cause for this is not known (possibly a breakage of the initial hydration products or a particle dispersion problem as suggested by Powers, 1968). It is evident that dry-mix shotcrete's unique feature of water contacting the cement and reaching its final mixing position

---

[+] Throughout this thesis, R-square values are reported as a measure of the reliability of a trendline. For non linear cases, a transformed regression model is used by the software package (Microsoft Excel'97, Users Manual pp.350).

within a fraction of a second, provides it with inherently unique workability features, that are distinct from those of a cast concrete mix of identical mixture proportions.

When carrying out a research program in concrete technology, it is important to set certain criteria that guarantee comparability among mixtures of widely different compositions. In the case of dry-mix shotcrete, there are basically two possibilities: an "equal shooting water" criterion, in which the nozzleman keeps the water flow constant regardless of the shooting consistency, or an equal workability criterion, for which the nozzleman is allowed to change the water to achieve the desired consistency.

In practice, the first possibility, i.e. "equal shooting water", would not be realistic since mixtures containing more fines (greater cement content or with silica fume) are known to demand more water while shooting[10]. Therefore, throughout this research program, the equal workability criterion was adopted with the 9 mm cylindrical needle penetrometer plateau resistance adopted as the reference to guarantee uniformity in this criterion.

3.3.1.2 – Variation of Rebound with Shooting Consistency and Pre-moisturization

Results for the rebound tests for 15 test panels produced at various shooting consistencies (identical mix proportions but different water contents) are shown in Fig. 3.7. These data show a linear increase in rebound with the stiffness of the mix as expressed by the plateau penetration stress using the 9 mm cylindrical needle. The best fit line indicates a 3.8% increase in the rate of rebound per MPa of shooting consistency.

As a consequence of the increased rebound, and because rebound is composed primarily of aggregates, the in-situ cement content was also found to increase with the shooting stiffness (Fig. 3.8). Therefore, although the design mix contained 400 kg of cement per m³, the trend line indicates that the in-situ cement content varied from approximately 440 kg/m³ for a "wet"

---

[10] For a fixed shooting consistency, the fact that mixes containing more fines demand a greater water flow while shooting, does not imply in a greater in-situ cementitious content. In fact, as demonstrated by Table 1 for the case of varying the cement content and Fig. 3.14 for the case of silica fume addition, the in-situ water to cementitious ratio is *not* changed. This is a consequence of the lower overall rebound for mixes containing more fines - i.e. a greater water flow is required because shotcrete builds-up faster.

shooting consistency (1 MPa) to more than 600 kg/m^3 for a "dry" shooting consistency (8 MPa). This undesired enrichment of the in-situ mix clearly shows that, in addition to the high rates of rebound, there are other disadvantages of shooting at too stiff a consistency.

As mentioned earlier, it is the in-situ water to cementitious ratio that determines the yield strength of fresh shotcrete (Fig. 3.6), therefore it is not surprising that the compressive strength was found to increase for stiffer shooting consistencies (Table 1). However, Table 1 also shows that the volume of permeable voids increases rapidly for a shooting consistency greater than 5 MPa, resulting in a sharp drop in compressive strength to 48 MPa for the driest mix. This is another disadvantage of shooting at a very stiff (dry) consistency.
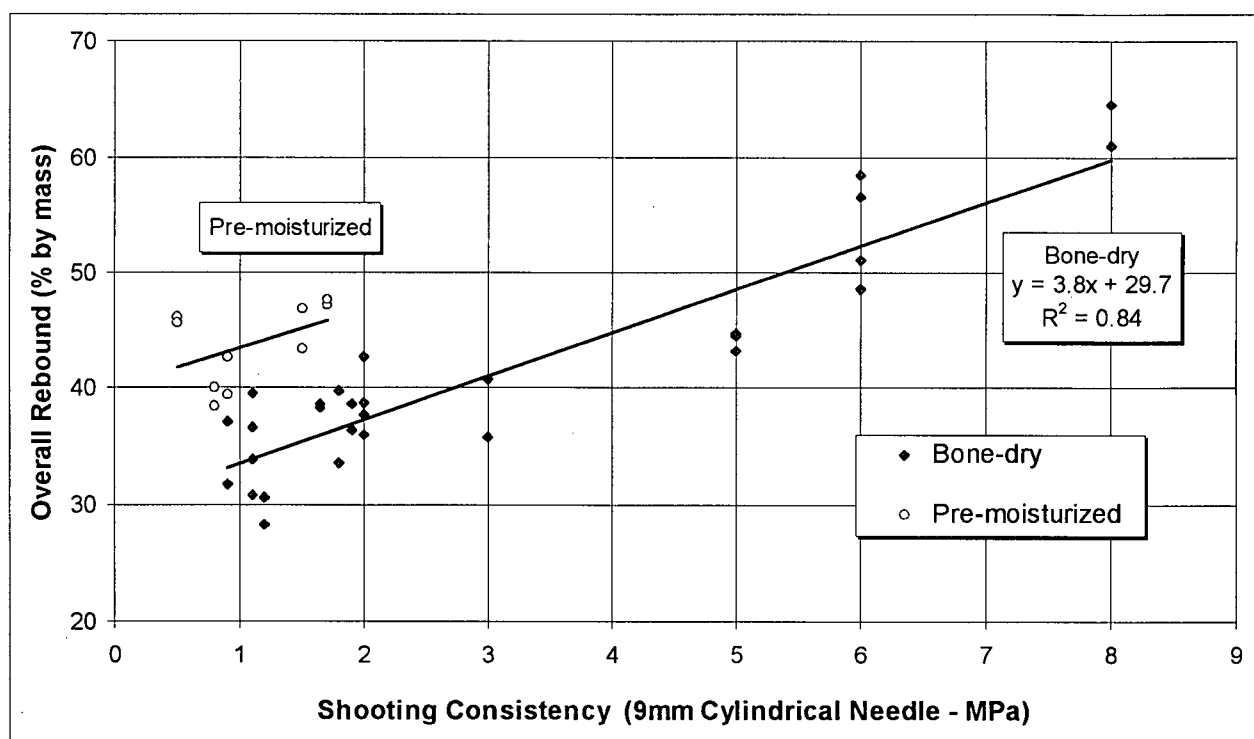
Fig. 3.7 - Variation in the overall rebound with the shooting consistency as measured using the penetrometer.

The effect of pre-moisturization on the overall rate of rebound is also shown in Fig. 3.7. These data indicate that, for a given shooting consistency, pre-moisturized mixes have a somewhat increased overall rate of rebound. However, *for a given consistency*, the pre-moisturized mixes

showed an increased compressive strength when compared with mixes shot using bone dry materials (Table 1).

The explanation for this can be found in Fig. 3.6, in which the relationship between the shooting consistency and the in-situ water to binder ratio is presented. In this figure, it can be seen that the pre-moisturized mixes do not show the same dependence of the consistency on the water to binder ratio as the mixes shot in the bone-dry state. Instead, for the same water to binder ratio, the pre-moisturized mixes show a lower shooting consistency, close to that of mixes that have been subjected to mixing after shooting (Fig. 3.6). While the exact reasons for this are not known, one can assume that, similar to the effect of mixing, pre-moisturizing also causes a disruption of initial hydration products and/or has a particle dispersion effect that leads to a lower shooting stiffness. This effect requires using less shooting water in order to achieve an adequate shooting consistency, and hence a lower in-situ water to cement ratio and greater compressive strength.
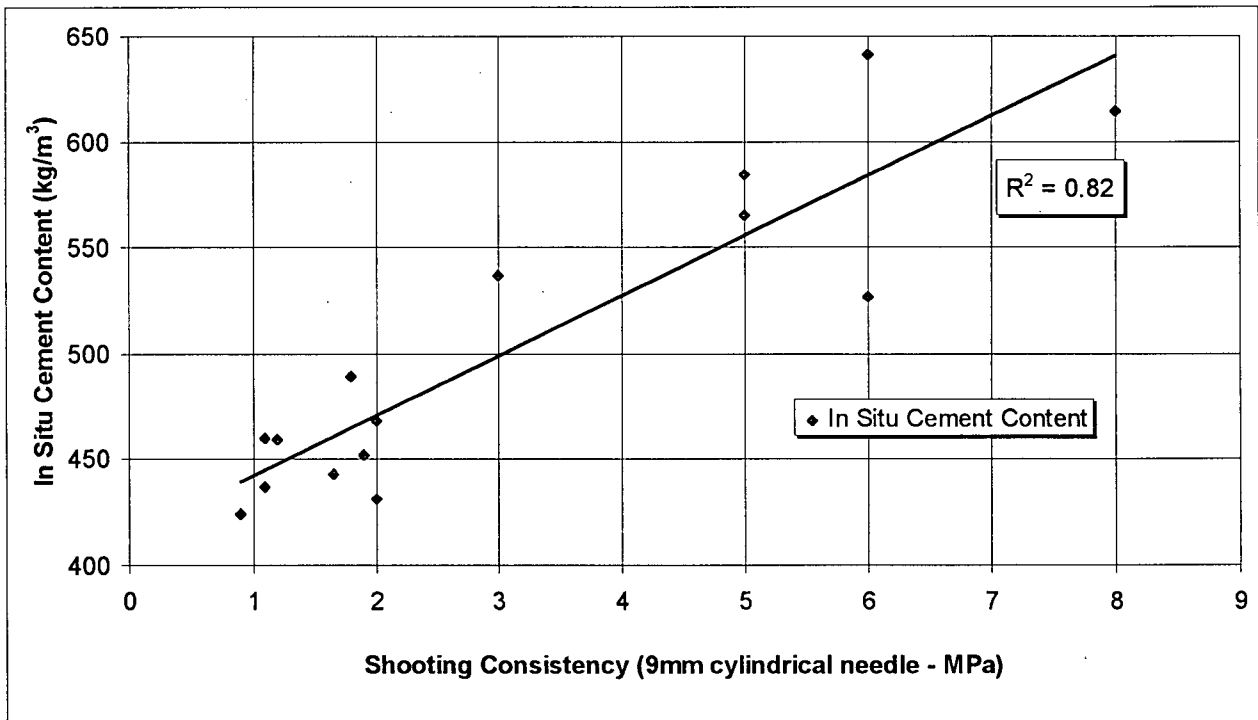
Figure 3.8 - Variation in the in-situ cement content with the shooting consistency measured using the penetrometer.

Table 3.1 - Parameters tested and numerical results obtained (continued on next page).

Panel	Parameter Tested	Amount Varied	Consistency[a] (MPa)	Water[b] Content (%)	w/c	Cement[c] (kg/m³)	Rebound 1[d] (%)	Rebound 2 (%)	Rebound 3 (%)	Com. Str.[e] (MPa)	Voids[f] (%)
1	Shooting Consistency	0.9 MPa	0.9	9.65	0.51	424	36.7	31.7	37.1	55.7	14.2
2		1.1 MPa	1.1	9.17	0.47	437	46.6	39.5	36.6	54.7	14.9
3		1.1MPa	1.1	10.10	0.49	460	38.4	30.8	33.9	56.3	13.6
4		1.2 MPa	1.2	9.77	0.48	459	40.7	28.3	30.6	72.8	12.4
5		1.65 MPa	1.7	8.70	0.44	443	43.0	38.3	38.7	69.8	11.9
6		1.8 MPa	1.8	8.85	0.40	489	46.3	39.7	33.6	66.5	12.2
7		1.9 MPa	1.9	9.06	0.45	452	41.3	36.4	38.6	51.6	15.0
8		2 MPa	2.0	8.46	0.44	431	39.7	38.7	36.0	48.9	14.5
9		2 MPa	2.0	8.34	0.40	468	46.7	37.7	42.7	74.6	11.8
10		3 MPa	3.0	8.90	0.37	537	n.a.	40.7	35.8	65.2	13.9
11		5 MPa	5.0	8.23	0.33	565	49.7	43.2	44.5	62.8	15.3
12		5 MPa	5.0	8.46	0.33	584	46.1	44.7	44.6	76.8	10.7
13		6 MPa	6.0	8.70	0.31	641	54.6	48.6	58.5	72.7	15.3
14		6 MPa	6.0	7.76	0.33	527	n.a.	51.1	56.5	82.6	13.9
15		8 MPa	8.0	7.07	0.26	614	64.9	64.5	61.0	48.4	17.0
16	Cement Content	350 kg/m³	3.0	9.41	0.41	520	57.4	53.8	41.0	72.3	11.3
17		400 kg/m³	2.0	8.34	0.40	467	46.7	37.7	42.7	74.6	11.8
18		450 kg/m³	3.0	9.65	0.36	609	49.8	34.2	33.4	72.6	10.2
19		500 kg/m³	2.5	11.11	0.39	634	51.8	36.1	35.0	67.0	8.5
20		555 kg/m³	2.0	9.41	0.39	543	42.3	31.4	30.8	72.4	9.7
21	Aggregate Gradation	fine	1.9	9.40	0.48	441	36.7	28.4	37.6	70.1	12.5
22		medium	2.0	9.40	0.49	432	na	43.0	43.9	57.3	13.6
23		medium	2.0	8.81	n.a.	n.a.	n.a.	42.9	43.1	56.2	13.5
24		medium	2.3	9.29	n.a.	n.a.	n.a.	46.3	45.2	54.1	13.5
25		med. coarse	2.0	8.34	0.40	467	46.7	37.7	42.7	74.6	11.8
26		med. coarse	2.3	8.81	0.36	551	58.4	n.a.	42.6	69.4	10.5
27		med. coarse	2.5	8.34	0.41	456	53.3	43.2	50.1	72.3	12.3
28		coarse	1.4	9.05	0.41	489	56.0	49.0	46.3	75.9	11.1
29		Discont. I	2.0	8.58	0.39	489	39.5	36.0	35.0	na	na
30		Discont. II	2.5	10.00	0.40	526	52.4	38.7	29.2	61.1	12.1
31	Silica Fume	0%	2.0	8.34	0.40	467	46.7	37.7	42.7	74.6	11.8
32		0%	2.5	8.34	0.41	456	53.3	43.2	n.a.	72.3	12.3
33		4%	2.0	7.99	0.39	459	41.0	36.0	33.9	58.0	10.5
34		8%	2.0	7.87	0.42	421	41.2	27.0	35.0	62.1	8.0
35		12%	2.0	8.34	0.41	459	39.4	28.7	33.9	62.8	8.0
36		16%	2.0	9.29	0.47	442	40.3	22.7	33.8	60.5	11.7
37	Accelerator	0%	2.0	8.34	0.40	467	46.7	37.7	42.7	74.6	11.8
38	caustic powder (A)	0%	2.5	8.34	0.41	456	53.3	43.2	n.a.	72.3	12.3
39		0.5%	4.0	9.05	0.42	486	52.6	37.1	38.9	70.2	12.2
40		1.5%	5.0	9.65	0.53	407	50.4	37.4	41.5	45.0	14.4
41		3.0%	6.5	10.99	0.54	455	52.8	47.0	52.0	41.7	16.6
42		6.0%	8.0	11.11	0.47	527	56.2	44.5	46.9	33.7	18.7
43	non-caustic powder (B)	1.5%	2.5	8.93	0.43	463	52.7	41.3	41.3	71.8	12.4
44		3.0%	4.0	8.70	0.45	433	56.3	44.6	43.4	65.9	12.4
45		6.0%	6.0	8.58	0.43	452	57.7	40.4	46.0	61.8	12.9
46	aluminate liquid (C)	1.5%	4.5	7.76	0.40	437	61.8	n.a.	41.4	47.2	16.6
47		3.0%	6.5	8.34	0.46	411	49.8	47.7	43.8	45.2	17.9
48		6.0%	8.0	9.05	0.53	380	52.2	46.8	48.5	37.6	17.5
49	Air Flow	100 cfm	1.0	7.41	0.43	386	n.a.	63.3	74.6	n.a.	17.5
50		100 cfm	1.0	9.53	n.a.	na	71.5	61.0	74.0	n.a.	15.0
51		150 cfm	2.2	9.05	0.41	500	62.0	45.7	49.8	64.0	14.4
52		150 cfm	2.5	n.a.	n.a.	n.a.	n.a.	56.1	55.8	n.a.	14.6
53		200 cfm	1.7	n.a.	n.a.	n.a.	n.a.	48.5	44.3	n.a.	15.0
54		250 cfm	2.0	9.65	0.38	570	44.6	34.0	39.3	70.5	12.1
55		300 cfm	2.0	8.34	0.40	467	46.7	37.7	42.7	74.6	11.8
56		350 cfm	2.2	9.65	0.39	515	49.0	40.0	41.0	73.4	11.8
57		400 cfm	1.5	n.a.	0.44	434	n.a.	46.3	45.8	62.6	15.2

Table 3.1 -Shotcrete parameters tested and numerical results obtained (continuation).

Panel	Parameter Tested	Amount Varied	Consistency[a] (MPa)	Water[b] Content (%)	w/c	Cement[c] (kg/m³)	Rebound 1[d] (%)	Rebound 2 (%)	Rebound 3 (%)	Com. Str.[e] (MPa)	Voids[f] (%)
58		wall	2.0	8.34	0.40	467	46.7	37.7	42.7	74.6	11.8
59	Shooting	wall	2.5	8.34	0.41	456	53.3	43.2	n.a.	72.3	12.3
60	Position	overhead	n.a.	8.46	0.40	472	52.4	40.6	38.8	na	na
61		overhead	n.a.	8.70	0.38	508	49.0	38.6	42.4	na	na
62		overhead	1.5	9.05	0.40	507	55.4	41.2	38.2	62.9	12.7
63	Shooting	0°	2.0	8.34	0.40	467	46.7	37.7	43.0	74.6	11.8
64	Angle	15°	2.0	8.34	0.37	505	44.6	44.7	40.0	65.4	12.0
65		30°	2.0	9.65	0.46	468	51.1	50.2	47.2	63.9	13.1
66		0.70%	1.5	8.58	0.37	516	55.7	46.8	43.4	72.2	13.5
67		1.20%	0.5	8.93	0.42	n.a.	47.2	46.1	45.6	64.9	12.8
68	Pre-moist	1.40%	0.9	8.70	0.38	516	50.0	42.7	39.4	76.1	11.7
69		1.40%	1.7	7.87	0.35	503	51.9	47.1	47.6	76.5	12.6
70		2.25%	0.8	8.58	0.43	447	53.8	40.0	38.4	75.4	12.2
71		shot	1.9	8.58	0.41	465	52.2	36.4	32.6	n.a.	n.a.
72	Mixing	shot+mixed	0.7	8.58	0.41	465	n.a.	n.a.	n.a.	60.8	12.4
73		shot	2.5	7.99	0.36	502	54.0	36.5	42.1	n.a.	n.a.
74		shot+mixed	0.5	7.99	0.36	502	n.a.	n.a.	n.a.	55.0	12.8
75		0%	2.0	n.a.	n.a.	n.a.	n.a.	36.5	38.6	60.2	12.0
76	Limestone	0%	2.0	n.a.	n.a.	n.a.	n.a.	44.2	44.3	54.8	13.1
77		8%	1.5	n.a.	n.a.	n.a.	n.a.	34.8	43.2	59.5	13.2
78		16%	1.5	n.a.	n.a.	n.a.	n.a.	28.7	38.6	60.2	13.1

a - penetration stress using the 9 mm diameter cylindrical needle   b - mass water to dry-materials ratio obtained by heat drying
c - cement content obtained by wash-out of a 4 kg shotcrete sample   d - from 1st, 2nd and 3rd layers (thickness of resp. 25, 50 and 50 mm)
e - 28 day compressive strength (average of 3 spec.) corrected for h/d   f - void content at 28 days (average of 2 spec.)

3.3.1.3 - Variation of Rebound with Cement Content

The influence of the design mix cement content on the overall rate of rebound is presented in Fig. 3.9. A decreasing rate of rebound for the mixes containing more cement can be noticed. It is interesting to note that the slope of the best fit trend line indicates a 7.4% decrease in rebound per 100 kg of cement in the design mix, a value that is close to the value described by Austin (1995) who reported 6.7% less rebound per 100 kg of cement.

Although the cement phase rebounds far less than the aggregates, this drop in the overall rate of rebound for richer mixes cannot be attributed only to a lower aggregate content of the design mix. In effect, gradation analysis of the in-situ and rebound material reveals that the rate of rebound of all individual aggregate sizes is reduced with the greater cement content. From Fig. 3.10, it may be seen that, for the 4.8 mm aggregates, the rate of rebound decreases from 65 to 45 % for a cement content increasing from 350 to 555 kg/m³.
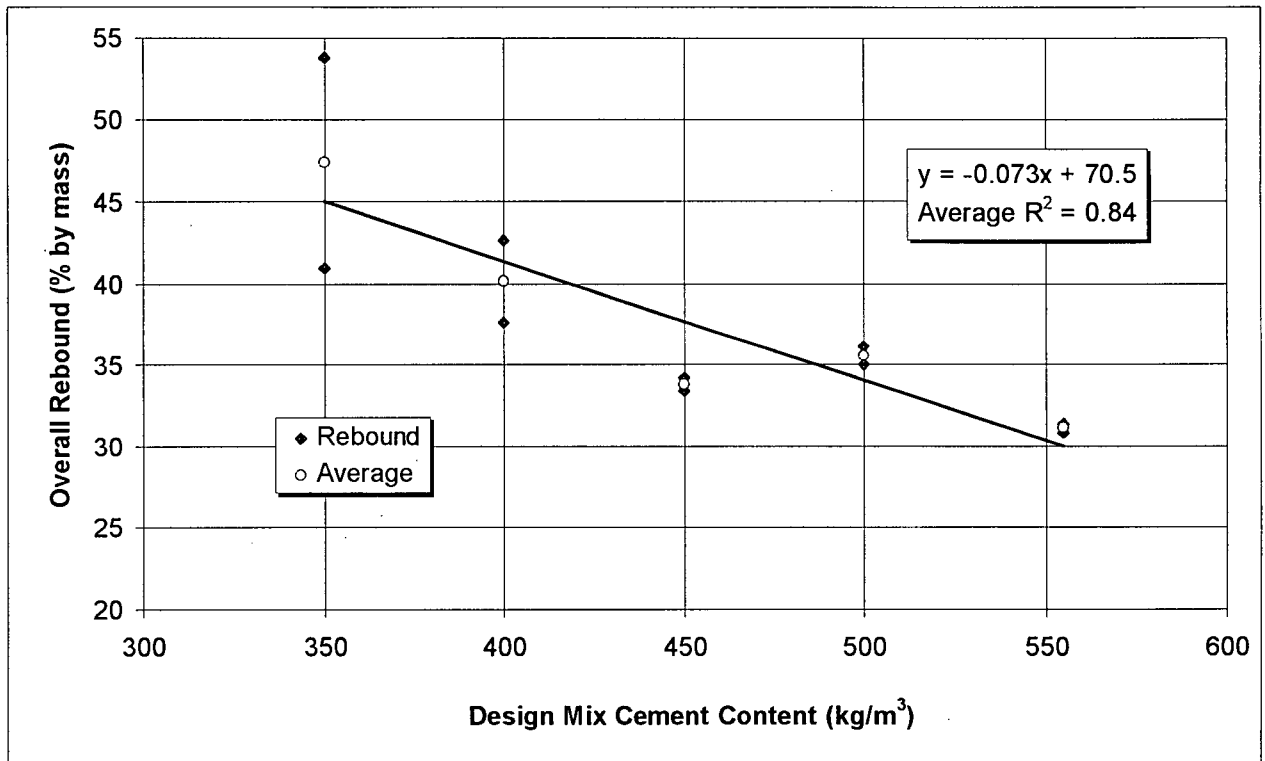
Figure 3.9 - Variation in the overall rate of rebound with the design mix cement content.
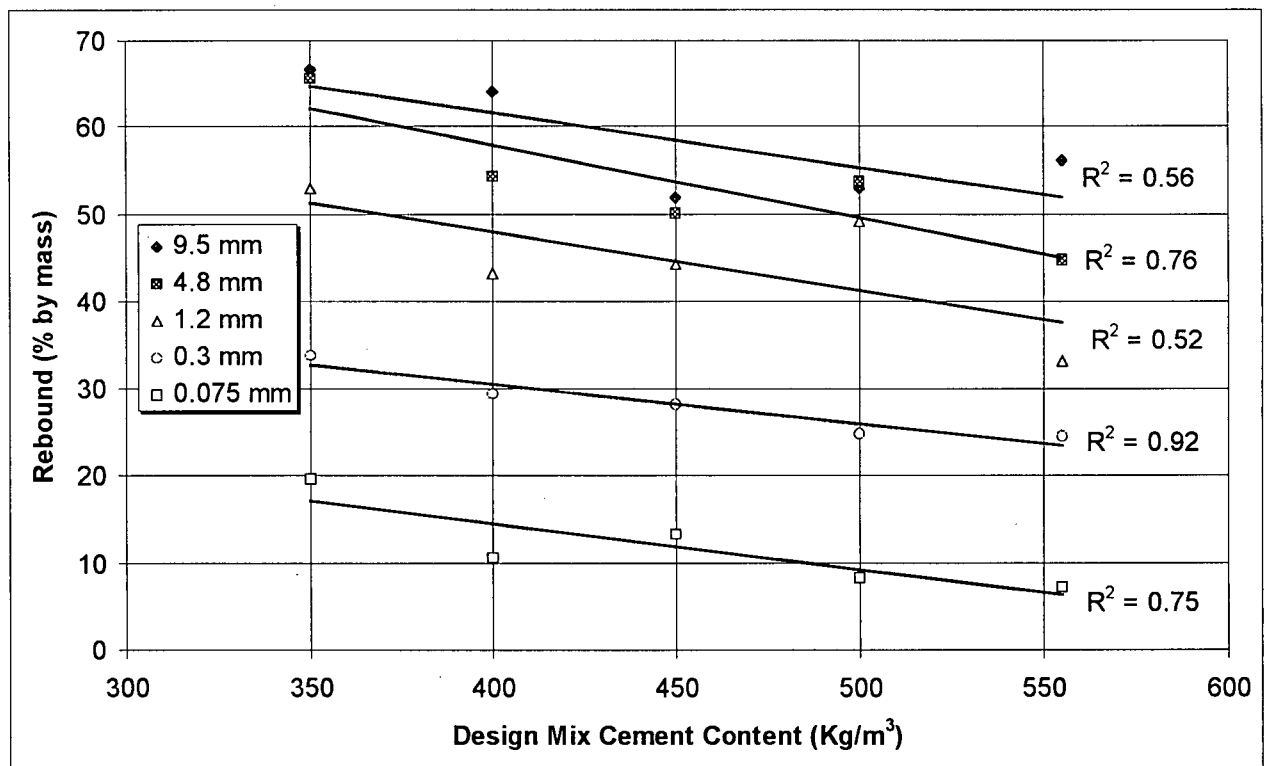
Figure 3.10 - Variation in the aggregate rebound with the cement content for different aggregate sizes.

As a result of the decreased aggregate rebound and despite the fact that the in-situ cement content increases with the design mix cement content (Fig. 3.11), this increase is not proportional to the amount of cement in the design mix. Thus, the ratio between the in-situ cement content and the design cement content decreases from 1.5 to 1.0 for a design mix changing from 350 to 555 kg of cement per m^3.
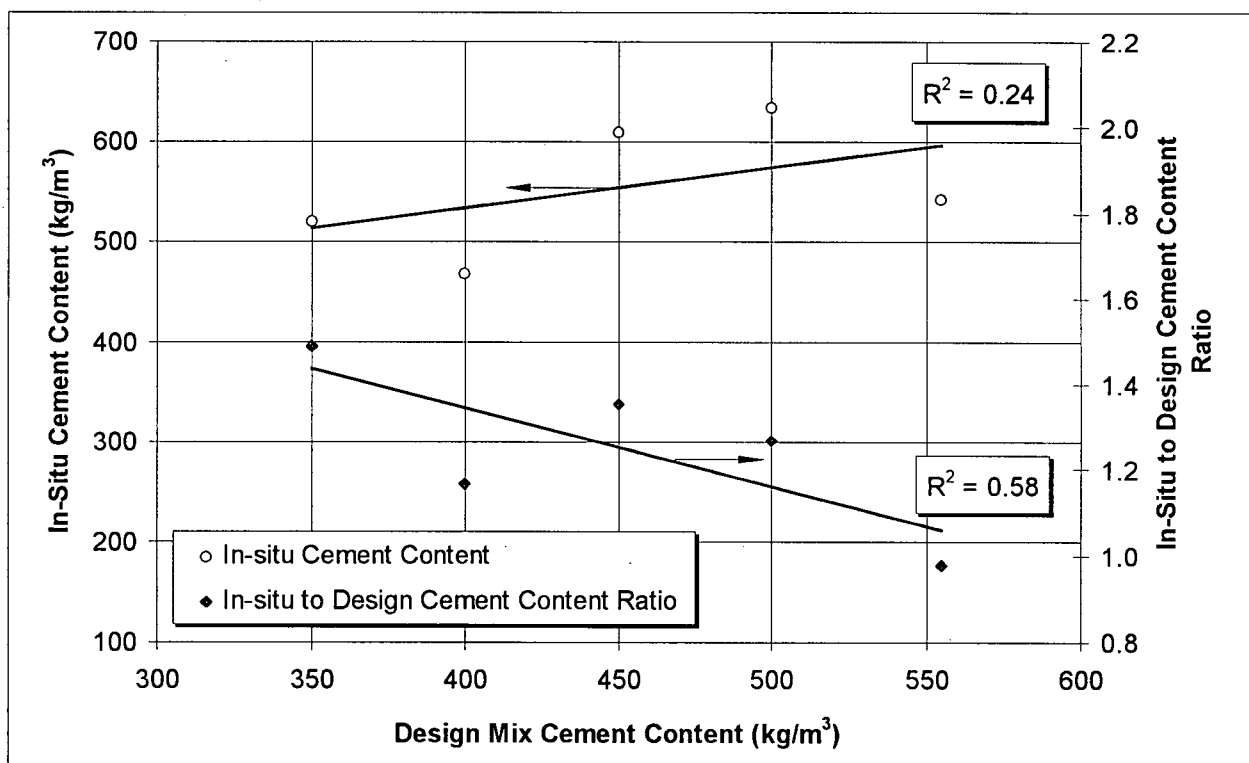
Figure 3.11 - Variation in the in-situ cement content and in-situ to design mix cement content ratio with the design mix cement content.

It is interesting to note that, contrary to fresh cast concrete, dry-mix shotcrete is not required to flow while placing. With dry-mix shotcrete a stiff consistency is desirable to allow for a greater build-up of thickness. Therefore, assuming that the rheology of fresh concrete is generally determined by the water to cement ratio, it should be possible to produce shotcrete at low design cement contents and still attain the desired strength by reducing the shooting water[11]. However, the results presented here show that, at low cement contents, the aggregate rebound increases and therefore the in-situ cement content rises. As a result, it is generally found that it is not cost-

---

[11] It is implied here that, in theory, it should be possible to, while maintaining a constant water to cement ratio, reduce both the cement and water contents without a significant effect on strength.

effective to produce dry-mix shotcrete at cementitious contents below approximately 400 kg/m³. The reason for this and the mechanism through which a higher cement content leads to a lower aggregate rebound are analytically presented in Chapter 6.

As for the influence of the cement content on the strength of the hardened shotcrete, Table 1 shows that, despite the widely varying as-batched cement contents tested (between 350 and 555 kg/m³), the compressive strength was virtually unaffected. This is a consequence of the condition of equal workability (i.e. equal penetration resistance) imposed which, in turn, led to virtually equal in-situ water to cement ratios (Table 1) and hence equal strengths[12].

3.3.1.4 - Variation of Rebound with Aggregate Gradation

Results for the variation in the overall rate of rebound with the various aggregate gradations tested are shown in Fig. 3.12. These data confirm that, on an average, coarser aggregate gradations lead to greater rebound. This can be attributed to the greater tendency to rebound that larger aggregates have. Thus, mixes containing a greater proportion of large aggregates result in a greater overall rate of rebound.

It is interesting to note that, on average, the discontinuous (gap graded) mixes tested had an overall rate of rebound similar to, or lower than, that of the continuous gradation mixes. This result leads one to question the universality of the ACI Committee 506 (1990) recommendation for continuous aggregate gradations for shotcrete or, at least, shows that shotcrete of comparable rebound performance can be produced even if certain aggregate sizes are not available.

3.3.1.5 - Variation of Rebound with Silica Fume Content

Results for the variation in the overall rate of rebound with the silica fume content are presented in Fig. 3.13. This figure shows a decreasing rate of rebound with an increase in the silica fume content. The best fit trend line indicates that this decrease in rebound is, on average, of the order of 8% less rebound per 10% of silica fume substitution for cement. This value is, once again, in

---

[12] It should be noticed that, for conditions of equal aggregate rebound, an increase in the cement content should lead to a greater compressive strength due to a decreased water to cement ratio (i.e. increased shooting stiffness).

close agreement with the data reported by Austin, 1995 (6 to 7% less rebound per 10% of silica fume).
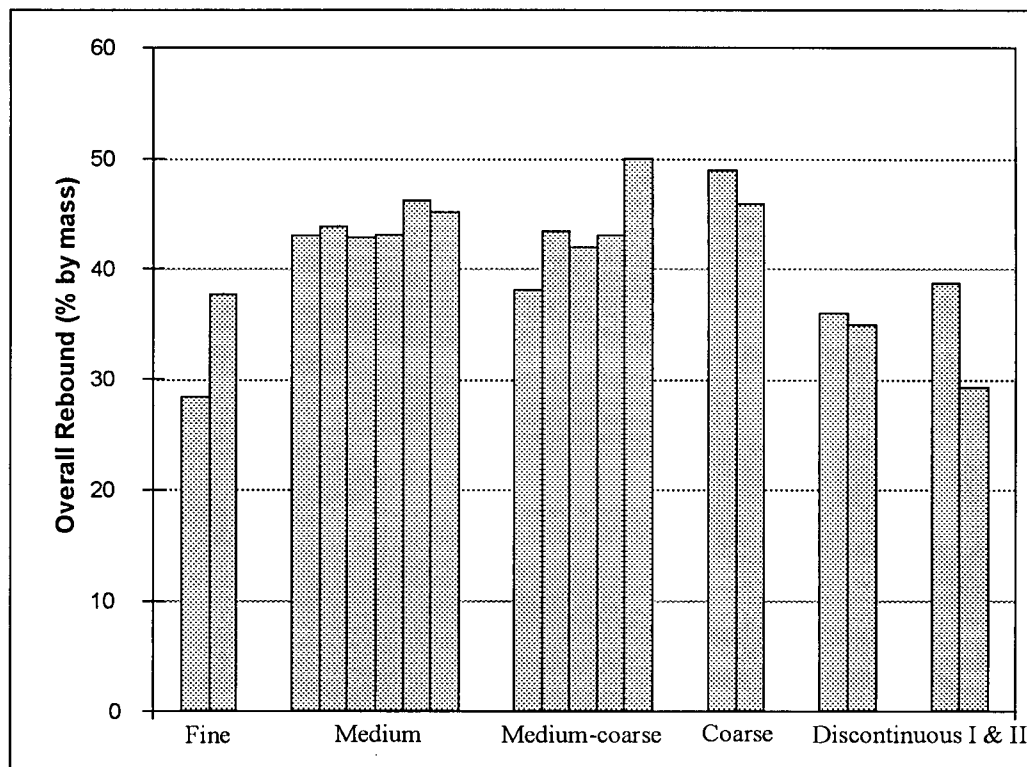
Figure 3.12 - Variation in the overall rate of rebound with the aggregate gradation (each column represents one trial).

Due to the decrease in overall rebound and given that rebound consists mainly of aggregates, the in-situ cementitious content is also found to decrease with an increasing silica fume content (Table 1). To illustrate this point, it may be said that gradation analysis done on the in-situ and rebound material reveals that, for the 9.5 mm aggregate size, the rebound decreased from 70 to 37% for silica fume contents of 0 and 12%, respectively.

With respect to the compressive strength of the hardened shotcrete, Fig. 3.14 reveals that this property was virtually unaffected by the silica fume content. In part, this can be explained by the fact that the conditions of equal workability imposed led to very uniform in-situ water to cementitious ratios for all mixes shot (with the exception of the mix containing 16% silica fume which required more water - Fig. 3.14). However, it should also be considered that, at a given water to cementitious ratio, the increase in compressive strength that is usually seen for *cast*
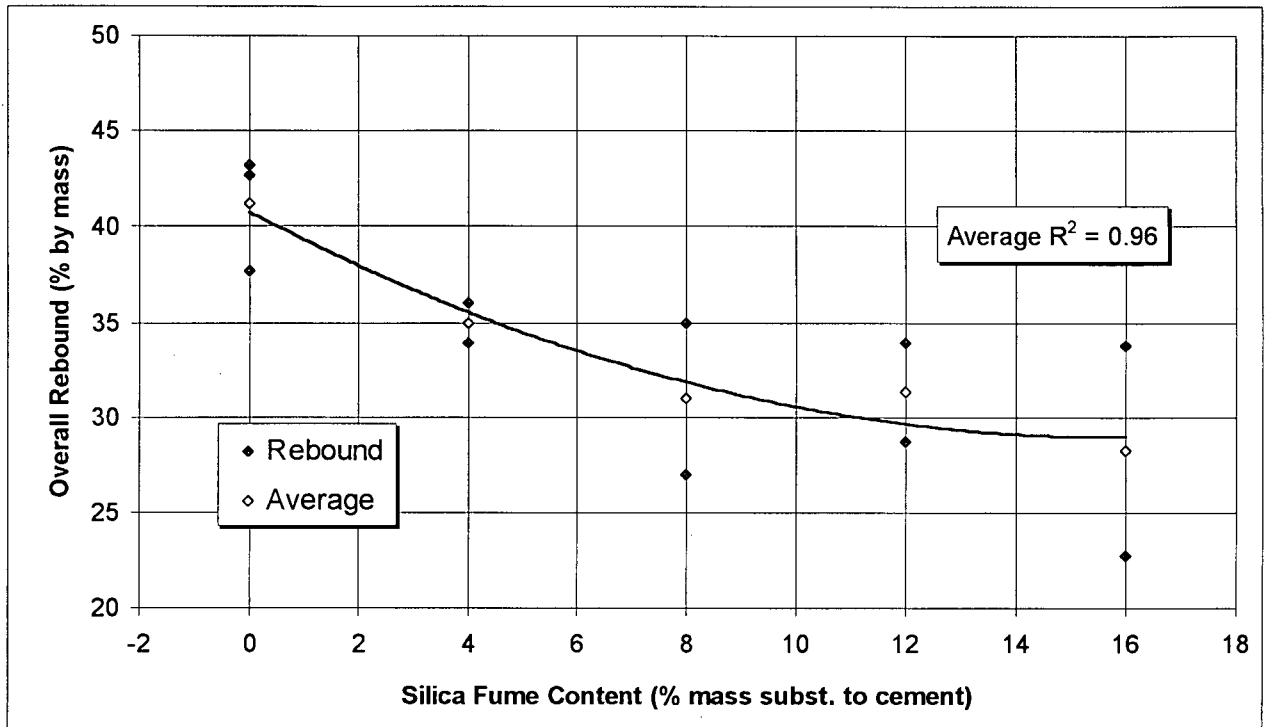
Figure 3.13 - Variation in the overall rate of rebound with the silica fume content.
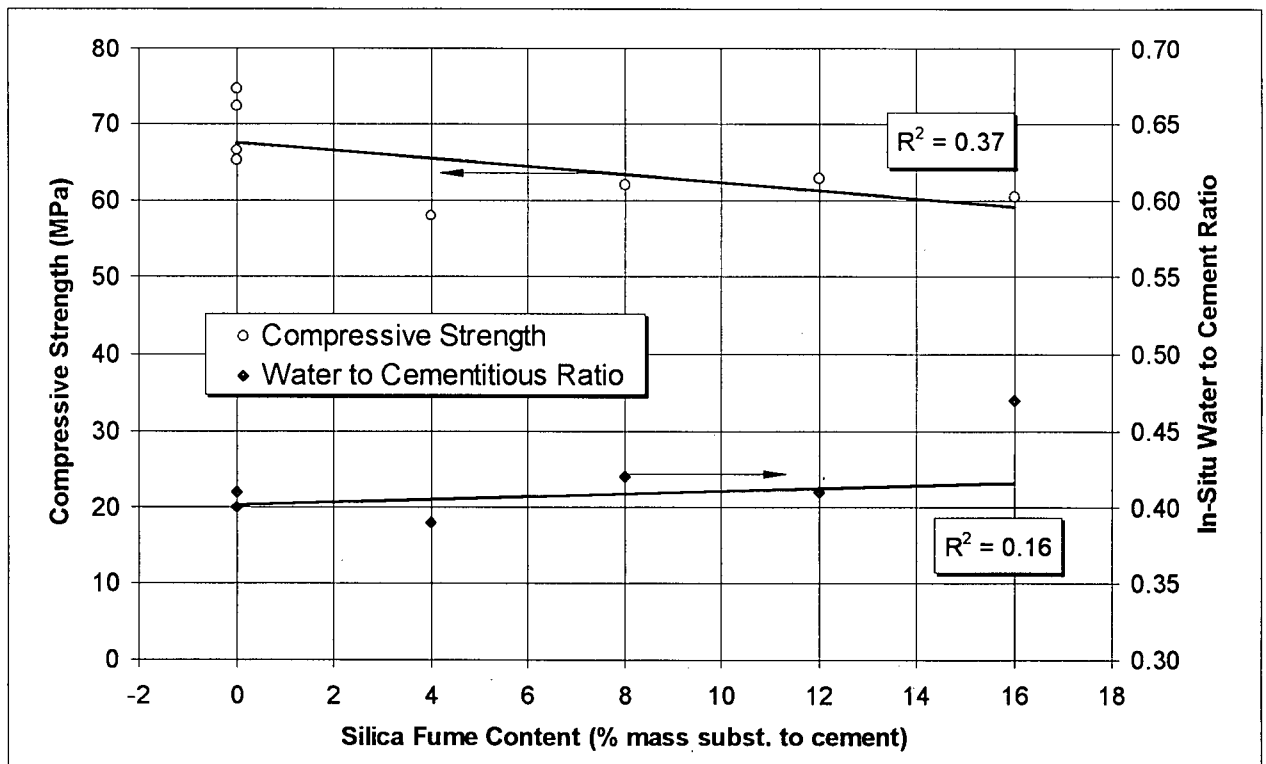
Figure 3.14 - Variation in the compressive strength and in-situ water to cementitious ratio with the silica fume content.

concrete containing silica fume is attributable not only to the pozzolanic action, but also to a densifying action at the paste-aggregate interface (Goldman & Bentur, 1994). This may not apply to the same extent in dry-mix shotcrete mixtures given their distinct (stiff) rheology with virtually no bleeding water. Similar results of silica fume showing no significant increase in the compressive strength of dry-mix shotcrete were reported by Wolsiefer & Morgan (1993)[13].

3.3.1.6 - Variation of Rebound with Accelerator Type and Content

Results for the variation in the overall rate of rebound with the accelerator type and content are shown in Fig. 3.15. These data indicate that all of the products tested led to an increased average rate of rebound for accelerator contents greater than 1.5%.
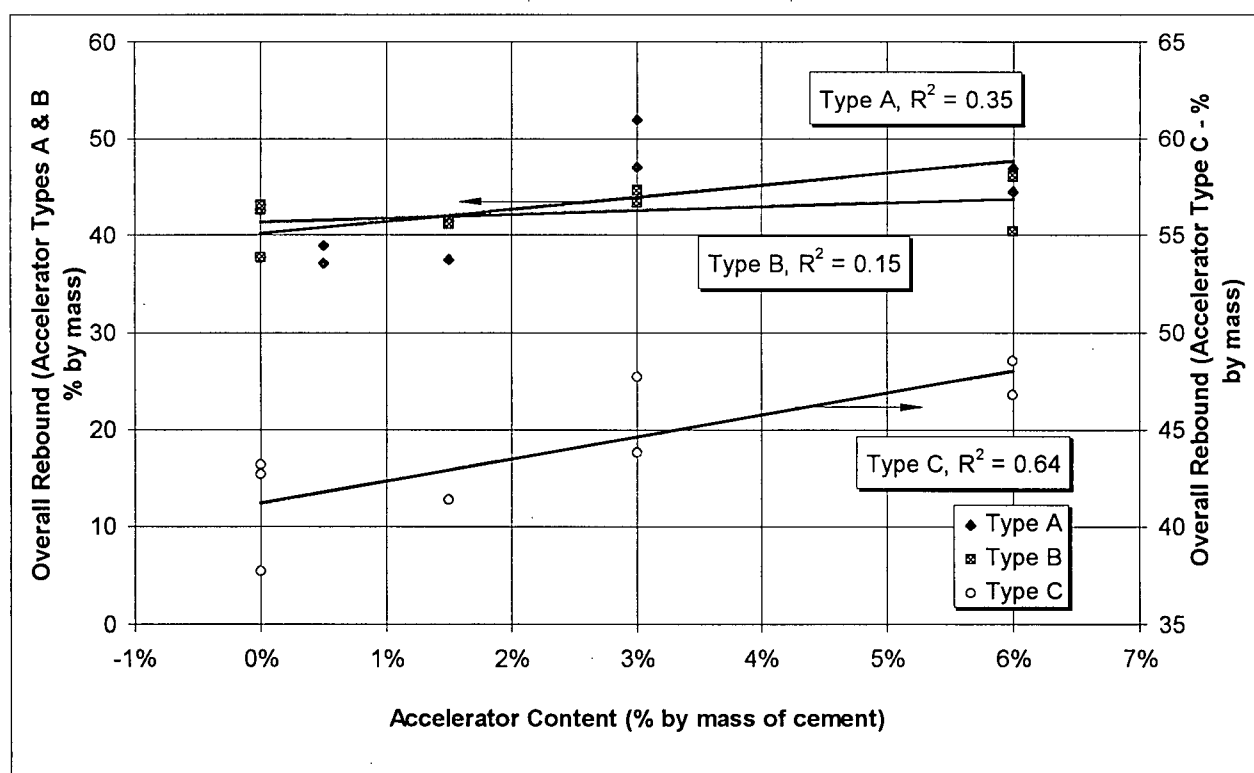
Figure 3.15 - Variation in the overall rate of rebound with the accelerator admixture type and content.

---

[13] Again, for conditions of equal aggregate rebound, it is expected that an increase in the silica fume content may allow for a lower water to cementitious ratio and therefore an increased compressive strength.

An explanation for this can be found in Fig. 3.16 in which the penetration resistance, measured immediately after shooting using the 9 mm cylindrical needle, is presented as a function of the accelerator type and content. This figure reveals that there is a close relationship between the yield strength of fresh shotcrete and its rebound, with stiffer mixes leading to a greater rebound (in analogy to Fig. 3.7). This indicates that accelerators that cause flash setting can make it more difficult for the aggregate particles to embed themselves upon impact, thus leading to a greater rebound.
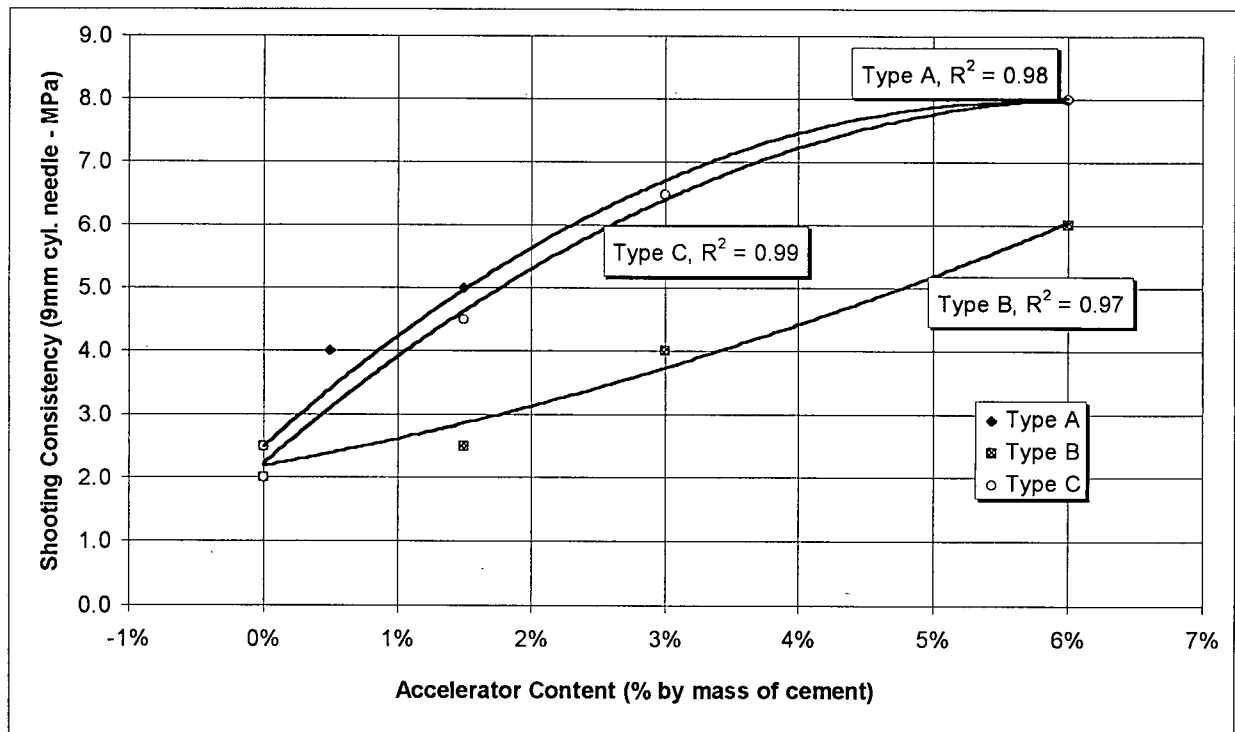
Figure 3.16 - Variation in shooting consistency with the accelerator admixture type and content.

This increase in the overall rate of rebound with the accelerator content is in disagreement with results reported by Schultz (1982). However, it must be considered that commercial accelerator admixtures tend to have widely different compositions and perform differently depending on the properties of the cement used. Therefore, it is possible that some cement/admixture combinations may lead to a reduced rebound. However, as the results presented here indicate, this should not be

considered a rule for dry-mix shotcrete. Similar results of the accelerator admixtures' inneficiency in reducing dry-mix shotcrete rebound[14] were reported by Jolin (1996).

With respect to the hardened properties of the accelerated shotcrete mixes, all accelerator admixtures led to some degree of loss in the compressive strength and caused a greater void content (Table 1). However, it is interesting to note that, unlike the other two compositions tested, the non-caustic accelerator (type B) caused a relatively smaller loss in compressive strength at 28 days and virtually no increase in the volume of permeable voids. This, added to its low toxicity, demonstrates the superior overall performance of this non-caustic admixture.

3.3.2 - Variation in Aggregate rebound with the shooting technique

3.3.2.1 - Variation of Rebound with Air Flow

Results for the variation in the overall rate of rebound with the air flow are shown in Fig. 3.17. The best fit trend line for these data indicates a parabolic variation of rebound with the air flow, with an optimum air flow rate of approximately 300 cfm for the 50 mm internal diameter hose used[15].

These data demonstrate that the high rate of rebound in dry-mix shotcrete is not necessarily related to the high shooting velocity involved, as argued by Warner (1995) and Maidl & Sommavilla (1995). The rebound may be extremely high, even at low shooting velocities, reaching 70% at a 100 cfm air flow. The relationship between air flow and aggregate velocity is further examined in Chapter 4.

In Chapter 6, it is analytically demonstrated that there is an ideal air flow value for which the aggregates have just enough velocity to embed themselves into the spraying surface, without the reaction from the fresh shotcrete substrate causing these particles to debond and thus rebound.

---

[14] It is unquestionable that accelerator admixtures lead to greater maximum build-up thickness on overheads (see Fig. 3.16 and Fig. 3.5).

[15] In Chapter 4, section 4.3.1.1, it is demonstrated that it is actually the nominal air speed (the air flow divided by the hose cross-sectional area) that determines aggregate velocities. Therefore, for different hose diameters, the optimum air flow that leads to minimized rebound should be calculated using a 70 m/s nominal air speed (100 cfm = 0.0472 m^3/s).
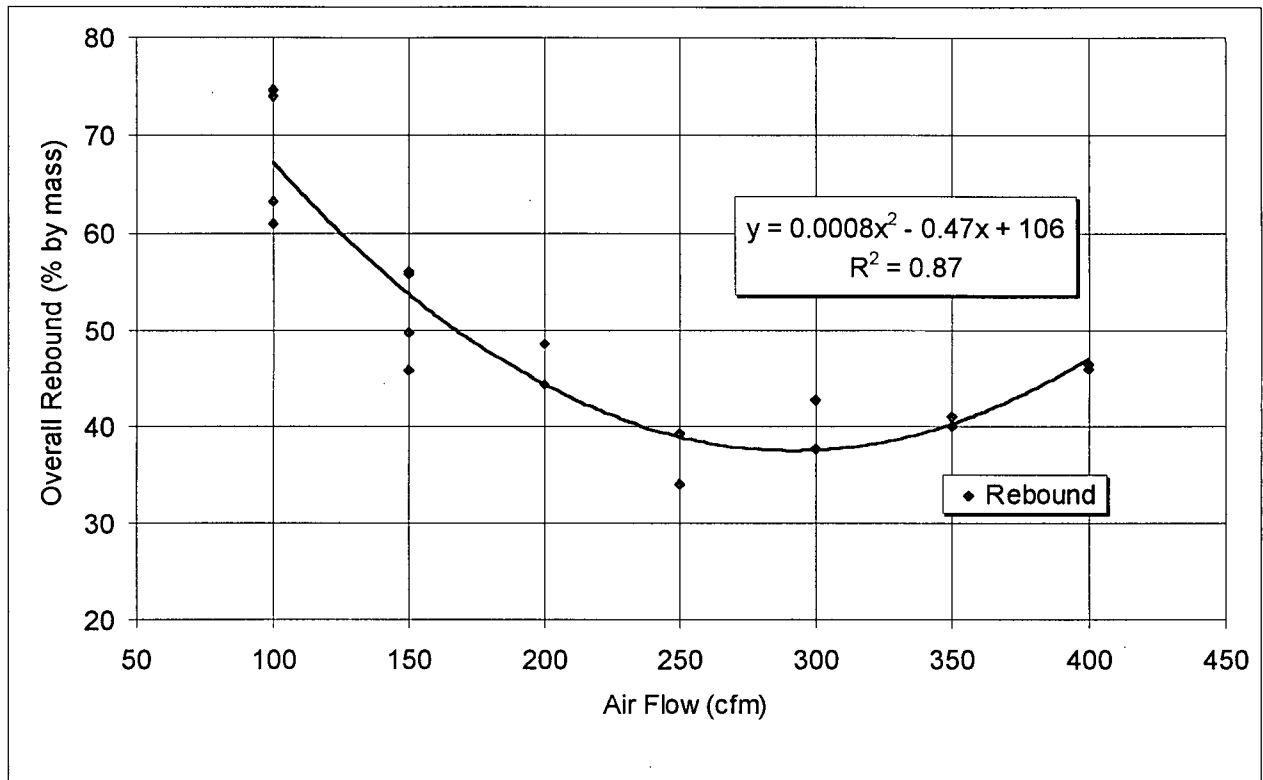
Figure 3.17 - Variation in the overall rate of rebound with the air flow (400 cfm value was obtained using a 38 mm hose, all others used a 50 mm hose).

It is interesting to note that the variation in the air-flow also had an effect on the properties of the hardened shotcrete, with higher values of voids content for very high and very low air-flow values (Table 1). Once again, optimum hardened properties are found at 300 cfm for the 50 mm diameter hose employed.

3.3.2.2 - Variation of Rebound with Thickness of Application

In Table 1, rebound values are reported for the various parameters tested in terms of the first layer applied (approximately 25 mm in thickness) and the subsequent two layers (approx. 50 mm thick each). In virtually all of the panels tested, the rebound in the first layer is greater than in the second layer (on average, approximately 10% greater) while a comparison between the second and third layers reveals that, for a thickness of application greater than 25 mm, the rate of rebound no longer varies.

These data are consistent with results reported by Parker (1976) who found that the rate of rebound decreases exponentially with an increase in the thickness of application up to approximately 50 mm and remains virtually constant thereafter. An explanation for this phenomenon can be given on the basis that, in order for rebound not to occur, the aggregate particles must be able to penetrate into the fresh shotcrete and thus embed themselves. In Chapter 6, it is analytically demonstrated that this depth of penetration is of the order of half the particle diameter, and thus, even for larger aggregates, it does not exceed approximately 5 mm (reason why after the first 25 mm layer had been applied the rate of rebound no longer varied).

3.3.2.3 - Variation of Rebound with Position of Shooting and Inclination Angle

Results for the variation in the overall rate of rebound with the position of shooting are shown in Fig. 3.18. These data indicate that rebound in the overhead and wall positions is very similar, with an average value of approximately 40%. This result is supported by the findings reported in Wolsiefer & Morgan (1993) who described four cases of wall and overhead rates of rebound of equivalent value, with three cases that actually showed greater rebound for wall shooting.
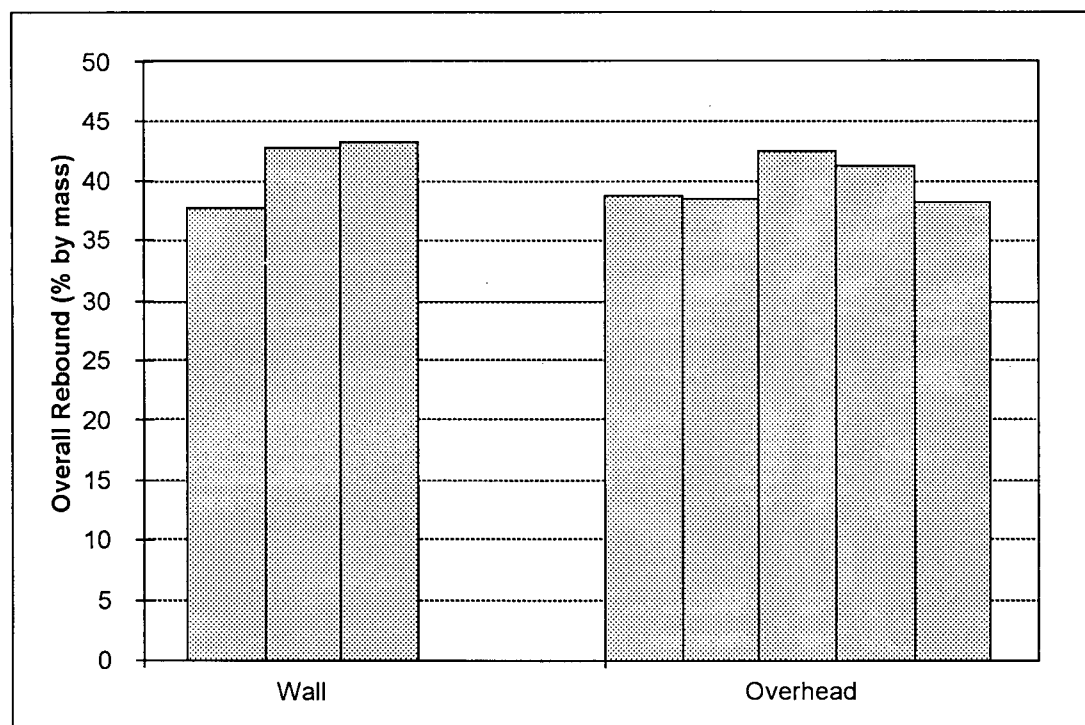
Figure 3.18 - Variation in the overall rate of rebound with the shooting position.

Although somewhat contrary to intuition, results of test panels shot on the overhead and wall positions showing similar rates of rebound, are not uncommon (Morgan, 1990). As will be demonstrated in Chapter 5, careful examination of the mechanics of an aggregate particle rebounding from a fresh shotcrete substrate reveals that the accelerations involved in the process are hundreds of times greater than that of gravity. Therefore, it should not be surprising that, in controlled laboratory shooting conditions of equal shotcrete consistency and ideal shooting distance, the position of shooting (overhead or wall) does not play a major role in the rebound process.

In actual shotcrete job sites, however, overhead shooting for an extended period of time, with material constantly rebounding on the nozzleman, makes it difficult to keep the spray at a 90 degree angle with the shooting surface at all times causing increased rebound. The influence of the shooting angle formed between the nozzle and the direction normal to the spraying surface is presented in Fig. 3.19. These data show a growth in material loss with an increase in the inclination angle with rebound increasing from 40 to 50% for a 30 degree inclination. It is interesting to note that this 10% increase in rebound is close to the 15% figure reported by Melbye et. al. (1995) for the same inclination angle.
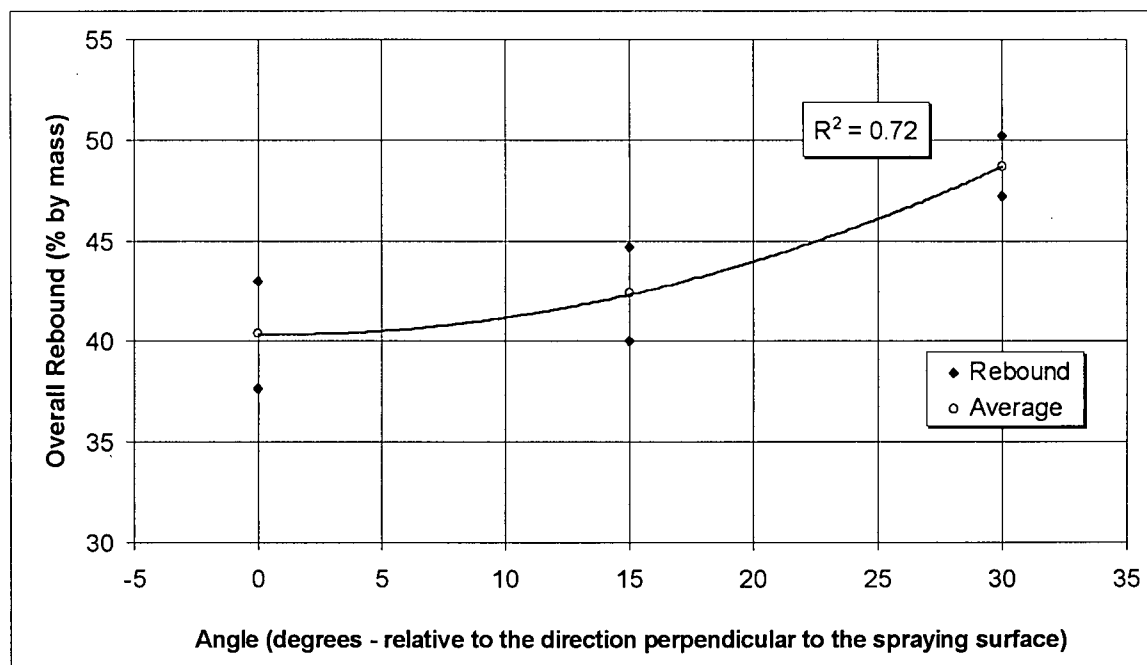
Figure 3.19 - Variation in the overall rate of rebound with the shooting angle (wall shooting).

3.3.3 - Alternative methods of reducing rebound

3.3.3.1 - Limestone Addition

As shown in 3.3.1.5, silica fume is the most effective means of reducing dry-mix shotcrete rebound known to date. However, this addition has the disadvantage of being relatively expensive when compared to cement. Also, for repair projects, the darker color of silica fume causes shotcrete to have a coloration different from the damaged structure, which may be unacceptable for applications in which aesthetics is an issue.

Therefore, ground limestone[16] (average particle size of 1 μm) an admixture often found in concrete, especially in France and South America, was evaluated as a means of reducing the overall dry-mix shotcrete rebound. Addition rates used were 8 and 16% by mass substitution to cement.

Results obtained are presented in Fig. 3.20 and show that, like silica fume, ground limestone is also capable of reducing the overall rate of rebound without a significant influence on the compressive strength (Fig. 3.20).

As for the efficiency of ground limestone in reducing rebound, it should be considered that the 8% decrease in average overall rebound that was obtained using 16% of this addition could be obtained using only 8% of silica fume (Fig. 3.13). Nevertheless, depending on the region in which shotcrete is being used, ground limestone may be an economically viable option for reducing rebound.

---

[16] The use of hydrated lime (calcium or magnesium hydroxide) is also a possibility and has been used in Europe. However, given the frequent occurrence of white stains on the shotcrete surface caused by leaching and subsequent carbonation of Mg ++, Ca++ and Na+ ions, this more chemically stable addition was preferred.
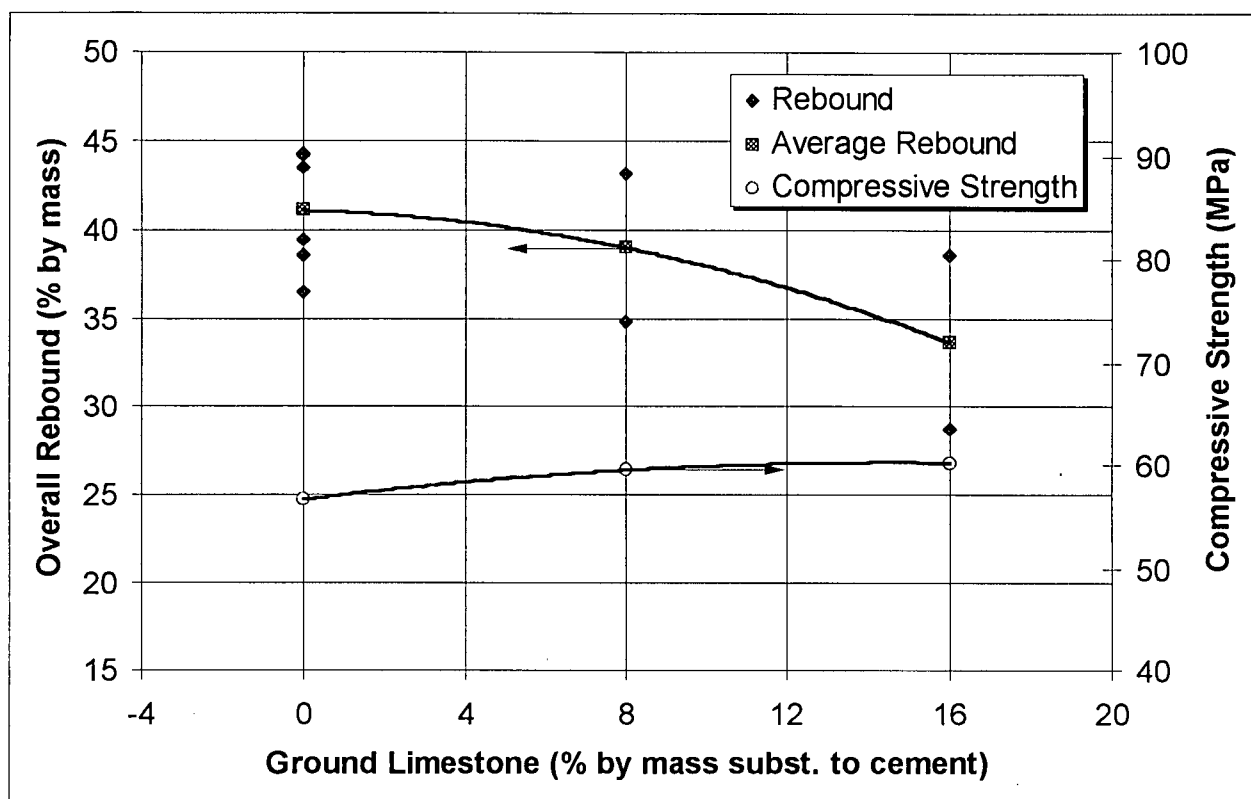
Figure 3.20 - Variation in the overall rate of rebound and compressive strength with the ground limestone addition rate.

3.4 - Conclusions

In this chapter, experimental data on the various parameters that influence dry-mix shotcrete rebound have been presented. More specific conclusions to be extracted from this chapter are as follows:

1 - The penetration test, as a measure of dry-mix shotcrete workability, is actually a measure of the shotcrete yield strength. This is the reason why shooting consistency correlates well with the maximum achievable overhead build-up.

2 - The yield strength of fresh dry-mix shotcrete is determined by its water to binder ratio in an exponential relationship which is different from that of cast concrete of equal mix proportions or pre-moisturized dry-mix shotcrete.

3 - Rebound was found to increase linearly with the shooting consistency, with pre-moisturized mixes showing a greater rate of rebound for a given consistency, but yielding higher compressive strengths at 28 days.

4 - Rebound was found to decrease with an increase in the design mix cement content. This is a direct consequence of the reduced aggregate rebound for a higher cement content and leads to a reduced in-situ to design cement content.

5 - Similar to an increase in the cement content, the presence of silica-fume caused a decrease of aggregate rebound, thus reducing the in-situ cementitious content.

6 - None of the three accelerator admixtures tested improved the shotcrete performance with respect to rebound. On the contrary, for accelerator addition rates greater than 1.5% by mass of cement, all accelerators led to an increase in rebound caused by a stiffening in the shooting consistency.

7 - Rebound showed a parabolic relationship with air flow, with a minimized rebound value occurring at approximately 300 cfm for the shotcrete equipment used.

8 - Rebound was not significantly affected by the shooting orientation (overhead or wall). However, an increase in the angle of inclination of the nozzle with respect to the shooting surface had a negative effect on rebound.

9 - The use of limestone seems to be a viable alternative for simultaneously reducing rebound and the cement content without the inconvenience that the dark coloration of silica fume may cause.

Chapter 4 - Kinematics of Dry-mix Shotcrete

4.1 - Introduction and Objectives

As mentioned earlier, ACI's definition of shotcrete describes it as "concrete that is applied at a high velocity". Ironically, however, this unique feature of shotcrete, that sets it apart from all other forms of Portland cement concrete, is also one of its least known characteristics. Given the high speeds developed by the shooting process, it is impossible to observe "in-flight" shotcrete using the naked eye or other conventional methods. As a result, although attempts have been made to use pressure measurements and high speed still photography (Parker, 1976), results on particle velocity reported in the literature are highly scattered, with reported figures ranging from 27 to 150 m/s (Table 4.1). This has led to suggestions that "it is obvious that there is no consensus ... a series of tests to measure shooting velocity using high speed photography should be undertaken" (Glassgold, 1989).

Table 4.1 - Shooting velocities as reported in the literature (from Glassgold, 1989).

Author	Reported Shooting Velocity (m/s)
Stewart (1933)	90 to 150 m/s
Ryan (1973)	90 to 120 m/s
Valencia (1974)	135 m/s
Ward & Hills (1977)	35 to 56 m/s
Parker (1977)	30 to 60 m/s
Blumel et. al. (1978)	27 to 35 m/s

The motivation to seek further understanding of particle kinematics in shotcrete goes beyond mere characterization of velocity figures for definition purposes. The basic rebound mechanism by which particles impinge upon the shooting surface, and either stay embeded or ricochet off is essentially an impact process, with the particle velocity of impact being one of its main determining parameters. The poor understanding that characterizes the present state-of-the-art on shotcrete kinematics is one of the main reasons why an analytical model, based on rational principles of mechanics, has never been developed to address the shotcrete rebound problem.

It has been suggested that the reason why dry-mix shotcrete shows such high rates of rebound is associated with the high particle velocities that are produced (Warner, 1995 and Maidl & Sommavilla, 1995). However, no rationale has ever been given to justify this hypothesis and results presented in item 3.3.2.1 demonstrate that at a low air flow, dry-mix shotcrete rebound tends to be extremely high, reaching 70%. Similarly, it has been hypothesized that the cause of fiber rebound is related to fiber accelerations in the shotcrete stream and that foil-like fiber geometries tend to rebound more due to the greater velocity they develop (Banthia et al., 1992) although the latter authors did not actually measure fiber velocities.

Therefore, the objective of this chapter was to use high speed filming, in an environment of controlled air flow, to characterize aggregate and fiber velocities in dry-mix shotcrete and to identify the main parameters that influence them. This information leads to answers to some of the basic questions raised in Chapter 2 on the fundamental mechanisms involved in shotcrete rebound. Additionally, results on aggregate and fiber velocity obtained here will serve as input to an analytical model of rebound mechanics developed in Chapters 5 and 6.

4.2 - Material and Methods

The shotcrete equipment used was the same described in 3.2, instrumented with a spring-loaded in-line air flowmeter (model OMEGA FL8945). Two different hose/nozzle systems were used: a 20 m long 50 mm (2 in) diameter[1] hose and nozzle (Fig. 4.1a) and a 20 m long 50 mm diameter hose coupled to a 2.5 m long 38 mm (1.5 in) hose (Fig. 4.1b). The high-speed camera used was a KODAK model EKTAPRO operating at 1000 frames per second.

In order to be able to track the smallest aggregate sizes and to be certain of their dimensions, aggregates were first sieved in order to separate the standard ASTM sizes (12.7, 9.5, 4.8, 2.4 and 1.2 mm)[2] and shot separately (one size at a time) without any cement or water[3]. The same procedure was used for steel fibers.

---

[1] Throughout this thesis, hose diameters are reported in inches since this is the standard in the shotcrete industry (1 in = 25.4 mm).

[2] These sieve sizes are also commonly referred to as, respectively, ASTM 1/2", 3/8", #4, #8 and #16.

[3] Actual shotcrete tests are described in section 4.3.3 to validate this technique.
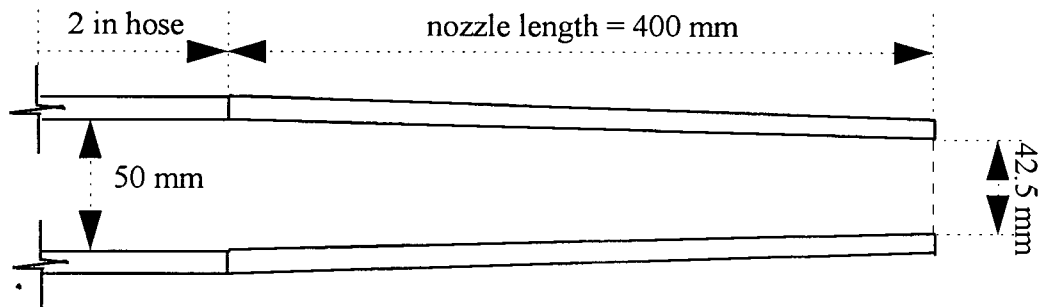
(a) - 2 inch hose system
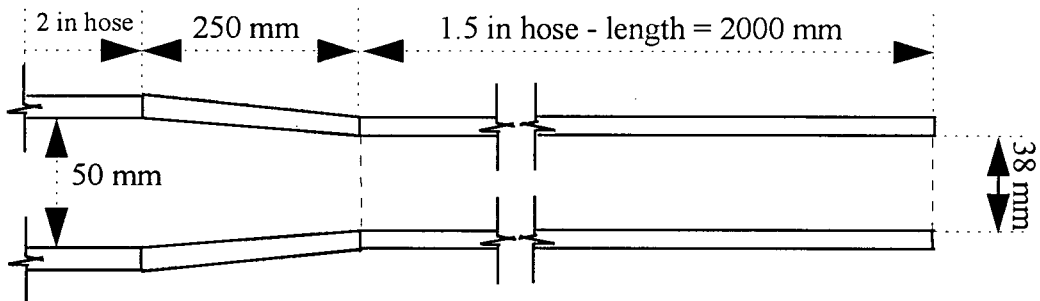
(b) - 1.5 inch hose system

Figure 4.1a & b - Shape and dimensions of the two hose/nozzle systems used.

During shooting, the rate of air flow was set to the desired value (100, 200, 300 or 400 cfm[4]) and the high speed camera was used with a square 50 mm grid as background, allowing determination of particle positions (Fig. 4.2). The time was reported in milliseconds on the camera screen, with average velocities calculated using the times of particle entrance and exit over a 300 mm wide window (for the smaller aggregates a 150 mm wide window was used). For all tests, the entrance to the 300 or so millimeters wide sampling window was located 1000 mm away from the end of the nozzle.

---

[4] Throughout this thesis, air flow values are reported in cubic feet per minute since these are the units used by the shotcrete industry - 100 cfm = 0.047 m^3/s.
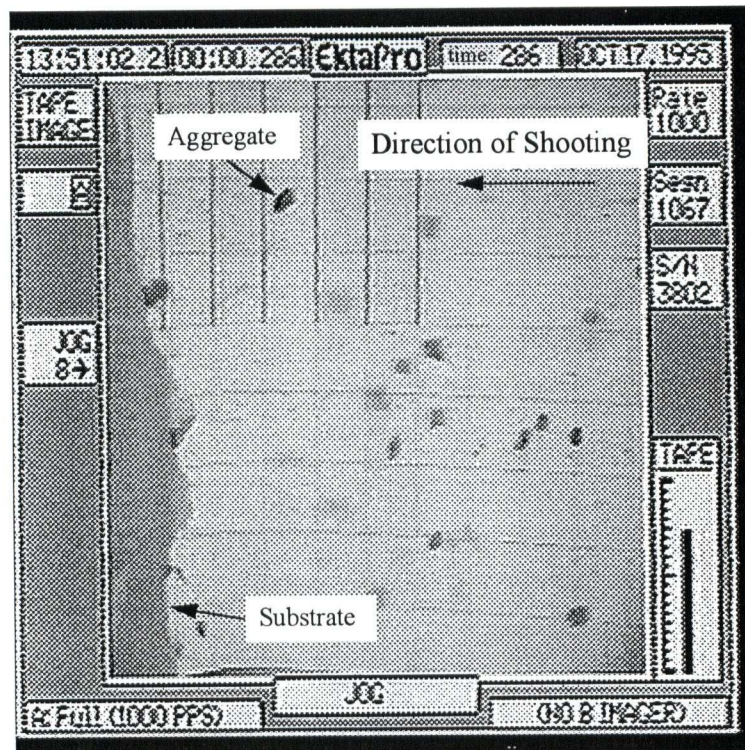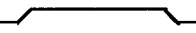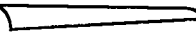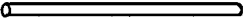
Figure 4.2 - High speed image of in-flight aggregates (9.5 mm aggregate, 400 cfm, grid size = 50 mm).

Velocity measurements were made using a four head VCR capable of jog-shuttle functions that allowed following frame by frame movement of particles. For all aggregate and fiber sizes tested, 15 individual velocity measurements were made to calculate the average speed. For the larger aggregates (4.8 mm and greater) the particle size was also measured on screen using calipers and scaled to actual size to determine the particle size vs. velocity relationship. For aggregates too small to be measured on screen with accuracy (less than 4.8 mm) the particle size was assumed to be the average between the retaining sieve size and the sieve opening immediately above it (e.g. for the material retained on the 2.4 mm sieve, the mean particle dimension was assumed to be the average between 2.4 and 4.8 mm = 3.6 mm).

The aggregates used were concrete sand and river gravel. With the exception of the 0.50 mm diameter, 25.4 mm long fiber which had hooked ends and flat geometries which are commercially available, all other steel fibers tested had a straight cylindrical geometry and were produced specifically for this study. Fiber geometries tested are presented in Table 4.2.

Table 4.2 - Shape and dimensions of the steel fibers tested.

Shape	Cross Section*	Length (mm)
Hooked	◯ D = 0.5	25.4
Flat	t = 0.4, w = 2.7	32
Flat-Crimped	t = 0.4, w = 2	25.4
Cylindrical	◯ D = 0.5	40, 25.4 and 12.5
Cylindrical	◯ D = 0.65	25.4 and 12.5
Cylindrical	◯ D = 1.0	40, 25.4, 12.5 and 3
Cylindrical	◯ D = 1.6	40, 25.4, 12.5 and 3

*Drawings are not to scale. D, t and w = diameter, thickness and width in mm.

4.3 - Results and Discussion

4.3.1 - Aggregate Velocity

4.3.1.1 - Aggregate Velocity vs. Particle Size and Air Flow

Results on the variation in the aggregate velocity as a function of size are presented in Fig. 4.3a for the 2 in (50 mm) diameter hose and nozzle and in Fig. 4.3b for the 1.5 in (38 mm) diameter hose. In both cases, air flow values tested were 100, 200, 300 and 400 cfm.

These data indicate a dependence of aggregate velocity on size, with larger aggregates showing roughly half the speed of the smaller aggregates for a given hose and air flow. The average numerical results are presented in Table 4.3. In Chapter 6, it is analytically demonstrated that the low velocity of larger aggregates (9.5 mm) is one of the reasons why they tend to rebound approximately four times more than fines (passing the 0.3 mm sieve).

A comparison between Figs. 4.3a and b indicates that, for a given air flow, the diameter of the hose/nozzle system strongly influences the particle velocities, with the smaller diameter hose leading to greater velocities (Fig. 4.3c). This is considered to be a direct consequence of the increased air velocity that is associated with a reduction in the hose cross sectional area for conditions of equal rate of air flow.

The influence of the variation in the air flow on the average aggregate velocity is shown in Fig. 4.4a for a 2 in (50 mm) hose and 4.4b for a 1.5 in (38 mm) hose. In both cases, and for all aggregate sizes tested, it may be seen that, for a given hose size, there is a linear relationship between aggregate velocity and air flow, therefore indicating that particle velocities are directly proportional to the nominal air speed (estimated by the air flow divided by the hose cross sectional area).
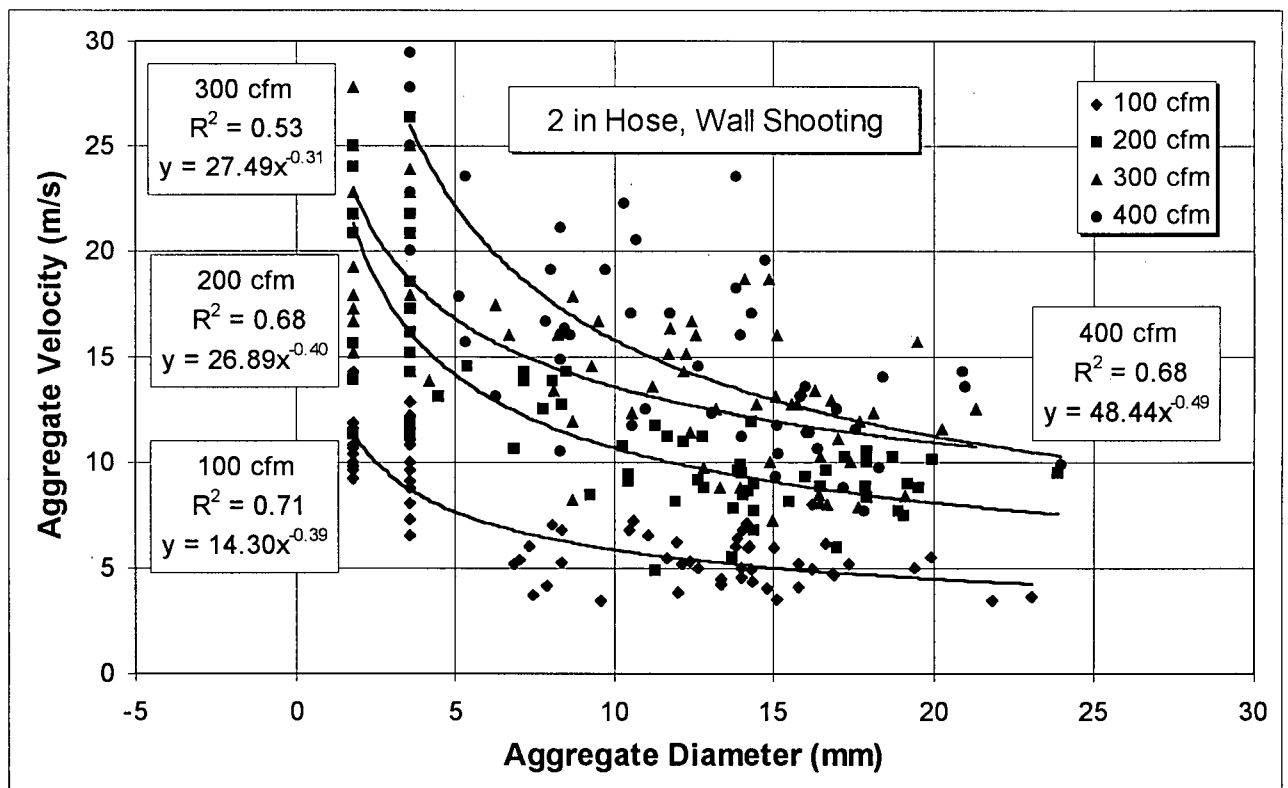
Figure 4.3a - Variation in aggregate velocity with size for a 2 in (50 mm) hose.
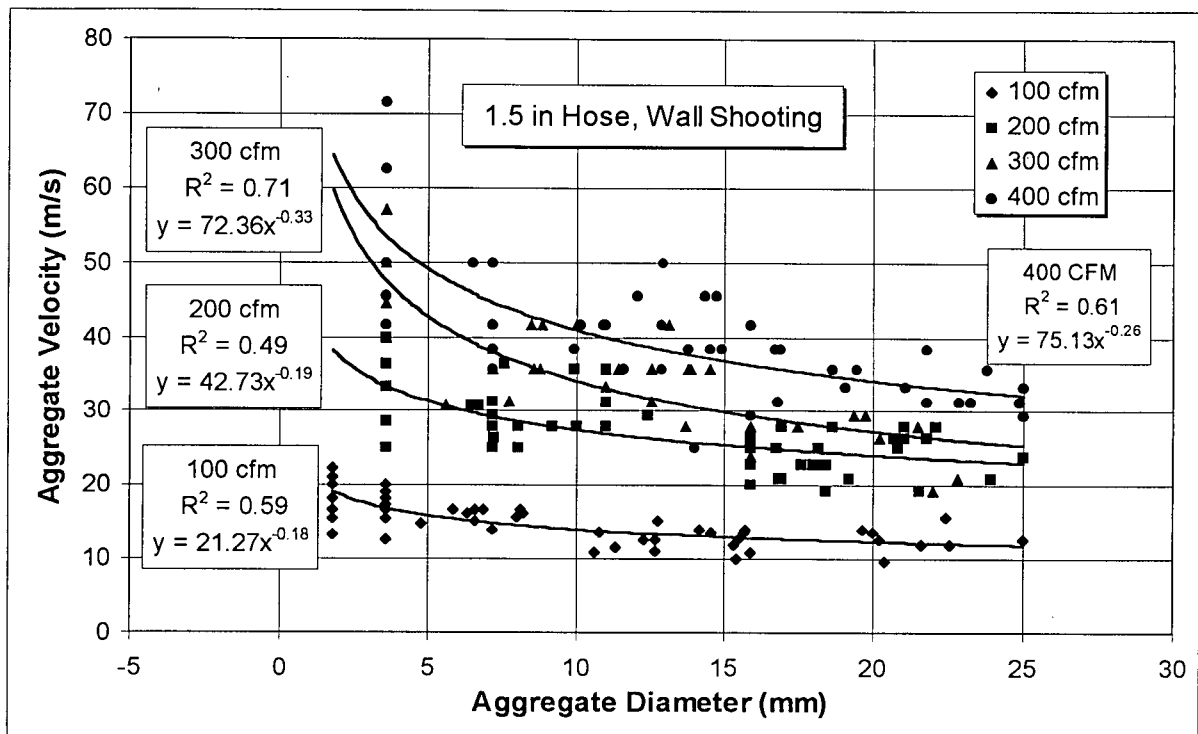
Figure 4.3b - Variation in aggregate velocity with size for a 1.5 in (38 mm) hose.
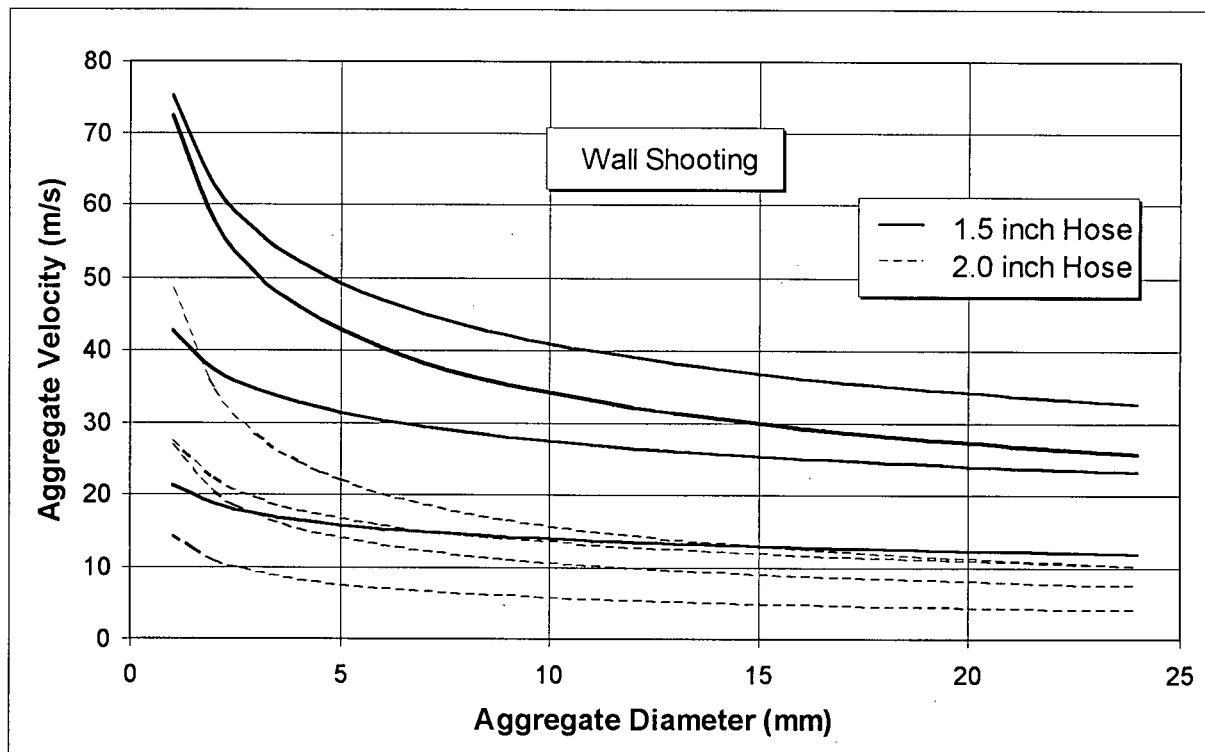
Figure 4.3c - Comparison of trendlines for the variation in aggregate velocity with size for two different hose diameters (trendlines obtained using, respectively from top to bottom, 400, 300, 200 and 100 cfm).

Table 4.3 - Average results obtained for aggregate and fiber translational velocities.

Type	Shape	Diam.[a]	l (mm)	Hose (in)	Position[b]	Translational Velocity (m/s)[c]			
						100 cfm	200 cfm	300 cfm	400 cfm
Agg.	-	1/2"	-	2"	W	4.7 / 0.23	8.7 / 0.15	11.1 / 0.24	11.6 / 0.17
					O.H.	1.6 / 0.43	5.9 / 0.23	8.9 / 0.22	10.3 / 0.20
				1.5"	W	12.7 / 0.14	23.1 / 0.12	26.2 / 0.13	32.7 / 0.13
Agg.	-	3/8"	-	2"	W	5.6 / 0.17	9.6 / 0.14	13.0 / 0.25	15.7 / 0.28
					O.H.	2.5 / 0.38	8.2 / 0.18	13.1 / 0.27	13.7 / 0.17
				1.5"	W	12.5 / 0.11	26.5 / 0.15	34.2 / 0.09	39.8 / 0.13
Agg.	-	#4	-	2"	W	5.7 / 0.21	11.0 / 0.28	14.0 / 0.20	17.6 / 0.17
					O.H.	5.2 / 0.20	8.8 / 0.21	15.3 / 0.16	17.5 / 0.17
				1.5"	W	15.8 / 0.06	28.4 / 0.09	37.6 / 0.09	41.5 / 0.09
Agg.	-	#8	-	2"	W	9.9 / 0.20	17.0 / 0.25	20.7 / 0.18	26.4 / 0.17
					O.H.	7.4 / 0.19	11.9 / 0.16	16.6 / 0.20	18.0 / 0.12
				1.5"	W	17.2 / 0.12	33.2 / 0.14	46.3 / 0.15	54.8 / 0.17
Agg.	-	#16	-	2"	W	11.1 / 0.12	21.1 / 0.32	20.4 / 0.19	-
					O.H.	8.5 / 0.20	14.6 / 0.19	17.2 / 0.25	19.2 / 0.16
				1.5"	W	18.9 / 0.17	-	-	-
Fiber	Cylindrical	0.5	40	2"	W	10.1 / 0.18	14.3 / 0.33	15.9 / 0.34	18.8 / 0.40
Fiber	Cylindrical (Hooked)	0.5	25.4	2"	W	9.3 / 0.14	12.8 / 0.17	20.6 / 0.09	22.1 / 0.30
					O.H.	6.7 / 0.13	9.6 / 0.24	12.4 / 0.27	14.3 / 0.23
				1.5"	W	14.6 / 0.15	22.5 / 0.13	29.8 / 0.21	41.9 / 0.18
Fiber	Cylindrical	0.5	12.5	2"	W	9.7 / 0.24	15.0 / 0.20	16.6 / 0.28	20.3 / 0.27
Fiber	Cylindrical	0.65	25.4	2"	W	6.9 / 0.22	13.0 / 0.19	16.4 / 0.27	18.4 / 0.30
				1.5"	W	8.2 / 0.32	12.7 / 0.32	18.1 / 0.22	22.3 / 0.19
			12.5	2"	W	8.7 / 0.18	15.3 / 0.26	18.6 / 0.16	23.9 / 0.21
Fiber	Cylindrical	1.0	40	2"	W	6.4 / 0.28	6.9 / 0.45	10.8 / 0.36	15.7 / 0.22
			25.4	2"	W	7.3 / 0.18	11.0 / 0.28	13.6 / 0.23	17.3 / 0.21
				1.5"	W	9.8 / 0.31	14.1 / 0.20	17.4 / 0.37	24.3 / 0.21
			12.5	2"	W	8.3 / 0.10	12.1 / 0.34	16.9 / 0.18	20.3 / 0.19
			3	2"	W	7.3 / 0.16	11.7 / 0.25	15.5 / 0.19	-
Fiber	Cylindrical	1.6	40	2"	W	0 / 0	0 / 0	7.4 / 0.33	7.9 / 0.54
			25.4	2"	W	5.7 / 0.23	10.7 / 0.25	13.9 / 0.21	16.6 / 0.29
				1.5"	W	6.5 / 0.22	15.3 / 0.23	18.1 / 0.27	22.0 / 0.21
			12.5	2"	W	5.9 / 0.16	11.9 / 0.19	14.9 / 0.20	18.4 / 0.24
			3	2"	W	7.0 / 0.15	12.9 / 0.13	15.0 / 0.18	16.3 / 0.22
Fiber	Flat	0.4 x 2.7	25.4	2"	W	9.6 / 0.35	15.2 / 0.41	18.9 / 0.28	23.1 / 0.26
Fiber	Flat-Crimped	0.4 x 2.0	25.4	2"	W	8.0 / 0.28	14.0 / 0.22	20.6 / 0.25	22.8 / 0.25

a - Aggregate diameter: 1/2", 3/8", #4, #8, and #16 (respectively, 12.7, 9.5, 4.8, 2.4 and 1.2 mm).
b - Positions of shooting: W = wall and O.H. = overhead.
c - Average velocity (m/s) / Coefficient of variation (sample size = 15 measurements).

51
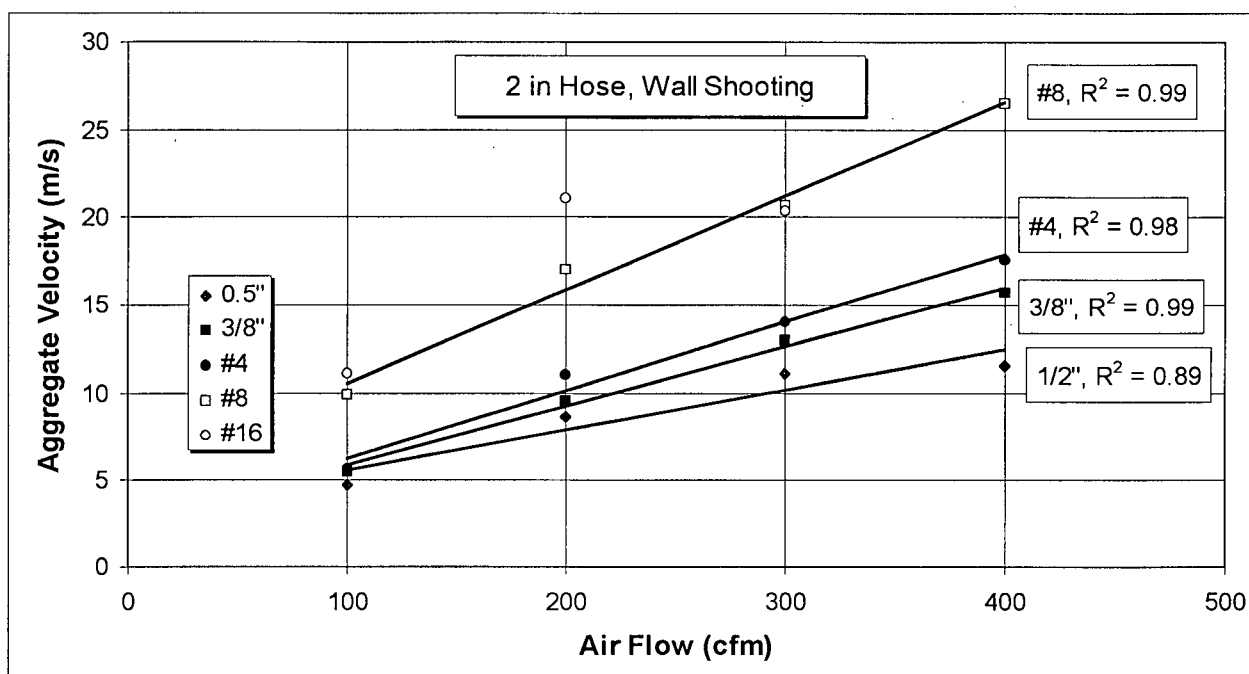
Figure 4.4a - Variation in aggregate velocity with air flow for a 2 in (50 mm) hose.
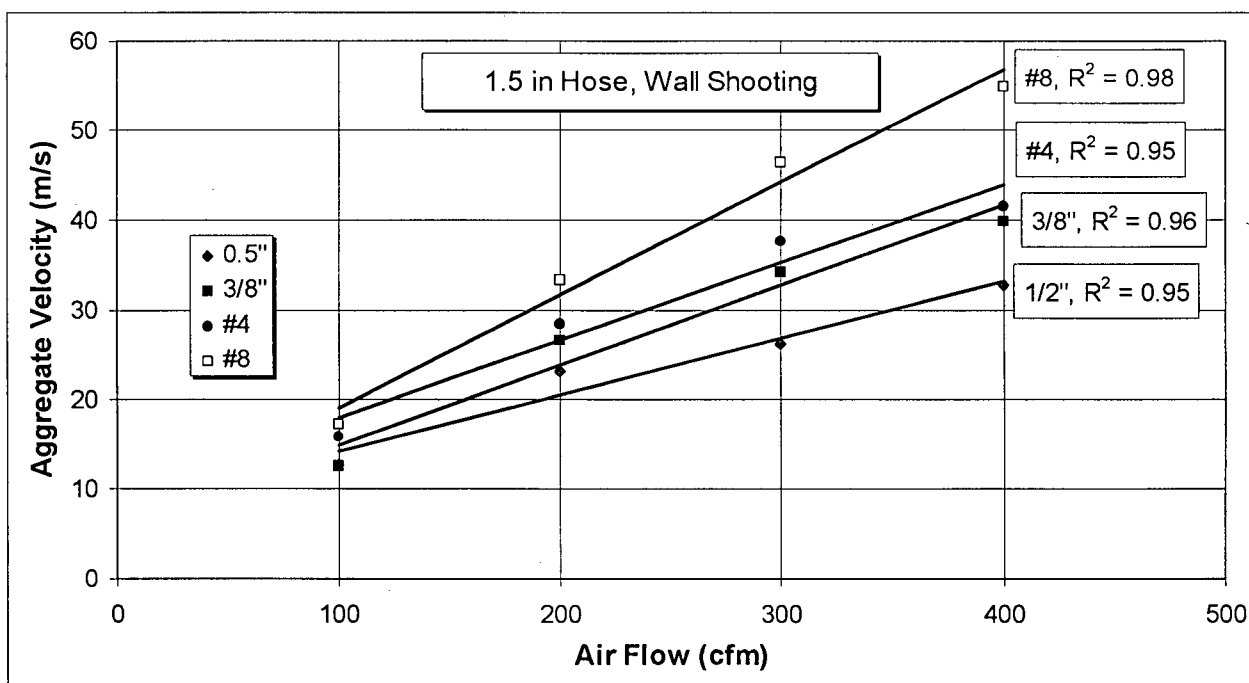
Figure 4.4b - Variation in aggregate velocity with air flow for a 1.5 in (38 mm) hose.

This strong correlation between aggregate velocity and air flow (average correlation coefficient, $R^2 = 0.96$) indicates that the use of an air flowmeter is an adequate means of controlling the shooting velocity and hence rebound in the field[5].

Since for a given hose/nozzle system the nominal air velocity was found to determine the average particle speed (Figs. 4.4a and b) the question remains as to how general this parameter is, i.e. whether the air speed determines the aggregate velocity irrespective of the hose and nozzle dimensions and shape. Therefore, in Fig. 4.4c, results on the average aggregate velocity obtained using the two hose systems tested are presented as a function of the nominal air speed (estimated as the air flow divided by the hose cross-sectional area).
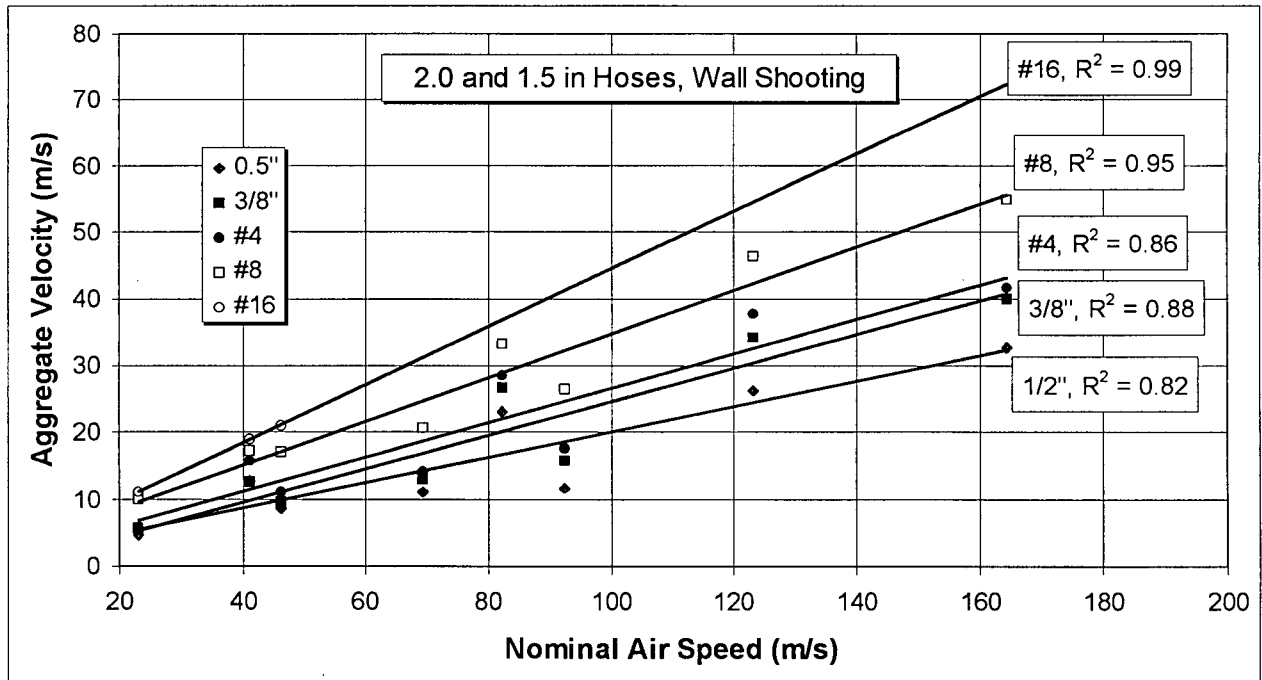
Figure 4.4c - Variation in average aggregate velocity with the nominal air speed for the two hose sizes tested.

[5] Assuming the air flowmeter is installed directly to the air supply that conveys shotcrete (i.e. for pneumatically powered shotcrete machines or for air compressors powering other equipment, the air flow consumption cannot be assumed to determine shotcrete speed).

These results indicate that, although the two hose systems tested are different in shape and dimensions, their average velocity shows a close correspondence with the nominal air speed (average correlation coefficient, $R^2 = 0.90$) indicating that the ratio of air flow to hose cross sectional area is a parameter capable of giving a good prediction of the expected average aggregate speed irrespective of hose dimensions (average error in the prediction is less than 3 m/s).

4.3.1.2 - Aggregate Velocity vs. the Position of Shooting

The influence of the position of shooting (wall or overhead) on the aggregate speed was also evaluated. In Fig. 4.5a, the dependence of aggregate velocity on particle size and air flow is presented for the case of overhead shooting. In Fig. 4.5b the best fit trend lines are compared with the case of wall shooting (Fig. 4.3a).
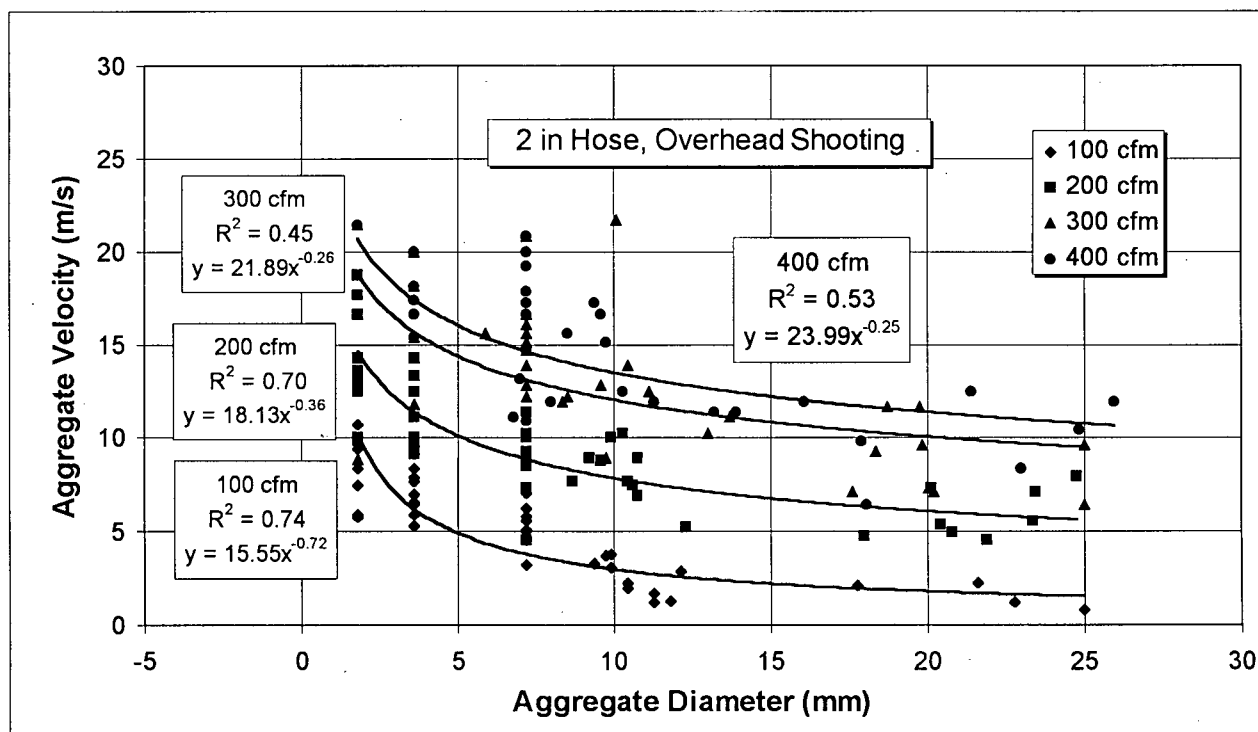
Figure 4.5a - Variation in aggregate velocity with size for overhead shooting.
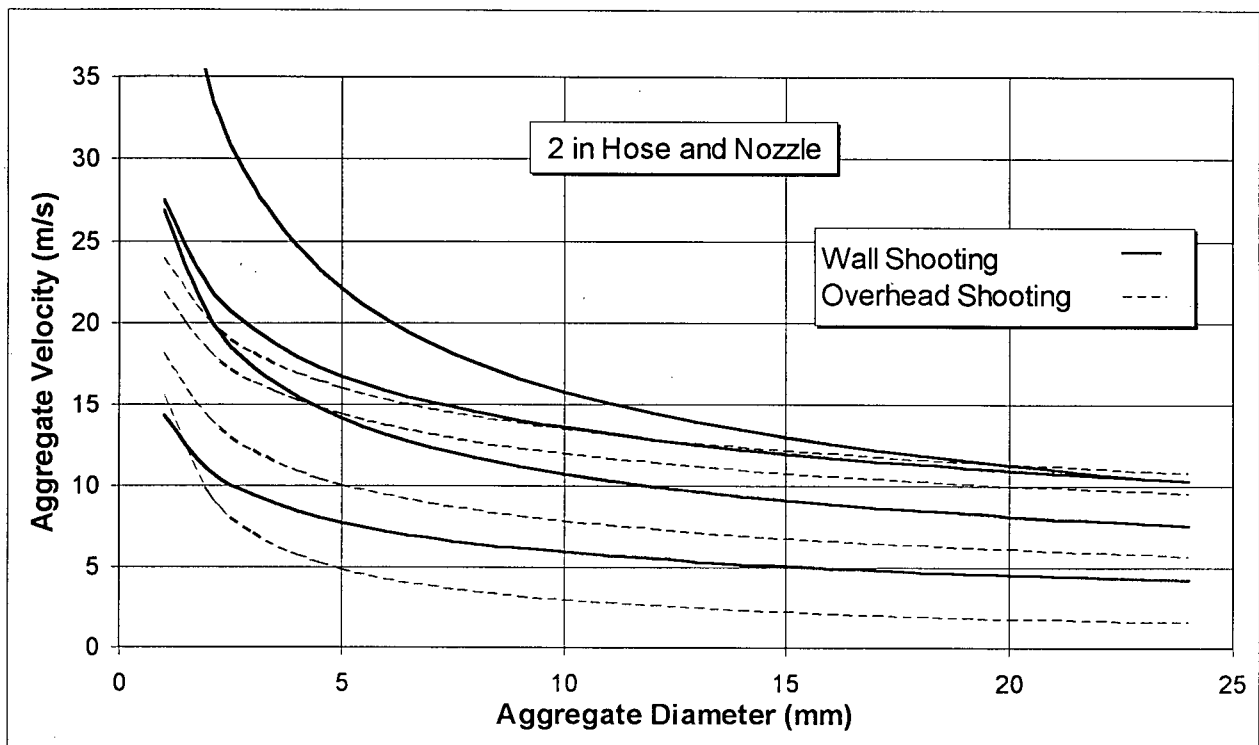
Figure 4.5b - Comparison of trendlines for the variation in aggregate velocity with size for overhead and wall shooting (trendlines obtained using, respectively from top to bottom, 400, 300, 200 and 100 cfm).

These data indicate that, similar to wall shooting, overhead spraying also shows a dependence of aggregate speed on size (Fig. 4.5a). However, a comparison between the best-fit trend lines for cases of equal air flow (Fig. 4.5b) indicates that overhead shooting leads to lower aggregate speeds. For example, at a 300 cfm air flow, the average speed is on an average 3 m/s lower for the overhead case.

Despite the fact that overhead shooting leads to an aggregate speed vs. size profile distinct from wall shooting, in Fig. 4.5c, it may be seen that it still maintains a linear relationship between the air flow and the average particle speed for all different aggregate sizes tested (average correlation coefficient, $R^2 = 0.94$).
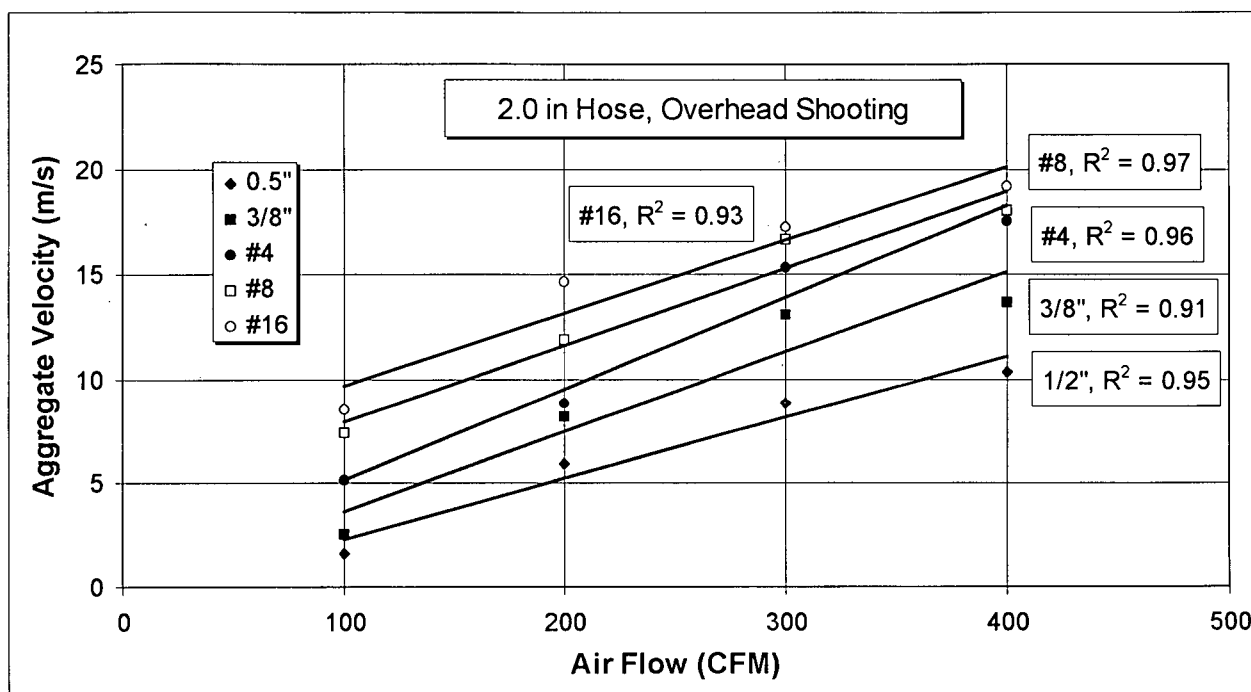
Figure 4.5c - Variation in aggregate velocity with air flow for overhead shooting.

4.3.1.3 - A General Parameter of Aggregate Velocity

Based on the data presented in Figs. 4.3 and 4.5, for all cases of hose/nozzle dimensions, air flow and direction of shooting, the aggregate velocity (V) was found to be related to the aggregate diameter (ϕ) by an equation of the type:

$$V = A \cdot \left(\frac{1}{\phi}\right)^B \qquad \text{where, } A \text{ and } B \text{ are constants[6]} \qquad (4.1)$$

Therefore, it is expected that the logarithm of the velocity should vary linearly with the logarithm of the inverse of the particle diameter. This is shown in Figs. 4.6a to c, where the logarithm of the average aggregate speed is found to vary linearly with the logarithm of the inverse of the particle diameter for both hose sizes, at all air flow values and for both wall and overhead shooting (average correlation coefficient, $R^2 = 0.93$).

---

[6] Numerical values for the constants A and B are given in Figs. 4.3a, 4.3b and 4.5a.
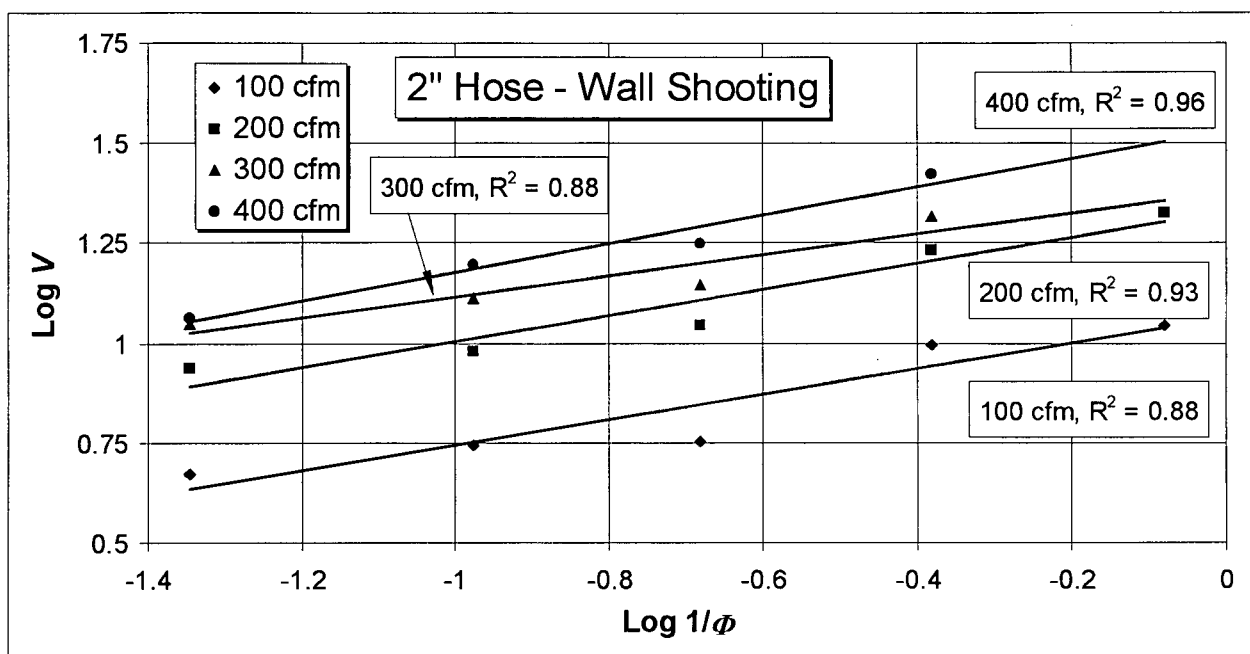
Figure 4.6a - Variation in aggregate velocity with the inverse of the aggregate diameter (log vs. log) for a 2 in (50 mm) hose, wall shooting.
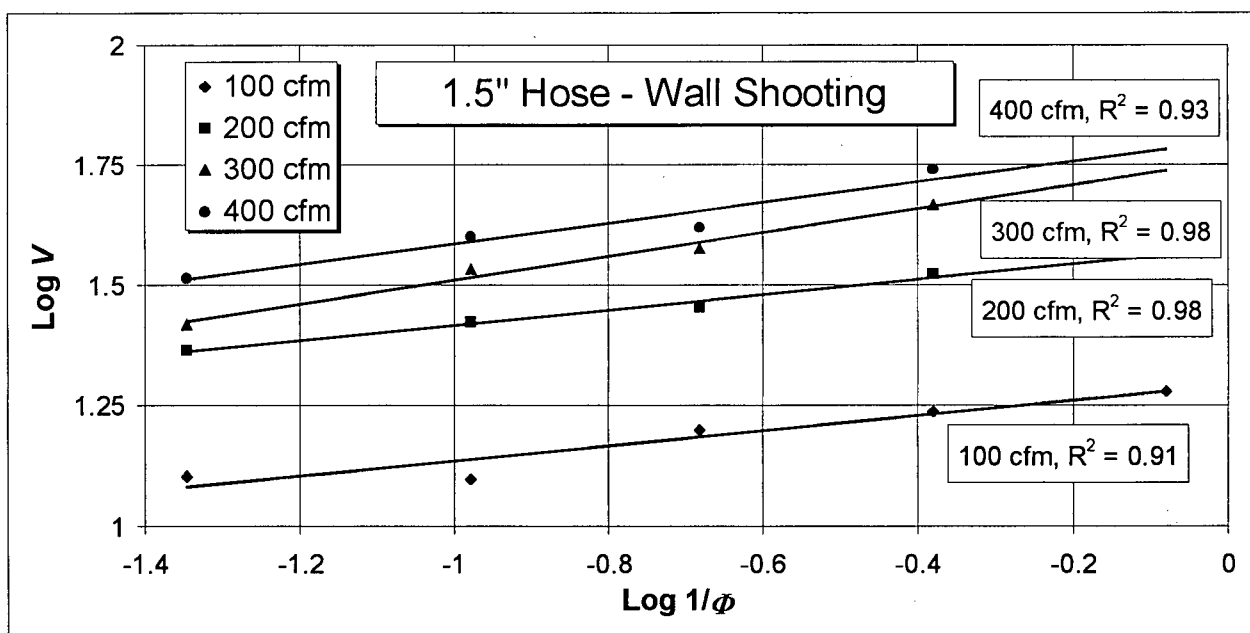
Figure 4.6b - Variation in aggregate velocity with the inverse of the aggregate diameter (log vs. log) for a 1.5 in (38 mm) hose, wall shooting.
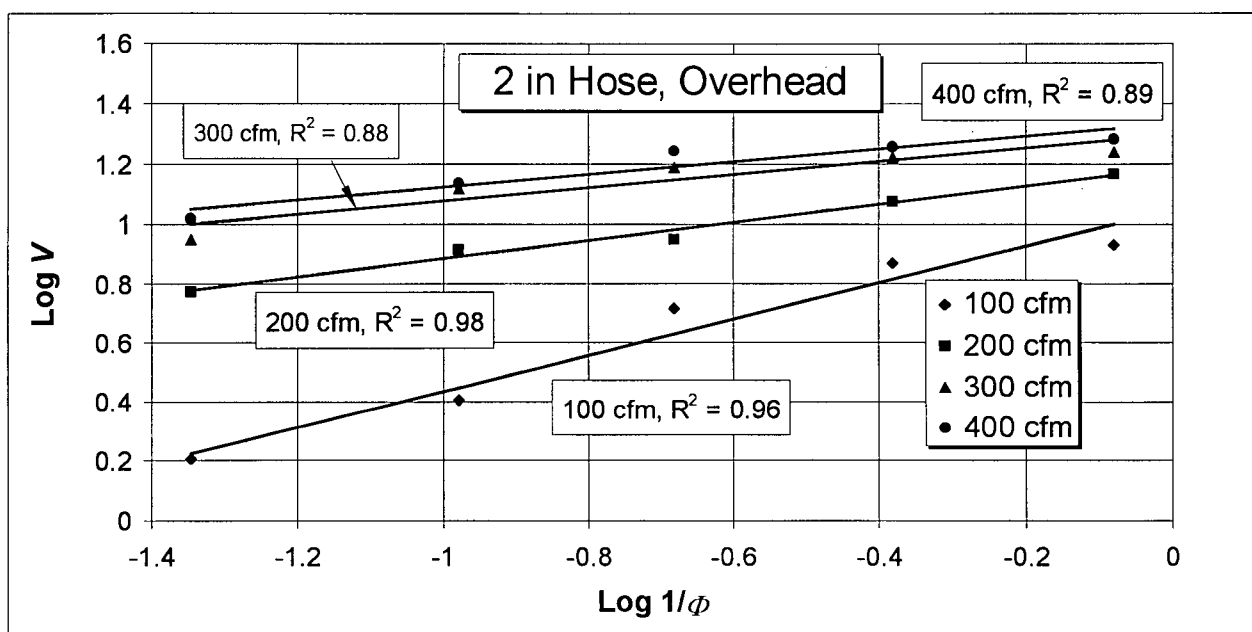
Figure 4.6c - Variation in aggregate velocity with the inverse of the aggregate diameter (log vs. log) for a 2 in (50 mm) hose, overhead shooting.

This result indicates that the logarithm of the inverse of the particle dimension is a general parameter capable of accounting for the size effect that influences aggregate velocity. In the following sections, it is shown that circular cross section steel fibers also show a similar dependence on this parameter, for which a possible physical explanation is given.

4.3.2 - Fiber Velocity

4.3.2.1 - Variation of Fiber Velocity with the Fiber Length and Air Flow

Results on the variation in the average fiber speed with the rate of air flow are presented in Figs. 4.7a to d for circular cross-section fibers with diameters of, respectively, 0.50, 0.65, 1.0 and 1.6 mm at fiber lengths of 40, 25.4, 12.5 and 3 mm. From these figures, it may be concluded that, like aggregate particles, steel fibers also have their velocity determined by the air flow. In all twelve cases of fiber dimensions tested, a linear trend was confirmed, with an average correlation coefficient, $R^2 = 0.94$.
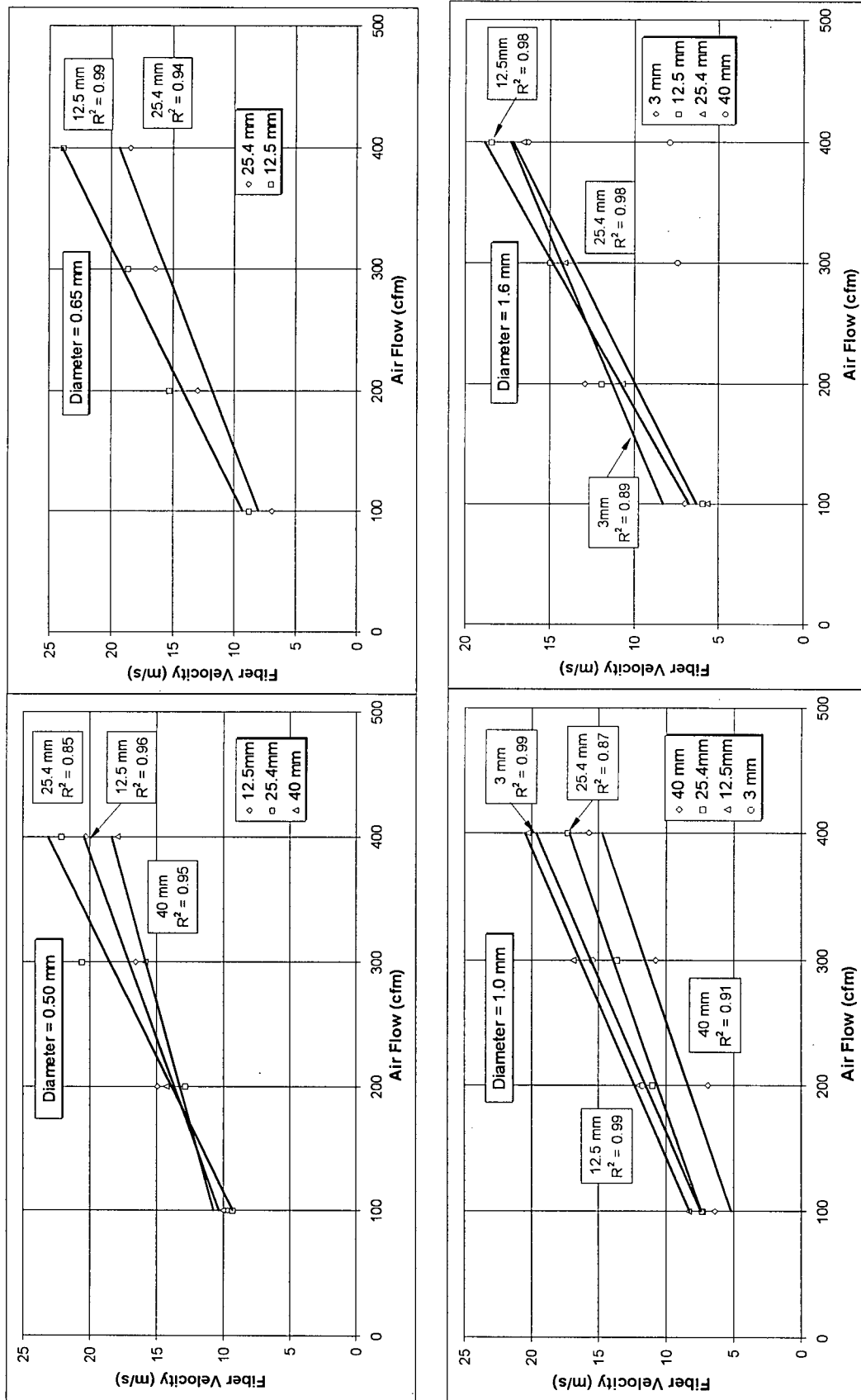
Figure 4.7 a to d - Variation in the mean steel fiber velocity with the air flow and length for four different fiber diameters.

With respect to the influence of fiber length on velocity, although this is not true of all fiber diameters tested, Figs 4.7a to d indicate that, for a given diameter, longer fibers develop lower speed, possibly due to greater restraint from the hose wall. This is especially true for the case of larger diameter fibers (Figs. 4.7c and d) for which the 40 mm length showed significantly lower speeds.

It is also interesting to note that, for all geometries tested (Figs. 4.7a through d), the average fiber speed is close to the aggregate speeds recorded in Figs. 4.3a and b. This result indicates that it is unlikely that particle interference (particle to particle collision) plays a major role in the shotcrete spray (as confirmed using high speed filming of the shotcrete stream in the sections to follow).

4.3.2.2 - Variation in the Fiber Velocity with the Fiber Diameter

The influence of the fiber diameter on velocity is shown in Figs. 4.8a to c for fiber lengths of 40, 25.4 and 12.5 mm, respectively. These data indicate a strong relationship between the fiber diameter and its speed, with greater diameters leading to lower velocities for all three fiber lengths tested.

This size dependence of fiber velocity suggests that, similar to aggregates, steel fibers may also have their velocity determined by the logarithm of the inverse of the fiber diameter. To test this hypothesis, in Figs. 4.9a through c, results on the average fiber velocity are presented as a function of this parameter. It may be seen that, for all ten combinations of fiber length and air volume tested, a positive correlation was found between the average velocity and the logarithm of the inverse of the fiber diameter (average correlation coefficient, $R^2 = 0.80$). A possible physical interpretation to this parameter is given in the following sections.
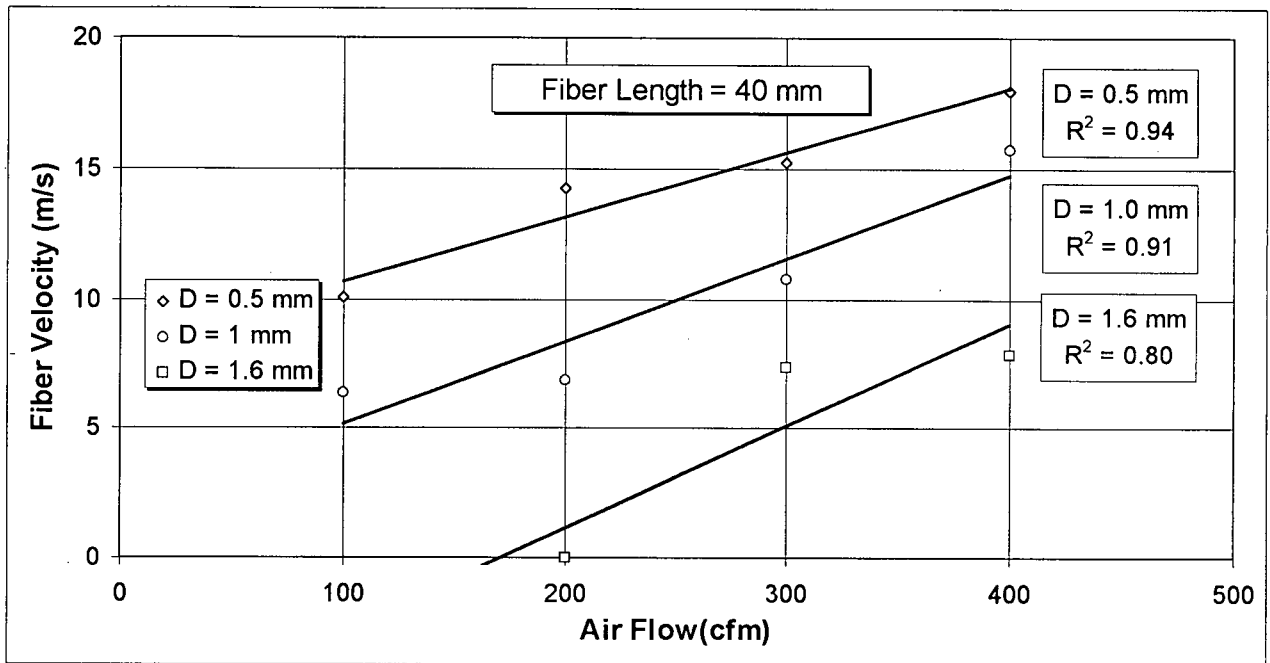
Figure 4.8a - Variation in mean steel fiber velocity with the air flow and fiber diameter (fiber length = 40 mm).
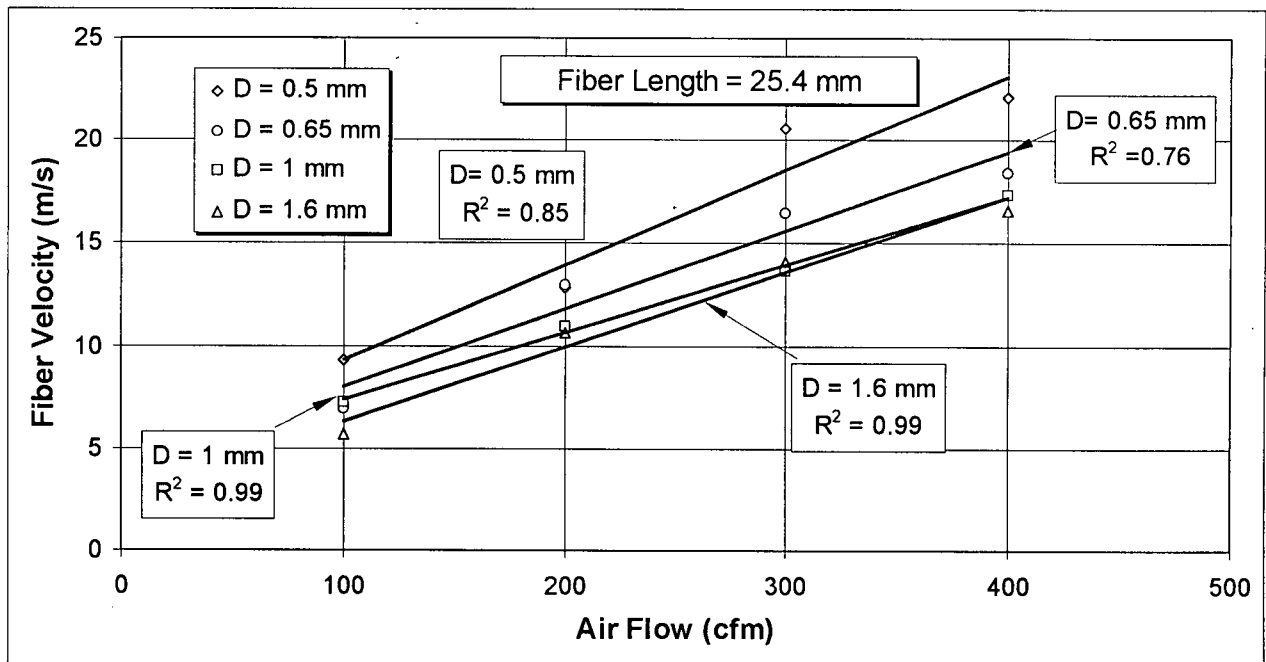
Figure 4.8b - Variation in mean steel fiber velocity with the air flow and fiber diameter (fiber length = 25.4 mm).
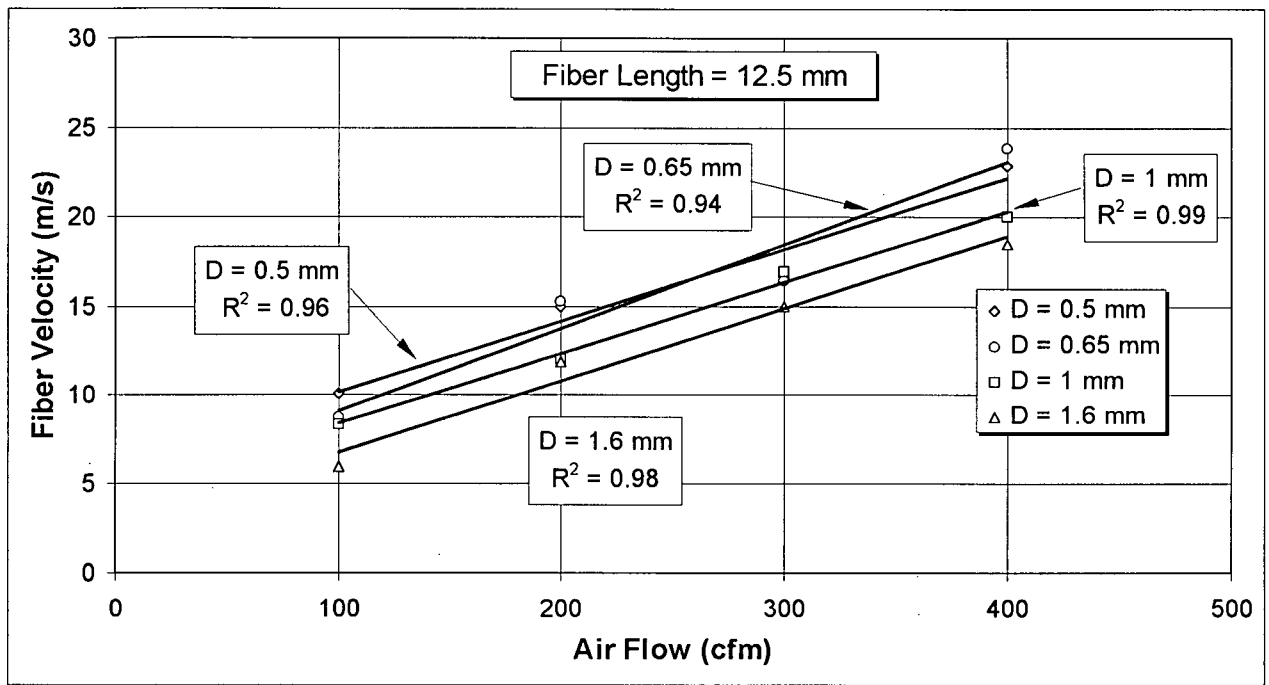
Figure 4.8c - Variation in mean steel fiber velocity with the air flow and fiber diameter (fiber length = 12.5 mm).
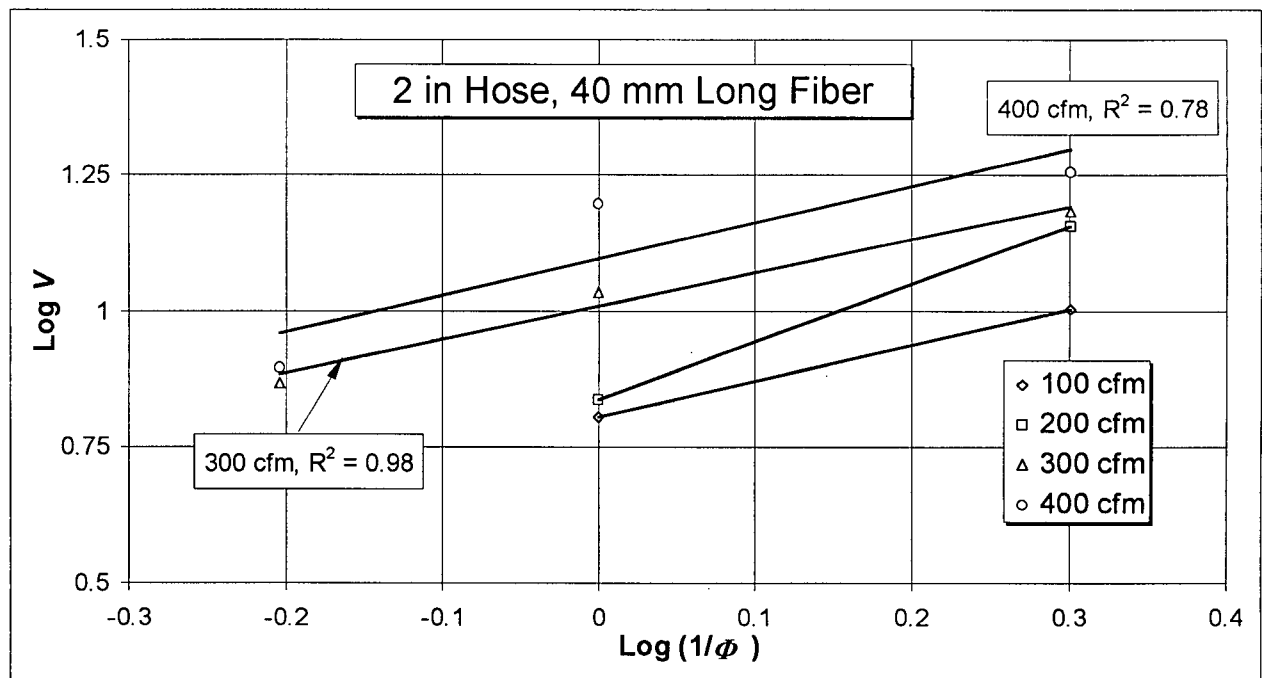
Figure 4.9a - Variation in mean steel fiber velocity with the inverse of the fiber diameter (log vs. log - hose diameter = 50 mm, fiber length = 40 mm).
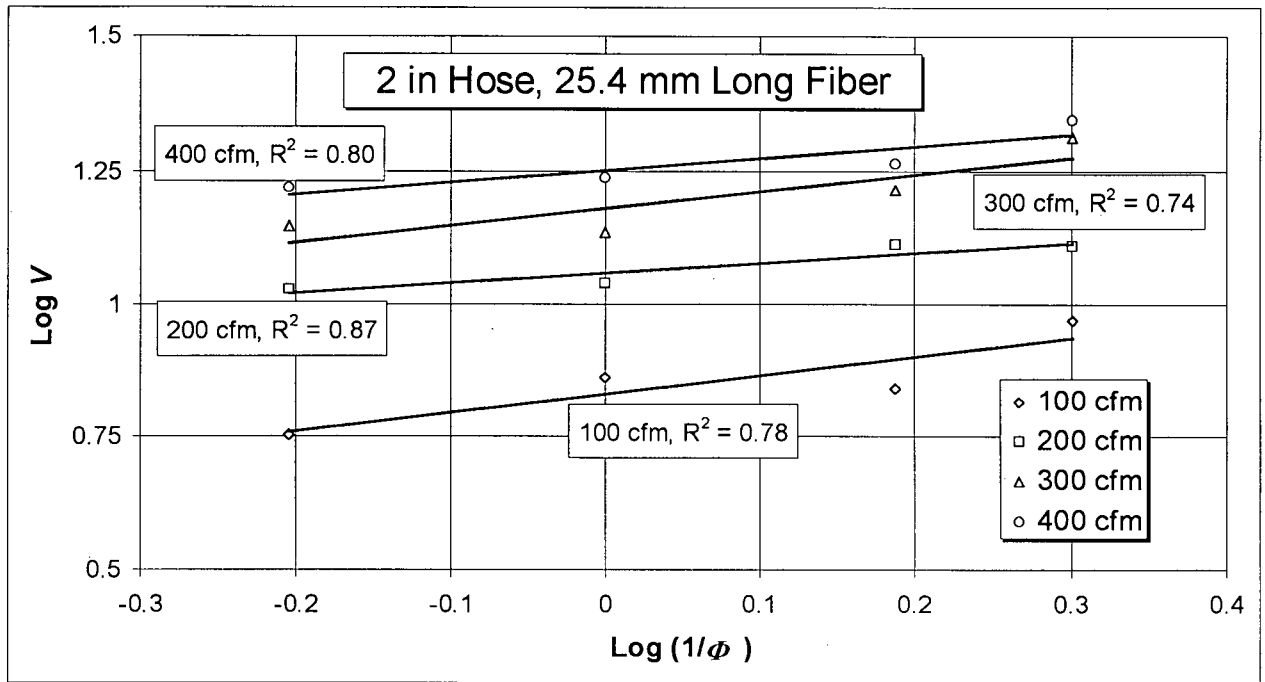
Figure 4.9b - Variation in mean steel fiber velocity with the inverse of the fiber diameter (log vs. log - hose diameter = 50 mm, fiber length = 25.4 mm).
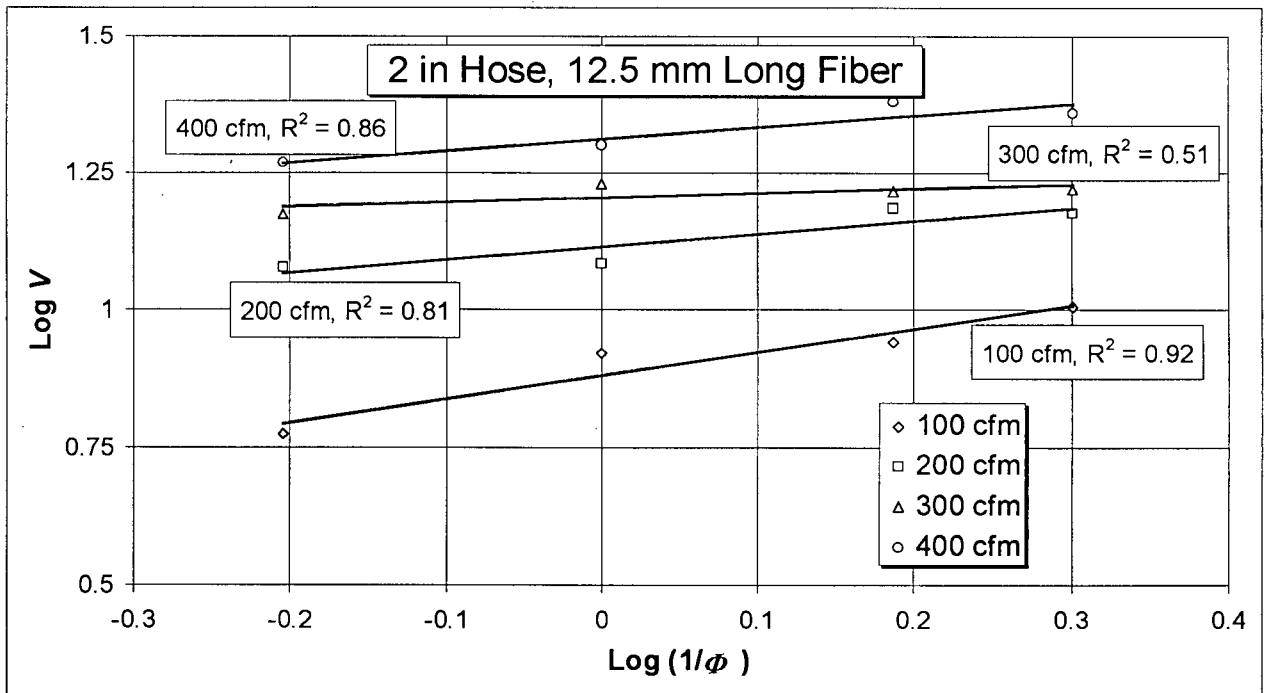
Figure 4.9c - Variation in mean steel fiber velocity with the inverse of the fiber diameter (log vs. log - hose diameter = 50 mm, fiber length = 12.5 mm).

4.3.2.3 - Variation of Fiber Velocity with the Hose Diameter

In Fig. 4.10a, fiber velocity results are presented for the case of 25.4 mm long fibers at diameters of 0.50, 0.65, 1.0 and 1.6 mm shot using a 1.5 in (38 mm) hose. Similar to the data presented in Figs. 4.8a through c, these data confirm the linear variation in the average fiber speed with the air flow for all four fiber diameters tested (average correlation coefficient, $R^2 = 0.96$). In addition, in Fig. 4.10a the influence of the fiber diameter on its velocity is also confirmed, with the greater diameter fibers leading to lower velocities (the 1.6 mm diameter fibers showed, on average, a 40% lower speed when compared to the 0.5 mm case).

The dependence of fiber velocity on the inverse of the diameter was also tested for the case of a 1.5 in hose. Results are presented in Fig. 4.10b and once more confirm the linear correlation. This is true for all four air flow values tested with an average correlation coefficient, $R^2 = 0.77$.
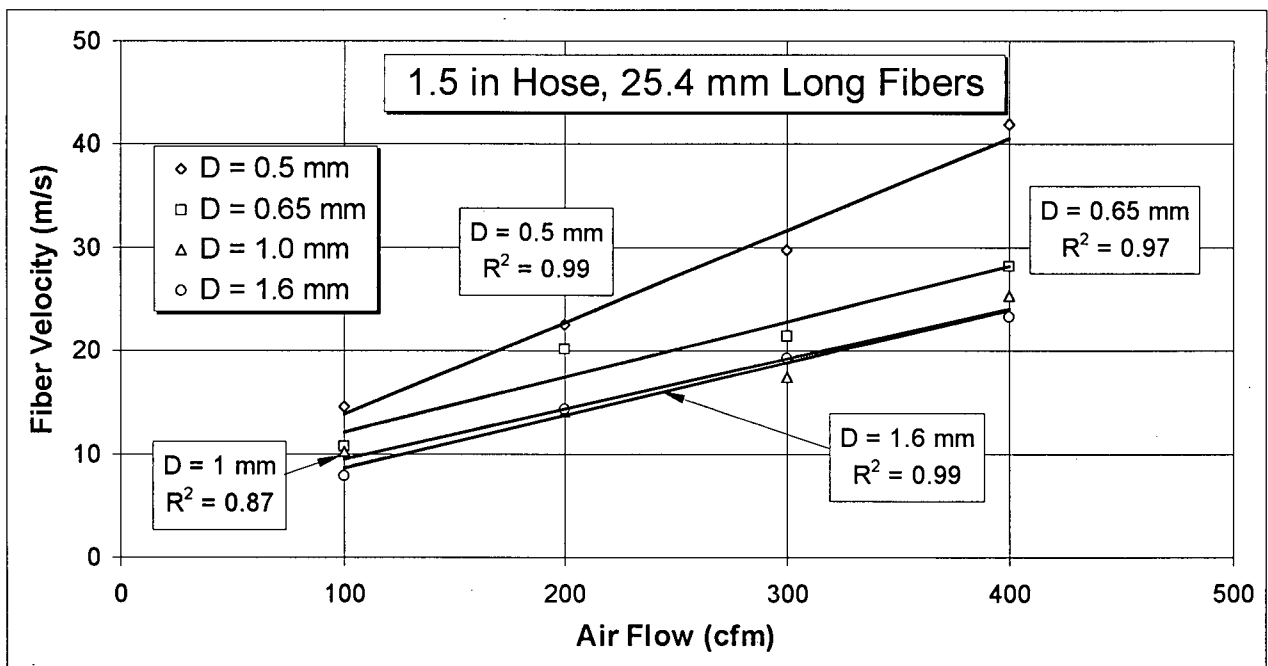
Figure 4.10a - Variation in the mean fiber velocity with air flow for a 1.5 in (38 mm) hose.
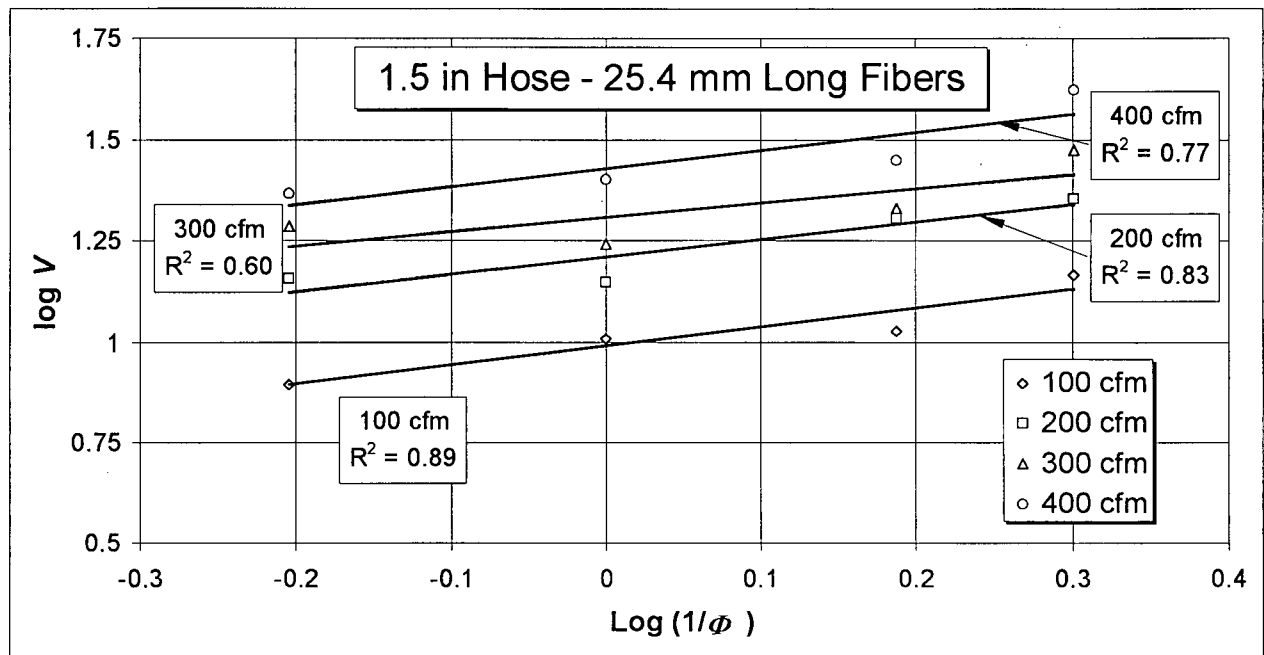
Figure 4.10b - Variation in the mean fiber velocity with the inverse of the fiber diameter (log vs. log - 38 mm hose).

Given that, as with aggregates, steel fiber velocities were also found to vary linearly with the air flow for the two hose diameters used (Figs. 4.8a through c and 4.10a) the hypothesis that the nominal air speed determines the mean fiber velocity irrespective of hose dimensions was also tested. Results are presented in Fig. 4.11 for a 25.4 mm fiber length and show that, for all fiber diameters tested, there is a good correlation between fiber velocity and air speed (average correlation coefficient, $R^2 = 0.88$). For a given fiber diameter, Fig. 4.11 allows prediction of the mean fiber velocity irrespective of hose dimensions with an average error of less than 2 m/s.

4.3.2.4 - Physical Interpretation and Generality of the Size Parameter ($1/\phi$)

It has been experimentally demonstrated here that a size parameter, given by the logarithm of the inverse of the diameter, is linearly related to the logarithm of the shooting velocity for both aggregates and steel fibers with a circular cross section. A possible physical interpretation to this parameter can be given by making use of the *specific projected area* ($\overline{A_{sp}}$) proposed by Banthia et al. (1992). They hypothesized that particle accelerations are directly proportional to the force

being applied to them by the compressed air flow (assumed to be determined by the particle projected area) and inversely proportional to the particle inertia (given by its mass).
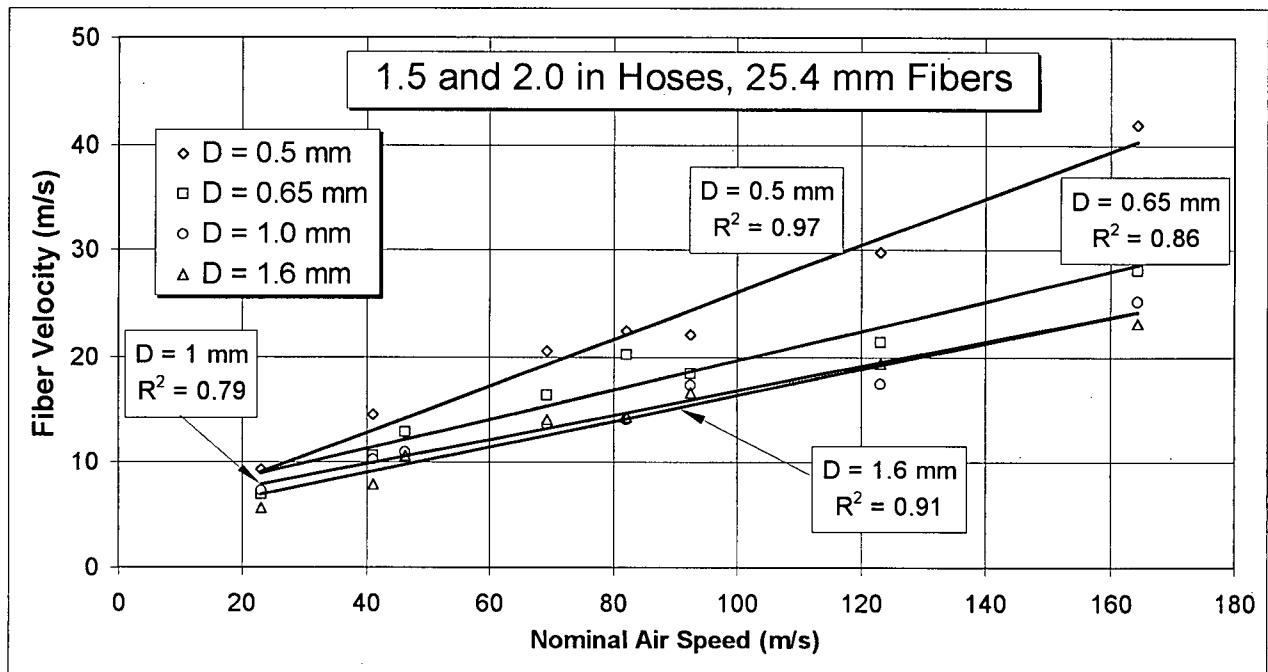
Figure 4.11 - Variation in the mean fiber velocity with the nominal air speed for 2 and 1.5 in hoses (50 and 38 mm, respectively).

Therefore, calculation of the specific projected area for an assumed spherical aggregate and cylindrical steel fiber shows that, in both cases, for a given mass density (ρ) the parameter proposed in Banthia et al. (1992) is determined by the inverse of the diameter, indicating that the latter may be a measure of the accelerations acting on the particle until it exits the nozzle. Thus, for a spherical aggregate having diameter Φ and mass density ρ:

$$\overline{A_{sp}} = \frac{\dfrac{\pi \cdot \phi^2}{4}}{\rho \cdot \left(\dfrac{1}{6}\pi \cdot \phi^3\right)} = \frac{3}{2 \cdot \rho} \cdot \frac{1}{\phi} \tag{4.2}$$

For a cylindrical steel fiber, having diameter Φ, length l_f and mass density ρ:

$$\overline{A_{sp}} = \frac{\phi \cdot l_f}{\rho \cdot \left[l \cdot \left(\frac{\pi \cdot \phi^2}{4} \right) \right]} = \frac{4}{\pi \cdot \rho} \cdot \frac{1}{\phi} \qquad (4.3)$$

However, while it is true that for these two cases, the specific projected area parameter is proportional to the inverse of the diameter factor found here, it cannot be said that $\overline{A_{sp}}$ is a general parameter able to account for fiber velocity irrespective of fiber shape (as originally proposed by Banthia et al., 1992[7]).

This is demonstrated in Fig. 4.12, where fiber velocity vs. air flow profiles are presented for three steel fibers of widely different shapes (flat and cylindrical) with A_{sp} as calculated by Banthia et al. (1992) between 245 and 574 mm^2/g. These data indicate that, despite the fact that the three fiber geometries tested have distinct specific projected areas, their velocity vs. air flow profiles are very similar.
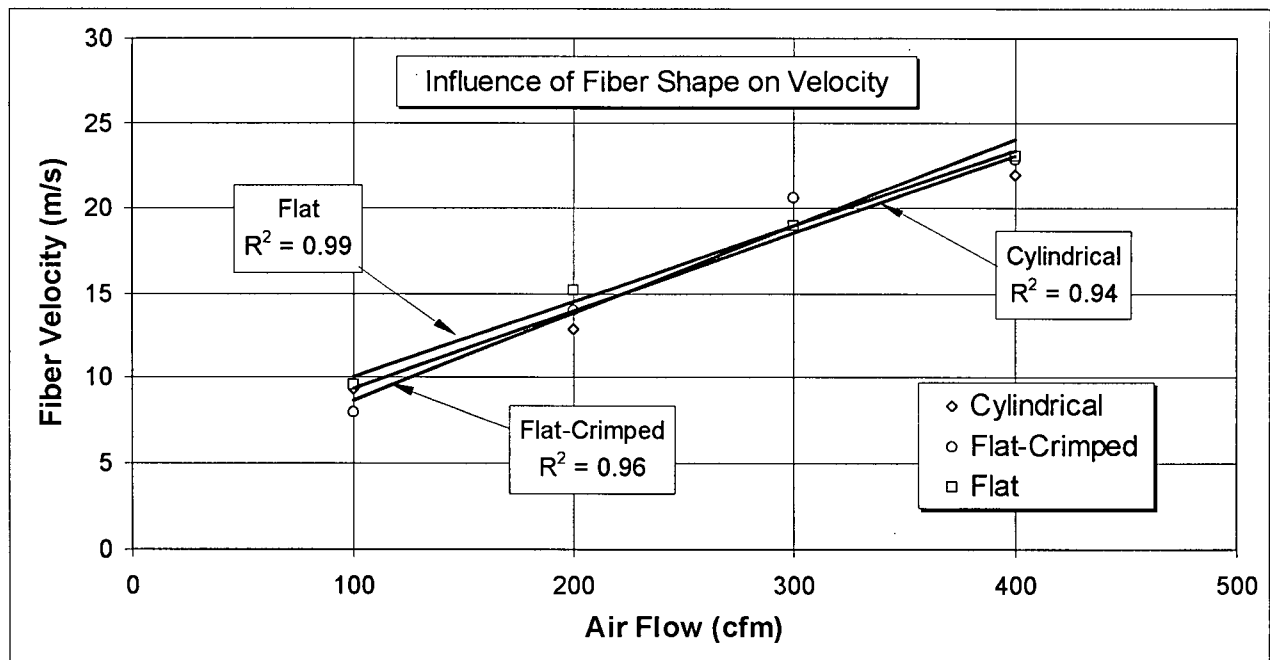
Figure 4.12 - Fiber velocity vs. air flow profiles of three steel fibers of widely different shapes (flat and cylindrical cross sections).

---

[7] Banthia et al. (1992) hypothesized on fiber accelerations (not velocities) being related to the specific projected area. However, the second is merely a consequence of the first; i.e. if a greater A_{sp} did lead to increased acceleration, a greater velocity should be expected.

This result leads to the conclusion that, although for a cylindrical shape, fiber velocities were found to be determined by the inverse of the diameter, the specific projected area alone cannot be considered general enough to account for the kinematics of fibers of different shapes (flat or cylindrical).

4.3.2.5 - Variation of Fiber Velocity with the Direction of Shooting and Rotational Velocity

For the 0.50 mm diameter, 25.4 mm long fiber, velocities were measured for both wall and overhead shooting. Results are presented in Fig. 4.13 and indicate that, similar to the case of aggregates, overhead shooting also leads to lower fiber velocities with an average 30% lower fiber speed for overhead shooting.
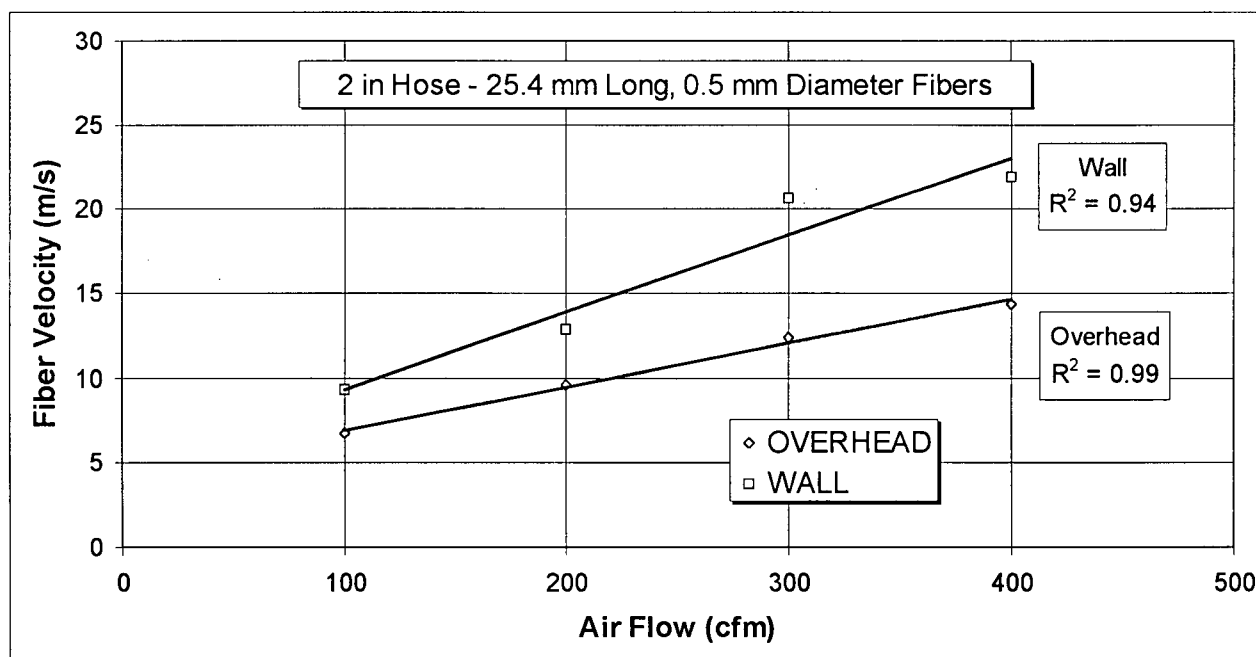
Figure 4.13 - Fiber velocity vs. position of shooting: overhead and wall spraying (hooked fibers).

For the larger aggregate sizes (12.7 and 9.5 mm) and for most steel fibers, it was possible to record the number of particle revolutions and thus calculate the average rotational speed[8] (ω). Results obtained indicate that, for the case of aggregates, the average angular velocity (ω) is

---

[8] From the high speed camera film it is only possible to detect plane motion rotational speed and therefore other rotational degrees of freedom are being neglected here.

approximately 314 rad/s (3000 rpm). A statistical test on the correlation between the angular and translational velocities of aggregates (ω and V) indicated no significant relationship between the two parameters (correlation coefficient, $R^2 = 0.16$).

Results on the angular velocities of fibers are presented in Fig. 4.14 as a function of the recorded translational velocity for all cases of fiber geometry, air flow, and position of shooting tested. These data show that fibers also tend to have angular velocities of the order of 314 rad/s. However, unlike aggregates they do show a statistical correlation between angular and translational velocity (correlation coefficient, $R^2 = 0.70$).
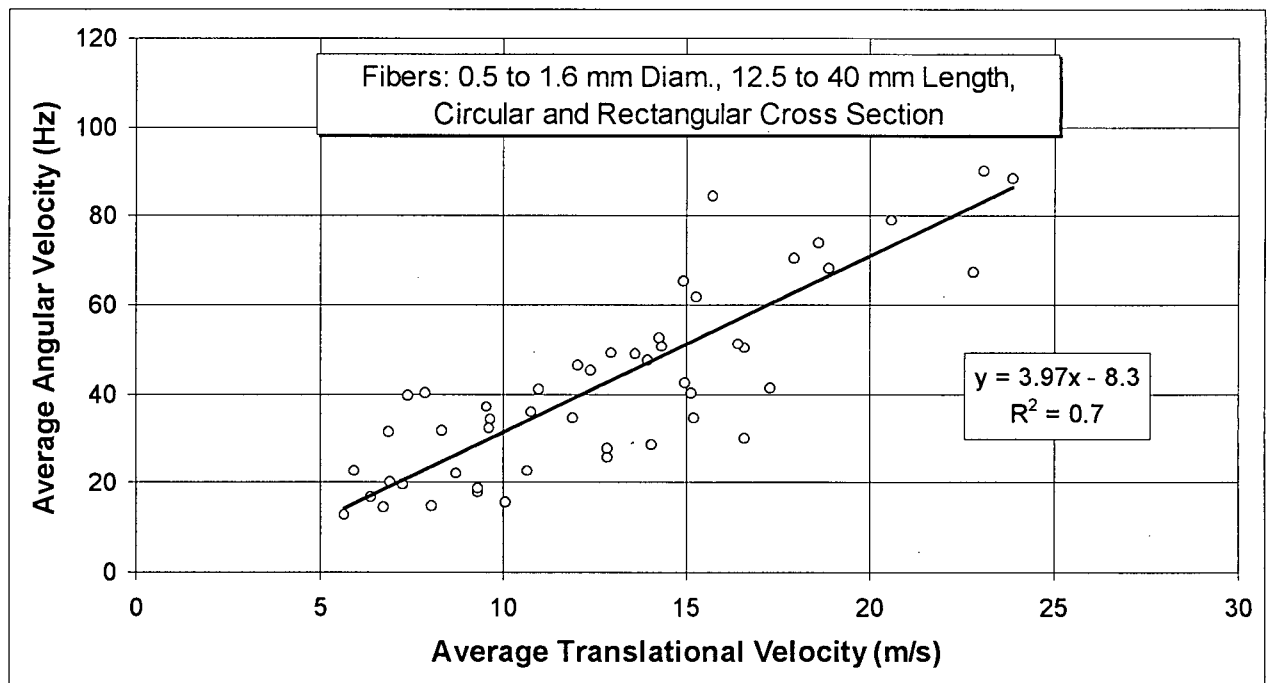
Figure 4.14 - Correlation between the angular and translational velocities of steel fibers for all fiber geometries tested.

In order to assess the relevance of the rotational component to the movement of a particle, making use of rigid body kinetics, the total kinetic energy (T) can be expressed in terms of its translational and rotational components (T_t and T_r). Thus, for a particle of general shape, having mass m, mass moment of inertia I_G and translational and angular velocities V and ω, the total kinetic energy can be calculated (Hibbeller, 1974). Assuming planar motion:

$$T = T_t + T_r = \frac{1}{2}m \cdot V^2 + \frac{1}{2}I_G \cdot \omega^2 \quad \text{where:} \quad I_G = \int_m r^2 dm \qquad (4.4)$$

Applying Eq. 4.4 to the case of a 3/8 in aggregate (radius = 4.8 mm, ρ = 2650 kg/m^3), with a translational velocity V = 13 m/s (equivalent to a 300 cfm air flow and a 2 in hose) and an angular velocity ω = 440 rad/s, the rotational component of the kinetic energy is found to account for only 1% of the total particle kinetic energy. The same calculation carried out for the case of a steel fiber (0.50 mm in diameter, 25.4 mm long, ρ = 7850 kg/m^3) having translational velocity V = 20 m/s, and angular velocity ω = 440 rad/s confirms that the rotational component accounts for only a small part (approximately 2.5%) of the total kinetic energy of steel fibers.

4.3.3 - High Speed Filming of Shotcrete

As mentioned in section 4.2, all velocity figures reported up to this point were obtained by separately shooting individual aggregate sizes or fibers without any cement or water. The reason for this is that the actual shotcrete environment creates too much dust for the delicate high speed filming equipment used, and does not allow for an accurate assessment of particle size nor the tracking of steel fibers or smaller aggregates.

However, in order to confirm the average velocity figures reported here for actual shotcrete, the technique described in section 4.2 and Fig. 4.2 was used to film dry-mix shotcrete sprayed onto the wall using a 300 cfm air flow. The analysis of this film shows that:

- The shotcrete stream is composed of isolated particles (coarse aggregates, sand and cement) that travel independently and separately (i.e. not as a whole mass or a unit body)[9].

- For those aggregates for which it was possible to track and thus measure their velocity (probable sizes between the 2.4 and 9.5 mm sieves) the average velocity was found to be 17.0 m/s, a value which lies within the 13 to 21 m/s range established for this spectrum of particle sizes when aggregates were shot without cement or water. This confirms that the technique employed here is representative of actual shotcrete.

---

[9] This is likely the reason why it is difficult to entrain air in dry-mix shotcrete without proper admixtures.

- The high speed camera footage also indicates that aggregate rebound is determined by whether or not the aggregate is able to attain a stable embedment position after impacting the shotcrete substrate. Aggregate entrapment was found to be the exception, rather than the rule[10].

4.4 - Conclusions

In this chapter, high speed filming was used to observe "in-flight" aggregates and steel fibers shot using an industrial scale dry-mix shotcrete equipment, allowing an accurate assessment of particle velocities. This has led to the characterization of shooting velocities for different combinations of aggregate and fiber dimensions and shapes, air flow, hose/nozzle dimensions and the direction of shooting. It was also shown that aggregate and fiber velocities are determined by a size parameter (the inverse of the diameter) and an air speed parameter (the air flow divided by the hose cross sectional area). The velocity figures found here will be implemented in a numerical model to be developed in Chapter 6, allowing calculation of the overall rate of rebound and describing the implications that the shooting velocity has on material loss due to rebound. More specific conclusions to be drawn from this chapter are:

1) The aggregate velocity (V) is related to the aggregate size (ϕ) by a relationship of the type $V = A \cdot \left(\frac{1}{\phi}\right)^B$, with larger aggregates generally traveling at half the speed of fines.

2) Similar to aggregates, steel fibers with circular cross-section also show a dependence of the shooting velocity on the diameter, with greater diameter fibers developing lower speeds.

3) For a given hose/nozzle system, the average aggregate and steel fiber velocities are directly proportional to the nominal air speed.

---

[10] For this test (and throughout this thesis) the nozzle was moved in a circular pattern, as ACI Committee 506 (1990) recommends and as would be done in the field with adequate nozzleman experience.

4) When comparing hose/nozzle systems of different shapes and dimensions, an estimate of aggregate and fiber velocities can be made with an average error of less than 3 m/s using the nominal air speed.

5) For a given air flow, overhead shooting leads to lower aggregate and steel fiber velocities compared to wall spraying.

6) High speed filming shows that the shotcrete stream is composed of isolated particles traveling independently rather than as a unit mass and that aggregate rebound is determined by particle embedment rather than entrapment[11].

---

[11] The distinction between the "entrapment" and "embedment" modes of rebound is further explored in Chapter 6 (section 6.3) where the embedment mode is used as the basis to develop an analytical model of aggregate rebound.

Chapter 5 - Mechanics of Aggregate Rebound

5.1 - Introduction and Objectives

As discussed previously, although one third to one half of all dry-mix shotcrete is lost in the form of rebound, a rational theory of aggregate rebound from a fresh concrete surface has never been developed. In part, this can be attributed to the high speed of the particles in the shotcrete spray, which makes it impossible to observe the rebound process using conventional methods. In fact, until recently, even the speed at which the particles tend to travel was largely unknown, as described in section 4.1.

Another factor that considerably complicates the development of a rational theory of rebound is the difficulty in modeling the rheology of fresh shotcrete. This is due to the fact that the usual simplification, which is used to assume that fresh concrete behaves rheologically as a Bingham fluid (Tattersal, 1983; Ghio, 1993 and Beaupre, 1994) is unable to account for rebound since it fails to recognize the elastic component of fresh concrete rheology that causes an impinging particle to spring out of the shooting surface. As a result, although some mix-design parameters are empirically known to influence aggregate rebound in shotcrete (cement content, shooting consistency and the presence of silica fume) the mechanism by which each of these factors acts is largely unknown. In fact, even more basic questions, such as the reason why coarse aggregates tend to rebound up to four times more than the smaller aggregate phases, remain unanswered.

Therefore, the objective of this chapter was to make use of solutions from theory of rebound, that are available in the literature, to develop a mechanical model for the case of an aggregate particle rebounding from a fresh concrete surface. It is expected that such a model will lead to gain in fundamental knowledge on the mechanics of the process, and thus lay ground for a rational theory of shotcrete rebound (subject of Chapter 6).

5.2 - Theory of Rebound

5.2.1 - The Penetration Phase

As an aggregate particle, traveling at a given velocity V, reaches the shooting surface, its kinetic energy will cause it to penetrate into the fresh concrete, in a process very similar to that of an indentation. From a micromechanical point of view, the indentation process consists of a classical problem of metal to metal contact mechanics that was initially addressed by Bishop et al. (1945) to analyze results from hardness tests. A complete review of the contact problem can be found in Johnson (1985).

Making use of the theory described in Bishop et al. (1945) and assuming that the geometry of an aggregate particle can be approximated by a sphere, a solution to the problem of determining the stresses in the shotcrete substrate during the penetration phase starts by recognizing that, due to symmetry, since displacements are radial, they can be assumed to be induced by a radially symmetric body. Thus, the assumption made is that, below the contact surface (radius a) a hemispherical core is formed in which a hydrostatic state of pressure (p) occurs (Fig. 5.1).
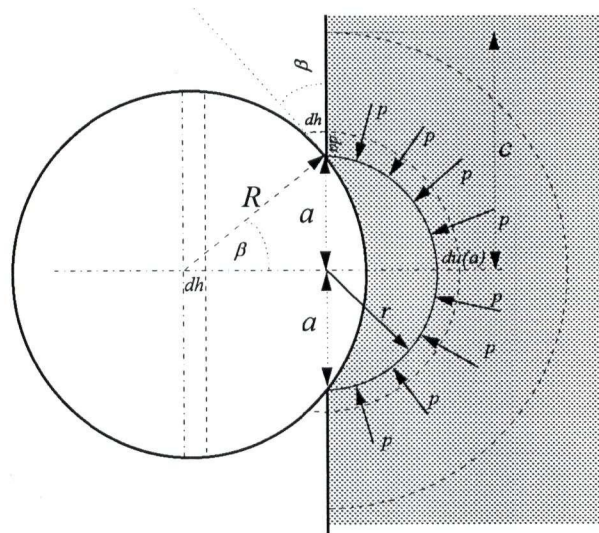
Figure 5.1 - Spherical impactor striking the elasto-plastic substrate with the formation of the hydrostatic cavity ($r < a$) and the elasto-plastic region ($r < c$).

Outside this hemispherical cavity, displacements are assumed to be radial and stresses are those of an infinite elastic-perfectly plastic body containing a spherical cavity under a pressure p - a problem solved by classical theory of plasticity (Hill, 1950). The elastic-plastic boundary is assumed to lie at a radius c ($c>a$) beyond which no plastic flow has occurred, and, therefore,

straightforward theory of elasticity can be applied in this region (Fig. 5.1). Thus the boundary conditions for this problem become:

1) Because the hemispherical cavity is under hydrostatic stress (p) and σ_r is a principal direction, on the surface of the cavity $\sigma_r|_{r=a} = p$.

2) For compatibility, displacements at the boundary of the core (da) must accommodate the volume displaced by the impactor (determined by dh) - Fig. 5.1.

Radial stresses in the plastic region are given by Hill (1950), thus assuming the Tresca yield criterion, with the yield strength of the medium Y, for $a \leq r \leq c$:

$$\frac{\sigma_r}{Y} = -2\ln\left(\frac{c}{r}\right) - \frac{2}{3}$$

(5.1)

And in the elastic zone:

$$\frac{\sigma_r}{Y} = -\frac{2}{3}\left(\frac{c}{r}\right)^3$$

(5.2)

Starting from the condition of compatibility, from Fig. 5.1:

$$Volume\ dislocated = Volume\ accommodated \Rightarrow 2\pi a^2 \cdot du(a) = \pi a^2 \cdot dh$$

(5.3)

And also, from Fig. 5.1:

$$\frac{dh}{da} = tg\beta \approx \sin\beta = \frac{a}{R}, \text{ and thus } dh = \frac{a}{R}da$$

(5.4)

From Eqs. (5.3) and (5.4), the condition of compatibility becomes:

$$du(a) = \frac{a}{2R}da$$

(5.5)

The radial displacements are also given by Hill (1950):

$$\frac{du(a)}{dc} = \frac{Y}{E}\left[3(1-v)\left(c^2 / a^2\right) - 2(1-2v)(a / c)\right] \tag{5.6}$$

by equating (5.5) and (5.6):

$$\frac{a}{2R} = \frac{Y}{E}\frac{dc}{da}\left[3(1-v)\left(c^2 / a^2\right) - 2(1-2v)(a / c)\right] \tag{5.7}$$

According to Johnson (1985), axial symmetry and similarity in the stress field require that $dc/da = c/a$, and therefore Eq. 5.7 may be written:

$$\frac{aE}{R} = Y\left[6(1-v)\left(\frac{c}{a}\right)^3 - 4(1-2v)\right] \tag{5.8}$$

Thus, the ratio between the core boundary (a) and the elastic-plastic boundary (c) can be found:

$$\left(\frac{c}{a}\right)^3 = \left[\frac{aE}{RY} + 4(1-2v)\right]\frac{1}{6(1-v)} \quad \text{or, for } v = \frac{1}{2}, \quad \frac{c}{a} = \left(\frac{aE}{3RY}\right)^{\frac{1}{3}} \tag{5.9}$$

Since the ratio (c/a) is known, we may go back to Eq. 5.1 to impose the first boundary condition: $\sigma_r\big|_{r=a} = p$ with the hydrostatic core at $r = a$:

$$\frac{\sigma_r}{Y}\bigg|_{r=a} = -2\ln\left(\frac{c}{a}\right) - \frac{2}{3} = \frac{-p}{Y} \tag{5.10}$$

From Eqs. (5.9) and (5.10), and assuming $v = \frac{1}{2}$:

$$\frac{p}{Y} = \frac{2}{3}\left[\ln\left(\frac{aE}{3RY}\right) + 1\right] \tag{5.11}$$

From Eq. 5.11, it is possible to find the contact stress (p) that acts between the indenter and the medium, at any position of contact (a), expressed as a function of the non dimensional $\left(\frac{aE}{3RY}\right)$.

According to Johnson's (1985) interpretation, this non-dimensional term represents a measure of the ratio between the strains imposed by the indenter to the medium (a/R) and the elastic strain limit of the medium (Y/E).

For the case of shotcrete, the most important results from this formulation are that the stresses acting on the surface of the aggregate as it penetrates into the concrete are constant throughout the contact region and, moreover, that this contact stress remains virtually unchanged at $p \cong 3Y$ throughout the penetration process[1].

This important result allows one to calculate the final depth of penetration of the particle $\left(\delta^{*}\right)$ by balancing its kinetic energy (W_I) with the work done by the contact stress (p) during penetration. With p = *constant*, the total resistance force acting on the particle $f(\delta)$ can be written as (Fig. 5.2):

$$f(\delta) = p \cdot \left[\pi \cdot a(\delta)^2 \right]$$
(5.12)

By ignoring inertial effects (i.e. a quasi-static approach) the energy balance becomes:

$$W_1 = \int_0^{\delta^*} f(\delta) \cdot d\delta$$
(5.13)

From Eqs. 5.4 and 5.12, Eq. 5.13 can be rewritten as:

$$W_1 = p \cdot \left(\frac{\pi \cdot a^{*4}}{4R} \right) = p \cdot V_a$$
(5.14a)

Eq. 5.14a shows that the apparent volume penetrated by the impactor $V_a = \left(\frac{\pi \cdot a^{*4}}{4R} \right)$ is related to its kinetic energy by the contact stress (p). At this point, it is necessary to recognize that the contact stress during a high-speed impact event, such as that of an aggregate in shotcrete, can lead to high strain-rates. And, since fresh concrete is known to be a strain-rate sensitive material (Tattersal, 1983; Ghio, 1993 and Beaupre, 1994), the dynamic contact stress can be significantly different from that measured under low strain-rate, quasi-static tests. Thus, in order to account for the viscous behavior of fresh concrete rheology, a distinction should be made between the contact

---

[1] The relationship p = *3Y* only holds true for a hemispherical indenter head. For a flat punch such as the cylindrical needle used in Chapter 3 to assess shotcrete workability, the relationship between contact and yield stresses is greater (approximately p = *6Y* as demonstrated by Johnson, 1985).

stress arising under dynamic conditions (p_d) and its static counterpart (p). Eq. 5.14a should, therefore, be rewritten as:

$$W_1 = p_d\left(\frac{\pi \cdot a *^4}{4R}\right) = p_d \cdot V_a \tag{5.14b}$$
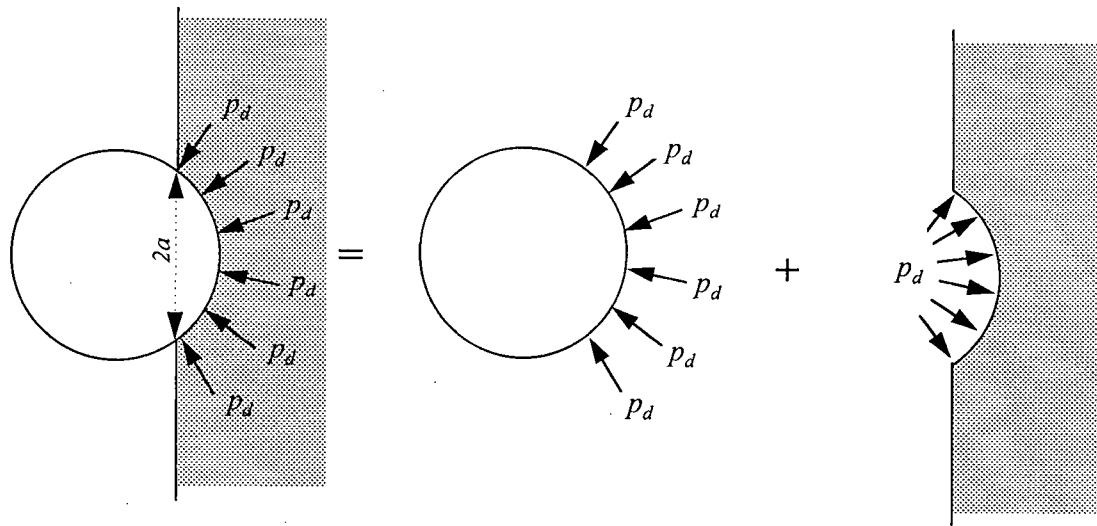
Figure 5.2 - Analysis of stresses acting on the impactor during the penetration phase.

5.2.2 - The Reaction Phase[2]

Once the aggregate particle has reached its full depth of penetration into the fresh concrete medium, the elastic strain energy stored in both the impactor and the medium will be transferred back to the particle, imparting it kinetic energy (W_2) that may eventually cause it to rebound.

From a theoretical point of view, it was Tabor (1948) who, working with the static and dynamic hardness of metals, originally developed a practical means of calculating the rebound energy (W_2) of a metal sphere striking a metal substrate. He did so by recognizing that, at the end of the

---

[2] The formulation described in this section is due to Tabor (1948).

spring-back process, the cavity originally occupied by the impactor (radius r_1) will be left with a greater radius (r_2) due to the release of elastic strains. Since this process is fully elastic, the maximum contact force (F - Fig. 5.3) is related to the final contact radius (a^*) by classical Hertzian theory of contact (Johnson, 1985), according to which:

$$a^* = \left(\frac{3FR}{4E^*}\right)^{\frac{1}{3}} \quad \text{where:} \quad \frac{1}{R} = \frac{1}{r_1} + \frac{1}{r_2} \quad \text{and} \quad \frac{1}{E^*} = \frac{1-v_1^2}{E_1} + \frac{1-v_2^2}{E_2} \tag{5.15}$$

From Eq. 5.15, the contact force (f) at any given contact radius ($\alpha : \alpha \leq a^*$) can be written as:

$$f(\alpha) = F \frac{\alpha^3}{a^{*3}} \tag{5.16}$$

Since the process is fully elastic, the rebound energy (W_2) that we wish to calculate is identical to the work necessary to bring the sphere into full contact with the cavity (i.e., $\alpha \rightarrow a^*$ and $f \rightarrow F$, Fig. 5.3) at which point the contact force (f) will have traveled a distance z^*. Thus:

$$W_2 = \int_0^{z^*} f(z)dz \tag{5.17}$$

unloaded: $\alpha = 0$ loaded: $\alpha = a^*$
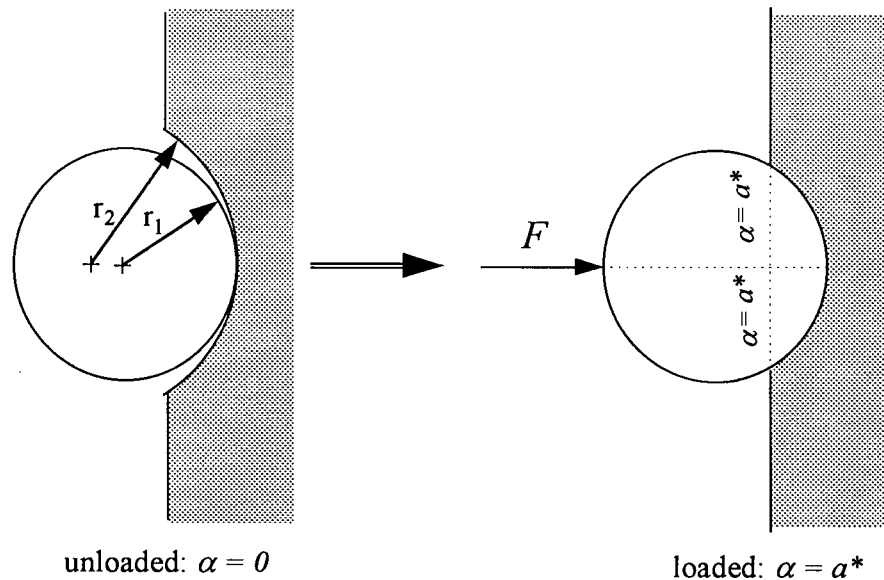
Figure 5.3 - Because the recovery process is fully elastic, the rebound energy can be calculated from the force necessary to bring the impactor into full contact with a spherical cavity.

Eq. 5.17 can be solved by making use of the relationship between z and α given by Hertzian theory (Johnson, 1985):

$$z(\alpha) = \frac{3}{4} \frac{f(\alpha)}{\alpha} \left[\frac{1-v_1^2}{E_1} + \frac{1-v_2^2}{E_2} \right]$$

(5.18)

From Eqs. 5.16 and 5.18:

$$dz = \frac{3}{2} F \frac{\alpha}{a^{*3}} \left[\frac{1-v_1^2}{E_1} + \frac{1-v_2^2}{E_2} \right] d\alpha$$

(5.19)

And, therefore, Eq. 5.17 can be rewritten as:

$$W_2 = \frac{3}{10} \frac{F^2}{a*} \left[\frac{1-v_1^2}{E_1} + \frac{1-v_2^2}{E_2} \right] \text{ or, for } v_1 = v_2 = 0.3, \quad W_2 = 0.27 \frac{F^2}{a*} \left[\frac{1}{E_1} + \frac{1}{E_2} \right]$$

(5.20)

Since at full contact ($\alpha = a*$) plastic behavior is assumed to begin, at this point, the contact stress is p (given by Eq. 5.11). Therefore, F can be expressed as $F = p \cdot (\pi a*^2)$ so that Eq. 5.20 can be rewritten as:

$$W_2 = \frac{3\pi^2}{10} p^2 a*^3 \left[\frac{1-v_1^2}{E_1} + \frac{1-v_2^2}{E_2} \right] \text{ for } v_1 = v_2 = 0.3, \quad W_2 = 0.27\pi^2 p^2 a*^3 \left[\frac{1}{E_1} + \frac{1}{E_2} \right]$$

(5.21)

From the expression for the apparent volume penetrated (V_a - Eq. 5.14a), $a*^3$ may be written as:

$$a*^3 = \left(\frac{4r_1 V_a}{\pi} \right)^{\frac{3}{4}}$$

(5.22)

From Eqs. 5.21 and 5.22 the energy of rebound (W_2) can be expressed in terms of the volume penetrated (V_a) as:

$$W_2 = \frac{3\pi^2}{10} p^2 \left(\frac{4r_1 V_a}{\pi} \right)^{\frac{3}{4}} \left[\frac{1-v_1^2}{E_1} + \frac{1-v_2^2}{E_2} \right]$$

(5.23)

From Eq. 5.14b the volume penetrated (V_a) can be calculated from the impact energy (W_1), and the energy of rebound can, therefore, be rewritten as a function of the impact energy as:

$$W_2 = \frac{3\pi^2}{10} p^2 \left(\frac{4r_1 W_1}{\pi \cdot p_d} \right)^{\frac{3}{4}} \left[\frac{1 - v_1^2}{E_1} + \frac{1 - v_2^2}{E_2} \right]$$ (5.24)

The coefficient of restitution (e), which gives a measure of the amount of impact energy converted back into rebound, can be expressed in terms of the velocities of impact and rebound (V and V') as:

$$e = \frac{V'}{V} \quad \text{or} \quad e^2 = \frac{V'^2}{V^2} = \frac{W_2}{W_1}$$ (5.25)

By making use of Eq. 5.24 and taking W_1 to be the kinetic energy of impact, Eq. 5.25 can be rewritten as:

$$e^2 = \frac{\dfrac{3\pi^2}{10} p^2 \left(\dfrac{4r_1}{\pi p_d} \right)^{\frac{3}{4}} \left[\dfrac{1 - v_1^2}{E_1} + \dfrac{1 - v_2^2}{E_2} \right]}{\left(\dfrac{1}{2} m V^2 \right)^{\frac{1}{4}}}$$ (5.26)

Therefore, grouping all constants, the coefficient of restitution (e) can be expressed as:

$$e = \sqrt{\frac{3\pi^2}{10} \left(\frac{4r_1}{\pi} \right)^{\frac{3}{4}} \left(\frac{1}{E^*} \right) \left(\frac{1}{2} m \right)^{-\frac{1}{4}}} \cdot p \cdot (p_d)^{-\frac{3}{8}} \cdot V^{-\frac{1}{4}}$$ (5.27)

Eq. 5.26 and its simplified form (Eq. 5.27) lead to Tabor's (1948) important conclusion that, since it also depends on the severity of the impact (V), the coefficient of restitution is not a material property. Thus, for very slow events, the elastic component of the rebound tends to predominate over the plastic, leading to a coefficient of restitution closer to unity. As will be discussed ahead, this has a direct implication on the rebound of the larger (and consequently slower - Chapter 4) aggregate particles.

5.2.3 - Contact Time

The time of contact between the impinging aggregate and the fresh concrete substrate can be considered of relevance in dealing with the specific case of shotcrete, especially in assessing the possibility that particles, that would otherwise rebound, be entrapped by the incoming material. In order to calculate the time of penetration, it is necessary to solve the differential equation of motion for the impactor. Thus, for a particle of mass m, it may be written (Fig. 5.2):

$$m\frac{d^2\delta}{dt^2} = -\left(\pi \cdot a(\delta)^2\right) \cdot p_d \qquad (5.28)$$

By making use of the approximation $a^2(\delta) \approx 2r\delta$, Eq. 5.28 can be rewritten as:

$$\delta'' + \left(\frac{2\pi r p_d}{m}\right)\delta = 0 \qquad (5.29)$$

This homogeneous differential equation has a solution of the type:

$$\delta(t) = A_o\sin(\varpi t) \quad, \quad \text{where} \quad \varpi = \sqrt{\frac{2\pi r p_d}{m}} \quad \text{and} \quad A_o = \delta* \qquad (5.30)$$

From Eq. 5.30, equating $\delta(t) = \delta*$, the time of penetration (t_{pen}) can be calculated:

$$t_{pen} = \left(\frac{m\pi}{8rp_d}\right)^{\frac{1}{2}} \qquad (5.31)$$

In the case of shotcrete, for which particles have similar mass density (ρ) but widely different dimension (r), it is more appropriate to write Eq. 5.31 as:

$$t_{pen} = \pi r\left(\frac{\rho}{6p_d}\right)^{\frac{1}{2}} \qquad (5.32)$$

It is interesting to note that, as pointed out by Johnson (1985), the time of penetration is independent of the impact velocity. Also, taking actual values of aggregate density (ρ = 2650

kg/m^3) and dynamic contact stress (p_d = 10 MPa)[3], even for the largest aggregates (r = 12.5 mm) the total penetration time does not exceed a fraction of a millisecond (t_{pen} = 0.3 msec). During this time frame, the incoming spray of material, traveling at an average[4] speed of approximately 25 m/s (Chapter 4) does not advance more than 8 mm, rendering the entrapment process an unlikely one (as confirmed by the high speed camera footage of actual shotcrete in item 4.3.3).

Another important conclusion that can be extracted from calculating the time of penetration is that the average acceleration involved in the penetration and reaction phases (V/t_{pen}) is hundreds of times greater than that of gravity: for a 9.5 mm aggregate the average accelerations during the penetration and reaction[5] phases are 50,000 and 2,000 m/s^2, respectively. These figures are at least two orders of magnitude greater than g, allowing one to conclude that, for a given impact velocity, gravity has little effect on the rebound mechanism of aggregates (as is experimentally demonstrated for actual shotcrete in 3.3.2.3).

5.3 - Material and Methods

In order to measure velocities of impact and rebound, the high speed camera (model EKTAPRO 1000) capable of shutter rates of up to 1000 frames per second was used. The particle positions were monitored with the aid of a grid mesh background and the time was reported by the camera on screen. The rebound experiments were performed using a single particle accelerator. This apparatus consists of a compressed air gun that allows any geometry of particle to be shot against a fresh concrete substrate. The velocity at which the particles are shot can be varied by changing the air flow supplied to the gun (Fig. 5.4).

To represent aggregate particles, 14 and 25.4 mm diameter glass spheres were used. Glass was the material of choice in these tests since it has a mass density very similar to that of concrete aggregates. The fresh concrete substrate was produced using concrete sand and 9.5 mm

---

[3] the value p_d = 10 MPa was determined experimentally to be an average value for the dynamic contact stress - see Fig. 5.10a.

[4] For an ACI No. 2 gradation curve, the average aggregate size is 1.2 mm (Fig. 3.2) which, at a 300 cfm air flow, for a 2 in (50 mm) hose will have an average speed of 25 m/s (Fig. 4.4a).

[5] The reaction time is given as a function of the coefficient of restitution by Johnson (1985), pp. 365.

aggregate. A constant coarse to fine aggregate ratio of 0.35 was used since this is a typical value for dry process shotcrete mixtures. Aggregate to cement ratios varied between 2.5 and 4.5 and enough water was added to obtain the desired workability.

During shooting of the particles, a thin plastic sheet was loosely placed on the surface of the fresh concrete in order to prevent adhesion between the fresh concrete and the impactor. Such adhesion would have a decelerating affect, causing lower rebound velocities. After each impact event, the depth of penetration was measured using a pair of calipers in order to calculate the volume displaced by the impactor.

The static contact stress (also used as an assessment of the workability of the mixes produced) was measured by a static indentation test, in which a 25.4 mm diameter steel hemisphere was penetrated into the fresh concrete surface using the penetrometer equipment described in section 3.3.1.1 (Fig. 3.3). The signals from the penetration test were recorded using a digital data acquisition system at a sampling rate of 10 Hz and processed in order to obtain the average depth of penetration and contact stress (the penetration force divided by the projected contact area).
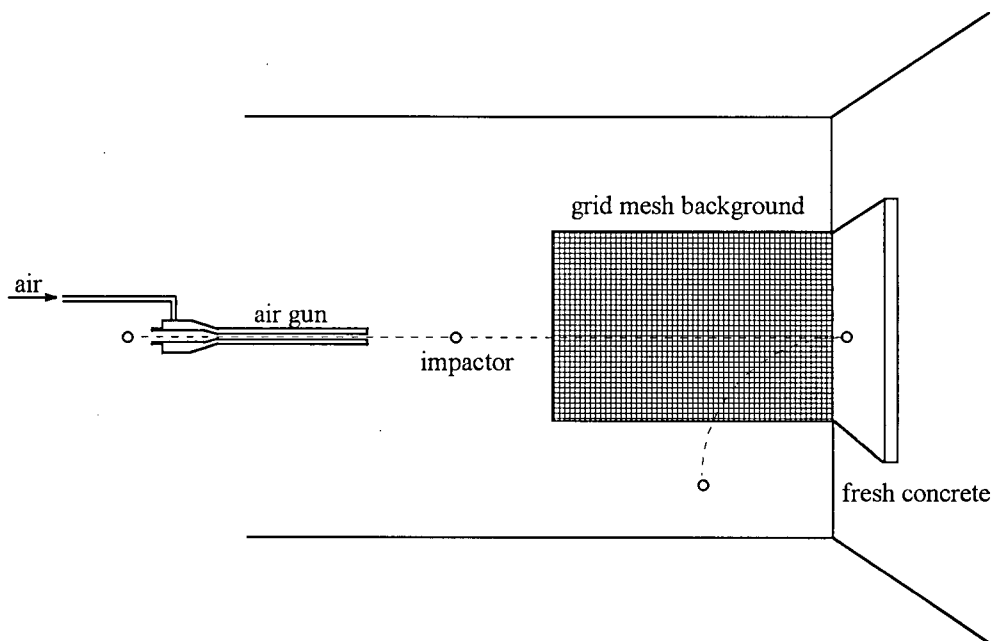
Figure 5.4 - Single particle shooting apparatus used for measurements of velocities of impact and rebound.

5.4 - Results and Discussion

5.4.1 - The Penetration Phase

Results from the indentation tests performed using a 25.4 mm diameter hemisphere to penetrate into fresh cast concrete and shotcrete of various consistencies are presented in Fig. 5.5 in terms of the contact stress (the penetration load divided by the projected contact area) expressed as a function of the depth of penetration. For each situation, three to six tests were performed and, in all cases, the contact stress was found to rise to a maximum value very early in the penetration phase (typically before a 1 mm depth of penetration) and remain constant from this point on. This result is in good agreement with Eq. 5.11, which predicts that a yield value of contact stress $(p \cong 3Y)$ should be reached as soon as the penetration event enters the fully plastic regime.

This indicates that the assumption of an elasto-plastic material, behaving according to Tresca's yield criterion of maximum shear stress, is valid when dealing with the rheology of fresh concrete and shotcrete. As shown in Fig. 5.5, the static contact stress (p) varies between 0.3 and 1 MPa for dry-mix shotcrete ranging from what would be considered a wet to a dry consistency (overhead build-up of respectively 50 and 150 mm). The typical value for an usual dry-mix consistency is approximately 0.50 MPa.

The assumption of a constant contact stress (p) throughout the penetration process, was also made in adopting a quasi-static approach to arrive at the relationship between the kinetic energy of the impactor (W_1) and the apparent volume penetrated $(V_a$ - Eq. 5.14b). According to the theory presented, these two quantities should be directly related through the dynamic contact stress (p_d). Therefore, in order to validate this hypothesis, the measured volume penetrated by 14 mm and 25.4 mm diameter impactors shot at various velocities is presented as a function of the measured kinetic energy of the impactor in Fig. 5.6. Results from this analysis show that indeed the two quantities linearly correlate (Fig. 5.6), confirming Eq. 5.14b.
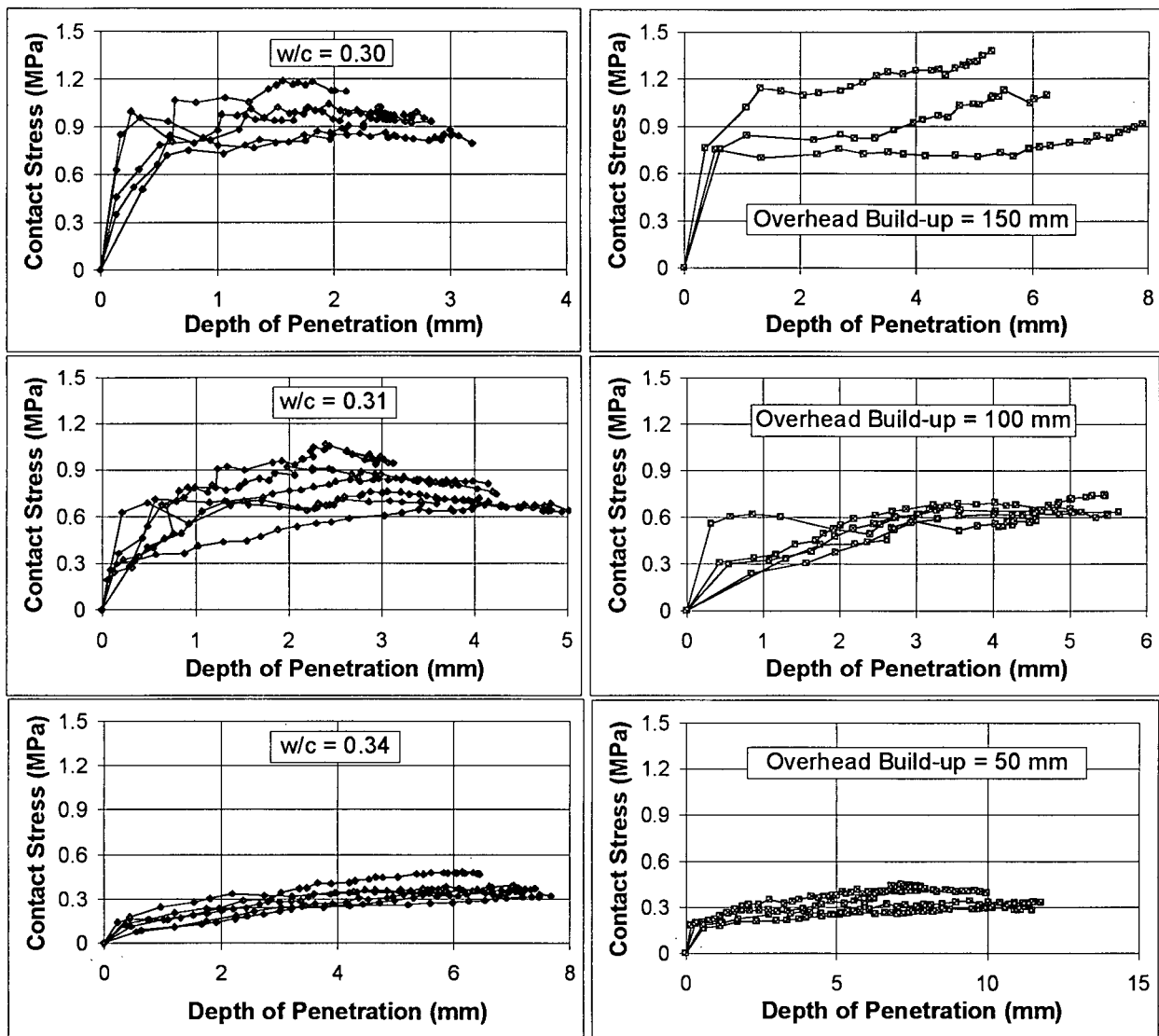
Figure 5.5 - Static contact stress (*p*) vs depth of penetration of the hemispherical indenter head: fresh cast concrete (left) and shotcrete (right). Age of mixes = 5 min.

The theory also predicts that the ratio between these two quantities is the contact stress $(p_d = W_1 / V_a)$. In the case presented in Fig. 5.6, this ratio results in a value of stress $(p_d = 1/ slope)$ of 3.33 MPa, a value much larger than the static contact stress shown in Fig. 5.5. As mentioned earlier, this is due to the high strain rate involved in the penetration process and the viscous nature of fresh concrete rheology.
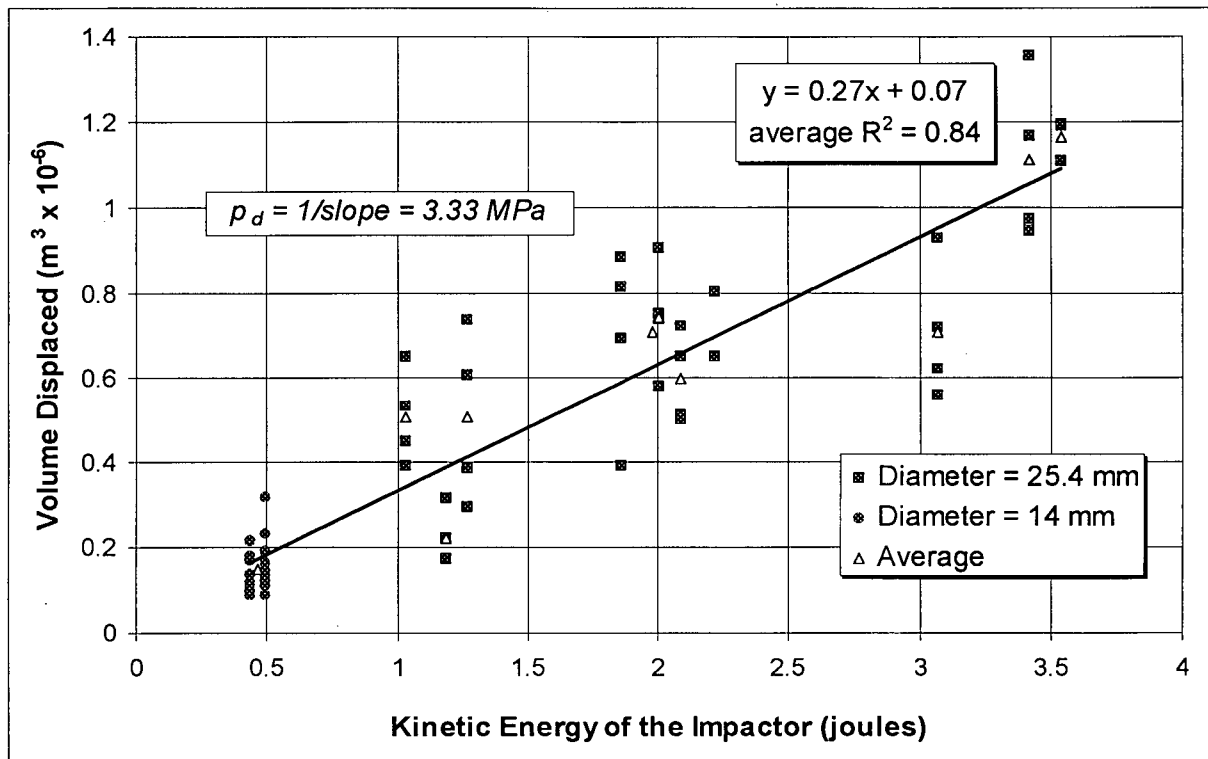
Figure 5.6 - Correlation between the kinetic energy of the impactor and the volume penetrated by it. Determination of the contact stress $(p_d = 1/slope)$.

Dynamic and static contact stresses determined for mixes of equal proportions but different water to cement ratios are presented in Fig. 5.7. These data show that, for fresh concrete, the dynamic contact stress is one order of magnitude greater than its static counterpart. Similar results were obtained by Tabor (1948) for soft metals.

In the theory described earlier, the dynamic contact stress (p_d) is introduced to calculate the final depth of penetration that allows one to compute the size of the final contact radius (a^* in Eq. 5.22). In a further effort to model the overall rebound process for actual shotcrete (Chapter 6), results for the dynamic contact stress (p_d) obtained experimentally, using the technique outlined in Fig. 5.6, were used to predict the probability that the impactor should reach a specified depth of penetration (step 7 in Fig. 6.3). Experimental results from this analysis are presented in Fig. 5.8 along with the predicted values for 14 and 25.4 mm diameter impactors. The agreement between experiment and model once again corroborates the notions that, during the penetration process, the contact stress remains constant at a value p_d and also that a quasi static approach is a valid approximation in dealing with the penetration phase of the rebound process.
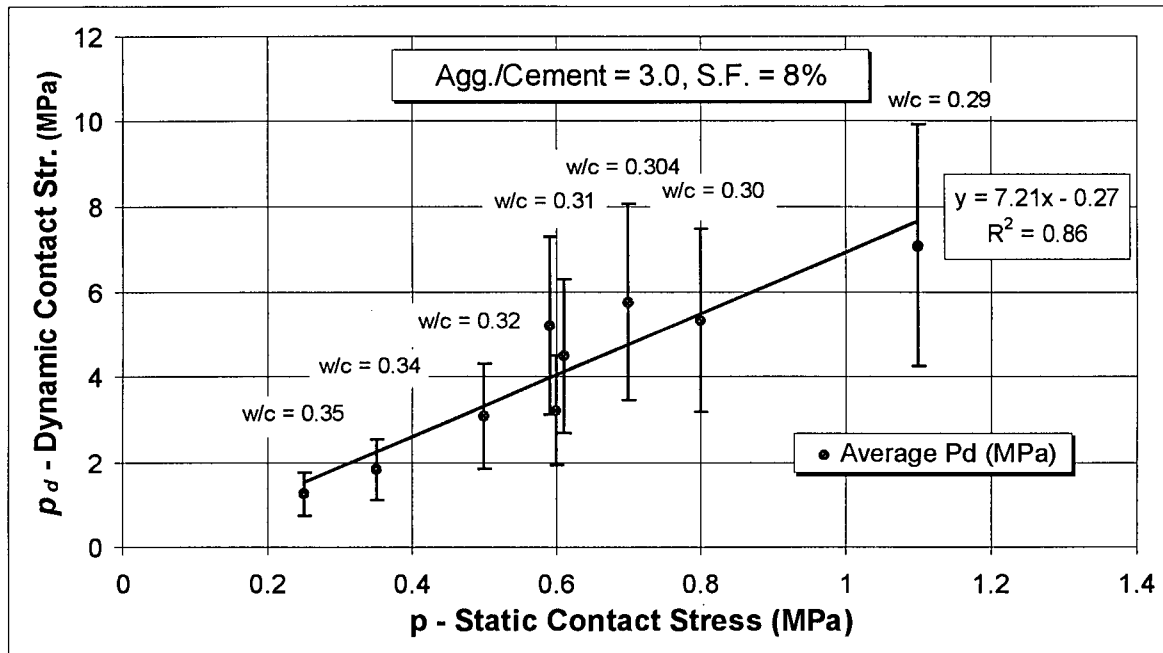
Figure 5.7 - Correlation between the static and dynamic contact stresses for mixes of equal dry-materials composition but different water to cement ratio.
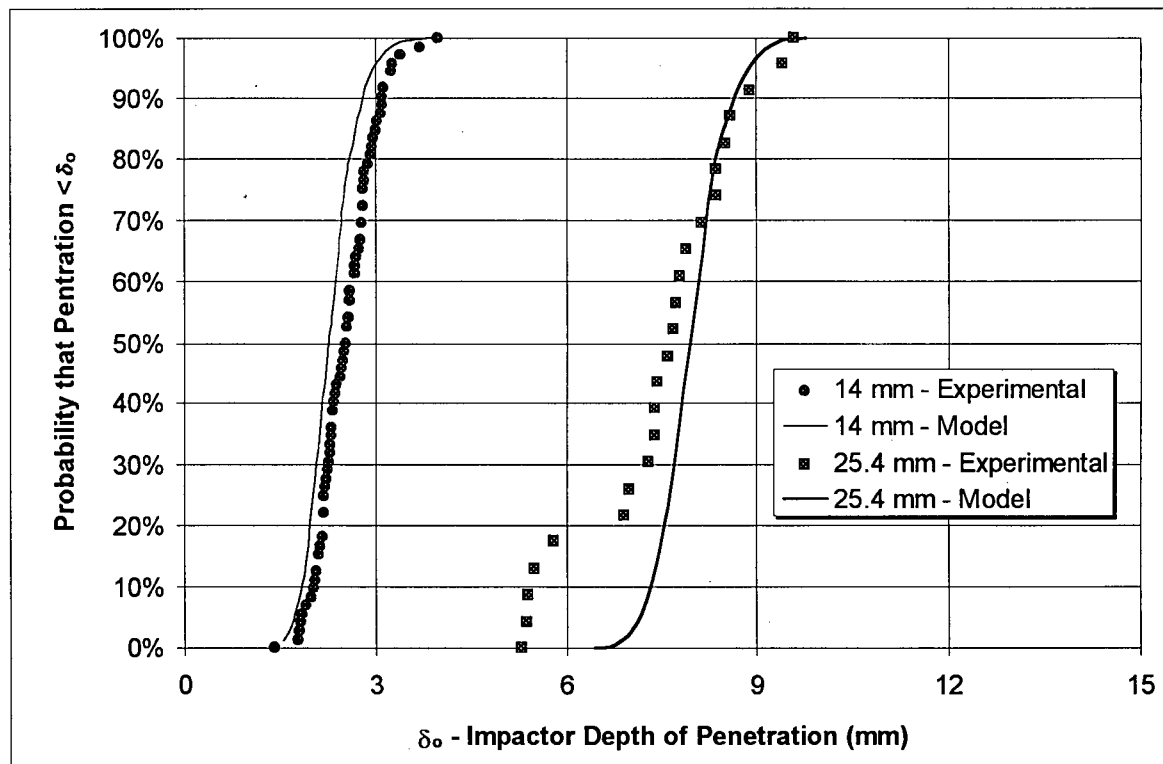
Figure 5.8 - Comparison between the experimental and predicted probability of depth of penetration for 14 and 25.4 mm diameter impactors.

5.4.2 - The Reaction Phase

One of the main results from the formulation presented here is that the coefficient of restitution $(e = V'/V)$ is not a material property, but depends also on the velocity of impact (V), with greater velocities leading to a lower coefficient of restitution (Eq. 5.27). In order to confirm this hypothesis, a test series was carried out in which, for a constant fresh concrete substrate (i.e. constant p and p_d) the same impactor (constant mass and radius) was shot at various velocities, with the rebound velocity measured with the aid of the high-speed camera.

The results are presented in Fig. 5.9 in terms of the coefficient of restitution $(e = V'/V)$ as a function of the impact velocity (V). It can be seen that, in accordance with Eq. 5.27, the trend line for the coefficient of restitution shows lower values for higher impact velocities, with a slope close to the predicted dependence of e on $V^{-1/4}$. The fact that the slower particles tend to have a greater coefficient of restitution is one of the reasons why, in actual shotcrete, the smaller aggregate particles, traveling at greater velocities (Chapter 4), tend to rebound less than the coarse aggregate phases (as demonstrated in Chapter 6).
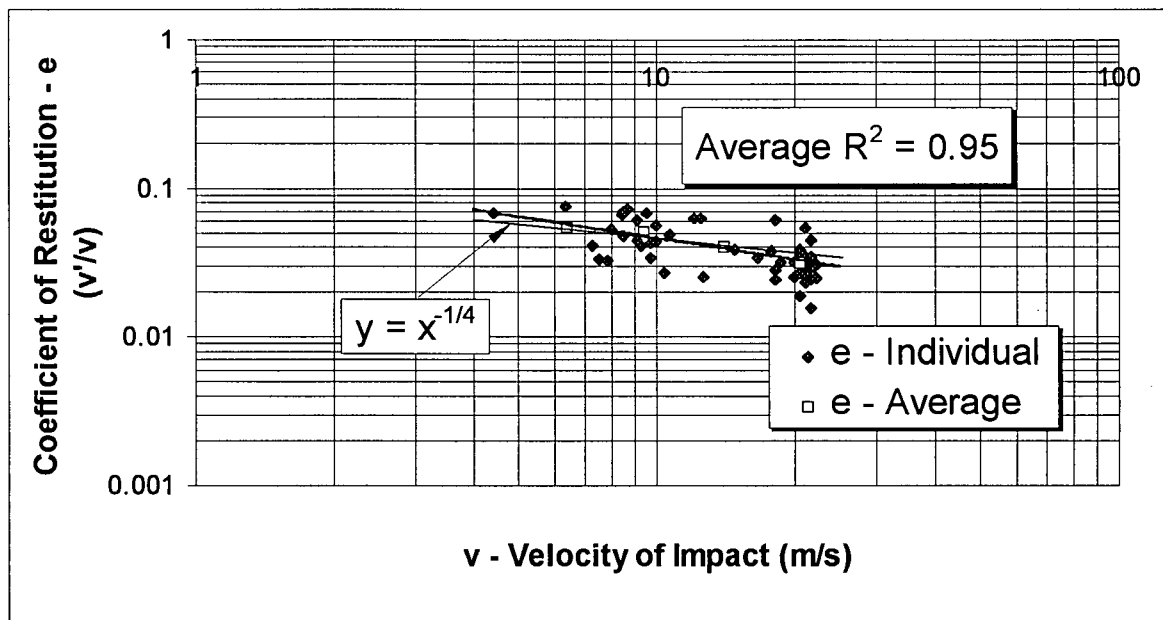
Figure 5.9 - Variation in the coefficient of restitution with the impact velocity for a constant impactor and substrate.

5.4.3 - The Influence of the Mix Design

In order to investigate the influence of the cement content on the dynamic contact stress, two series of mixes (with and without silica fume) of equal static contact stress (p) were tested at five different aggregate to cement ratios. Since, from Eq. 5.11, the static contact stress is a measure of the yield strength $(p = 3Y)$ of the fresh concrete (Y), the equal static contact stress criterion adopted in this test is equivalent to a condition of equal workability that would be used for shotcrete in practice.

Results for the variation in the dynamic contact stress (p_d) as a function of the aggregate to cement ratio are shown in Fig. 5.10a for two different cements. In both cases, it can be seen that, although all mixes have an equal static contact stress (p) variation in the cement content causes the dynamic contact stress (p_d) to change drastically from 3 to 7 MPa for cement B and from 10 to 21 for cement A.

Since, for the equal workability criterion adopted, the water to cement ratio is actually found to increase with the aggregate to cement ratio (Fig. 5.10a), the viscosity of the paste itself cannot be considered the cause of this marked increase in p_d. However, an explanation for this phenomenon can be given as follows: for a given deformation in the fresh concrete $(\Delta D = D_o)$, occurring in a given time frame $(\Delta t = t_o)$, mixes that contain less paste (i.e. a high aggregate to cement ratio) will undergo a greater *strain* imposed in the paste phase, and thus, for a given time frame, a greater *strain-rate*, resulting in more viscous resistance (Fig. 5.11). This is due to the fact that it is the paste that accommodates the permanent *deformation* imposed by the impactor (aggregates can be assumed rigid).
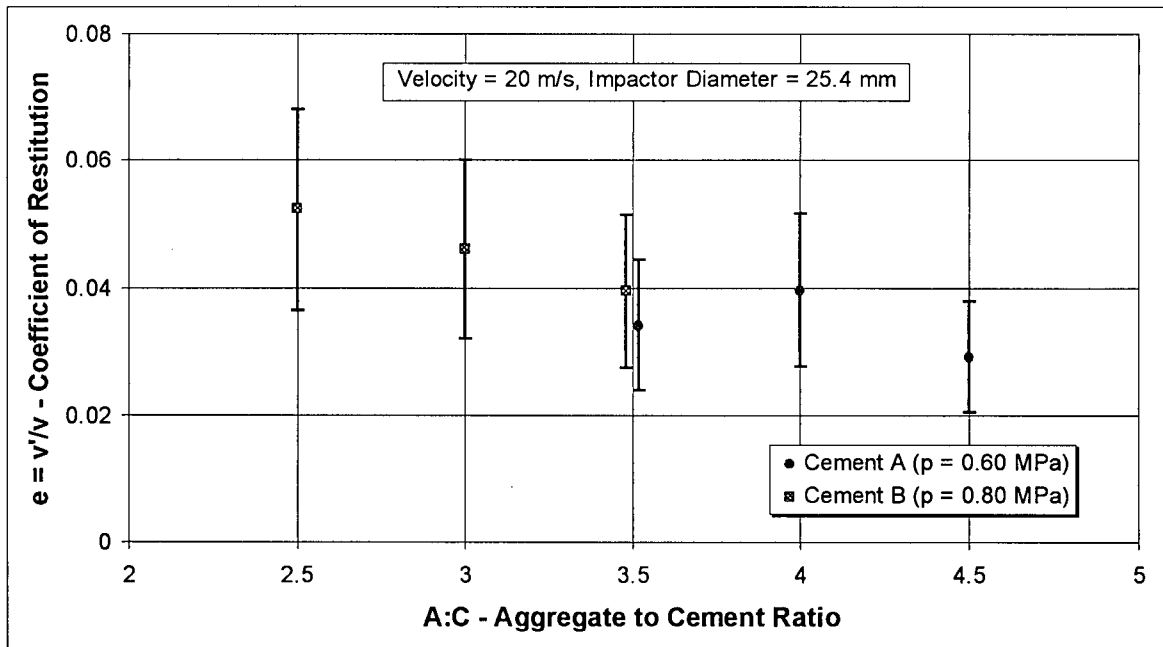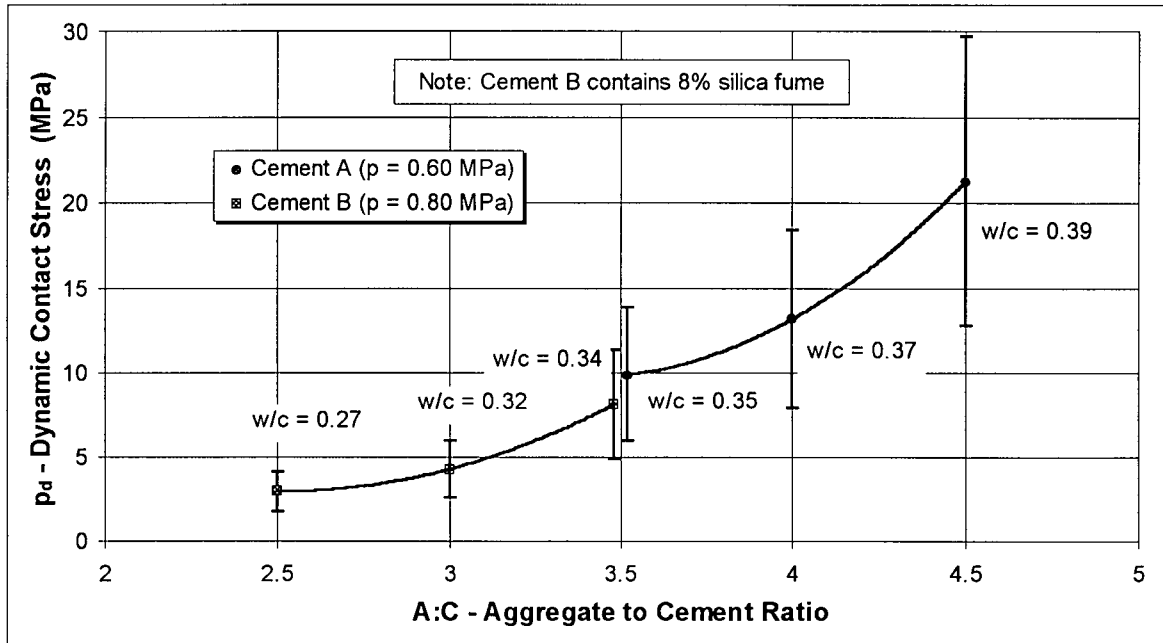
Figures 5.10a and b - Variation in the dynamic contact stress (p_d) and coefficient of restitution (e) with the aggregate to cement ratio (A:C) for a constant workability (p).
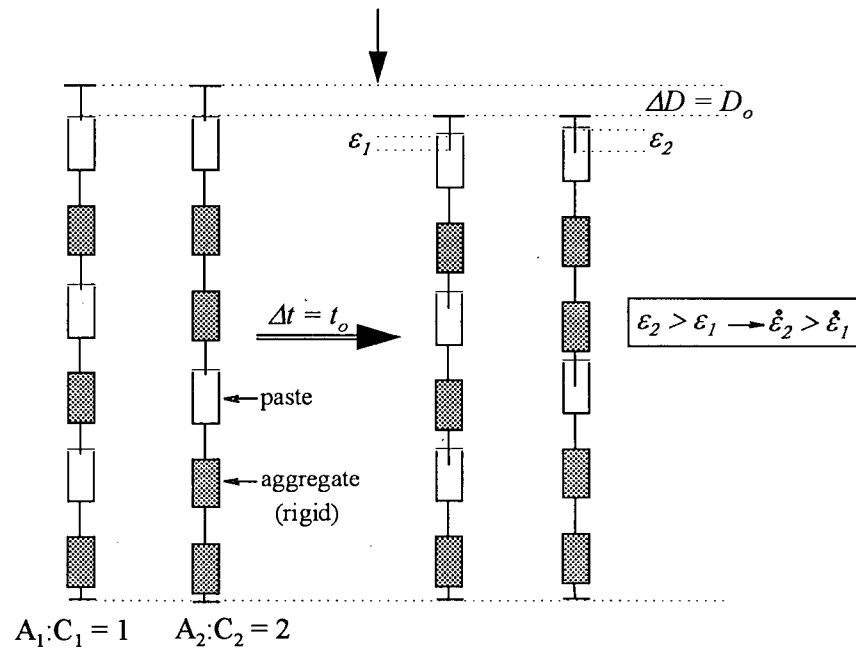
Figure 5.11 - Schematic representation used to show how a lower cement content leads to a higher strain rate in the paste for a given displacement (ΔD) and time frame (Δt).

Similar equi-workability tests performed on mixes of identical mix proportions, but with a varying silica fume content, show that 8% of silica fume in substitution to cement causes the dynamic contact stress (p_d) to be reduced by half (Fig. 5.12a and b). This result was systematically observed throughout these tests. Considering the identical water to cement ratios and the rationale presented in Fig. 5.11, an explanation for this phenomenon must be given on the basis that silica fume acts by lowering the viscosity of the paste phase so that, for a given strain rate, the viscous resistance is reduced and a greater depth of penetration is necessary to consume the kinetic energy of the impactor. Reports of silica fume reducing the viscosity of fresh concrete have previously been made by Tattersal (1991).
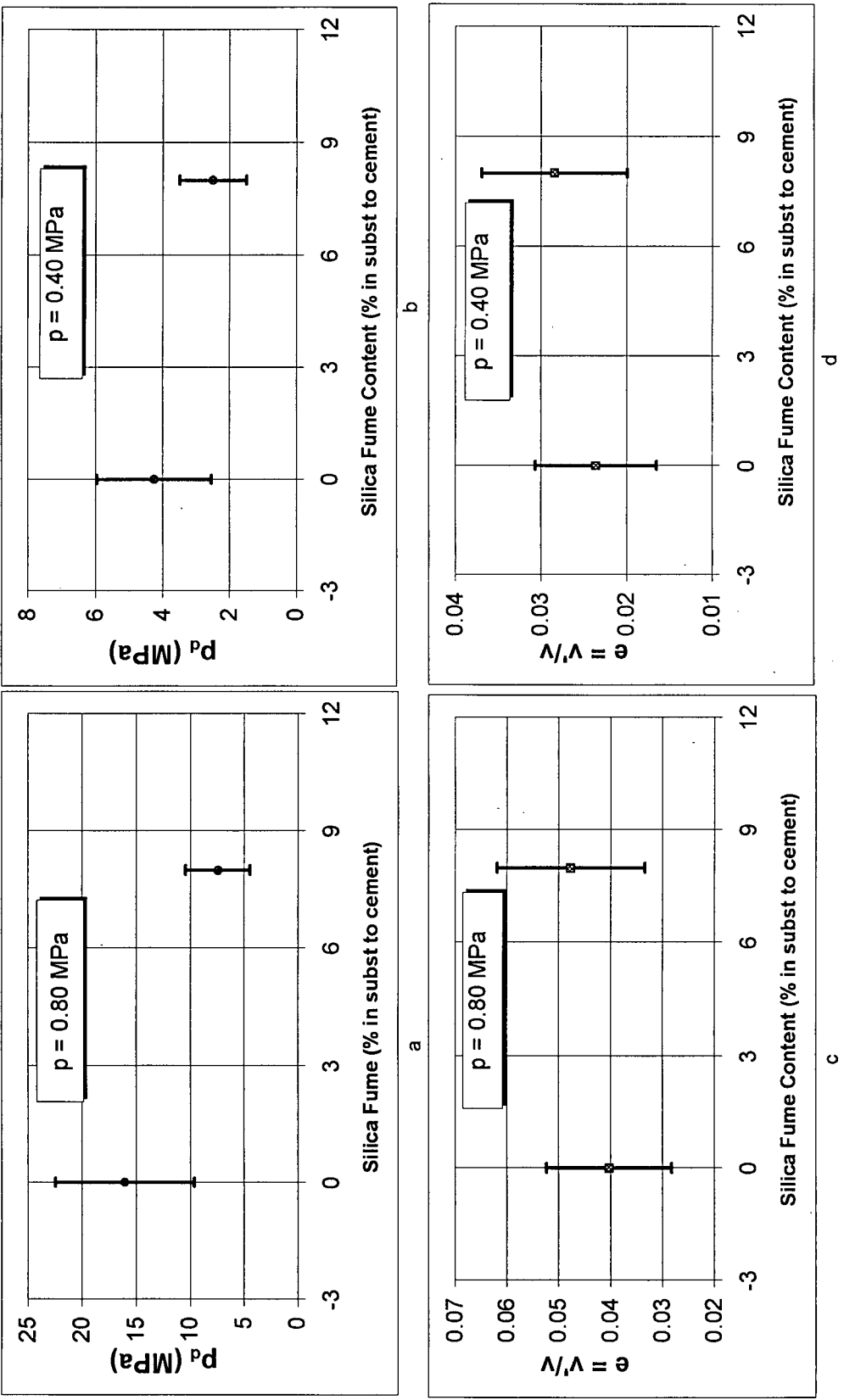
Figure 5.12 - Variation in the dynamic contact stress (p_d) and coefficient of restitution (e) with the silica fume content for a constant workability (p).

For both the aggregate content and silica fume test series, the rebound velocity (V') was also measured. The results, expressed in terms of the coefficient of restitution, are presented in Figs. 5.10b, 5.12c and d. In the case of the aggregate content series, it can be seen that there is a tendency for a greater coefficient of restitution for higher cement contents (Fig. 5.10b). The same trend is found for the silica fume series, in which mixes containing 8% silica fume presented higher average coefficients of restitution when compared to their plain counterparts (Figs. 12c and d).

Given that a high cement content and silica fume are known to effectively reduce shotcrete rebound (Chapter 3), these results may be considered somewhat contrary to intuition[6]. However, they are consistent with the theory described in that, for mixes of equal static contact stress (p) and a constant impactor and velocity of impact (V), Eq. 5.27 predicts that the coefficient of restitution (e) should grow for lower values of dynamic contact stress (p_d). In a physical interpretation of this result, it must be considered that lower values of p_d cause a greater volume penetrated for a given impact velocity and, therefore, a greater contact radius $(a^*$ in Eq. 5.22) that allows the substrate to accumulate more elastic strain energy $(W_2$ in Eq. 5.21) by the end of the penetration phase.

5.4.4 - A General Theory of Rebound for Shotcrete

Up to this point, the experimental results presented here indicate that the theory of impact and rebound, as originally developed by Tabor (1948) in order to study the dynamic yield stress of metals, can be extended to the case of an aggregate particle rebounding from a fresh concrete surface for the limited cases of varying only one parameter at a time (i.e. p_d, p or V). However, ideally, one would like to obtain a formulation that is as generalized as possible, and able to account for any combination of velocity of impact and substrate composition.

---

[6] This apparent contradiction is resolved in items 6.6.2 and 6.6.4.

In order to do so, it must be considered that, in dealing with a relatively stiff impactor (elastic modulus E_i) and a fresh concrete (or shotcrete) substrate, the composite elastic modulus (E^*) is dominated by the elastic modulus of fresh concrete (E_c). From Eq. 5.15:

$$\frac{1}{E^*} = \frac{1-v_c^2}{E_c} + \frac{1-v_i^2}{E_i} \ , \quad \text{for} \ \ E_i \gg E_c, \quad E^* = \frac{E_c}{1-v_c^2} \tag{5.33}$$

Therefore, Eq. 5.27 can be rewritten as:

$$e = \sqrt{\frac{3\pi^2}{10}\left(\frac{4r_1}{\pi}\right)^{\frac{3}{4}}\left(\frac{1-v_c^2}{E_c}\right)\left(\frac{1}{2}m\right)^{-\frac{1}{4}} \cdot p \cdot (p_d)^{\frac{-3}{8}} \cdot V^{\frac{-1}{4}}} \tag{5.34}$$

And from the definition of the elastic modulus of an elasto plastic material, with yield strength Y, obeying Tresca's maximum shear yield criterion and elastic strain limit ε_{pc}:

$$E_c = Y/\varepsilon_{pc} \tag{5.35}$$

For $v = \frac{1}{2}$, and using $p = 3Y$ from Eq. 5.11, Eq. 5.27 can be rewritten as:

$$e = \sqrt{\frac{3\pi^2}{10}\left(\frac{4r_1}{\pi}\right)^{\frac{3}{4}}\left(2.25\varepsilon_{cp}\right)\left(\frac{1}{2}m\right)^{-\frac{1}{4}} \cdot (p)^{\frac{1}{2}} \cdot (p_d)^{\frac{-3}{8}} \cdot V^{\frac{-1}{4}}} \tag{5.36}$$

Another advantage of expressing the coefficient of restitution (e) in terms of ε_{pc} as opposed to E_c is that, while the elastic modulus of the fresh concrete is expected to vary considerably, especially for mixes of differing consistencies, the elastic strain limit of cohesive materials is thought to be a rather stable property. Thus, assuming that ε_{pc} is a constant value and grouping all constants from Eq. 5.36 into a single constant (K), a general expression for the coefficient of restitution can be written:

$$e = K \ \psi \tag{5.37}$$

where: $K = \sqrt{\dfrac{3\pi^2}{10}\left(\dfrac{4r_1}{\pi}\right)^{\frac{3}{4}}\left(2.25\varepsilon_{pc}\right)\left(\dfrac{1}{2}m\right)^{-\frac{1}{4}}}$ · and $\psi = p^{\frac{1}{2}} \cdot p_d^{\frac{-3}{8}} \cdot V^{\frac{-1}{4}}$

According to this expression, for cases of rebound from fresh concrete, the coefficient of restitution is solely determined by the impact factor (ψ) which, at the same time, accounts for the material properties of the substrate (p and p_d) and the severity of the impact (V).

In order to investigate the validity and generality of Eq. 5.37, fourteen mixes of widely different aggregate to cement ratios (A:C from 2.5 to 4.5) using two different types of cement and silica fume additions of zero and 8% were tested at various impact velocities. The high-speed camera was used to determine the velocities of impact and rebound. The results are shown in Fig. 5.13 in terms of the coefficient of restitution as a function of the impact factor (ψ) that was calculated using Eq. 5.37 with p, p_d and V values obtained experimentally for each individual event.

It should be noticed from Fig. 5.13 that the best-fit trend line corresponds exactly to the dependence of e on ψ^1 that Eq. 5.37 predicts, thus confirming that the impact factor (ψ), as developed here, is a general parameter capable of describing the rebound event.

Additionally, by taking the value of the slope of the best fit line in Fig. 5.13 (*slope = 0.19*) and equating it to K in Eq. 5.37, the value of the elastic strain limit (ε_{pc}) can be determined to be between 2 to 4 x 10^{-3} mm/mm. In order to verify the validity of this number, one can use Eq. 5.11, where the parameter $\dfrac{aE}{3RY}$ determines the depth of penetration at which the static contact stress reaches its plateau yield value, which is thought to occur for $\dfrac{aE}{3RY} > 30$ (Johnson, 1985). Therefore, by using Eq. 5.35 and the approximation $a^2(\delta) \approx 2r\delta$, one can find the expected yielding depth of penetration for a 25.4 mm diameter spherical indenter to be:

$$\frac{aE}{3RY} = \frac{a}{3R\varepsilon_{pc}} > 30 \rightarrow \delta_{yield} > 10^{-1} mm$$

Coefficient of Restitution, e = v'/v

y = x^1

R^2 for average = 0.60

Best Fit: y = 0.19x

- ◆ A:C=3.0, w/c=0.34, S.F=8%
- ▲ A:C=3.0, w/c=0.30, S.F=8%
- ▣ A:C=3.0, w/c=0.32, S.F=8%
- ✸ A:C=3.0, w/c=0.30, S.F=0%
- ◇ A:C=3.0, w/c=0.30, S.F=8%
- ○ A:C=3.0, w/c=0.30, S.F=8%
- ◌ A:C=3.0, w/c=0.30, S.F=0%
- ▨ A:C=3.0, w/c=0.34, S.F=0%
- ○ A:C=2.5, w/c=0.31, S.F=0%
- ○ A:C=3.0, w/c=0.35, S.F=0%
- ▵ A:C=3.5, w/c=0.35, S.F=0%
- ▢ A:C=4.0, w/c=0.37, S.F=0%
- ◇ A:C=4.5, w/c=0.39, S.F=0%
- ✸ A:C=3.0, w/c=0.35, S.F=8%
- ■ Average e

Impact Factor, ψ = $(\rho^{0.5} . p_d^{-3/8} . v^{-1/4})$
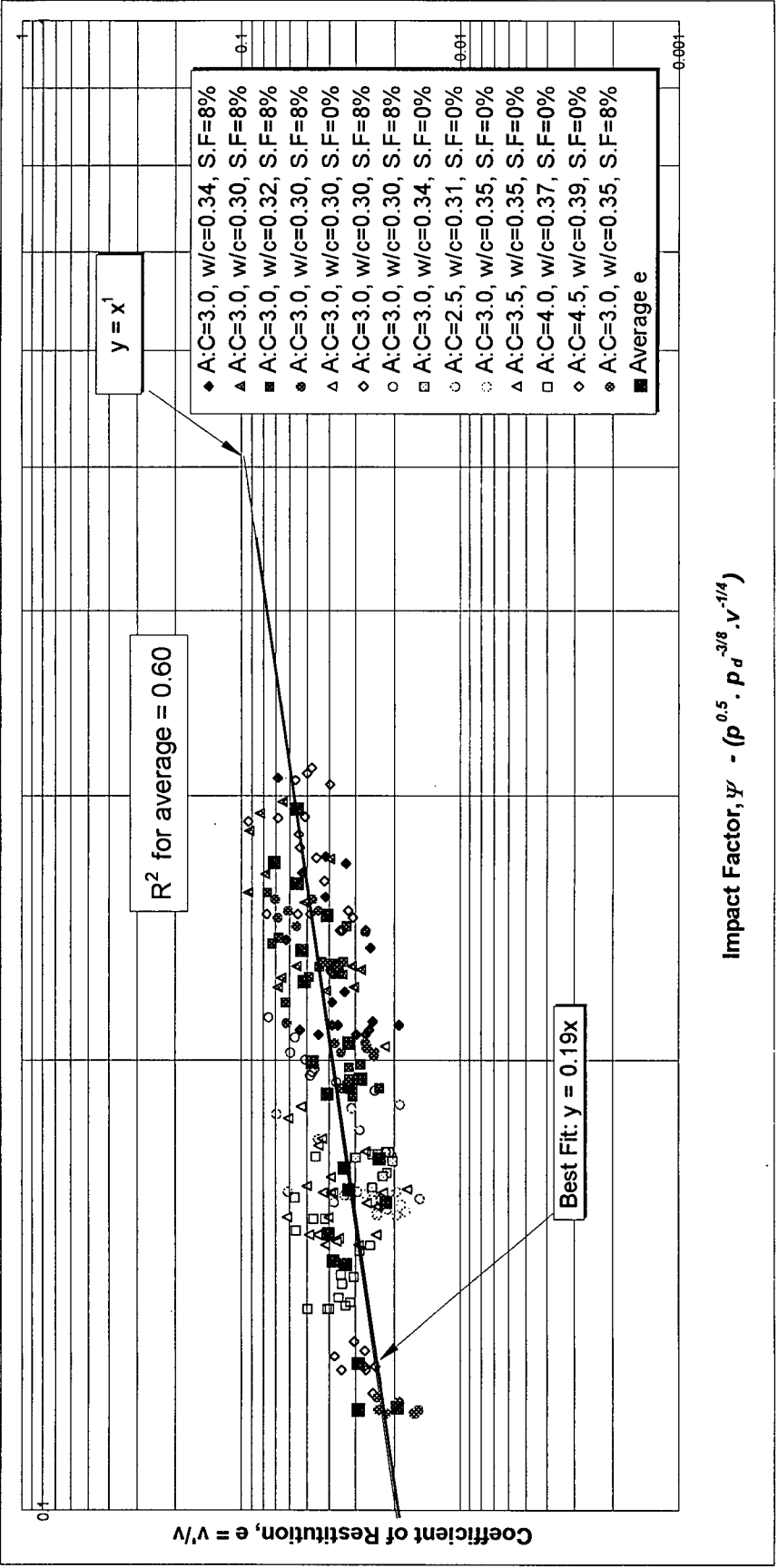
Figure 5.13 - Variation in coefficient of restitution (e) with the impact factor (ψ) for various mix compositions and impact velocities - best fit regression line and theoretical overlap.

It should be noticed that the value found agrees with the experimental indentation tests shown in Fig. 5.5, in which the yielding plateau stress is generally found to be reached within a few tenths of a millimeter of penetration for both fresh concrete and dry-mix shotcrete of various consistencies. This experimentally confirms the value found for ε_{pc} from Eq. 5.37 and the slope of the linear regression in Fig. 5.13.

5.4.5 - Contact Time

It was shown earlier (Eq. 5.32) that, according to the theory described, the contact time between the impactor and the fresh concrete should only be a fraction of a millisecond. Experimentally, although the high speed camera used is not capable of shutter rates greater than 1000 frames per second, it was generally found that the full penetration event, i.e. from the time the impactor first touches the substrate until it reaches its stationary position (at full depth of penetration), generally took less than 1 millisecond as predicted by the theory. This is shown in Fig. 5.14, in which two successive pictures (i.e. 1 millisecond apart) of a 25.4 mm diameter projectile are presented at first contact and at full penetration (Figs 5.14b and c).

Once again, this agreement between the predicted and measured results is a good indication of the adequacy in the theoretical approach proposed. Additionally, as mentioned earlier, the short time of contact developed between the impactor and the substrate makes it unlikely that the rebound process should be governed by entrapment of particles by the incoming material since, in a fraction of a millisecond, the incoming shotcrete spray only advances a few millimeters. Therefore, an embedment process, in which the energy of rebound is compensated by the adhesion that develops between the particle and the substrate, must be regarded as the main mechanism involved. This was visually observed in the high speed films of shotcrete in item 4.3.3 and is further demonstrated in Chapter 6.
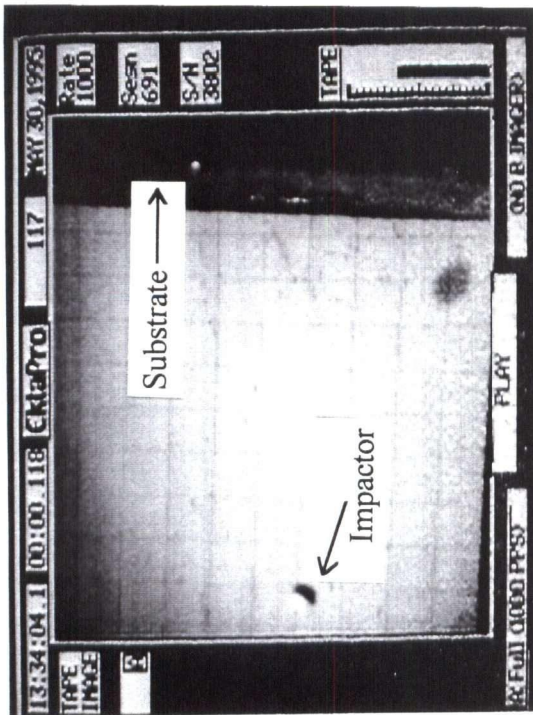
(a) - time = 117 millisec
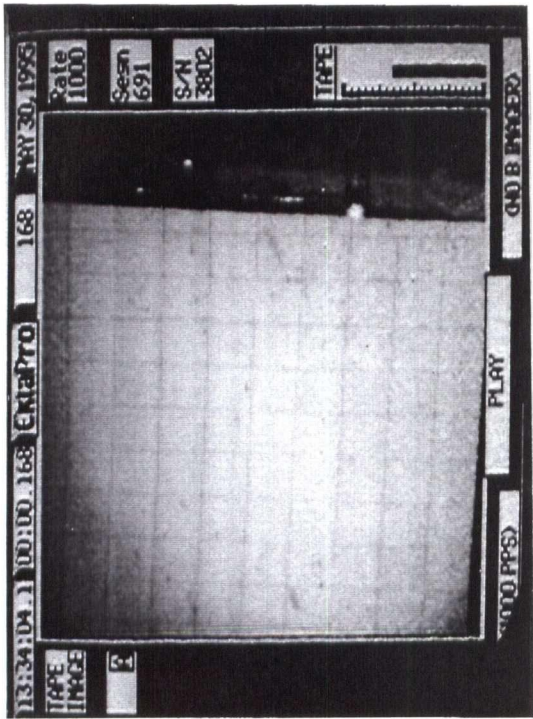
(b) - time = 168 millisec
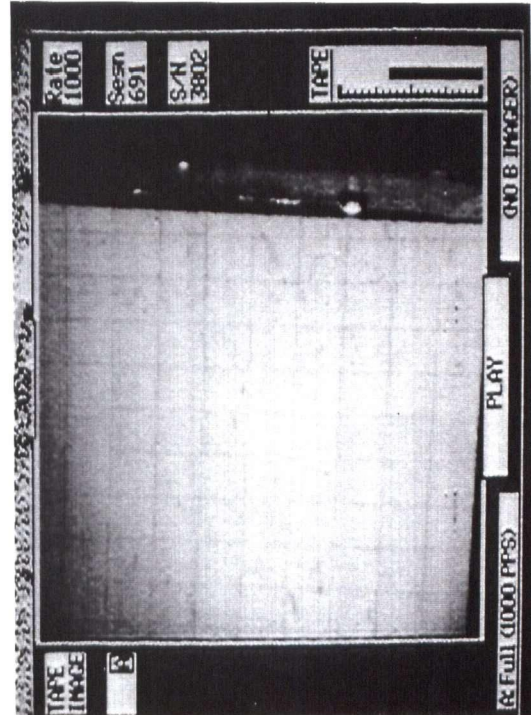
(c) - time = 169 millisec
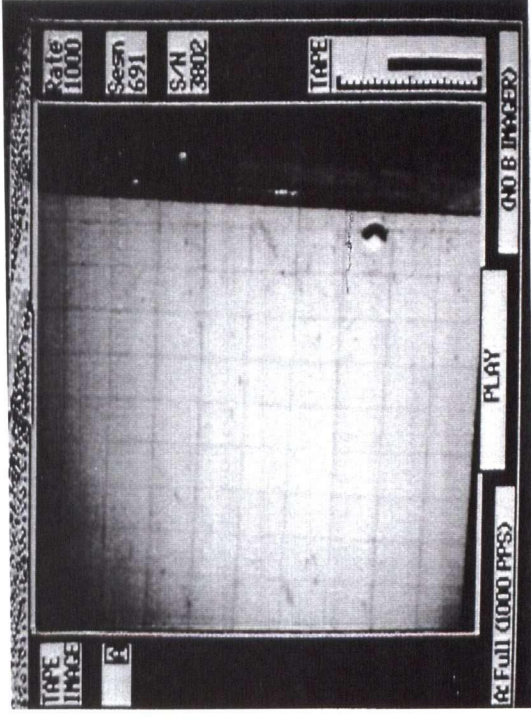
(d) - time = 291 millisec

Figure 5.14 - High speed camera pictures showing a 25.4 mm diameter impactor (a) cruising towards the fresh concrete substrate, (b) at initial contact with the substrate, (c) at full penetration and (d) at rebound.

5.5 - Conclusions

In this chapter, the theory of dynamic hardness, as originally developed to deal with the case of a metal projectile striking a metal substrate, was reviewed and the modifications necessary to tackle the problem of a rigid projectile striking a fresh concrete substrate were presented. This formulation is the theoretical basis that will allow the development of a comprehensive theory of rebound, able to predict the amount and composition of the aggregate rebound for actual dry-mix shotcrete in Chapter 6. More specific conclusions to be extracted from this chapter are:

1) With respect to rheology, during the rebound process, fresh concrete and dry-mix shotcrete were found to behave as elastic-perfectly plastic materials obeying the Tresca yield criterion.

2) During the penetration phase, an aggregate particle faces a constant dynamic contact stress (p_d) that is approximately one order of magnitude greater than its static equivalent (p).

3) For a fixed workability and impactor speed, both the cement content and the presence of silica fume were found to significantly reduce the dynamic contact stress (p_d) with direct implications on the coefficient of restitution (e).

4) The coefficient of restitution (e) is not solely a material property of the substrate, but also depends on the velocity of impact (V) with lower velocity events leading to a higher coefficient of restitution.

5) The coefficient of restitution, as controlling the possibility of rebound is described by the impact factor ($\psi = p^{\frac{1}{2}} \cdot p_d^{\frac{-3}{8}} \cdot V^{\frac{-1}{4}}$).

Chapter 6 - Modeling of Aggregate Rebound in Dry-mix Shotcrete

6.1 - Introduction and Objectives

The experimental work described in Chapter 4 using high-speed filming allowed the characterization of aggregate velocities in the shotcrete stream and Chapter 5 presented a theoretical formulation that allows dealing with the mechanics of an aggregate impacting a fresh concrete substrate. The next step, as presented in this chapter, is to link the aggregate velocities to the mechanical model of impact in order to develop a general theory of aggregate rebound for dry-mix shotcrete and, therefore, analyze the dependence of aggregate rebound on particle size, cement content, silica fume, air flow, aggregate gradation and shooting consistency.

6.2 - The Mechanical Model

In the formulation presented in the previous chapter, the rebound event was divided into two phases: penetration and reaction. In the first phase, the process was considered similar to an indentation and therefore the kinetic energy of the impacting particle (W_1) was shown to be related to the volume penetrated (V_a) by the dynamic contact stress (p_d). From Eq. 5.14b:

$$V_a = \frac{W_1}{p_d}$$

(6.1)

It was shown that, during the reaction phase, once all the kinetic energy of the particle (W_1) has been consumed by the contact stress (p_d) and the full depth of penetration and contact radius (δ^* and a^*) have been reached, the elastic strain energy stored throughout is transferred back to the particle. This causes the aggregate to spring out of the fresh concrete bedding with a kinetic energy of rebound of magnitude W_2 given by Eq. 5.21:

$$W_2 = \frac{0.27 \cdot \pi^2 \cdot p^2 \cdot a^{*3}}{E^*}$$

(6.2)

It was also shown in Chapter 5 that, in order to render the model applicable to any substrate composition, it is necessary to approximate the composite elastic modulus to the elastic modulus of concrete ($E^* \cong E_c$ - Eq. 5.33). By using this approximation and $p = 3Y$ (Eq. 5.11), Eq. 6.2 can be written as:

$$W_2 = \frac{0.27 \cdot \pi^2 \cdot p \cdot a *^3 \cdot 3Y}{E_c} \quad , \quad \text{or for} \quad \varepsilon_{pc} = \frac{Y}{E_c} \quad , \quad W_2 = 0.27 \cdot \pi^2 \cdot p \cdot a *^3 \cdot 3\varepsilon_{pc} \tag{6.3}$$

6.3 - Rebound Criterion

In order to calculate the energy of rebound in the reaction phase, the model developed in Chapter 5 assumes conditions of zero adhesion between the impactor and the substrate. However, both experimentally and analytically (Fig. 5.13) one observes that the coefficient of restitution ($e = V'/V$) is approximately 4%, resulting in rebound velocities (V') of the order of 1 m/s. Therefore, from a physical point of view, unless some degree of adhesion is assumed to develop between the aggregate and the fresh concrete substrate, all particles would rebound. Since this is not the case, one has to conclude that a failure criterion, based on the existence of an adhesion mechanism of particle embedment, governs the process.

It should be mentioned that, although an entrapment mechanism, in which the rebounding particle would be covered by the incoming spray of material is possible, this was not observed in high speed camera footage of actual shotcrete (item 4.3.3). Additionally, it has been analytically demonstrated and high speed camera footage confirms (item 5.4.5), that the time of contact between the impacting particle and the fresh concrete substrate does not exceed a millisecond. Within this time frame, the incoming material advances only a few millimeters, rendering the entrapment mode an unlikely mechanism. Other indications supporting particle embedment as the prevailing mode are:

- It has been experimentally shown in 3.3.2.2 and by Parker (1976) that rebound varies with the thickness of application, with almost all the aggregates rebounding until the first millimeters of shotcrete deposit on the shooting aim. If entrapment were the prevailing mode, there is no reason why the rebound should depend on the built-up thickness.

- It has been demonstrated that coarse aggregates travel at a lower speed than fines (Fig. 4.4). Therefore, if entrapment were to be the prevailing mode, it would be reasonable to assume that larger (slower) aggregates are more likely to be entrapped than fines. On the contrary, however, rebound is four times greater for coarse aggregates.

Therefore, assuming that the embedment mode is the prevailing mechanism that determines aggregate rebound, the penetrometer described in 3.3.1.1 was used in order to investigate the nature and magnitude of the adhesive forces that develop between the impacting particle and the fresh concrete substrate by the end of the reaction phase. This was done by processing the load and displacement data during a penetration and pull-out cycle using the spherical indenter head, thus allowing calculation of the penetration and pull-out stresses (i.e. the load divided by the projected contact area) as a function of the depth penetrated (δ).

Results from such an analysis, carried out five consecutive times on a dry-mix shotcrete test panel of average consistency, shows (Fig. 6.1) that, as demonstrated in Chapter 5, the contact stress rises to a constant value very early in the penetration process and remains virtually constant throughout. The pull-out process, on the other hand, is characterized by non-linearity in the beginning, followed by a constant pull-out strength value at which the great majority of the debonding process takes place. The final pull-out displacements are of the same order of magnitude as the maximum depth of penetration.

A simplified approach may be taken to describe the work necessary to debond an aggregate (W_D). From Fig. 6.1, with an adhesive strength σ_o (an assumed material property), once the particle has reached its full depth of penetration (δ^*), and the final contact radius (a^*) has been established, the energy necessary to cause debonding (i.e., the area contained by the pull-out curves) can be calculated as:

$$W_D = \delta^* \cdot \left[\sigma_o \cdot \left(\pi a *^2 \right) \right]$$

(6.4)
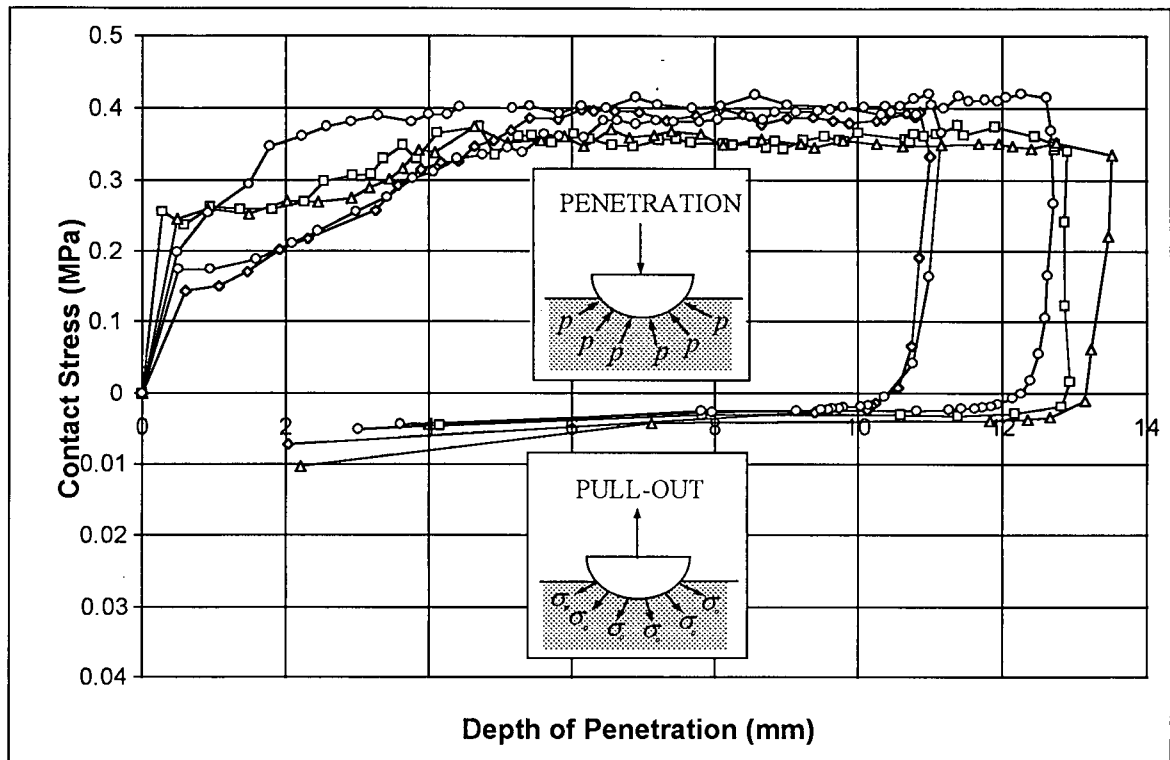
Figure 6.1 - Variation in the contact stress during penetration and pull-out of a 25.4 mm hemisphere into fresh dry-mix shotcrete. Values above the x-axis indicate penetration, while those below indicate pull-out.

Therefore, the rebound criterion can be expressed in terms of the energy required to debond the particle (W_D) and the available elastic rebound energy imparted by the fresh concrete substrate (W_2 - Eq. 6.2). The condition of rebound becomes:

$$\frac{W_2}{W_D} \geq 1 \ \Rightarrow \ Rebound \tag{6.5}$$

In order to evaluate the magnitude of the adhesive strength (σ_o), pull-out tests identical to those described earlier have been carried out on shotcrete panels ranging from a wet to a dry consistency ($p = 0.25$ to 2.0 MPa; overhead build up of, respectively, 50 and 200 mm). The results (Fig. 6.2) indicate that the adhesive strength (σ_o) grows from approximately 0.002 to 0.02 MPa depending on the shotcrete consistency, with an usual consistency ($p = 0.5$ MPa) showing an adhesive strength of approximately 0.0055 MPa.
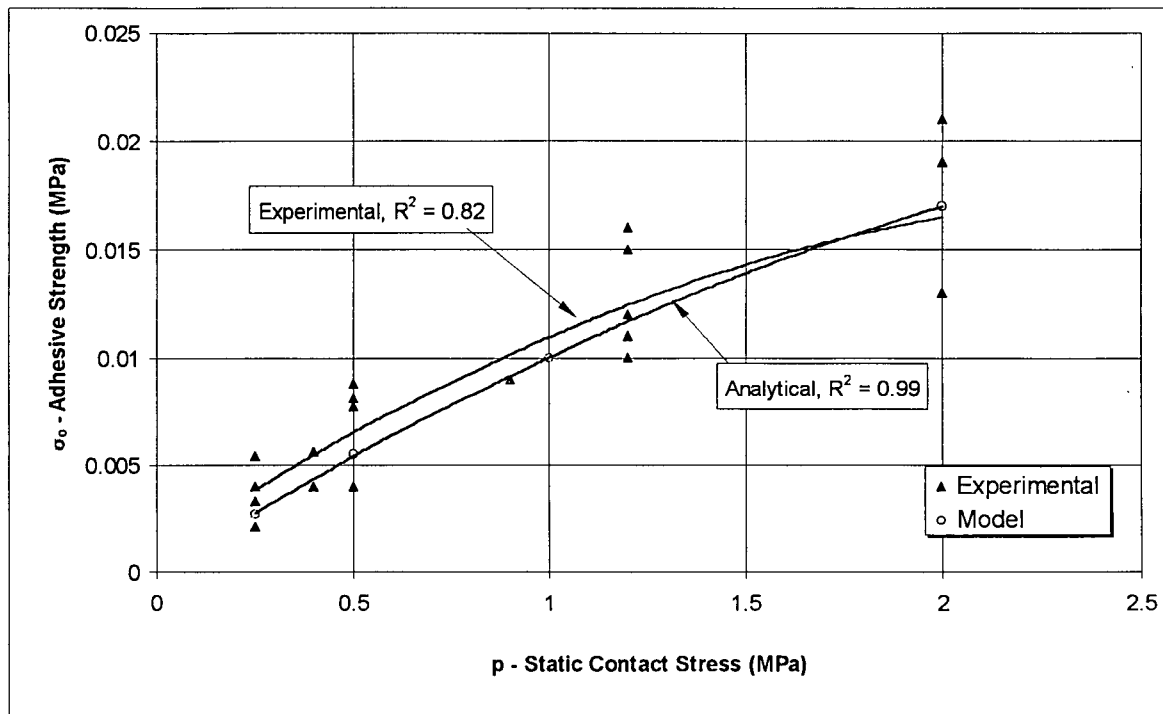
Figure 6.2 - Variation in the adhesive strength (σ_o) with the shotcrete consistency: Comparison between experimental results and those assumed in the model.

6.4 - Implementation of the Model

In seeking the best approach to model aggregate rebound in shotcrete, initially it must be recognized that rebound is not a deterministic process in the sense that it is not whether or not a particle will rebound that one wishes to determine, but rather, for a given particle size, it is the *percentage* of particles that will rebound that is sought. The problem is therefore *stochastic* in nature.

In order to deal with stochastic models, basically two distinct approaches are available: Monte-Carlo Simulations and Reliability Analysis. Although both are considered to yield equivalent results, they constitute very distinct schools of thought, with each having its own merits and drawbacks. In this case, the second option (Reliability Analysis) was chosen and used with a program developed at UBC (named RELAN - Foschi et. al., 1993). The program is based on an iterative routine that, for a given pre-determined physical model and stochastic variables, finds the probability with which the condition of failure should be reached.

For the determination of the probability of rebound, the condition of failure was set as described earlier (i.e. $W_2/W_D > 1 \Rightarrow$ *Rebound*). In order to calculate the energy necessary to debond a particle (W_D), Eq. 6.4 was used. The rebound energy (W_2) was calculated using Eq. 6.3, with the elastic strain limit of concrete (ε_{pc}) set at 2 millistrains, as determined both analytically and experimentally in 5.4.4. The volume penetrated (V_a) was determined using Eq. 6.1, with the impact energy (W_1) calculated as the kinetic energy of the impacting particle. The particle velocity was taken to be a function of the aggregate diameter (ϕ) and air flow, according to the relationships established in Chapter 4 using high-speed filming (shown in Fig. 4.3a). With a known volume penetrated (V_a) and the particle size (r), both the maximum depth of penetration (δ^*) and the maximum contact radius (a^*) were calculated. A schematic representation of the various steps taken by the computer code is shown in Fig. 6.3.

The particle velocity was taken to be a stochastic variable, with average value as determined by the relationships found in Chapter 4, and a 20% coefficient of variation (as determined experimentally - Table 4.3). The fresh shotcrete material properties related to the penetration and reaction phases (p, p_d and ε_{pc}) were also taken to be stochastic variables, but with a 40% coefficient of variation. This considerably greater scatter was commonly seen in experimental evaluations of the static and dynamic contact stresses (p and p_d - Chapter 5) and is considered to be caused by the non-homogeneous nature of fresh concrete, which tends to be very irregular, depending on whether or not large aggregate particles are present in the vicinity of the penetration region[1].

The average values for the static and dynamic contact stresses (p and p_d) were taken to be a function of the mix composition (i.e., water content, presence of silica fume, cement content, etc.) as experimentally determined in Chapter 5. The average value of the adhesive strength (σ_o) was assumed to be dependent on the shotcrete consistency, according to the experimental relationship found using pull-out tests (Fig. 6.2). Actual figures used for the average values of these properties are shown in Table 6.1. For the sake of simplicity, all stochastic variables were assumed to be normally distributed.

---

[1] Although the formulation presented in Chapter 5 assumes the shotcrete substrate to be a homogeneous medium, by allowing its rheological properties to be stochastic variables, this assumption no longer has to be made and therefore the heterogeneous nature of the substrate is captured by the model.

INPUT

1) Input material properties of shotcrete: p, p_d, σ_o

2) Input shooting conditions: air flow, hose diameter and position of shooting.

DEFINITION OF IMPACT CONDITIONS

3) From step 2, obtain the velocity function : $V = A.\phi^{-B}$

4) For a given aggregate diameter (ϕ), obtain V using step 3

PENETRATION PHASE

5) Calculate the kinetic energy of impact: $W_1 = \dfrac{1}{2} m \cdot V^2$

6) Calculate the volume penetrated: $V_a = \dfrac{W_1}{P_d}$

7) Using V_a and ϕ, iterate on δ to find the final depth of penetration (δ^*)

8) Calculate the contact radius: $a^* = \sqrt{\phi \cdot \delta^* - \left(\delta^*\right)^2}$

REACTION PHASE

9) Calculate the kinetic energy of rebound: $W_2 = 0.27 \cdot \pi^2 \cdot p \cdot a^{*3} \cdot 3\varepsilon_{pc}$

DEBONDING PHASE

10) Calculate the debonding energy: $W_D = \delta^* \cdot \left[\sigma_o \cdot \left(\pi \cdot a^{*2}\right)\right]$

RELIABILITY ANALYSIS

11) Using The First Order Reliability Method, calculate the rate of rebound: $R = probability\ that\ W_2 > W_D$

Figure 6.3 - Computer algorithm to predict aggregate rebound using the model.

The probability of rebound was determined for each situation of shotcrete composition by changing the average material properties of the shotcrete substrate (p, p_d and σ_o). Different shooting conditions were tested by changing the velocity vs. particle size relationship (for cases of varying the air flow or overhead shooting).

In all cases of shotcrete composition and shooting conditions, the probability of rebound was computed for eight different aggregate diameters, corresponding to the standard sieve sizes of 9.5, 4.8, 2.4, 1.2, 0.6, 0.3, 0.15 and 0.075 mm. Thus, for each situation, eight individual rates of rebound (r_i) were computed, allowing to determine the composition of the expected rebound. In order to calculate the overall rate of rebound (R = *material rebounded/material shot*), the percentage of the design-mix retained in each individual sieve (p_i - taken from the gradation curve for the combined aggregates) was used and, therefore, for a known mass cement and aggregate contents in the mix (C and A, respectively), the overall rate of rebound was computed assuming the rebound of the cement phase as constant at $r_c = 5\%$:

$$R = \left\{ \left[\left(\sum r_i \cdot p_i \right) \right] \cdot A + \left(r_c \cdot C \right) \right\} \tag{6.6}$$

Table 6.1 - Test parameters and input values used in the model.

Parameter Varied	Situations Tested	p (MPa)	p_d (MPa)	σ_o (MPa)	Velocity (m/s) Function*	Consistency**	Shooting Direction
Aggregate Size	9.5 to 0.075 mm	0.5	10	0.0055	$v = 27.493\, \phi^{-0.3073}$	Normal	Wall
Cement Content	350 kg/m³	0.5	13	0.0055	$v = 27.493\, \phi^{-0.3073}$	Normal	Wall
	400 kg/m³		10				
	450 kg/m³		7				
	550 kg/m³		5				
Air Content	100 cfm	0.5	10	0.0055	$v = 14.301\, \phi^{-0.39}$	Normal	Wall
	200 cfm				$v = 26.887\, \phi^{-0.4003}$		
	300 cfm				$v = 27.493\, \phi^{-0.3073}$		
Silica Fume	0%	0.5	10	0.0055	$v = 27.493\, \phi^{-0.3073}$	Normal	Wall
	8%		7				
	16%		5				
Water Content	Wet	0.25	5	0.0027	$v = 27.493\, \phi^{-0.3073}$	Wet	Wall
	Normal	0.5	10	0.0055		Normal	
	Dry	1	15	0.01		Dry	
	Very Dry	2	20	0.017		Very Dry	
Shooting Direction	Wall	0.5	10	0.0055	$v = 27.493\, \phi^{-0.3073}$	Normal	Wall
	Overhead				$v = 21.899\, \phi^{-0.2602}$		Overhead
Gradation	Coarse	0.5	10	0.0055	$v = 27.493\, \phi^{-0.3073}$	Normal	Wall
	Medium Coarse						
	Medium						
	Fine						
	Discontinuous I						
	Discontinuous II						

* From Chapter 4, velocity in *m/s* and aggregate diameter in *mm*

**Wet, Normal, Dry and Very Dry refer to an equivalent overhead build-up of approximately 50, 100, 150 and 200 mm (Fig. 3.5).

6.5 - Material and Methods

The analytical results reported here are compared with data obtained from the shotcrete experiments described in Chapter 3 (for a complete description of shooting procedures refer to item 3.2). Gradation analysis of the washed-out samples allowed calculating the composition of both in-situ shotcrete and rebound as well as the individual rates of rebound (r_i) for each sieve size. The latter value was calculated using the experimental masses of shotcrete and rebound (respectively, M_s and M_R) and the experimental proportion of the shotcrete and rebound gradation curves retained in a sieve of size i (respectively, p_{is} and p_{iR}):

$$r_i = \frac{p_{iR} \cdot M_R}{\left(p_{iR} \cdot M_R + p_{is} \cdot M_s\right)} \tag{6.7}$$

6.6 - Results and Analysis

6.6.1 - Variation of Rebound with the Aggregate Size

In order to investigate the variation of the rate of rebound as a function of the aggregate size for a constant shotcrete composition and consistency, the model was used with material properties of static and dynamic contact stresses of shotcrete at $p = 0.50$ and $p_d = 10$ MPa, as determined experimentally in Chapter 5 (Table 6.1), and an assumed air flow of 300 cfm (100 cfm = 0.05 m^3/s). The adhesive strength used in this case was $\sigma_o = 0.0055$ MPa. The analytical results obtained are presented in Fig. 6.4 along with experimental data from four different test panels shot using the same conditions of mix-design, workability and 300 cfm air flow.

As shown in Fig. 6.4, the model predicts a linear variation in the rate of rebound with the logarithm of the aggregate size, a trend that is clearly confirmed by the experimental data. In addition, it can be seen that the model is accurate in predicting the individual probability of rebound for each aggregate size, with the best-fit average lines showing an error of less than 5% between the experimental and predicted values. This level of precision indicates that the model is accurate not only in predicting the linear trend, but also the aggregate composition of the rebound.
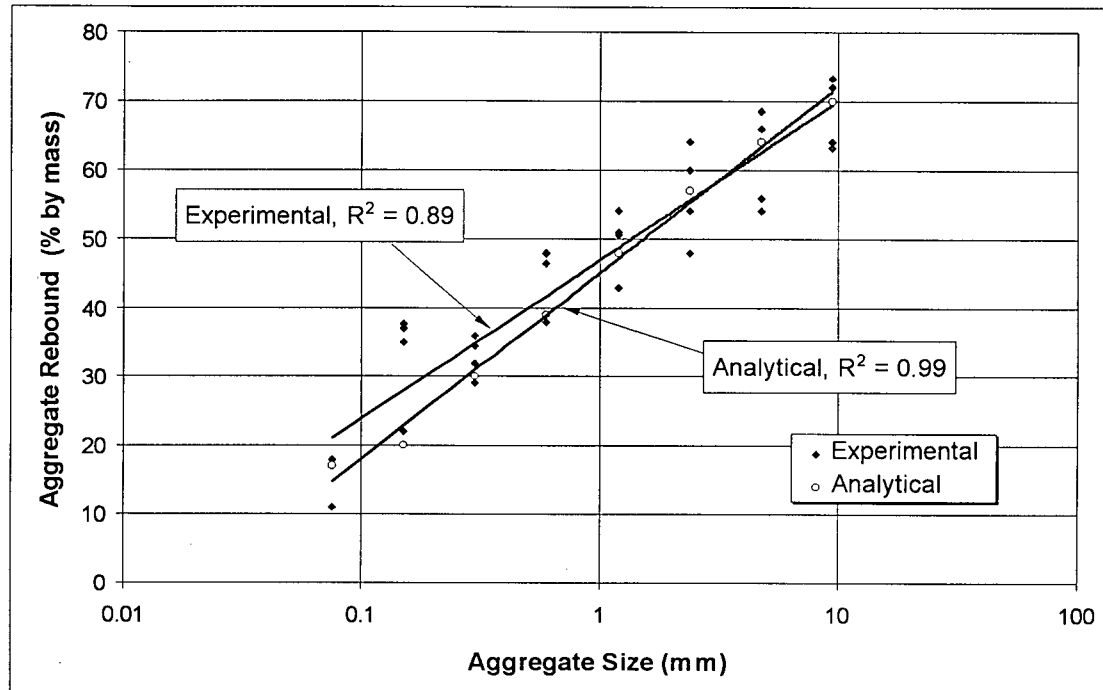
Figure 6.4 - Comparison between analytical and experimental results for the variation in aggregate rebound with size.

As shown by both experimental data and the model, the larger aggregate phases show a rate of rebound approximately four times greater than the smaller phases (70 against 15% respectively for 9.5 and 0.075 mm diameter). The reason for this large difference can be explained using the mechanical model developed to derive the average expected rebound and debonding energies (W_2 and W_D). In Table 6.2, notice that, relative to their diameter, the smaller aggregates tend to have a greater impact velocity (V) and thus tend to reach a greater depth of penetration (δ^*), leading to a greater contact to particle radius ratio (a^*/r). Thus, it can be seen that, while the 0.075 mm aggregate reaches maximum contact radius ($a^*/r = 1$), in the 9.5 mm case this ratio is only 0.59. Relative to the particle diameter, this leads to a considerably smaller contact area and, consequently, less energy necessary to debond the particle from its shotcrete embedment (W_D).

Table 6.2 - Average output values obtained using the model for the various parameters tested.

Input Parameters			Average Model Output											
Diam (mm)	Variable	p, pd, σ₀ (MPa)	v (m/s)	W₁ (l)	Vₐ (m³)	δ* (mm)	a* (mm)	a*/r	Area (mm²)	W₂ (l)	e (%)	W_D (l)	W₂/W_D	Rebound
0.075			60.9	1.09E-06	1.09E-13	0.037	0.04	1.00	4.41E-10	4.21E-10	1.97%	8.98E-10	0.47	17%
0.15			49.3	5.68E-06	5.68E-13	0.057	0.07	0.97	1.66E-02	3.08E-09	2.33%	5.22E-09	0.59	20%
0.3			39.8	2.97E-05	2.97E-12	0.089	0.14	0.91	5.90E-02	2.06E-08	2.63%	2.89E-08	0.71	30%
0.6	standard	0.5, 10, 0.0055	32.2	1.55E-04	1.55E-11	0.14	0.25	0.85	2.02E-01	1.31E-07	2.90%	1.56E-07	0.84	39%
1.2	mix		26.0	8.09E-04	8.09E-11	0.22	0.46	0.77	6.77E-01	7.99E-07	3.14%	8.19E-07	0.98	48%
2.4			21.0	4.23E-03	4.23E-10	0.355	0.85	0.71	2.28E+00	4.94E-06	3.42%	4.45E-06	1.11	57%
4.8			17.0	2.21E-02	2.21E-09	0.57	1.55	0.65	7.57E+00	2.99E-05	3.68%	2.37E-05	1.26	64%
9.5			13.8	1.13E-01	1.13E-08	0.9	2.78	0.59	2.43E+01	1.72E-04	3.91%	1.20E-04	1.43	70%
Diam (mm)	Cement	p, pd, σ₀ (MPa)	v (m/s)	W₁ (l)	Vₐ (m³)	δ* (mm)	a* (mm)	a*/r	Area (mm²)	W₂ (l)	e (%)	W_D (l)	W₂/W_D	Rebound
9.5	350 kg/m³	0.5, 13, 0.0055	13.8	1.13E-01	8.66E-09	0.785	2.62	0.55	2.15E+01	1.43E-04	3.56%	9.27E-05	1.54	74%
9.5	400 kg/m³	0.5, 10, 0.0055	13.8	1.13E-01	1.13E-08	0.9	2.78	0.59	2.43E+01	1.72E-04	3.91%	1.20E-04	1.43	70%
9.5	450 kg/m³	0.5, 7, 0.0055	13.8	1.13E-01	1.61E-08	1.08	3.02	0.63	2.86E+01	2.19E-04	4.41%	1.70E-04	1.29	65%
9.5	550 kg/m³	0.5, 5, 0.0055	13.8	1.13E-01	2.25E-08	1.29	3.25	0.69	3.33E+01	2.75E-04	4.94%	2.36E-04	1.17	59%
Diam (mm)	Air Flow	p, pd, σ₀ (MPa)	v (m/s)	W₁ (l)	Vₐ (m³)	δ* (mm)	a* (mm)	a*/r	Area (mm²)	W₂ (l)	e (%)	W_D (l)	W₂/W_D	Rebound
9.5	100 cfm		6.0	2.13E-02	2.13E-09	0.38	1.86	0.39	1.09E+01	5.15E-05	4.92%	2.27E-05	2.27	87%
9.5	200 cfm		10.9	7.09E-02	7.09E-09	0.71	2.50	0.53	1.96E+01	1.25E-04	4.19%	7.65E-05	1.63	77%
9.5	300 cfm		13.8	1.13E-01	1.13E-08	0.9	2.78	0.59	2.43E+01	1.72E-04	3.91%	1.20E-04	1.43	71%
9.5	400* cfm	0.5, 10, 0.0055	41.5	1.02E+00	1.02E-07	2.93	4.39	0.92	6.04E+01	6.75E-04	2.57%	9.74E-04	0.69	66%
1.2	100 cfm		13.3	2.13E-04	2.13E-11	0.11	0.3463	0.58	3.76E-01	3.32E-07	3.95%	2.28E-07	1.46	71%
1.2	200 cfm		25.0	7.48E-04	7.48E-11	0.21	0.4560	0.76	6.53E-01	7.57E-07	3.18%	7.54E-07	1.00	50%
1.2	300 cfm		26.0	8.09E-04	8.09E-11	0.222	0.4660	0.78	6.82E-01	8.08E-07	3.16%	8.32E-07	0.97	48%
1.2	400* cfm		71.6	6.14E-03	6.14E-10	0.6	0.6000	1.00	1.13E+00	1.73E-06	1.68%	3.73E-06	>1	>48%
Diam (mm)	Silica Fume**	p, pd, σ₀ (MPa)	v (m/s)	W₁ (l)	Vₐ (m³)	δ* (mm)	a* (mm)	a*/r	Area (mm²)	W₂ (l)	e (%)	W_D (l)	W₂/W_D	Rebound
9.5	0%	0.5, 10, 0.0055	13.8	1.13E-01	1.13E-08	0.9	2.78	0.59	2.43E+01	1.72E-04	3.91%	1.20E-04	1.43	70%
9.5	8%	0.5, 7, 0.0055	13.8	1.13E-01	1.61E-08	1.08	3.02	0.63	2.86E+01	2.19E-04	4.41%	1.70E-04	1.29	65%
9.5	16%	0.5, 5, 0.0055	13.8	1.13E-01	2.25E-08	1.29	3.25	0.69	3.33E+01	2.75E-04	4.94%	2.36E-04	1.17	59%
Diam (mm)	Consistency	p, pd, σ₀ (MPa)	v (m/s)	W₁ (l)	Vₐ (m³)	δ* (mm)	a* (mm)	a*/r	Area (mm²)	W₂ (l)	e (%)	W_D (l)	W₂/W_D	Rebound
9.5	wet	0.25, 5, 0.0027	13.8	1.13E-01	2.25E-08	1.3	3.26	0.69	3.35E+01	1.39E-04	3.51%	1.17E-04	1.18	61%
9.5	normal	0.5, 10, 0.0055	13.8	1.13E-01	1.13E-08	0.9	2.78	0.59	2.43E+01	1.72E-04	3.91%	1.20E-04	1.43	70%
9.5	dry	1.0, 15, 0.01	13.8	1.13E-01	7.51E-09	0.73	2.53	0.53	2.01E+01	2.59E-04	4.79%	1.47E-04	1.76	80%
9.5	very dry	2.0, 20, 0.017	13.8	1.13E-01	5.63E-09	0.63	2.36	0.50	1.75E+01	4.22E-04	6.12%	1.88E-04	2.25	87%

* 400 cfm refers to a 1.5 in (38 mm) hose, all other situations refer to a 2 in (50 mm) diameter hose

** Silica fume contents reported in mass substitution to cement

In addition, the model also predicts, and experimental data confirm (item 5.4.2) that the lower impact velocity of larger aggregates tends to cause greater coefficients of restitution (e), with a greater fraction of the impact energy being transformed into energy for rebound. As a result, when the ratio between the average expected rebound and debonding energies is computed (W_2/W_D), the 0.075 mm aggregate shows a ratio of only 0.47, while for the 9.5 mm case, this value approaches 1.43, making the rebound energy much greater than the capacity of the bond (Table 6.2).

6.6.2 - Variation in the Cement Content

In item 5.4.3 it was experimentally shown that, for a constant workability, the dynamic contact stress (p_d) is reduced with an increase in the cement content. Therefore, in order to use the model developed here to investigate the influence of the cement content on rebound, four different situations were analyzed: a usual cement content for dry-mix shotcrete (400 kg/m^3 - A:C = 4.25), one low (350 kg/m^3 - A:C = 4.9) and two high cement contents (450 and 550 kg/m^3 - A:C = 3.5 and 2.7, respectively).

Equal workability conditions were assumed with identical static contact stress ($p = 0.5$ MPa) and adhesive strength ($\sigma_o = 0.0055$ MPa). For the dynamic contact stress (p_d) values close to those experimentally obtained in Chapter 5 were used ($p_d = 5$, 7, 10 and 13 for A:C = 2.7, 3.5, 4.25 and 4.9, respectively). The exact p_d values obtained in Chapter 5 were not used since, for either a very low or a very high design cement content, the aggregate rebound will change, causing the in-situ aggregate to cement ratio to approach a value of four (as shown experimentally in item 3.3.1.3). Therefore, extreme values of very high or very low p_d should not be expected.

The analytical results obtained are compared with experimental data in Fig. 6.5. Notice that the model correctly predicts that the rebound should decrease, at all aggregate sizes, with an increase in the cement content. The model is also capable of predicting that a linear relationship between the rate of rebound and the logarithm of the aggregate size is maintained. With respect to the accuracy of these predictions, the analytical best fit lines lie close to the experimental ones, with an error that does not exceed 10%. This close agreement in the results is further reflected in the

prediction of the overall rate of rebound (R) which is within 5% of the experimental values (Fig. 6.6).
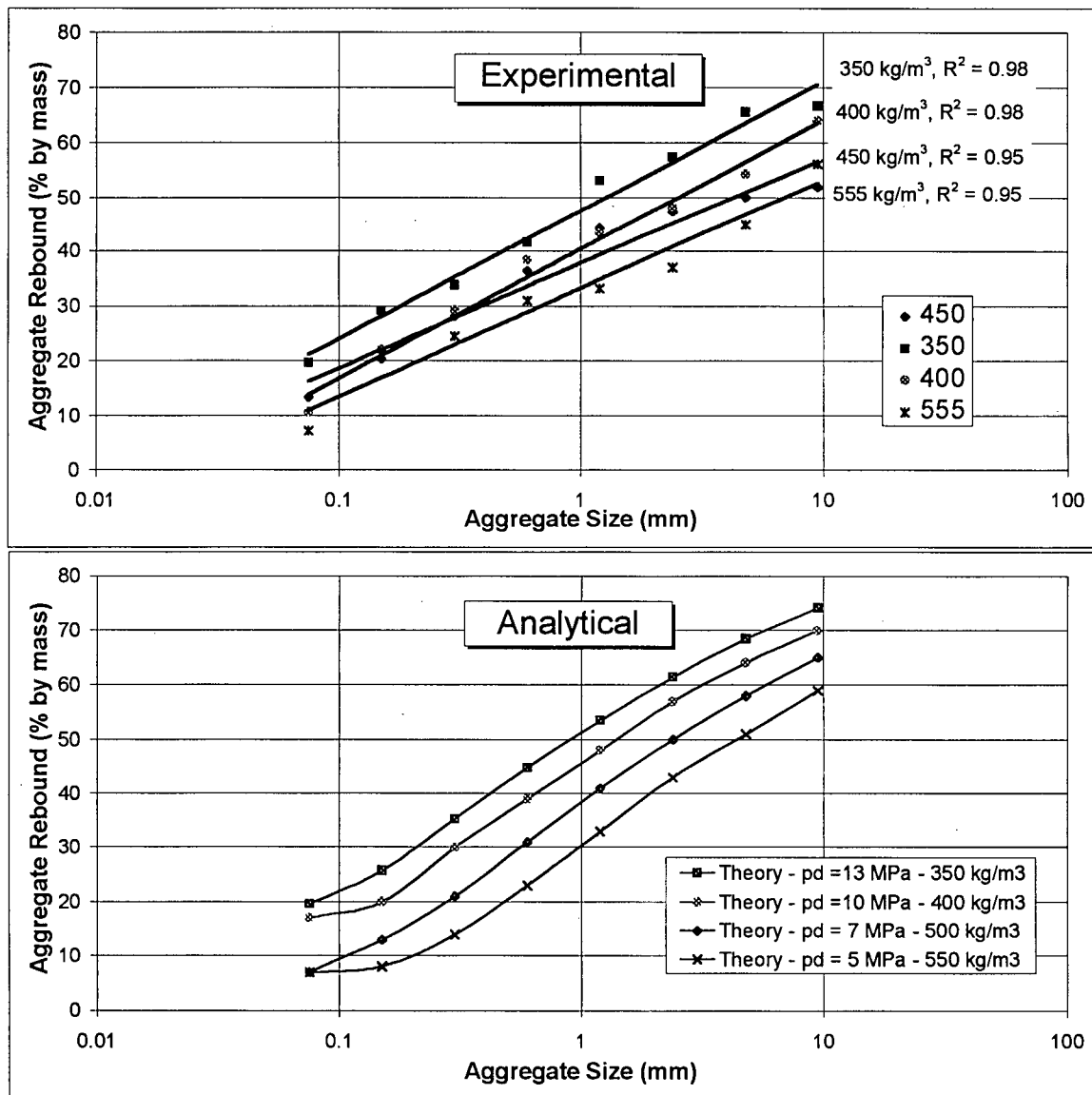
Figure 6.5 - Variation in aggregate rebound with the cement content: comparison between experimental and analytical results.

In item 5.4.3, it was shown that the mechanical model appropriately predicts that the coefficient of restitution (e) should increase with an increase in the cement content. It was also shown that this is due to an increase in the contact radius (a^*). However, this also leads to a greater contact area and depth of penetration, causing the debonding energy to increase. As a result, although the

rebound energy (W_2) increases with the cement content, the corresponding increment in the debonding energy (W_D) is greater. This causes the ratio between the two (W_2/W_D) to decrease, leading to less rebound. This is shown in Table 6.2, where, for the four cases analyzed (p_d, = 5, 7, 10 and 13 MPa) rebound and debonding energies are calculated for a 9.5 mm aggregate.
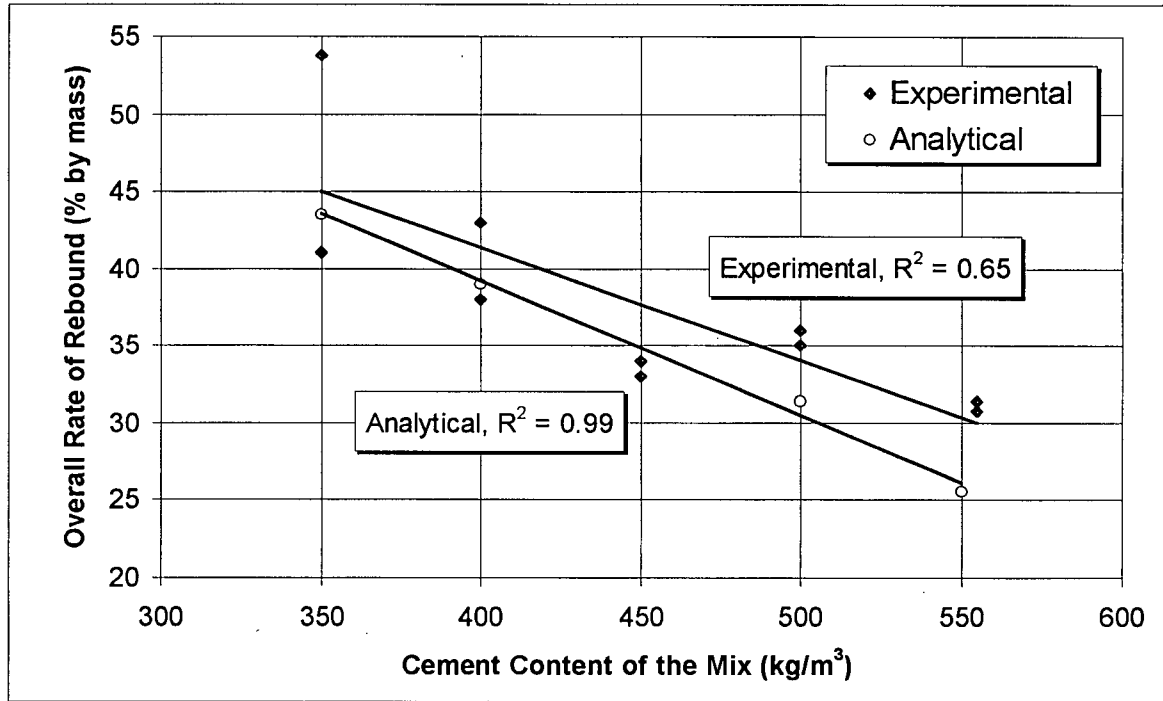
Figure 6.6 - Variation in the overall rate of rebound with the cement content: comparison between experimental and analytical results.

In item 3.3.1.3, it was shown that it is usually not cost-effective to produce dry-mix shotcrete at a cementitious content below approximately 400 kg/m^3. This model offers a physical explanation to this phenomenon: at low cement contents, the dynamic contact stress increases, causing the aggregates to rebound until the in-situ cement content reaches a level high enough to start re-accepting the aggregates. This gives rise to a self-regulating process that does not allow the in-situ cement content to fall below approximately 450 kg/m^3. Consequently, attempts to reduce the mix-design cement content below 400 kg/m^3 usually prove ineffective.

6.6.3 - Variation in the Air Flow

In order to use the model developed to analyze different conditions of air flow, the relationships between particle size and velocity obtained experimentally in Chapter 4 using high-speed filming were used (Table 6.1). Air flow rates between 100 and 300 cfm were analyzed for a 2 in (50 mm) hose and nozzle. In all cases, the material properties of the fresh shotcrete substrate were kept constant at p = 0.50, p_d = 10 MPa and σ_o = 0.0055 MPa - values considered to be characteristic of a standard shotcrete consistency.

The results from this analysis are shown in Fig. 6.7, along with the experimental data from item 3.3.2.1 from dry-mix shotcrete produced using a constant mix, at equal workability, but with a varying air flow. All shotcrete mixes were produced with a 2 in (50 mm) hose and nozzle except for the 400 cfm values, which employed a 1.5 in (38 mm) hose.

A comparison between the experimental and analytical results shows that, once again, the model is accurate in predicting individual rates of rebound for the various combinations of aggregate size and air flow, with an average error of less than 5%. The results for the prediction of the overall rate of rebound are presented in Fig. 6.8. Notice that the model correctly predicts the parabolic trend for the variation in the overall rebound with the air flow. An optimum air flow of approximately 300 cfm is observed in both experimental and analytical cases.

In order to physically interpret these results, rebound and debonding energies calculated using the model are presented in Table 6.2 for the cases of 9.5 and 1.2 mm aggregates shot at 100, 200 and 300 cfm with a 2 inch (50 mm) hose and nozzle and at 400 cfm with a 1.5 inch (38 mm) hose. For both aggregate sizes, it can be seen that, due to the greater impact velocities, the depth of penetration increases with increasing air flow, causing both the contact area and the debonding energy to rise. As a result, lower rebound to debonding energy ratios are observed and the rebound decreases.
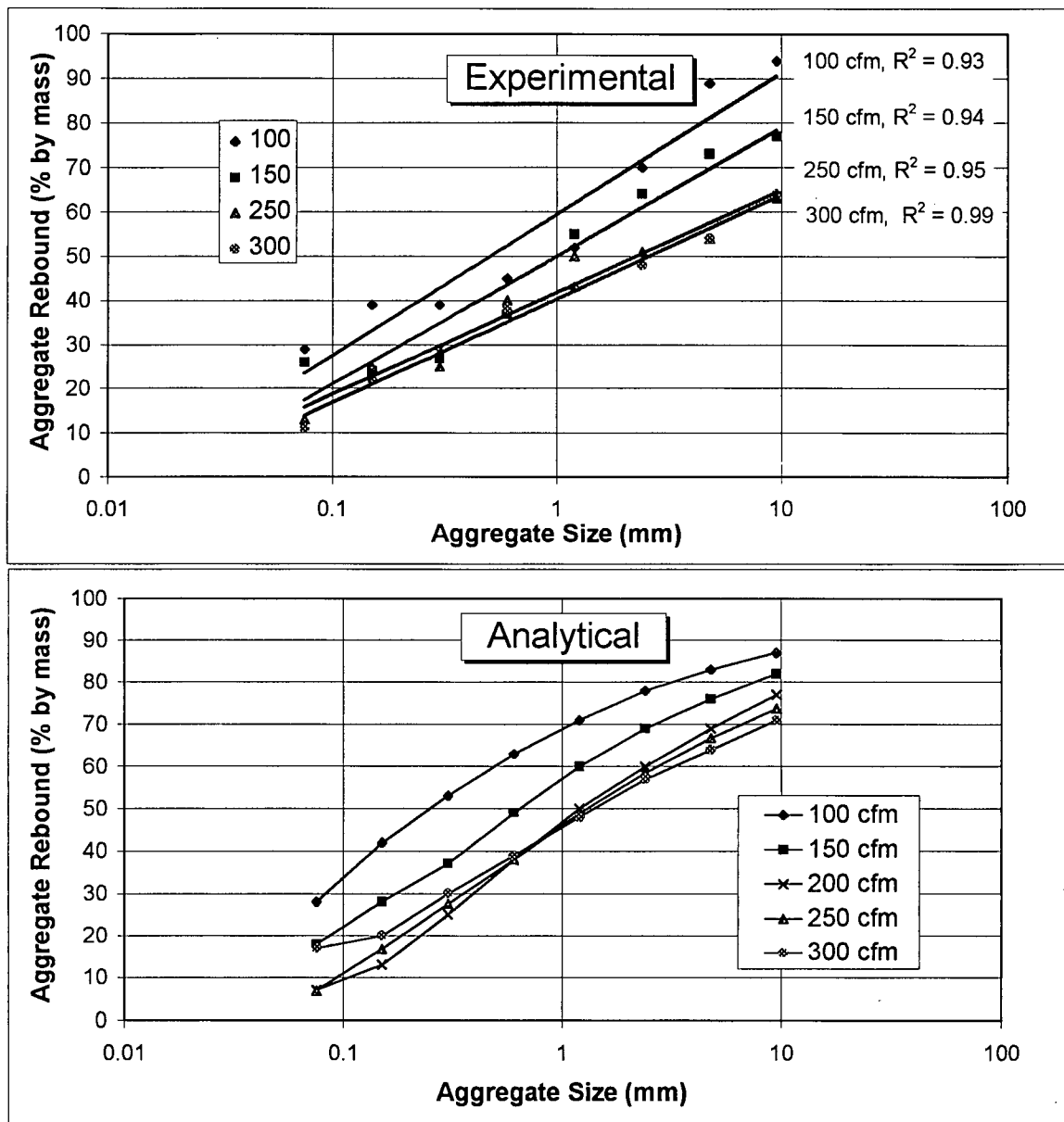
Figure 6.7 - Variation in aggregate rebound with the air flow: comparison between experimental and analytical results.

However, for smaller aggregates (less than 1.2 mm), at higher air flow values (above 300 cfm), the impact velocity is so great that the particle penetrates more than half of its diameter $(a^*/r = 1)$. From this point on, the debonding energy can no longer increase (as the contact area has already reached its maximum). Nevertheless, the rebound energy continues increasing since a greater portion of the substrate is strained. As a result, the particle rebound increases again, explaining why an optimum air flow is observed between 250 and 300 cfm in Fig. 6.8.
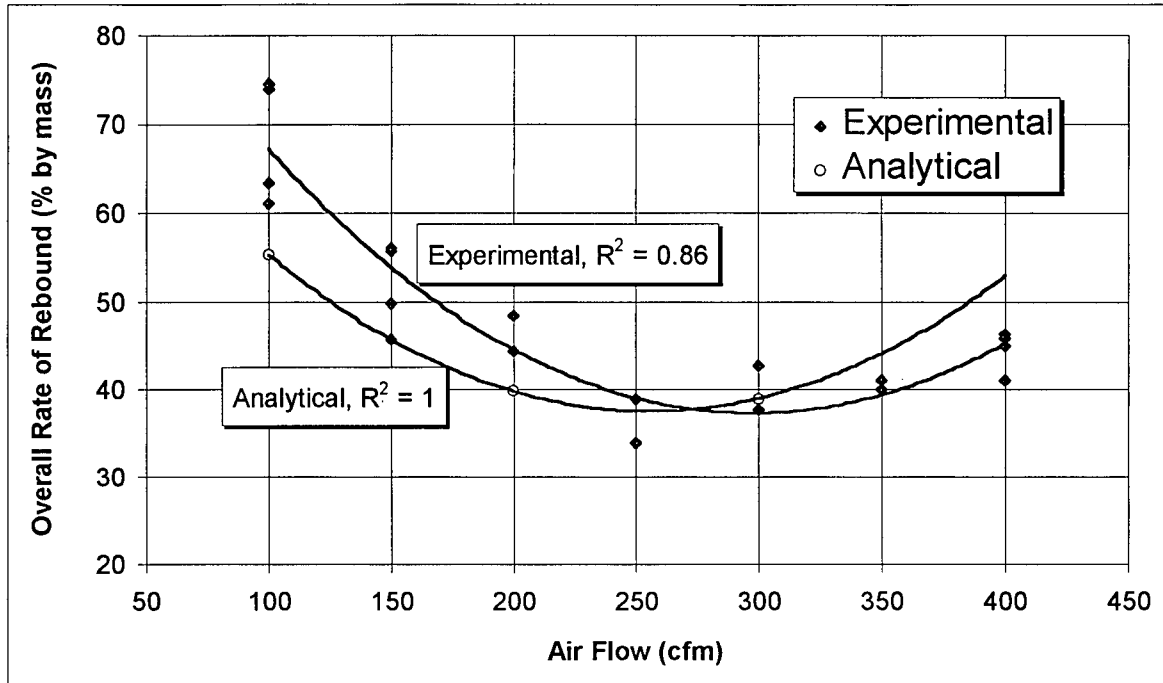
Figure 6.8 - Variation in the overall rate of rebound with the air flow: comparison between experimental and analytical results.

6.6.4 - Variation in the Silica Fume Content

It was experimentally shown in item 5.4.3 that, under conditions of equal workability, the presence of silica fume, at 8% by mass of cement, leads to a reduction in the dynamic contact stress (p_d). Therefore, in order to use the model developed to evaluate the influence of silica fume on rebound, three conditions were tested: $p_d = 10$, 7 and 5 MPa, representing situations of, respectively, 0, 8 and 16% of silica fume by mass of cement. In all cases, conditions of equal workability were kept $(p = 0.5$ MPa) and the adhesive strength was maintained constant at $\sigma_o = 0.0055$ MPa.

The analytical results obtained are shown in Fig. 6.9 along with experimental data from item 3.3.1.5 obtained from four shotcrete mixes produced at identical shooting and workability conditions, but with varying silica fume contents. A comparison between predicted and experimental results for individual aggregate sizes shows an average error of less than 10% at all

silica fume contents (Fig. 6.9). A comparison of the trend lines for the overall rate of rebound (Fig. 6.10) shows this error to be even smaller (less than 3%).
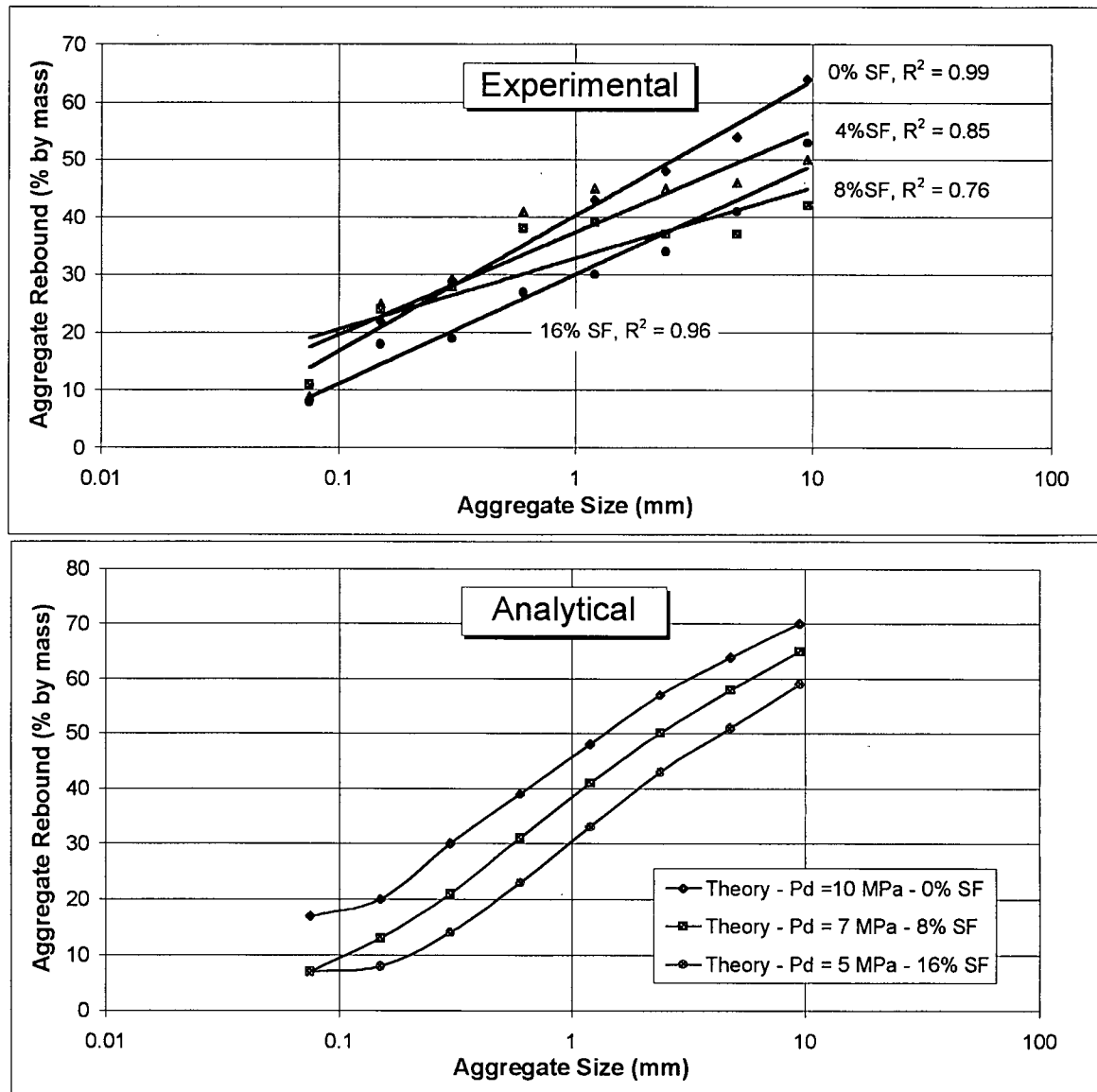
Figure 6.9 - Variation in aggregate rebound with the silica fume content: comparison between experimental and analytical results.

Thus, it appears that the mechanism by which silica fume acts is similar to that of a high cement content: due to a reduced dynamic contact stress (p_d), aggregates are able to reach a greater depth of penetration, leading to an increase in both the rebound and debonding energies. However, since the latter prevails, the ratio W_2/W_D decreases, with a resulting reduction in rebound (Table 6.2 presents the exact figures for the case of a 9.5 mm aggregate).

The chart shows Overall Rebound (% by mass) on the y-axis (20 to 50) versus Silica Fume Content (% mass subst to cement) on the x-axis (-2 to 18). Legend indicates "Experimental" (filled diamonds) and "Analytical" (open circles). Annotations: "Analytical, R² = 1" and "Experimental, Avg. R² = 0.96".
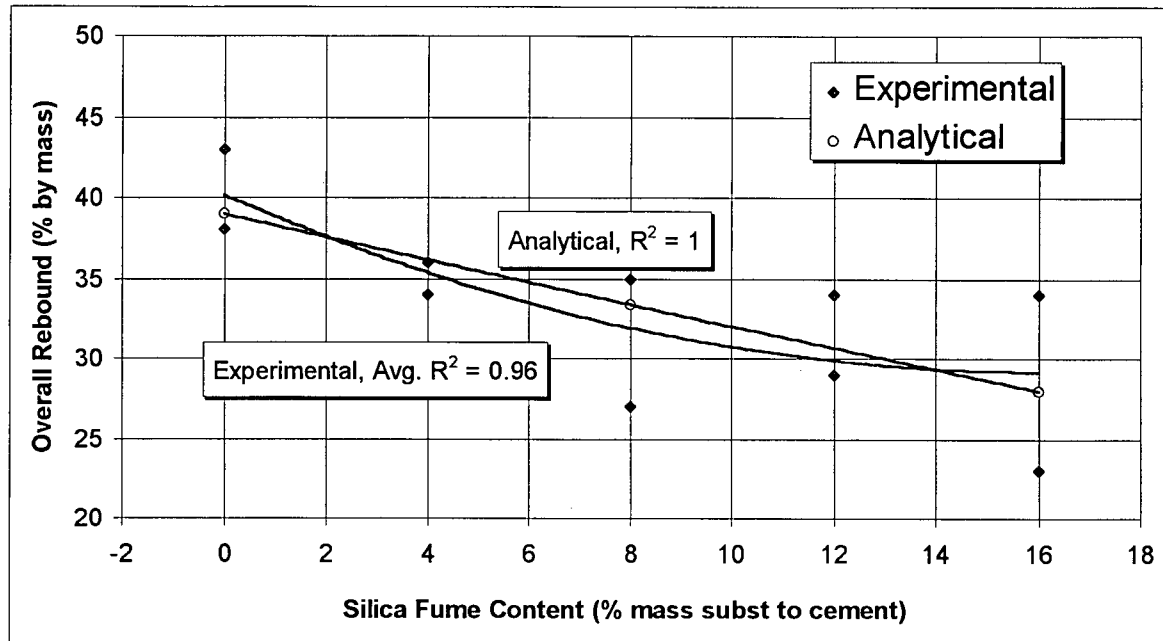
Figure 6.10 - Variation in the overall rate of rebound with the silica fume content: comparison between experimental and analytical results

6.6.5 - Variation in the water content

It was experimentally shown in item 5.4.1 (Fig. 5.7) that, when all other mix design parameters are kept constant, a reduction in the water content leads to an increase in both the static and dynamic contact stresses (p and p_d). Therefore, in order to investigate the influence of water content on rebound, four situations were analyzed, corresponding to an average shotcrete consistency ($p = 0.5$ and $p_d = 10$ MPa), one wet ($p = 0.25$ and $p_d = 5$ MPa), one dry ($p = 1$ and $p_d = 15$ MPa), and one very dry consistency ($p = 2$ and $p_d = 20$ MPa). These mixes were experimentally found (item 3.3.1.1) to correspond to an overhead build-up of, respectively, 50, 100, 150 and 200 mm.

The values used for the static contact stress (p) were those experimentally determined immediately after shooting using the penetrometer described in Chapter 3. The values used for the dynamic contact stress (p_d) were estimated from the experimental relationship found between p and p_d using cast concrete (item 5.4.1). The adhesive strength (σ_o) was assumed to vary with the shotcrete consistency in accordance with the pull-out experiments described earlier (Fig. 6.2). The exact figures used as input parameters are shown in Table 6.1.

The analytical results obtained are presented in Fig. 6.11 along with experimental data from item 3.3.1.1. The model is, once again, correct in predicting a linear variation in the rebound with the logarithm of the aggregate size for all consistencies tested. With respect to the accuracy of the model, the average error between experimental and predicted results lies below 10% for all aggregate sizes and shotcrete consistencies. Further, with respect to predicting the overall rate of rebound, it can be seen (Fig. 6.12) that the model correctly predicts a linear variation in the rebound with the shotcrete consistency and, in this case, the maximum error in the prediction lies below 5%.
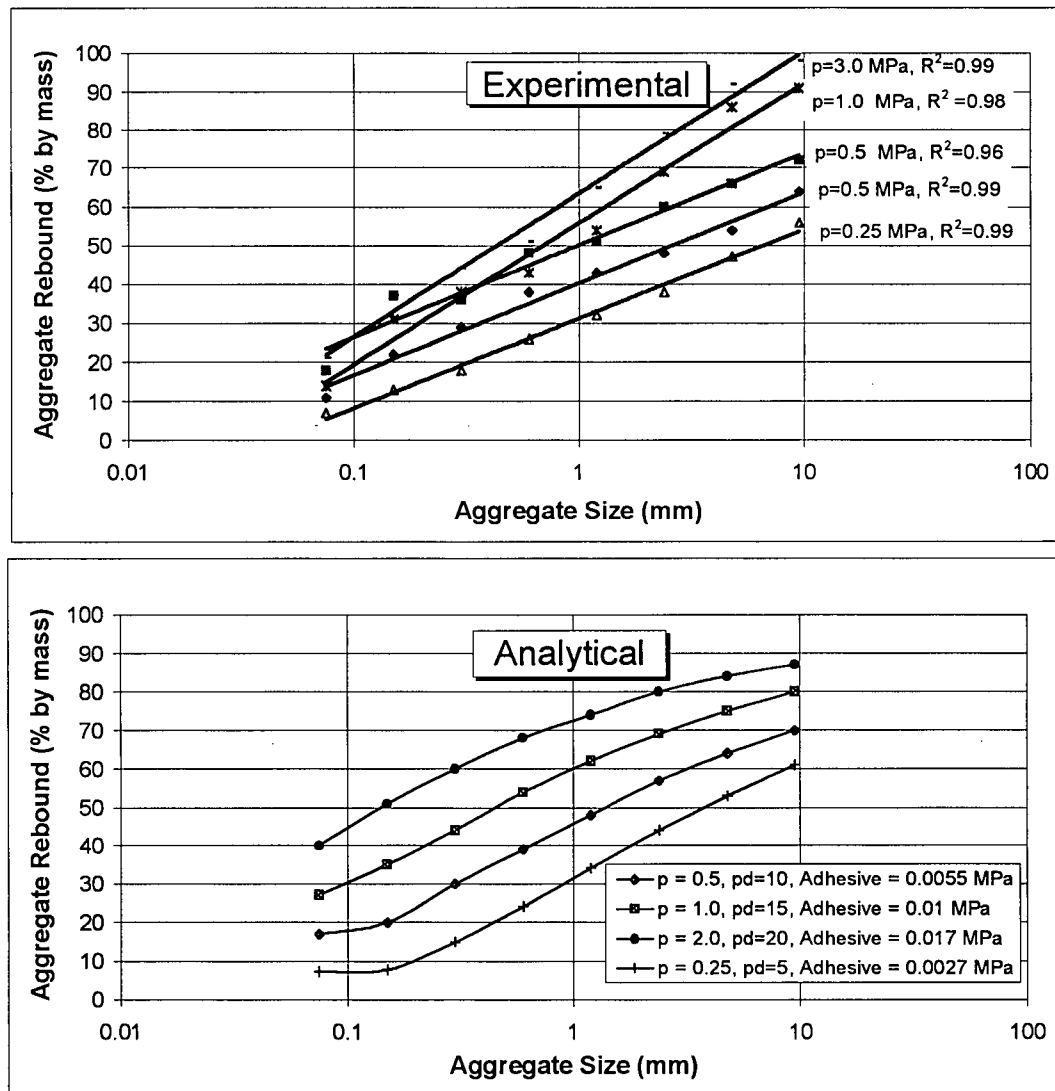
Figure 6.11 - Variation in aggregate rebound with the shooting consistency: comparison between experimental and analytical results.

From a mechanics point of view, Table 6.2 shows that a decrease in the water content leads to an increase in the rebound energy (W_2) due to the greater static contact stress (p). The corresponding debonding energy (W_D) also increases, but at a lower rate, due to the greater adhesive strength and in spite of the smaller contact area. Overall, the net result is a greater rebound to debonding energy ratio (W_2/W_D) with a corresponding increase in rebound.
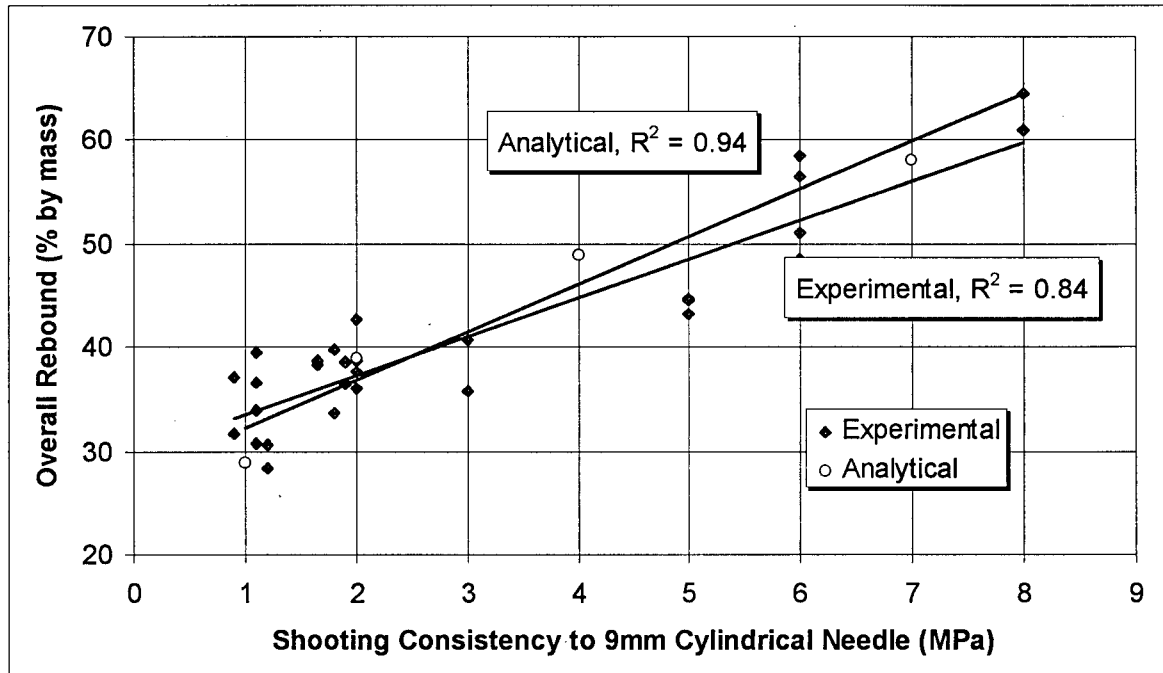
Figure 6.12 - Variation in the overall rate of rebound with the shooting consistency: comparison between experimental and analytical results

6.6.6 - Variation in the direction of shooting

In item 4.3.2.5, it was experimentally shown that overhead shooting leads to lower aggregate velocities for a fixed air flow. Also, it has been analytically demonstrated that the accelerations involved in the process of aggregate rebound are at least two orders of magnitude greater than those due to gravity (item 5.4.5). The latter result allows neglecting the effect of gravity and thus use the same model to analyze the case of aggregate rebound for overhead shooting. Therefore, the aggregate velocity versus size relationship obtained in Chapter 4 was used (Table 1). The

material properties of the shotcrete substrate were chosen to characterize a standard dry-mix shotcrete consistency ($p = 0.5$, $p_d = 10$ and $\sigma_o = 0.055$ MPa).

The results from this analysis are presented in Fig. 6.13a along with experimental data from item 3.3.2.3. Notice that, for different aggregate sizes, the model overestimates the overhead rebound by an average 10% (Fig. 6.13a) and shows an error of less than 5% in predicting the overall rebound (Fig. 6.13b). The average error in the prediction of the rebound for wall shooting is close to zero in both cases (Figs. 6.4 and 6.13b).
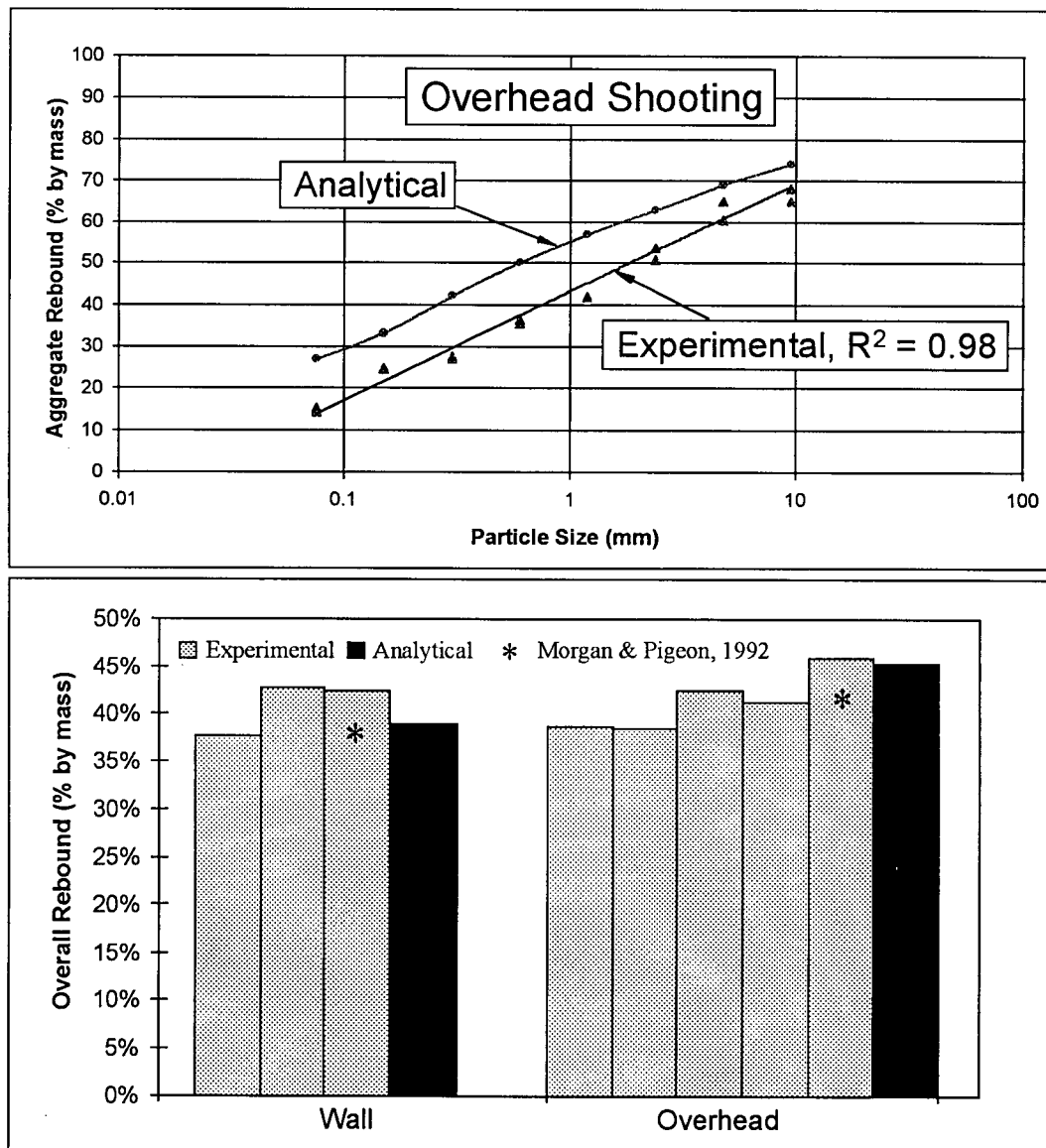
Figure 6.13a & b - Overhead vs. wall shooting: comparison between analytical and experimental results for the variation in the aggregate rebound (a) and overall rebound (b).

This confirms that the overhead rebound mechanisms are essentially the same as for wall shooting. The 7% increase in the overall rebound predicted by the model is due to the lower aggregate velocities that the equal air flow condition imposed causes. Ideally, this can be overcome by a small increase in the air flow, thus allowing the overhead rebound to be similar to the wall situation, as shown by the experimental results presented here, as well as those from Wolsiefer & Morgan (1993).

As mentioned earlier, in practice, prolonged overhead shooting has other implications: because the nozzleman is constantly being hit by the rebounding material, it is difficult to keep the nozzle normal to the shooting surface at all times, causing an increased rebound. This aspect of oblique shooting, however, cannot be accounted for in this model since it assumes conditions of normal impact. This, added to the greater shooting stiffness used while spraying the overhead are the probable causes for the increased rebound for overhead shooting in actual job sites.

6.6.7 - Variation in the Aggregate Gradation

The model developed here assumes that there is no particle to particle interaction. In other words, the probability of rebound of a given particle size is not influenced by the other aggregate sizes present in the mix. Therefore, in strict terms, the model predicts that, regardless of the aggregate gradation, the individual rate of rebound of each aggregate size does not change. The overall rate of rebound will, however, vary according to the composition of the mix, such that a coarser gradation will lead to a greater overall rebound.

In order to investigate the validity of this hypothesis, the model was used to predict the expected overall rate of rebound for the six different aggregate gradations tested in 3.3.1.4. Equal workability and shooting conditions were assumed and the material properties of the shotcrete were set at $p = 0.5$, $p_d = 10$ and $\sigma_o = 0.055$ MPa.

The results are presented in Fig. 6.14 along with experimental data from item 3.3.1.4. A comparison reveals that the model correctly predicts an increase in the overall rebound with the coarser gradations. Moreover, the model shows an average error of less than 5% in the prediction of the expected overall rate of rebound. With respect to the discontinuous gradations, the model appropriately predicts the rate of rebound with virtually no average error.
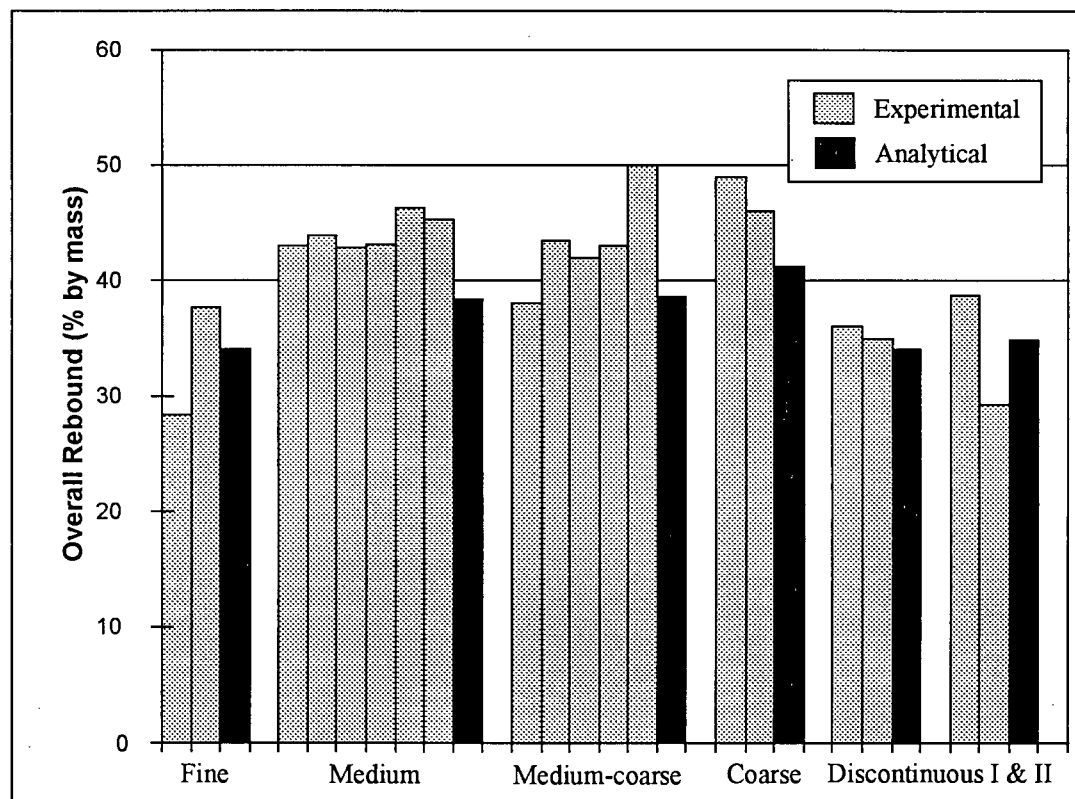
6.14 - Variation in the overall rate of rebound with the aggregate gradation: comparison between experimental and analytical results.

6.7 - Conclusions

In this chapter, a model has been developed to predict both the composition and the overall rate of rebound in dry-mix shotcrete. According to the model results, the following conclusions can be drawn:

1) The aggregate rebound process is governed by an embedment mode and the condition of rebound can be described by the ratio between the energy necessary to debond the aggregate (W_D) and the available rebound energy (W_2).

2) The reason why coarse aggregates tend to rebound up to four times more than fines is related to their low velocity, which causes a greater rebound to debonding energy ratio (W_2/W_D).

3) The mechanism by which a greater cement content and the presence of silica fume lead to a reduced aggregate rebound is related to a reduction in the dynamic contact stress (p_d) which, in turn, gives rise to an increase in the debonding energy (W_D).

4) There is an optimum air flow for minimized rebound. For air flow values above this point, aggregates are found to rebound more due to an increase in the rebound energy (W_2). For air flow values below optimum, rebound tends to increase due to a decrease in the debonding energy (W_D) and a greater coefficient of restitution (e).

5) For a lower water content, aggregate rebound increases due to an increase in the static contact stress (p) which, in turn, leads to a greater rebound energy (W_2).

6) The mechanism and forces involved in aggregate rebound for overhead shooting are essentially the same as for wall shooting. The increased rebound that is commonly observed in the field for overhead shooting is due to a reduced aggregate velocity and oblique spraying.

Chapter 7 - Experimental Evaluation of Steel Fiber Rebound: Influence of Mix Design and Shooting Technique

7.1 - Introduction and Objectives

As reported in article 2.5, the amount of data available in the literature on the subject of steel fiber rebound in dry-mix shotcrete is relatively limited and although it has been suggested that one of the primary causes of fiber rebound is fibers being blown away from the shotcrete stream before reaching the shooting plane (Parker, 1976) a later study (Peaston, 1993) demonstrated that fiber rebound is closely related to shotcrete overall rebound, thus indicating that both mix design and shooting technique may be of importance in the fiber rebound process.

Ultimately, however, it is not the fiber rebound, but the post-cracking load bearing capacity that defines the performance of fiber reinforced shotcrete and, although the two aspects are obviously connected, their correspondence is not immediate.

In order to better explore this aspect of fiber reinforced shotcrete, this chapter aimed at using the carefully controlled laboratory conditions of air flow and shotcrete consistency established for Chapter 3, in order to investigate fiber rebound and the influence of mix design and shooting technique as well as its consequences on the flexural toughness[1] performance of the material.

7.2 - Material and Methods

Shotcrete was produced using the same equipment described in Chapter 3 (model ALIVA 246 with a 3.6 liter, eight pocket drum) instrumented with a spring-loaded, in-line, air flowmeter (model OMEGA FL8945). The same conditions of air-flow (300 cfm), shooting workability (2 $\pm$ 0.5 MPa using the 9 mm diameter penetration needle) and shooting position (panels vertically standing on the wall, 1.5 m from the ground) were used.

---

[1] Given the fact that several toughness performance criteria exist and continue to be developed (ASTM, JSCE, template and others) and hoping to prevent the data presented from becoming readily obsolete, in this chapter and throughout this thesis, results from flexural toughness tests are reported in terms of the flexural post-cracking load bearing capacity in units of load (kN) at different levels of midspan deflection.

All panels were shot in three consecutive layers (thicknesses respectively of 25, 50 and 50 mm). Plastic tarpaulins were laid out inside the shooting chamber before each layer was shot and the panel was weighed after each layer. After shooting the third layer, the rebound material from each of the three tarpaulins was collected and weighed.

From each test panel, a 4 kg sample of shotcrete and two 8 kg samples of the rebound material (from each of the last two layers shot) were collected and washed over a 75 μm sieve to calculate the fiber mass contained per kilogram of both in-situ and rebound phases (respectively, FM_s and FM_r). From these quantities and knowing the shotcrete and rebound masses (M_s and M_r), the fiber rebound (R_f) was calculated in "exact" form (i.e. without any assumptions regarding the unit weight of shotcrete or the design fiber content[2]). Therefore:

$$R_f(\%) = \frac{Mass\ of\ Fibers\ in\ Rebound}{Mass\ of\ Fibers\ Shot} = \frac{FM_r \cdot M_r}{(FM_s \cdot M_s + FM_r \cdot M_r)} \cdot 100\% \qquad (7.1)$$

Steel fibers used throughout this chapter were 0.5 mm in diameter and 25.4 mm long with hooked ends. This particular fiber type was chosen since it is the most commonly used in dry-mix shotcrete to date. The aggregates used were concrete sand and river gravel with coarse to fine aggregate proportions set to comply with the ACI N° 2 gradation limits. The accelerator admixture used was a commercial powder (carbonate based). Unless otherwise specified, all shotcrete mixes were produced at 50 kg of fibers per m³ of shotcrete and using the same ordinary Portland cement added at a rate of 19% by mass of dry-materials (approximately 400 kg/m³ assuming a 0.40 water to cement ratio).

All test panels were demolded 24 hours after shooting and kept in the moist-room until the age of testing. After 28 days, three cores (85 mm in diameter and 100 mm in height) were drilled from each panel and tested for compressive strength (3 specimens) and voids content (ASTM C 642 - 2 specimens). Prismatic specimens (100 x 100 x 400 mm) were also sawed for flexural toughness

---

[2] In effect, the only assumption used in this formulation is that the experimental determinations of the mass fiber content in both in-situ shotcrete and rebound (respectively, FM_s and FM_r) are representative of the whole. This is guaranteed by the relatively large shotcrete and rebound masses sampled (respectively, 4 and 8 kg).

testing using ASTM C 1018-96 (3 or 4 specimens). All flexural toughness tests were performed using two LVDTs and a yoke set-up linked to a digital data acquisition system.

7.3 - Results and Discussion

7.3.1 - Estimation of Fiber Rebound vs. Actual Fiber Rebound

As mentioned in item 2.5, there has been considerable debate on how to properly calculate fiber rebound in shotcrete, with different formulas proposed by Robins & Austin (1985) and Banthia et. al. (1994). Given the fact that it does not require the specific gravity, water to cement or aggregate to cement ratios of in-situ shotcrete, in this study, the formula proposed by Armelin and Helene (1995) and given in Eq. 2.1 was used. In order to test the accuracy of this equation, results obtained from 19 test panels, shot using different fiber types and shooting consistencies, were compared against experimental results of fiber rebound calculated in "exact[3]" form using the fiber masses collected from the shotcrete and rebound samples (Eq. 7.1).

The results obtained are presented in Fig. 7.1. From this figure, it can be seen that not only a good correlation exists ($r^2 = 0.96$), but also the best-fit equation shows a slope close to unity, crossing both axes near the origin and thus indicating that the numerical results given by Eq. 2.1 are very close to those obtained by the "exact" form (Eq. 7.1). This demonstrates the adequacy of Eq. 2.1, making this expression the most practical means available for calculating fiber rebound.

7.3.2 - Correlation Between Fiber Rebound and Overall Rebound

It was first demonstrated by Peaston (1993) that fiber rebound is closely related to overall dry-mix shotcrete rebound. However, Peaston (1993) worked with shotcrete mixtures with overall rebound in the range of 15 to 30%. In Fig. 7.2, data is presented on the correlation between fiber rebound and overall rebound from 33 test panels produced for this study at different shooting consistencies (i.e. different water content), with different silica fume and cement contents and

---

[3] Ideally, fiber rebound should always be calculated using the exact form (Eq. 7.1) however, given the fact that this equation requires knowledge of the total shotcrete and rebound masses (M_r and M_s) this formula cannot be applied in industrial conditions when it is impossible to weigh the total shotcrete and rebound produced.

containing three different types of accelerator admixtures. Overall rebound figures obtained from these tests ranged from 30 to 50% and up to 70%.
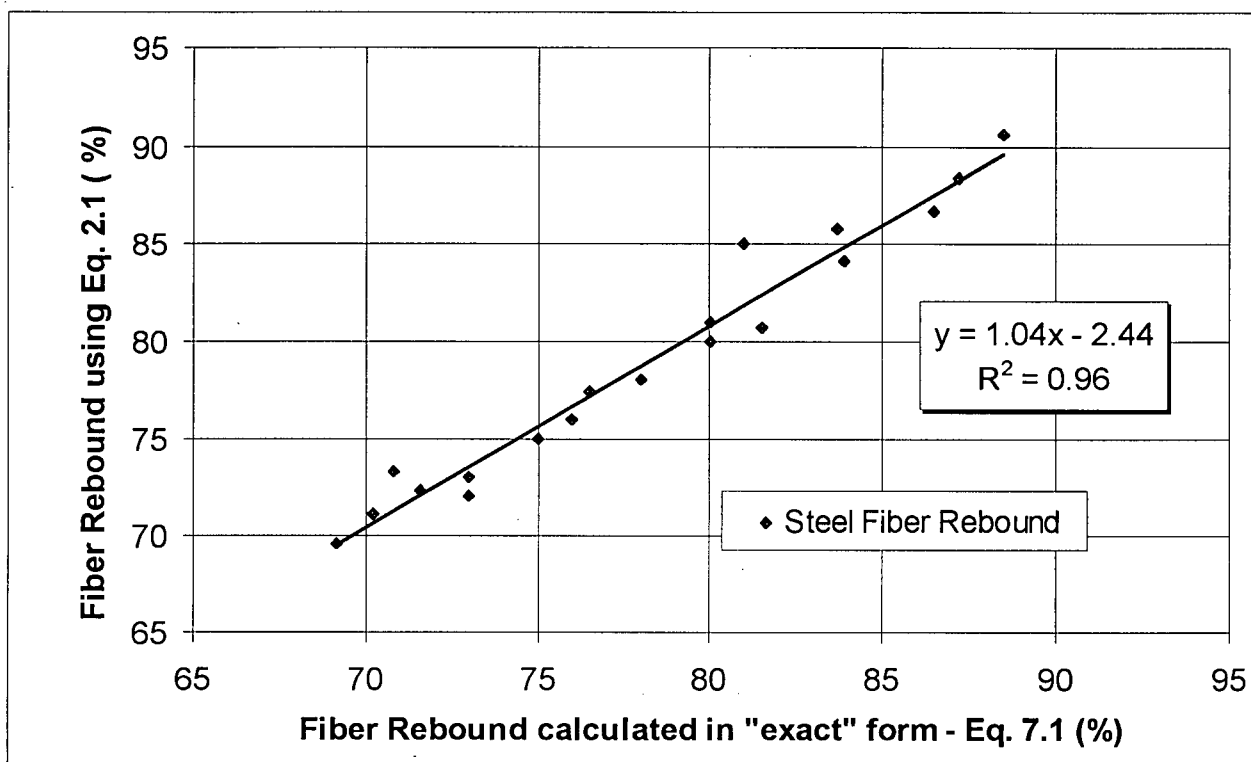
Figure 7.1 - Comparison between fiber rebound calculated using Eq. 2.1 and in "exact" form using the masses collected (Eq. 7.1).

From Fig. 7.2, it may be seen that the correlation between fiber and overall rebound is confirmed ($r^2 = 0.88$) with good agreement of the trend line between the data by Peaston (1993) and results from this study - the lower overall and fiber rebound values reported by Peaston (1993) are due to the relatively high cement content used (500 kg/m^3 vs. 400 kg/m^3 used for this study) as explained in section 7.3.4. As a general rule, it may be said that, within the range of usual dry-mix shotcrete rebound (between 20 and 40%), the slope of the trend line indicates that fiber rebound is approximately twice the overall rebound.

It should be noticed however that, although fiber rebound is directly related to the overall rebound, a decrease in the first does *not* necessarily lead to an increase in the in-situ fiber content and, consequently, a gain in post-cracking strength should not be automatically expected. As will be demonstrated ahead, this is a direct consequence of Eq. 2.2, from which it can be seen that, if

the overall rebound decreases at a greater rate than the fiber rebound, the in-situ fiber content may actually decrease (and vice versa).
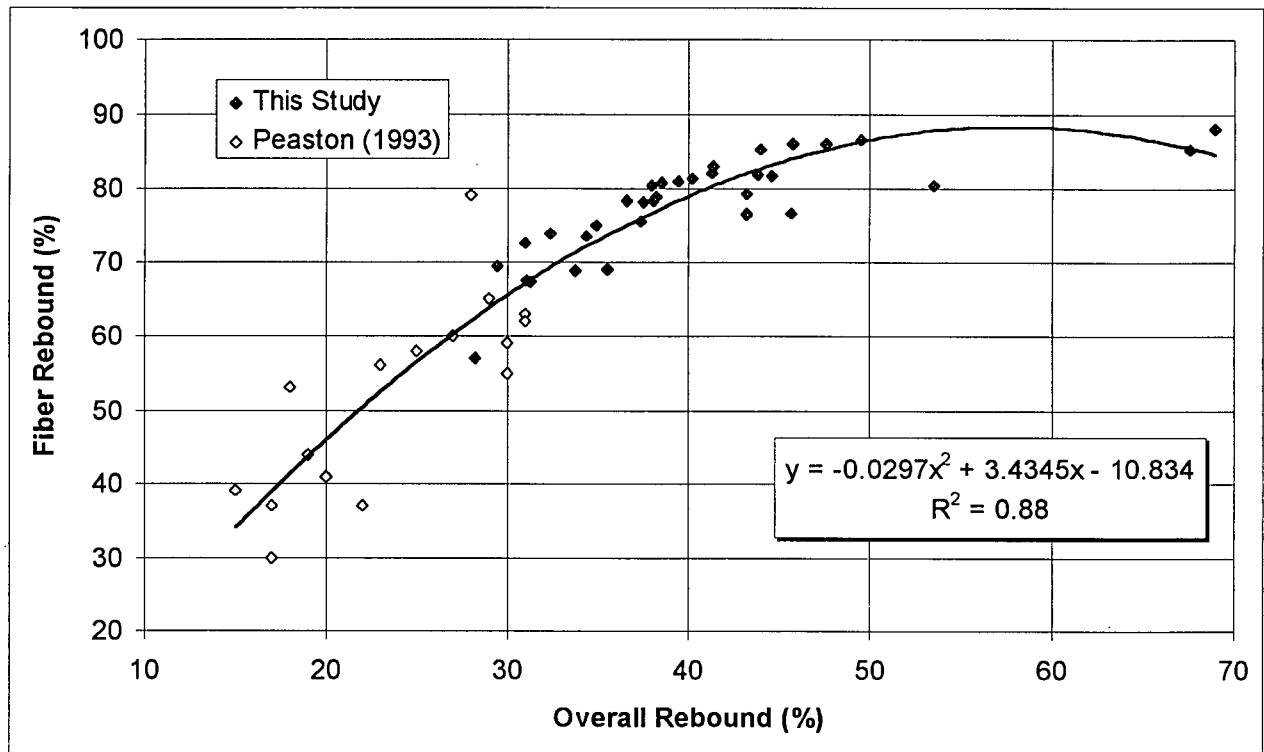
Figure 7.2 - Correlation between steel fiber rebound and shotcrete overall rebound (25.4 mm long fibers).

Also, the fact that overall and fiber rebounds have been demonstrated to be closely related indicates that, similar to aggregates, fiber rebound is determined by the interaction between the impacting fiber and the existing shotcrete substrate. A mechanism of fibers being blown away from the shotcrete stream before reaching the shooting target (as suggested by Parker, 1976) should therefore be regarded as only secondary.

7.3.3 - Variation in Fiber Rebound with the Shooting Consistency

Results for the variation in fiber rebound with the shooting consistency obtained by varying the water content of the mix or by the use of an accelerator admixture are presented in Fig. 7.3 and Table 7.1. These data show a positive correlation ($r^2 = 0.74$) between fiber rebound and shooting consistency (Fig. 7.3a) with stiffer mixes generally leading to a greater fiber rebound.
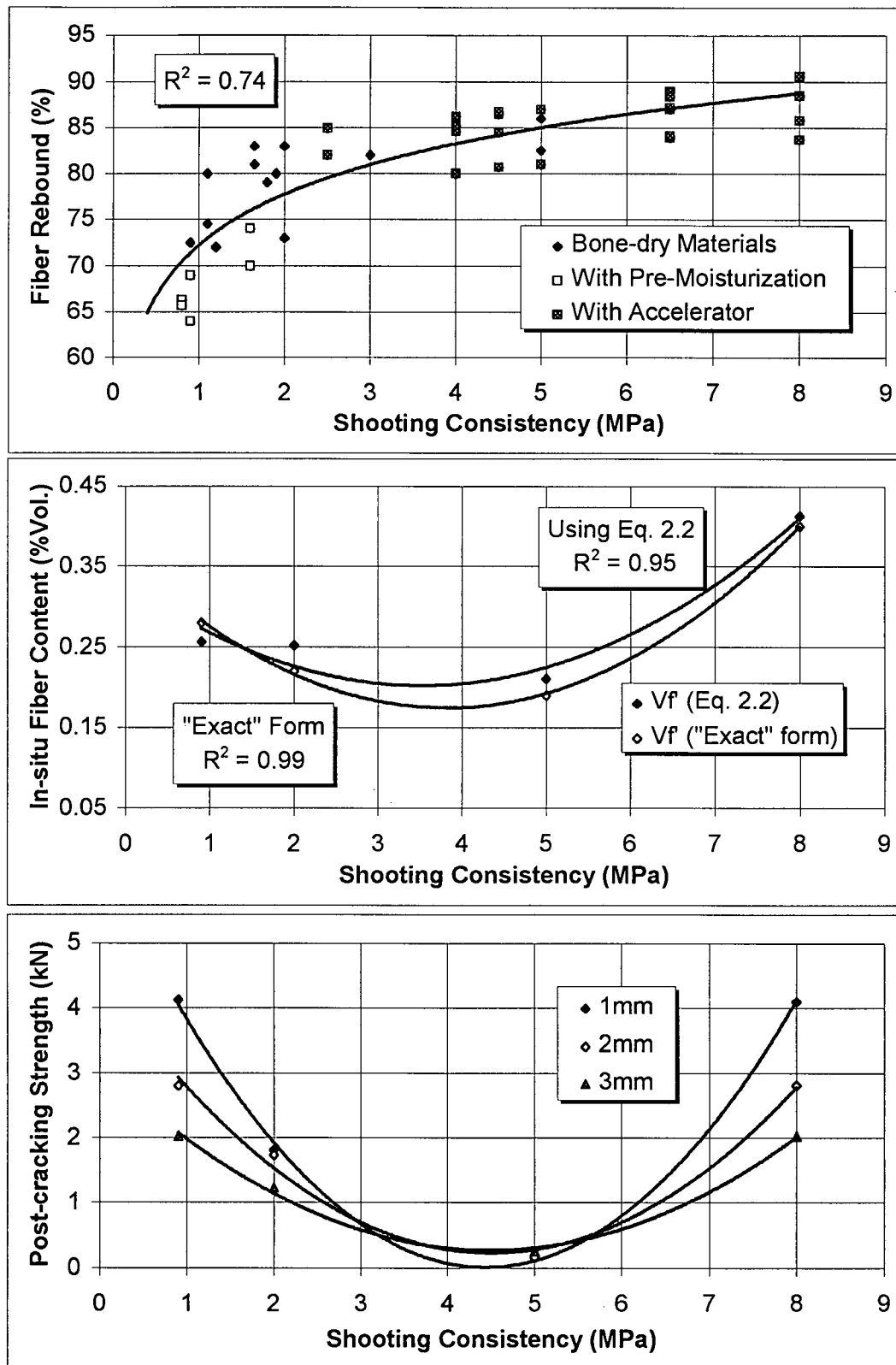
Figure 7.3 - Influence of shooting consistency on fiber rebound (a), in-situ fiber content (b) and post-cracking strength (c).
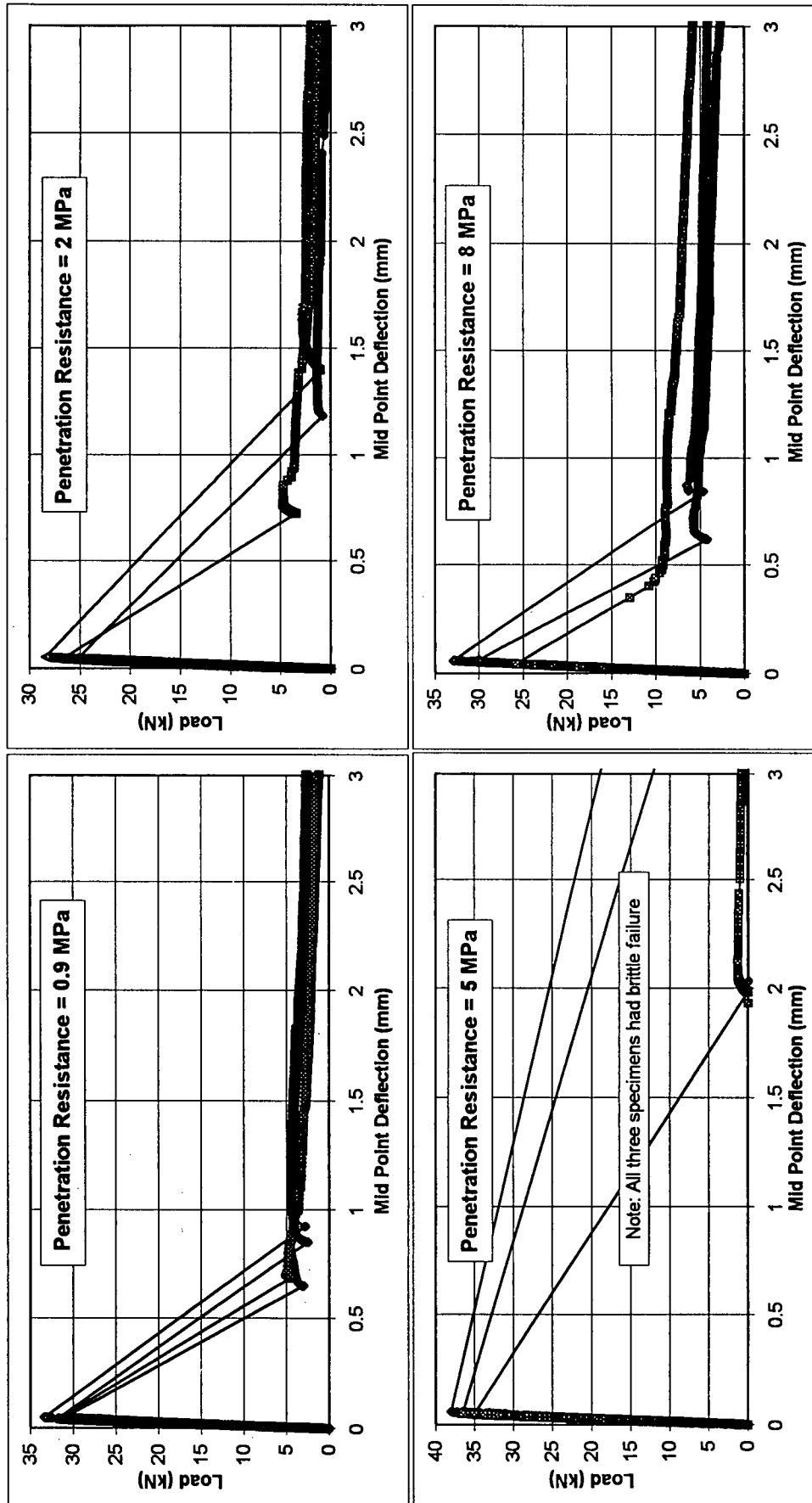
Figure 7.4 - Influence of shooting consistency on the flexural post-cracking behavior of fiber reinforced shotcrete (hooked fibers, 50 kg/m³)

Table 7.1 - Physical and mechanical properties of the various mixtures produced.

Variable	Shooting Consistency (MPa)	Overall Rebound (%)	Fiber[a] Rebound (%)	Fiber[b] Rebound (%)	In-situ fiber[c] Content (%)	In-situ fiber[d] Content (%)	Void Volume (%)	28d Comp. Str. (MPa)
Wet Consistency	0.9	34.0	73.4	71.6	0.28	0.26	14.2	55.7
Normal Consistency	2.0	37.4	75.5	78.3	0.22	0.25	11.7	74.6
Dry Consistency	5.0	44.6	81.7	83.2	0.19	0.21	10.5	76.8
Very Dry Consist.	8.0	63.0	76.0	76.7	0.40	0.41	16.9	48.4
Cement = 350 kg/m^3	3.0	47.0	73.4	76.1	0.29	0.32	11.3	72.8
Cement = 400 kg/m^3	2.0	37.4	75.5	78.3	0.22	0.25	11.7	74.6
Cement = 450 kg/m^3	3.0	33.8	68.7	71.4	0.28	0.30	10.2	72.6
Cement = 500 kg/m^3	2.5	35.5	68.9	71.0	0.29	0.31	10.6	66.9
Cement = 550 kg/m^3	2.0	31.0	67.5	65.1	0.32	0.30	9.7	72.4
Silica Fume = 0%	2.0	37.4	75.5	78.3	0.22	0.25	11.7	74.6
Silica Fume = 4%	2.0	35.0	74.5	75.5	0.24	0.25	10.5	58.0
Silica Fume = 8%	2.0	31.0	72.6	72.6	0.25	0.25	8.0	62.1
Silica Fume = 12%	2.0	31.3	67.2	69.4	0.27	0.30	8.0	62.8
Silica Fume = 16%	2.0	28.2	57.0	57.6	0.38	0.38	11.7	60.5
Air Flow = 150 cfm	2.2	47.0	62.2	61.3	0.47	0.45	14.4	64.4
Air Flow = 250 cfm	2.2	36.5	65.3	70.2	0.30	0.35	12.1	70.5
Air Flow = 300 cfm	2.0	37.4	75.5	78.3	0.22	0.25	11.7	74.6
Air Flow = 350 cfm	2.0	40.5	78.0	80.4	0.21	0.24	11.8	76.0
Air Flow = 400 cfm	1.6	43.0	80.3	80.4	0.22	0.22	13	56.2
Accelerator = 0.5%	4.0	38.0	80.3	84.6	0.16	0.20	12.2	70.2
Accelerator = 1.5%	5.0	39.4	81.0	86.9	0.14	0.20	14.4	45.0
Accelerator = 3.0%	6.5	49.5	86.6	89.3	0.14	0.17	16.6	41.7
Accelerator = 6.0%	8.0	45.7	76.7	81.9	0.21	0.27	18.7	33.7
Fibers = 25 kg/m^3	2.3	42.6	71.6	72.5	0.15	0.16	10.5	65.7
Fibers = 50 kg/m^3	2.0	37.4	75.5	78.3	0.22	0.25	11.7	74.6
Fibers = 60 kg/m^3	2.3	43.9	75.5	77.3	0.28	0.33	13.5	57.3
Fibers = 75 kg/m^3	2.5	43.4	76.5	77.4	0.41	0.42	12.31	67.9
Wall	2.0	37.4	75.5	78.3	0.25	0.25	14.5	48.9
Overhead	1.5	39.7	73.6	72.5	0.29	0.28	12.8	63.9
Inclined	2.0	25.0	63.2	66.6	0.34	0.38		53.8

a - Experimentally determined from the fiber masses collected from shotcrete and rebound (exact form, Eq. 7.1)
c - Experimentally determined from the 4 kg fiber mass collected from shotcrete.

b - Calculated using Eq. 2.1.
d - Calculated using Eq. 2.2.

In Fig. 7.3b, the resulting correlation between the shooting consistency and the in-situ fiber content is presented in terms of data obtained both by collecting the fibers from the 4 kg shotcrete sample and by using Eq. 2.2, with the overall and fiber rebounds as determined experimentally (respectively, R and R_f) and the known design fiber content (V_f). The results obtained show that, up to a 5 MPa shooting consistency (equivalent to a 200 mm overhead build up - Fig. 3.5), as expected, with an increase in the stiffness of the mix, because the fiber rebound increases, the in-situ fiber content tends to decrease. However, for a very dry consistency (8 MPa), the overall rebound is so high (R = 63%) and approaching the fiber rebound value that the in-situ fiber content is found to increase again. Once more, this is in agreement with Eq. 2.2.

Overall, the results presented in Fig. 7.3b show the importance of keeping an adequate shooting consistency when producing steel fiber reinforced shotcrete. Stiff consistencies (between 2 and 5 MPa) will invariably lead to a greater loss in fiber content. A comparison between the in-situ fiber content values obtained experimentally and using Eq. 2.2 (Fig. 7.3b and Table 7.1) shows that the values calculated using Eq. 2.2 are very close to the experimental, thus indicating that this equation is effective in predicting the in-situ fiber content with good accuracy.

The post-cracking residual strength results obtained from the flexural toughness tests are presented in Fig. 7.3c in terms of the average residual load at mid point deflections of 1, 2 and 3 mm. From this figure, it can be seen that the post-cracking strength follows the expected trend set by the in-situ fiber content (Fig. 7.3b), with greater fiber contents leading to a greater residual strength. Once again, notice the considerable loss in reinforcing performance caused by the low in-situ fiber content for stiffer shooting consistencies (between 2 and 5 MPa). For the 5 MPa shooting consistency, the combination of a high matrix strength and a low fiber content caused all three flexural toughness specimens to have an almost brittle failure (Fig. 7.4).

Also, the fact that, for a very dry consistency (8 MPa) the post cracking strength was relatively high despite its high fiber rebound demonstrates that the post-cracking strength cannot be used as an indication of the fiber rebound in shotcrete; a high in-situ fiber content can always be obtained as long as the overall rebound is high (Eq. 2.2).

7.3.4 - Variation in Fiber Rebound with the Cement Content

In order to assess the variation in fiber rebound with the cement content, shotcrete mixes were produced at cement contents ranging from 350 to 555 kg/m^3. The results obtained are presented in Fig. 7.5a. From these data it can be seen that a correlation exists between fiber rebound and cement content (average $r^2 = 0.90$), with richer mixes leading to a lower fiber rebound. In Chapter 3, it was experimentally shown that aggregate rebound follows the same trend shown in Fig. 7.5a.

Despite the fact that a greater cement content leads to a lower fiber rebound, Fig. 7.5b shows that this does not imply a significant gain in the in-situ fiber content. This is due to the fact that, as presented in Chapter 3, a greater cement content also leads to a reduction in the overall rebound (Table 7.1). As a result, the in-situ fiber content is not greatly affected by the cement content (in accordance with Eq. 2.2). Once more, a good correlation between the in-situ fiber content obtained experimentally and using Eq. 2.2 is found (Fig. 7.5b and Table 7.1).

It should also be noticed that, despite the lower fiber rebound, because the in-situ fiber content was not affected by the cement content, the post-cracking strength remained relatively unchanged with the cement content at all midspan deflection levels (Fig. 7.5c and Fig. 7.6).

7.3.5 - Variation in Fiber Rebound with the Silica Fume Content

In order to evaluate the effect of silica fume on fiber rebound, shotcrete mixes were produced with silica fume additions ranging between zero and 16% by mass substitution to cement. The results obtained are presented in Fig. 7.7a. From these data, it can be seen that a positive correlation exists with a greater silica fume content leading to a lower fiber rebound ($r^2 = 0.75$). A comparison of trend lines from Figs. 7.5a and 7.7a reveals that a 10% silica fume addition rate for a mix having a 400 kg/m^3 binder content is as effective in reducing fiber rebound as a mix having a 550 kg/m^3 cement content.
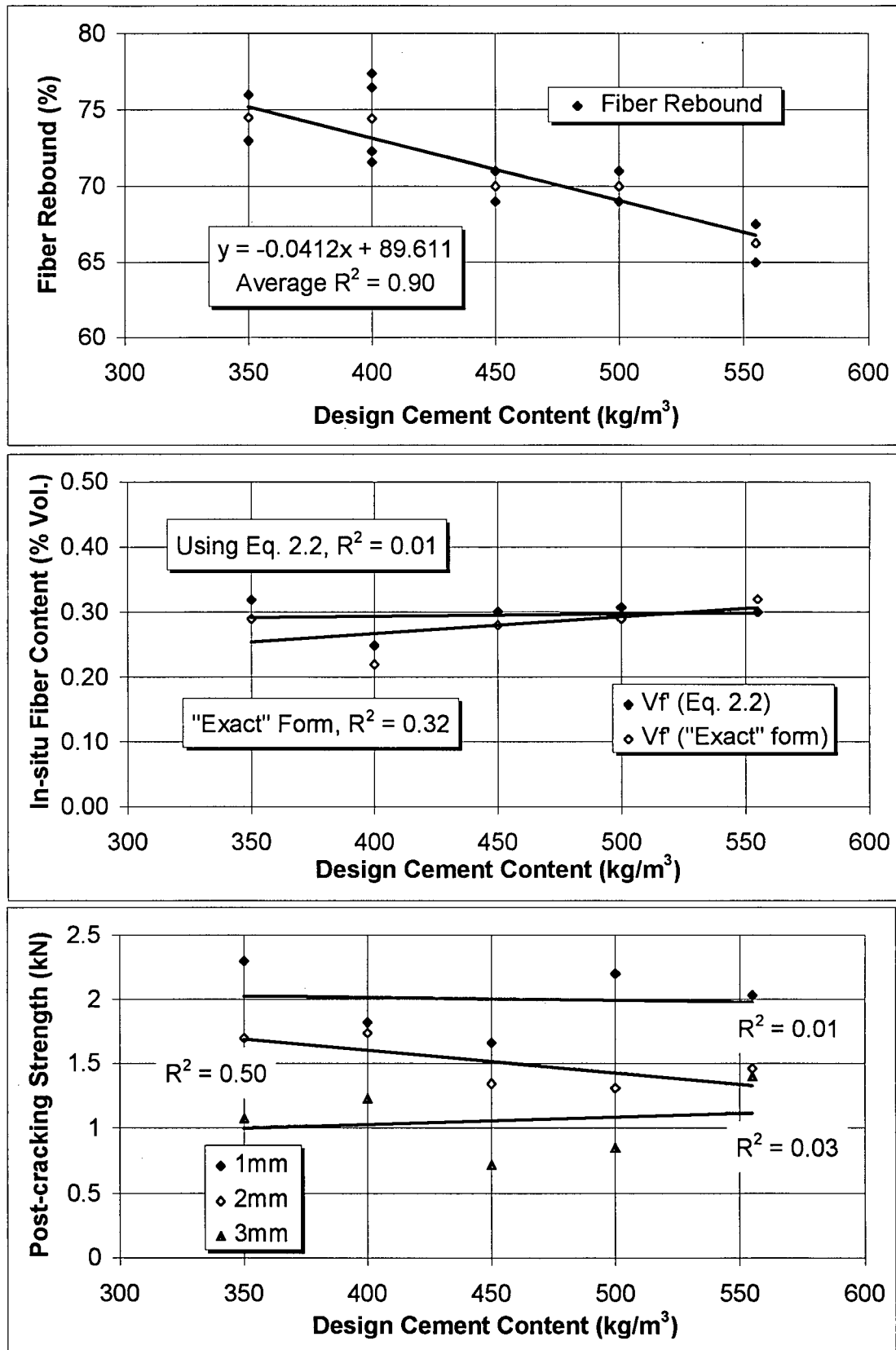
Figure 7.5 - Influence of the cement content on fiber rebound (a), in-situ fiber content (b) and post-cracking strength (c).
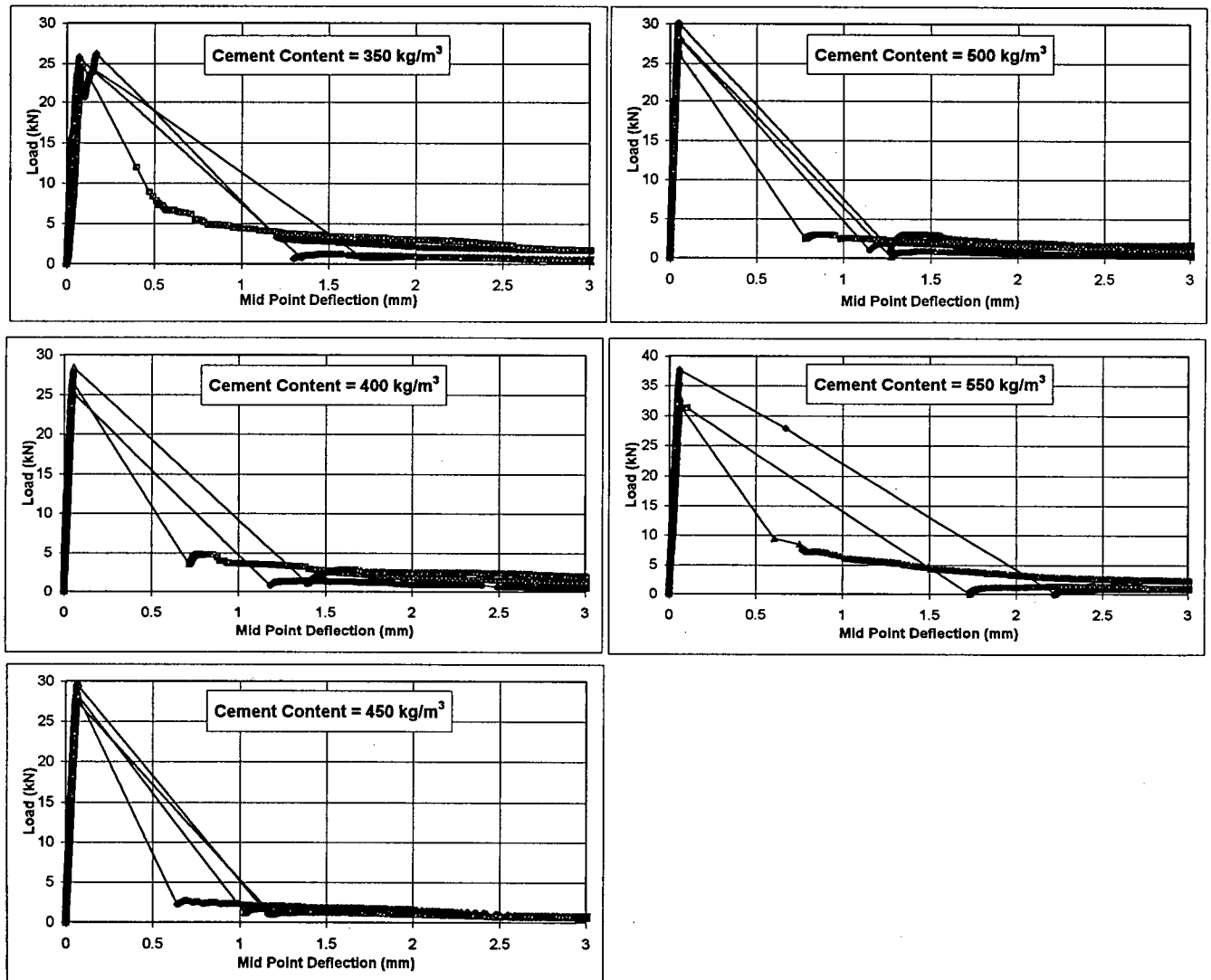
Figure 7.6 - Influence of the cement content on the flexural post-cracking behavior of fiber reinforced shotcrete (hooked fibers 50 kg/m³).
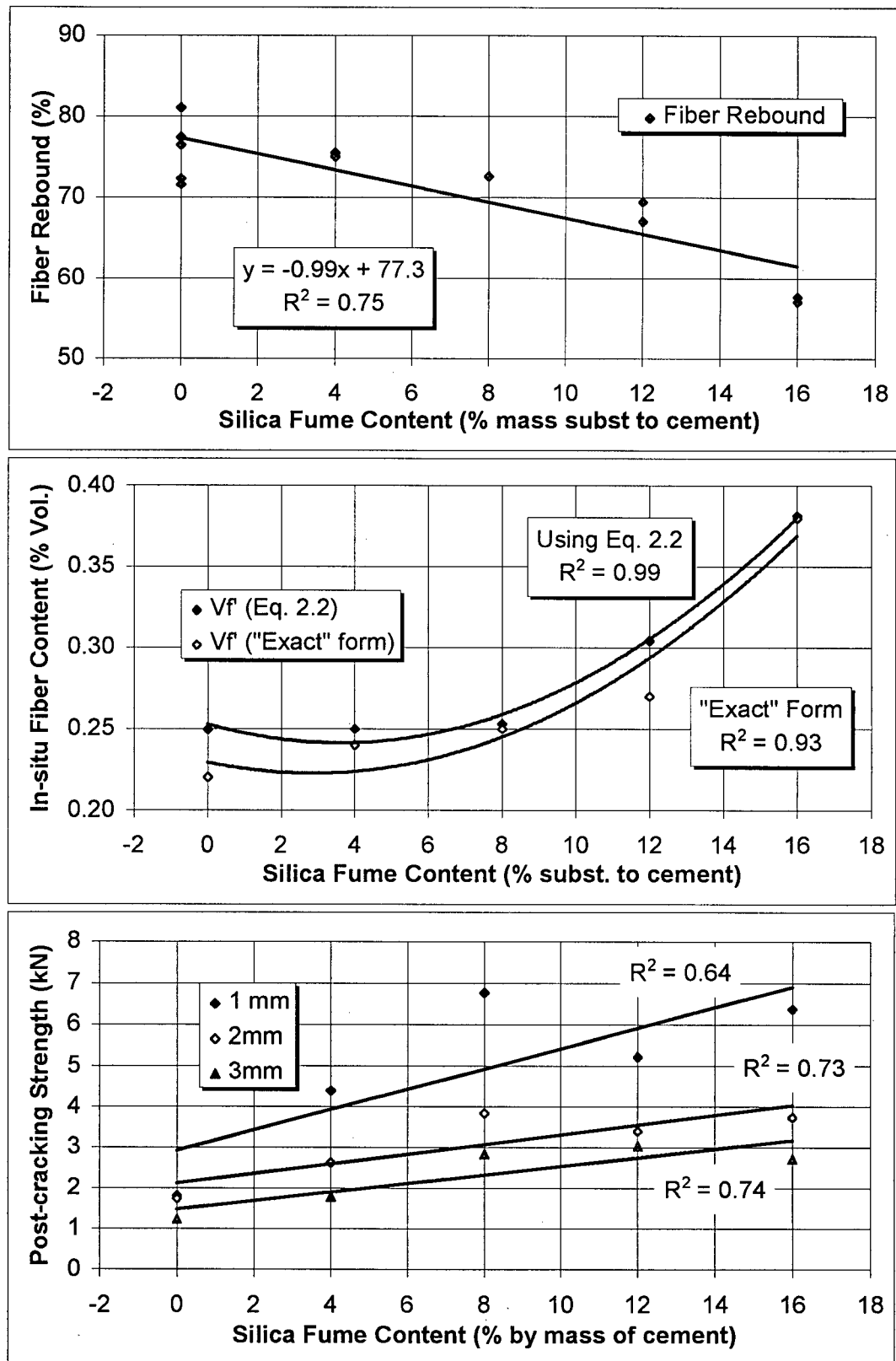
Figure 7.7 - Influence of the silica fume content on fiber rebound (a), in-situ fiber content (b) and post-cracking strength (c).
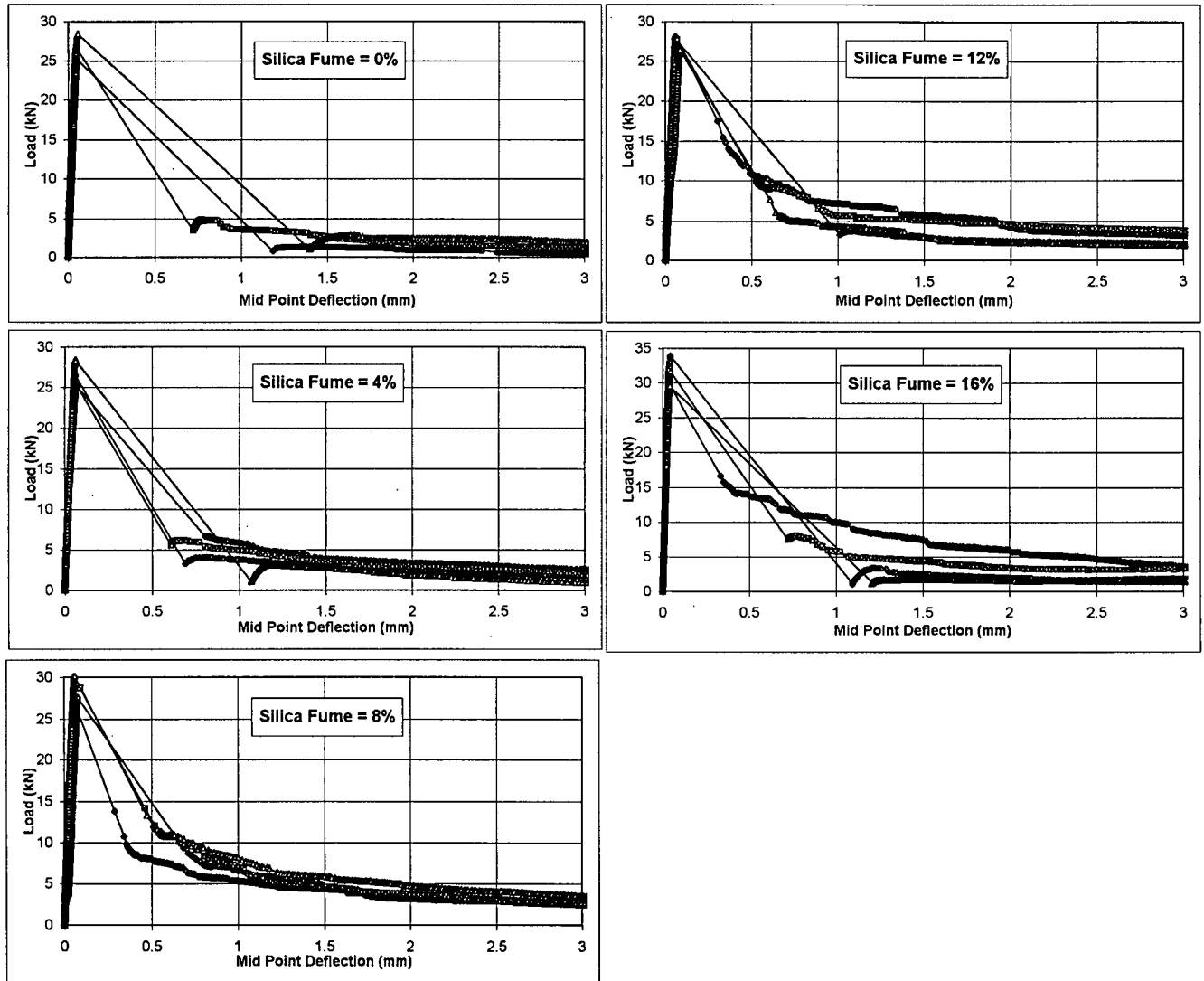
Figure 7.8 - Influence of the silica fume content on the flexural post-cracking behavior of fiber reinforced shotcrete (hooked fibers, 50 kg/m³).

Because silica fume is so effective in reducing fiber rebound, it also leads to a gain in the in-situ fiber content (Fig. 7.7b) and, consequently, an increment in post cracking strength (Fig. 7.7c and Fig. 7.8). Once more, a good agreement is found between in-situ fiber content values obtained experimentally and those estimated using Eq. 2.2 (Fig. 7.7b and Table 7.1).

7.3.6 - Variation in Fiber Rebound with the Accelerator Content

The variation in fiber rebound with the accelerating admixture content was evaluated using a commercially available powder alkaline admixture at the addition rates of zero, 0.5, 1.5, 3 and 6% by mass of cement. The results obtained are presented in Fig. 7.9a. From these data, it can be seen that, for the usual recommended addition rates of up to 3%, the accelerating admixture led to an increase in fiber rebound - most likely due to a stiffening effect on the shooting consistency. The decrease in fiber rebound observed at 6% should be considered a consequence of the large amount of shooting water that a mix with this high an admixture content requires, leading to a "softer" consistency while shooting.

As shown in Fig. 7.9b, for addition rates of up to 3%, because the accelerator admixture leads to an increase in fiber rebound, the in-situ fiber content (Fig. 7.9b) is found to decrease, increasing again at 6% due to the lower fiber rebound. Despite this fact, the post-cracking strength (Fig. 7.9c) is found to continually increase for all accelerator addition rates. This result may seem contradictory with the fiber content data in Fig. 7.9b, however it must be considered that the accelerator admixture leads to marked reductions in shotcrete strength (Table 7.1), in such a way that, at 6%, the rupture of the flexural toughness specimens occurs at a load 40% lower than at 0.5% (Fig. 7.10). This causes a much lower energy release at the moment of rupture, with a reduced post-peak instability and hence a greater post-cracking resistance.
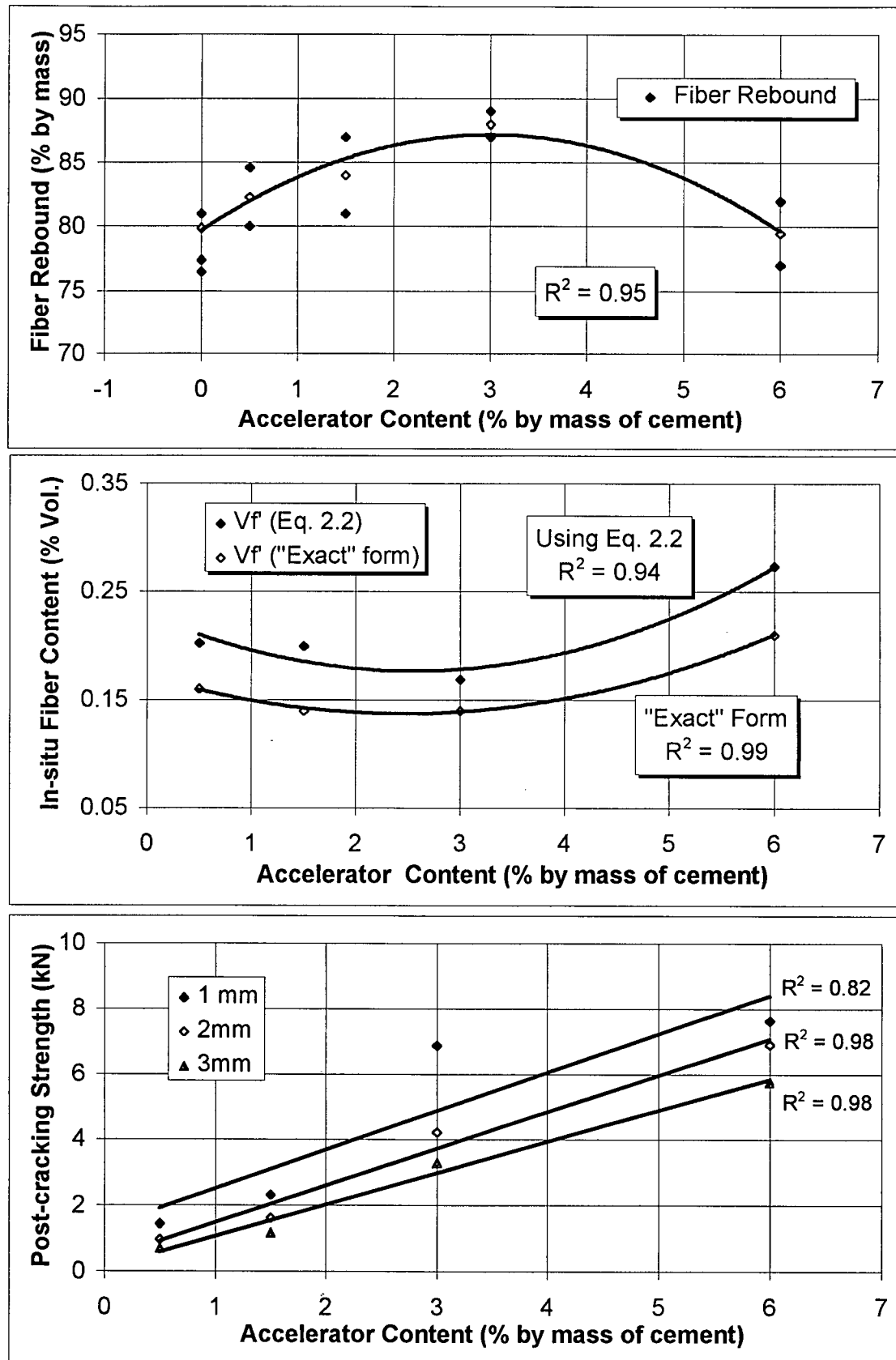
Figure 7.9 - Influence of the accelerator admixture content on fiber rebound (a), in-situ fiber content (b) and post-cracking strength (c).
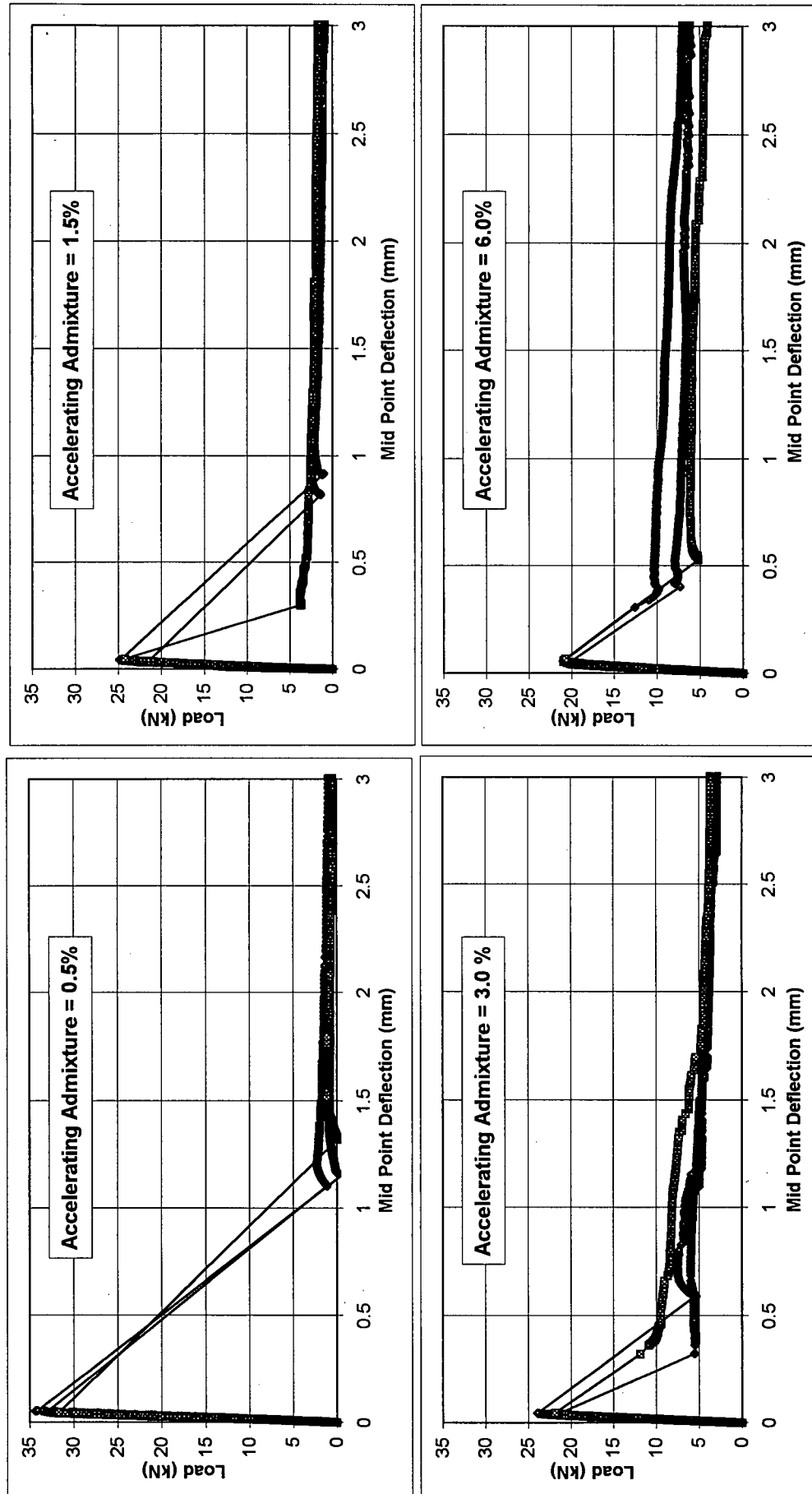
Figure 7.10 - Influence of the accelerating admixture on the flexural post-cracking behavior of fiber reinforced shotcrete (hooked fibers, 50 kg/m³).

7.3.7 - Variation in Fiber Rebound with the Fiber Content

The Variation in fiber rebound with the fiber content was examined for mixes containing 25, 50, 60 and 75 kg/m^3 of the steel fibers used (0.5 mm in diameter, 25.4 mm in length with hooked ends). Results for fiber rebound are presented in Table 7.1. These data show that no correlation between fiber content and fiber rebound was found. As will be demonstrated in Chapter 8, fiber rebound is a function of the fiber geometry and shotcrete composition and, consequently, a variation in fiber rebound with fiber content should not be expected.

Given that fiber rebound is not affected by the fiber content, Eq. 2.2 predicts a linear variation in the in-situ fiber content with the design fiber content. This is confirmed by the data presented in Fig. 7.11a, in which a linear trend line shows a good correlation ($r^2 > 0.89$) between design and in-situ fiber contents[4]. Once again, a good correspondence between experimental results for the in-situ fiber content and those obtained using Eq. 2.2 is found (Fig. 7.11a).

As a consequence of the increased in-situ fiber content, the post-cracking resistance of the flexural beams is also found to grow with the design fiber content (Fig. 7.11b and Fig. 7.12).

7.3.8 - Variation in Fiber Rebound with the Air Flow

In order to investigate the variation in fiber rebound with the air flow, the same mix was shot at air flow values ranging from 100 to 400 cfm (100 cfm = 0.05 m^3/sec) at the same shooting consistency. The results, presented in Fig. 7.13a, show that the fiber rebound tends to increase with the air flow from 62% for a 150 cfm up to 82% for 400 cfm. Very low values of air flow (100 cfm) were also found to lead to a high fiber rebound.

The low fiber rebound and high overall rebound at 150 cfm combine to lead to a high in-situ fiber content (Fig. 7.13b). With an increase in the air flow, up to 300 cfm, the fiber rebound increases as the overall rebound decreases (Table 7.1). As a result, the in-situ fiber content decreases (Fig.

---

[4] Further confirmation of the linear variation of in-situ fiber content with the design fiber content is found in item 8.3.1 where, for six mixes tested, a 50% increase in the design fiber content (from 50 to 75 kg/m^3) led to a proportional 50% increase in the in-situ fiber content.

7.13b). It should be noticed that the use of a low air flow value (below 250 cfm for a 50 mm diameter hose) should not be considered as an adequate means of obtaining a higher in-situ fiber
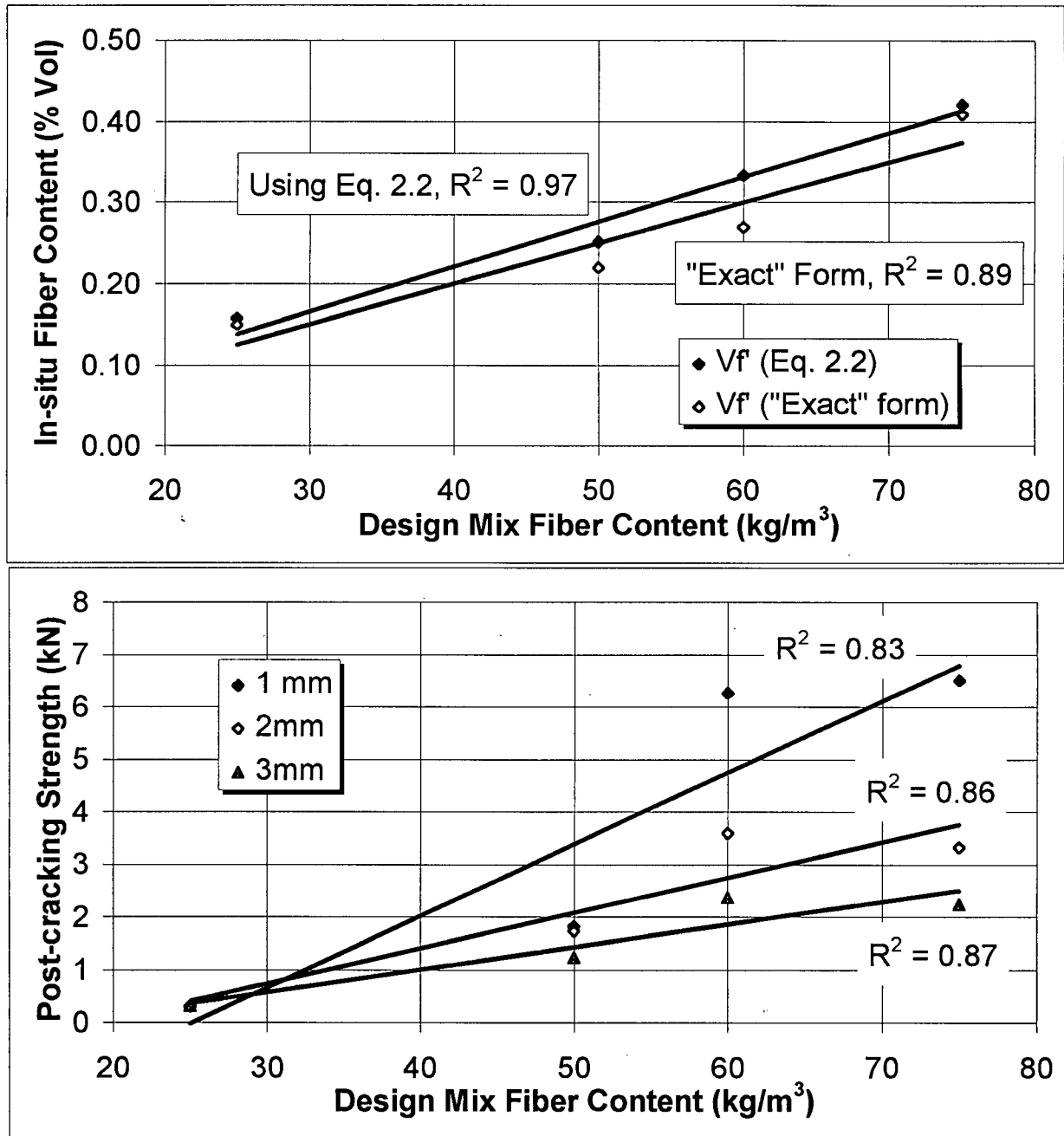
Figure 7.11 - Influence of the design mix fiber content on the in-situ fiber content (a) and post-cracking strength (b).

145
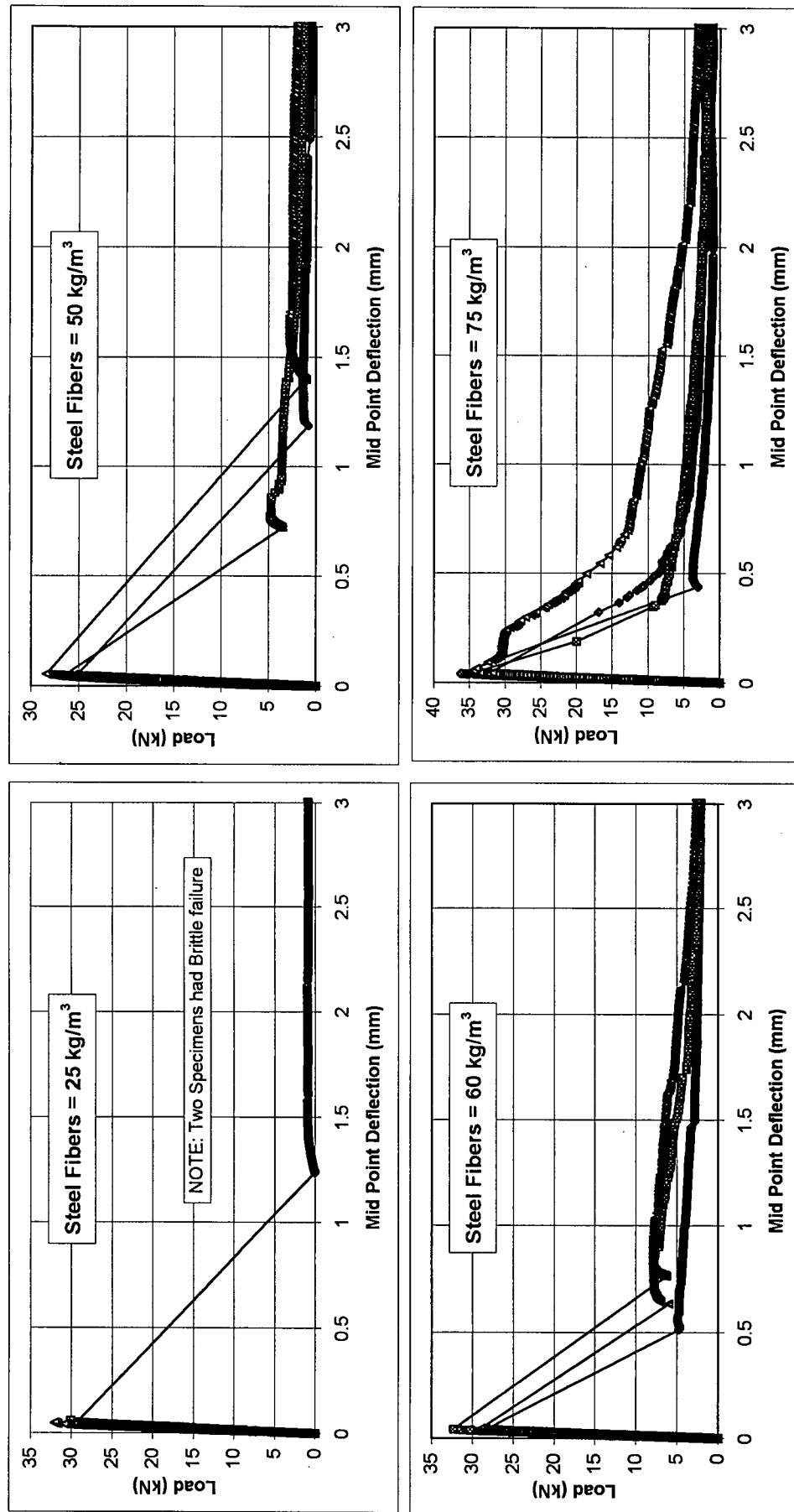
Figure 7.12 - Influence of fiber content on the flexural post-cracking behavior of fiber reinforced shotcrete (hooked fibers).
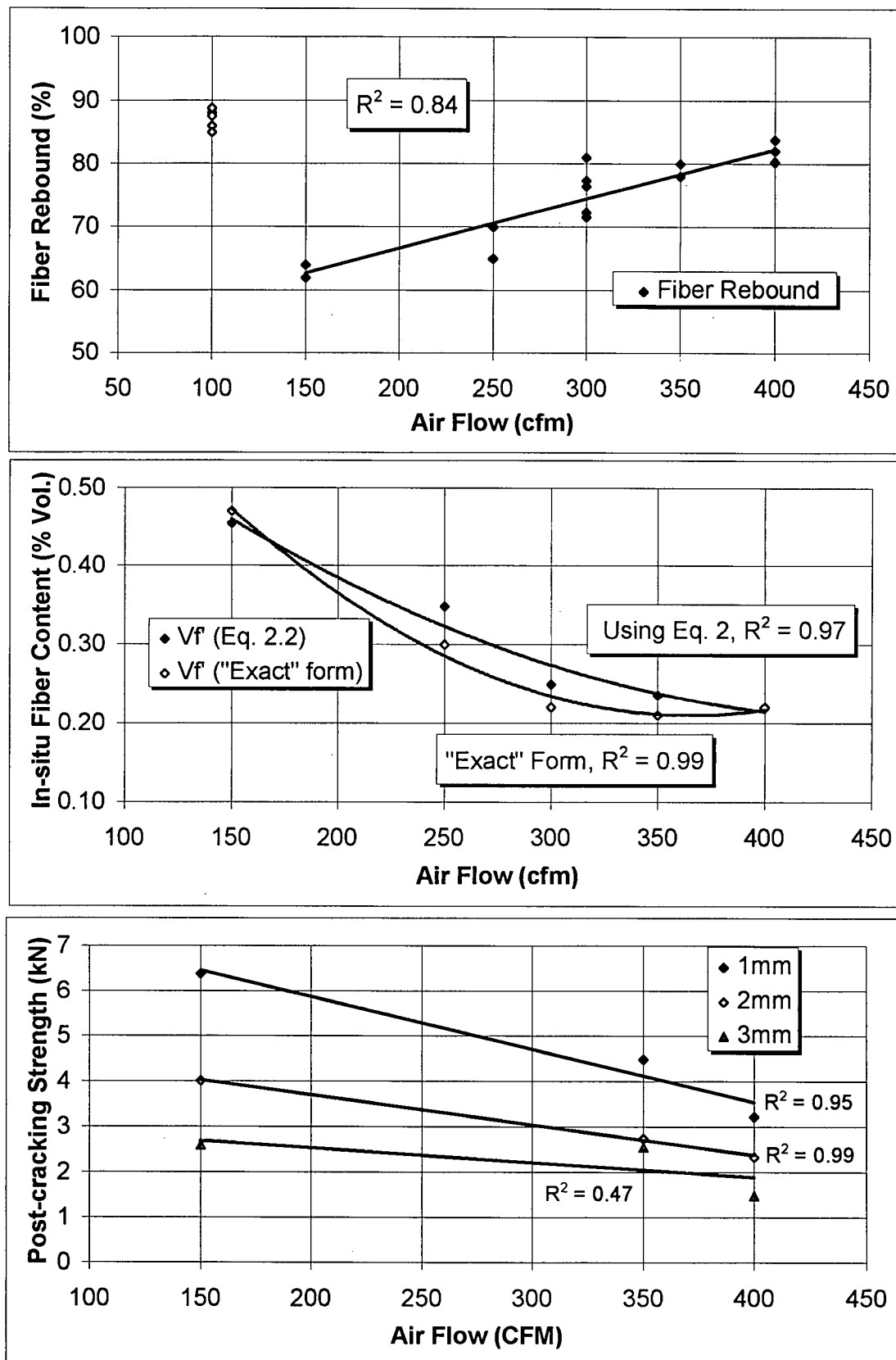
Figure 7.13 - Influence of the air flow on fiber rebound (a), in-situ fiber content (b) and post-cracking strength (c).
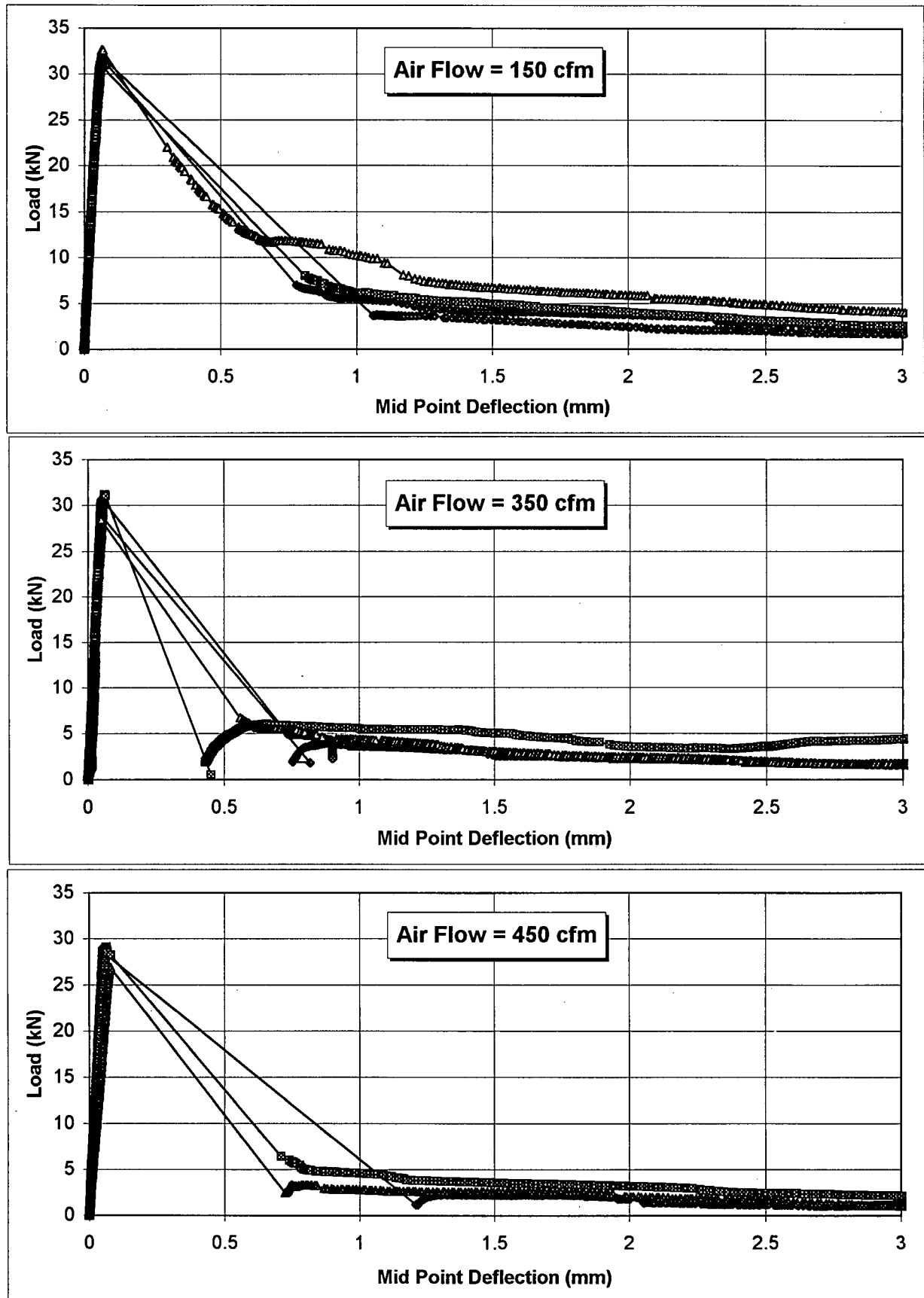
Figure 7.14 - Influence of air flow on the flexural post-cracking behavior of fiber reinforced shotcrete (hooked fibers, 50 kg/m³).

content since it does so by increasing the overall rebound. Also, Fig. 7.13b shows that too high an air flow value (above 300 cfm in this case) can lead to a significant loss in fiber content due to greater fiber rebound.

Fig. 7.13c shows that the post-cracking strength follows the trend set by Fig. 7.13b with the lower in-situ fiber contents resulting in a lower reinforcing performance (the complete flexural toughness curves are presented in Fig. 7.14).

7.3.9 - Variation in Fiber Rebound with the shooting position

The influence of the shooting position was investigated by shooting test panels on the wall and overhead positions. Also, a test panel was shot positioned on the floor and leaning against the wall, forming an angle of approximately 65 degrees with the horizon (here named as inclined position - Fig. 7.15). The latter position was included in this test series since it is often used for shooting test panels in research programs and for fiber shotcrete quality control in practice.

The results obtained for fiber rebound are shown in Fig. 7.15. This figure shows that, while a comparison between overhead and wall shooting shows similar fiber rebound values (respectively, 73 and 75%), a comparison between wall and inclined shooting shows that the latter position leads to a significantly lower fiber rebound (on average 12% lower).

This is further reflected in the post-cracking flexural toughness results presented in Fig. 7.16 where it may be noticed that the comparison between wall and inclined shooting (Fig. 7.16d) shows a significantly enhanced post-cracking load bearing capacity for the inclined case.

In an interpretation of this result, it may be said that, while for wall and overhead shooting, essentially all fibers that rebound tend to fall to the ground, in the inclined case, some of these fibers tend to fall back onto the test panel, being later covered by incoming shotcrete. Regardless of the exact cause, the main importance of this result is to show that inclined test-panel shooting (as is usually done in practice) may not lead to fiber shotcrete that is representative of the actual structure, in which shotcrete is usually sprayed on the wall and overhead positions.
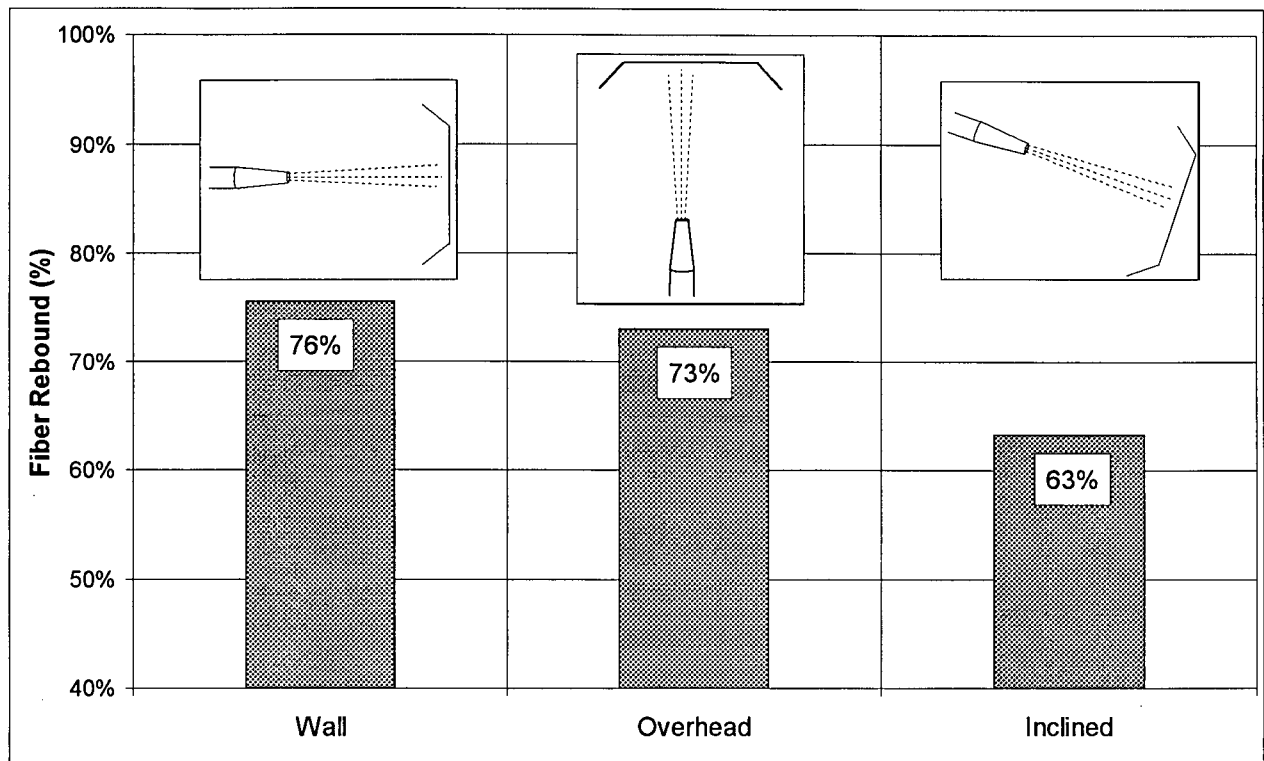
Figure 7.15 - Influence of the shooting position on steel-fiber rebound (hooked fiber).

7.4 - Conclusions

In this chapter, industrial scale shotcrete equipment was used under conditions of controlled shooting consistency and air flow, allowing for the characterization of the influence of the mix design and shooting technique on fiber rebound. More specific conclusions to be draw from this chapter are:

1) Equations 2.1 and 2.2 were extensively tested and shown to be in good agreement with the experimental data, thus proving to be a practical means for calculating fiber rebound and predicting the in-situ fiber content of shotcrete in practice.

2) A close correlation exists between fiber and overall rebound. In the usual range of dry-mix shotcrete overall rebound (between 20 and 40%) and for the steel fibers presently available in the market, fiber rebound tends to be approximately twice the overall rebound.
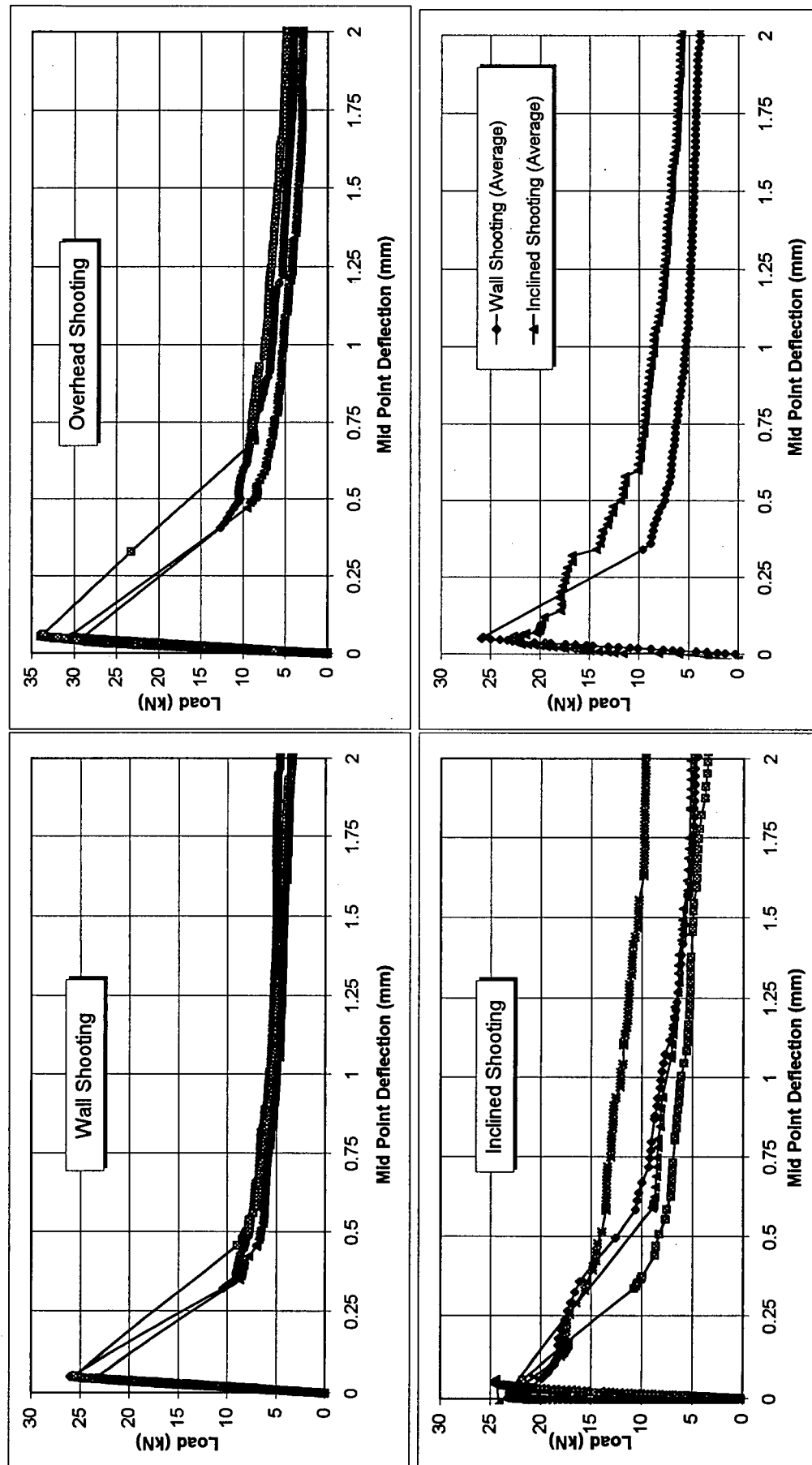
Figure 7.16 – Influence of the shooting position on the flexural post-cracking behavior of fiber reinforced shotcrete. Wall position (a), Overhead (b) inclined (c) and comparison of average responses (d),

3) The shooting consistency has a direct effect on fiber rebound, with stiffer consistencies leading to a greater fiber loss.

4) A higher cement content and the presence of silica fume were both found to decrease the fiber rebound, with silica fume proving to be the most effective and leading to a greater in-situ fiber content.

5) Both the presence of an accelerating admixture and the use of a high air flow were found to increase the fiber rebound.

6) As predicted by Eq. 2.2, the in-situ fiber content was found to increase linearly with the design fiber content.

7) The in-situ fiber content and the post-cracking reinforcing ability[5] of dry-mix shotcrete cannot be used as indicators of fiber rebound since they do not reflect the overall rebound. In order to calculate fiber rebound and in-situ fiber content Eqs. 2.1 and 2.2 should be used.

8) Although it is the most commonly used technique in practice, shooting test panels at an angle of less than 90 degrees with the horizon (inclined position) leads to a lower fiber rebound and therefore a shotcrete that may not be representative of the actual structure.

---

[5] The post crack load bearing capacity results reported throughout this thesis are relatively low compared to those generally presented in the literature. It is believed that the reasons for this are:

- The design fiber content adopted here (50 kg/m³) is 20% lower than the 60 kg/m³ generally employed.
- Most mixtures tested did not contain silica fume, leading to greater fiber rebound (section 7.3.5).
- All test panels were shot on the vertical (wall) position (section 7.3.9).
- Most mixtures tested did not contain a set accelerating admixture and, with exception to results presented in Chapter 10, all flexural toughness testing was carried out at 28 days (as opposed to 7 days). Both factors led to higher peak load in the flexural toughness test (up to 30 kN) causing greater test instability and fiber breakage.

Chapter 8 - Experimental Evaluation of Steel Fiber Rebound: Influence of Fiber Geometry

8.1 - Introduction and Objectives

As described in Chapter 2, the data presently available in the literature on the influence of the fiber geometry on fiber rebound is conflicting. While Banthia et. al. (1992) proposed that fiber rebound is determined by the "specific projected area" parameter, this was not confirmed by later studies by Peaston (1993) and Armelin & Helene (1995). Analogously, although Peaston (1993) suggested that the fiber mass determined fiber rebound, he later concluded that this was not an intervening parameter (Austin, Peaston and Robins, 1995).

Unlike aggregates, steel fibers are the result of an industrial process in which each fiber is individually manufactured with shape and dimensions as designed. Therefore, reliable data on the influence of fiber geometry on rebound is crucial if one wishes to develop a steel fiber that is optimized for dry-mix shotcrete. In fact, making use of Eq. 2.2, with an overall dry-mix shotcrete rebound between 30 and 40%, it can be shown (Fig. 8.1) that, if fiber rebound could be reduced from the 75% figure that characterizes most fibers available in the market today to 50%, the in-situ fiber content would be doubled (i.e. taking the V'_f/V_f ratio from 0.4 to 0.8 - Fig. 8.1) with a direct effect on the toughness performance of the composite.

Therefore, the objective of this chapter was to investigate the influence of steel fiber shape and geometry (diameter and length) on fiber rebound in dry-mix shotcrete. The information generated will be used in Chapter 10 to develop a fiber geometry of enhanced toughness performance for dry-mix shotcrete.

8.2 - Material and Methods

Experimental procedures used throughout this chapter were identical to those described in item 7.2 (same shooting equipment, mix proportions and shooting conditions). Analogously, fiber rebound was evaluated in "exact" form (Eq. 7.1) using the same procedures described in item 7.2.

Cylindrical steel fibers were produced especially for this study by cutting steel wire of different diameters into the desired length (16 diameter/length combinations were tested in a total of 25 test panels). Also, Three commercially available steel fiber geometries were used. The fiber shapes tested are described in Table 8.1. Procedures regarding the number of replicate specimens and the age of testing, were identical to those described in item 7.2.
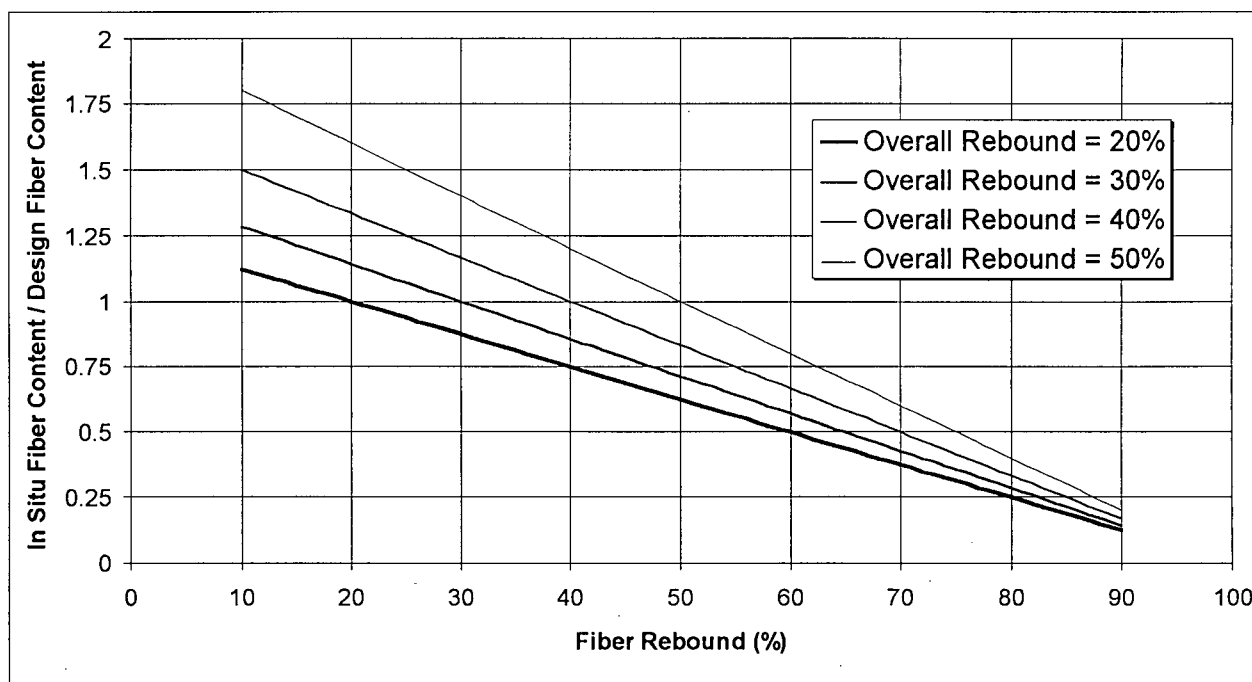
Figure 8.1 - Variation in fiber retention (V'_f/V_f) with the overall rebound (R) and fiber rebound.
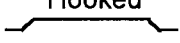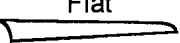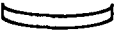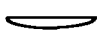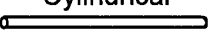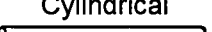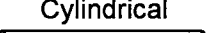
8.3 - Results and Analysis

8.3.1 - Variation in Fiber Rebound with Fiber Shape

In order to evaluate the influence of fiber shape on fiber rebound, three commercially available steel fibers, with similar length but widely different shapes, were tested at two different fiber contents (50 and 75 kg/m^3). The fiber shapes tested (flat, flat-crimped and hooked) are shown in Table 8.1. The results obtained for the fiber rebound are presented in Fig. 8.2a as calculated in "exact" form using Eq. 7.1. These data show that no significant correlation was found between fiber shape (flat versus cylindrical) and fiber rebound, with all six cases tested showing a 70 to 80% fiber loss. From Fig. 8.2a it should be noticed that the fiber content also did not show any

effect on fiber rebound. Fiber rebound is a function of fiber geometry (as will be shown in this chapter) and shotcrete composition (Chapter 7), and therefore a percentage variation in fiber rebound with the design fiber content should not be expected (as previously shown in item 7.3.7).

Table 8.1 - Shape and dimensions of the steel fibers tested.

Shape	Cross Section*	Length
Hooked	$\bigcirc$ D = 0.5	25.4
Flat	t = 0.4, w = 2.7	32
Flat-Crimped	t = 0.6, w = 2	25.4
Cylindrical	$\bigcirc$ D = 0.50	3, 12.5, 25.4** and 40
Cylindrical	$\bigcirc$ D = 0.61	25.4
Cylindrical	$\bigcirc$ D = 0.65	25.4
Cylindrical	$\bigcirc$ D = 0.76	25.4
Cylindrical	$\bigcirc$ D = 0.89	12.5, 19, 25.4 and 40
Cylindrical	$\bigcirc$ D = 1.0	3, 12.5, 25.4 and 40

*Drawings are not to scale. D, t and w = diameter, thickness and width in mm.

** Hooked fiber

In-situ fiber content results are presented in Fig. 8.2b and Table 8.2 as calculated from the 4 kg washout samples. As shown by this data, for both fiber contents tested, the fiber shape (flat or cylindrical) had no significant effect on the in-situ fiber content. Given that all six test panels showed similar overall rebound, the fact that all fiber shapes showed similar in-situ fiber contents is a consequence of the fact that they all had similar fiber rebound values (as shown by Eq. 2.2). The fact that the greater initial fiber content led to a proportionally greater in-situ fiber volume fraction is also a consequence of Eq. 2.2, as explained in item 7.3.7.

Finally, with respect to the post-cracking strength and flexural toughness performance, in Fig. 8.2c it can be seen that, despite the fact that all fiber shapes showed a similar in-situ fiber content,
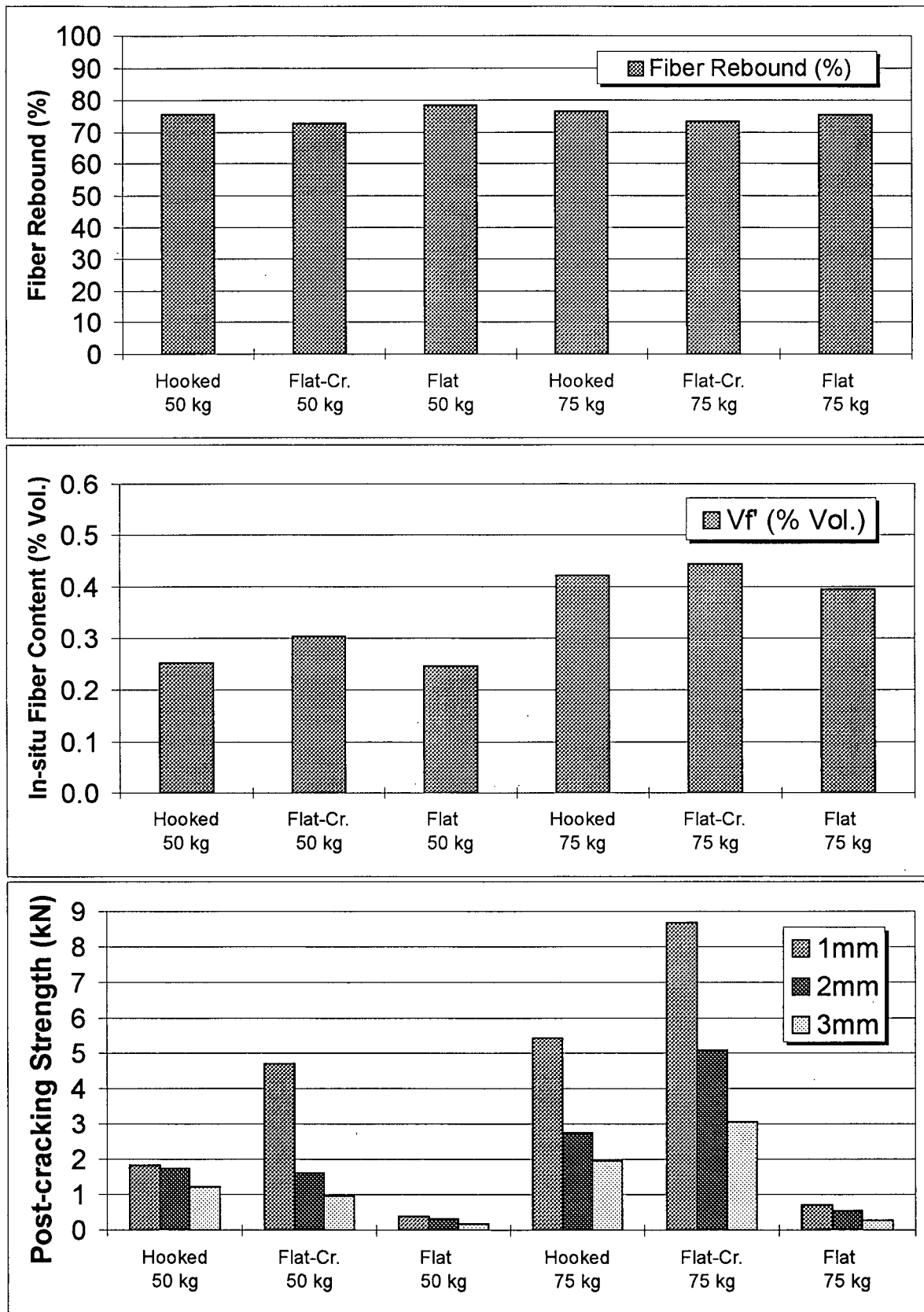
Figure 8.2 - Influence of fiber shape on fiber rebound (a), in-situ fiber content (b) and post-cracking flexural strength at three different levels of midspan deflection (c).
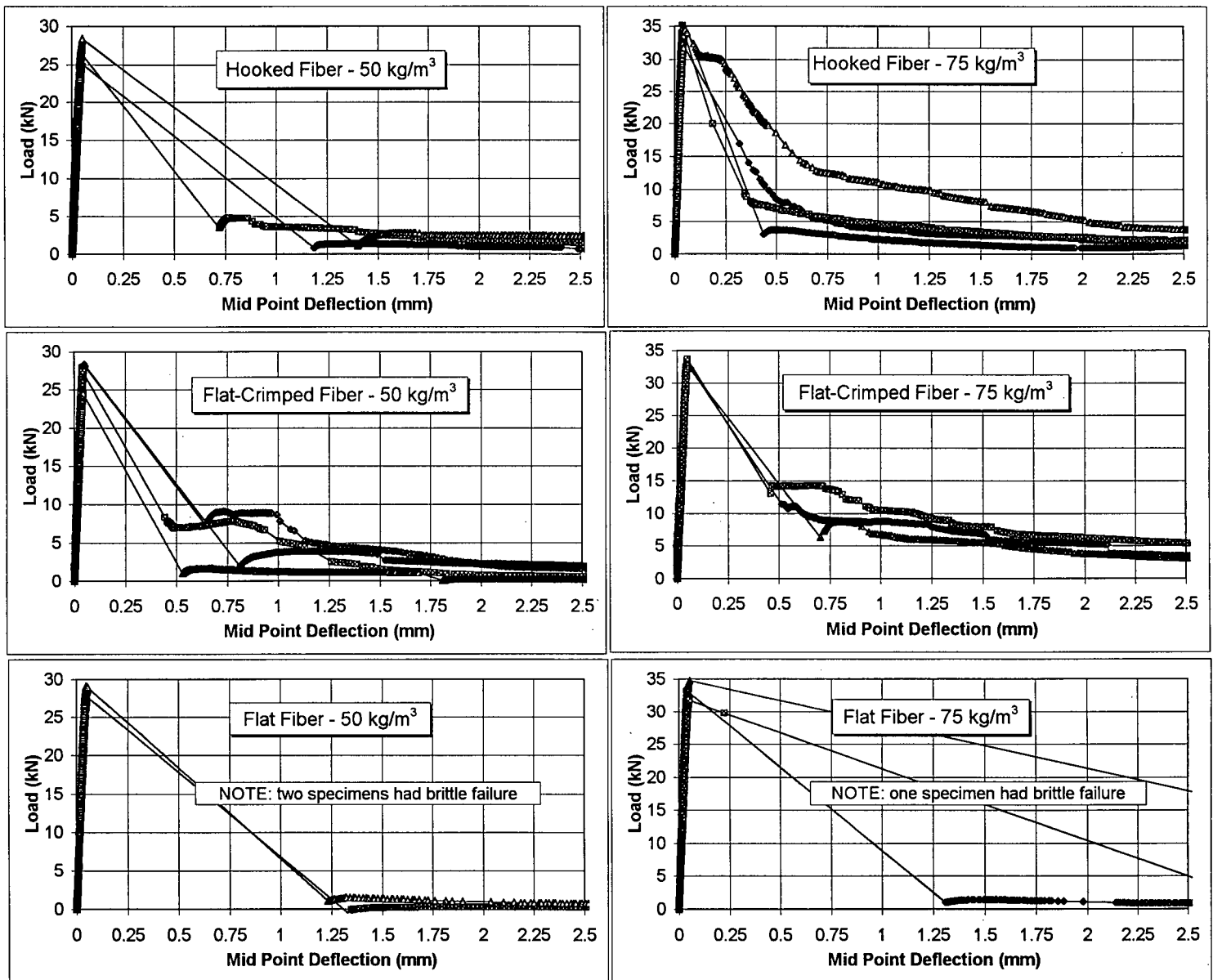
Figure 8.3 - Influence of fiber shape and content on the flexural post cracking behavior of steel fiber reinforced shotcrete.

Table 8.2 - Average numerical results obtained for the various shotcrete mixtures produced.

FiberType (mm)	Fiber Content (kg/m³)	Shooting Consistency (MPa)	Overall Rebound (%)	Fiber[a] Rebound (%)	In-situ fiber[b] Content (%)	Void Volume (%)	28d Comp. Str. (MPa)
Hooked	50	2.0	37.4	75.5	0.25	11.7	74.6
Flat-Crimped	50	2.0	43.1	72.0	0.31	10.9	69.4
Flat	50	2.0	44.0	77.6	0.25	11	60.5
Hooked	75	2.5	43.4	77.4	0.41	12.3	67.9
Flat-Crimped	75	2.0	42.6	73.3	0.45	12.3	66.5
Flat	75	2.0	40.4	75.4	0.40	12.2	65.8
D = 0.5, lf = 3	50	2.0	42.5	35.4	0.60	10.8	45.4
D = 0.5, lf = 12.5	50	2.0	43.5	60.2	0.41	11.4	63.9
D = 0.5, lf = 25.4	50	2.0	37.4	75.5	0.25	11.7	74.6
D = 0.5, lf = 40	50	1.2	39.3	91.0	0.09	16.1	48.3
D = 0.89, lf = 12.5	60	2.0	32.5	46.0	0.64	11.8	55.6
D = 0.89, lf = 19	60	2.0	31.0	59.0	0.43	12.4	63.6
D = 0.89, lf = 25.4	60	2.0	35.1	68.0	0.37	11.7	54.1
D = 0.89, lf = 40	60	2.0	31.0	86.0	0.16	12	52.1
D = 1.0, lf = 3	60	2.0	44.1	35.3	0.86	15.4	51.4
D = 1.0, lf = 12.5	60	2.0	43.5	52.4	0.65	15.4	48.8
D = 1.0, lf = 25.4	60	2.5	41.4	56.3	0.61	14.5	56.3
D = 1.0, lf = 40	60	2.0	41.7	73.4	0.39	15.1	56.4
D = 0.5, lf = 25.4	60	2.2	43.9	75.5	0.28	13.5	57.3
D = 0.61, lf = 25.4	60	-	37.6	74.3	0.28	12.0	60.2
D = 0.65, lf = 25.4	60	-	37.0	71.7	0.32	12.4	60.2
D = 0.76, lf = 25.4	60	2.0	41.5	70.4	0.38	12.9	55.0
D = 0.89, lf = 25.4	60	2.0	35.1	68.0	0.37	11.7	54.1
D = 1.0, lf = 25.4	60	2.5	41.4	56.3	0.61	14.5	56.3

a - Experimentally determined from the fiber masses collected from shotcrete and rebound (exact form, Eq. 7.1)
b - Experimentally determined from the fiber mass collected from shotcrete.

their reinforcing performance was quite varied depending on the reinforcing ability of each fiber. Therefore, from the flexural toughness test results presented in Fig. 8.3 it can be seen that, while the flat-crimped and hooked fibers showed a relatively good reinforcing capacity (especially at 75 kg/m³), the flat fiber shape exhibited almost brittle failures even at a high addition rate (75 kg/m³).

8.3.2 – Variation in Fiber Rebound with Fiber Length

In order to test the variation in fiber rebound with length, steel wire (diameters of 0.5, 0.89 and 1.0 mm) was cut into lengths of 3, 12.5, 19, 25.4 and 40 mm and shot into test panels. All fiber shapes were straight, undeformed lengths of wire, except for the 0.5 mm diameter, 25.4 mm length for which the hooked fibers were used.

The results obtained for the variation in fiber rebound with length are presented in Fig. 8.4. These data show a significant influence of fiber length on rebound (r^2 greater than 0.90 for all fiber diameters tested) with shorter fibers tending to rebound at 35 to 40% while the longer fibers showed a 75 to 90% rebound.

The overall rebound for all test panels produced in this series was approximately constant within each fiber diameter tested (Table 8.2). Therefore, as a consequence of the reduced fiber rebound, the shorter fiber lengths showed an in-situ fiber content (Fig. 8.5) two to six times greater than the longest fibers, in accordance with Eq. 2.2 and Fig. 8.1.

It is commonly accepted that the flexural toughness of fiber reinforced concrete is proportional to the ratio $V_f \cdot \dfrac{l_f}{\phi}$. Therefore, *for a fixed design fiber content*, the post-cracking strength is proportional to the fiber length, with longer fibers leading to greater post-cracking resistance. However, as shown in Fig. 8.6, in the case of dry-mix shotcrete, because of the lower fiber rebound for smaller lengths, this is not necessarily true. In Fig. 8.6, it can be seen that an optimum fiber length of 25 to 30 mm is found for both fiber diameters tested (the complete flexural toughness curves are presented in Figs. 8.7 and 8.8).
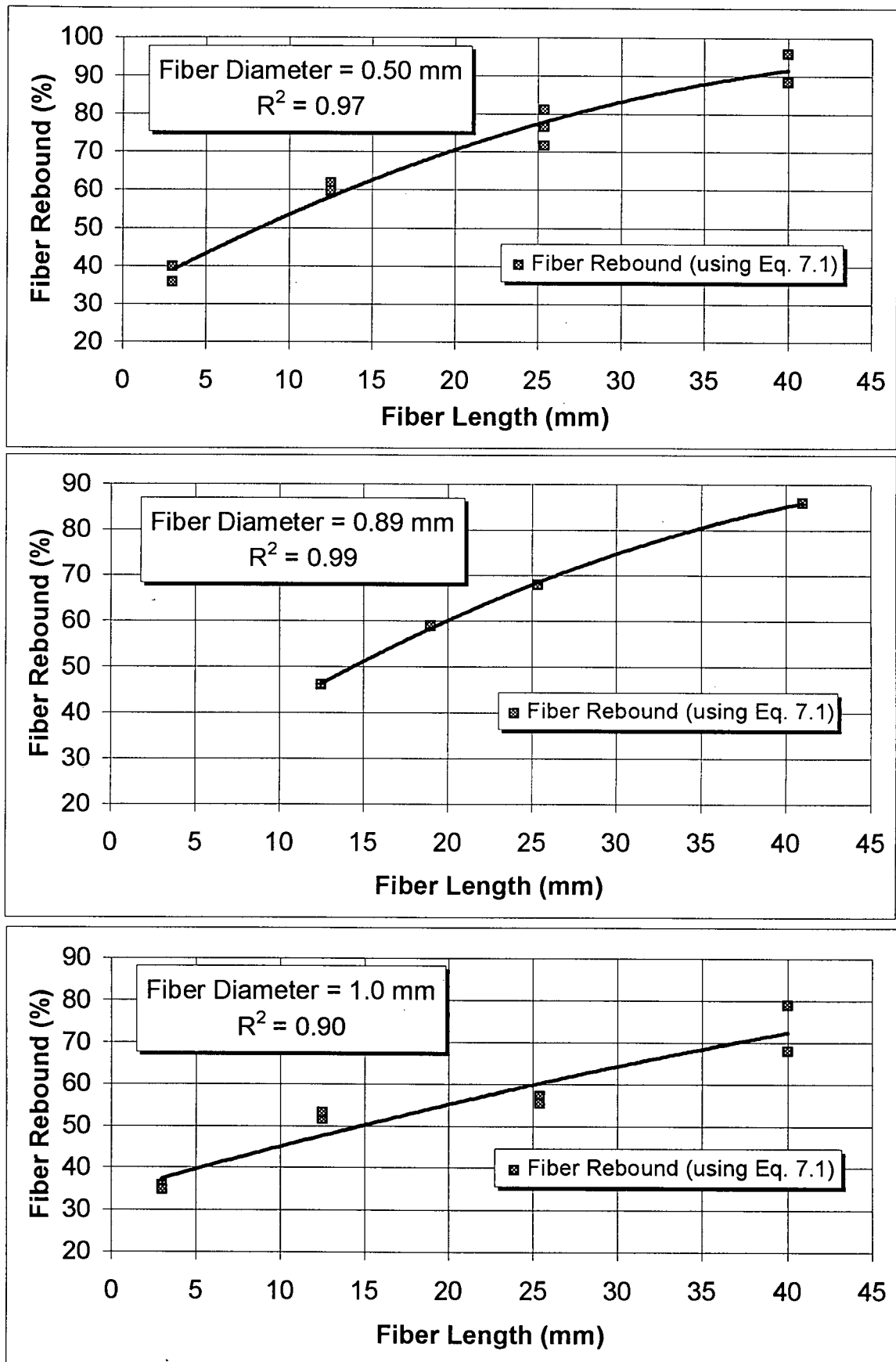
Figure 8.4 - Variation in fiber rebound with length at three different fiber diameters.
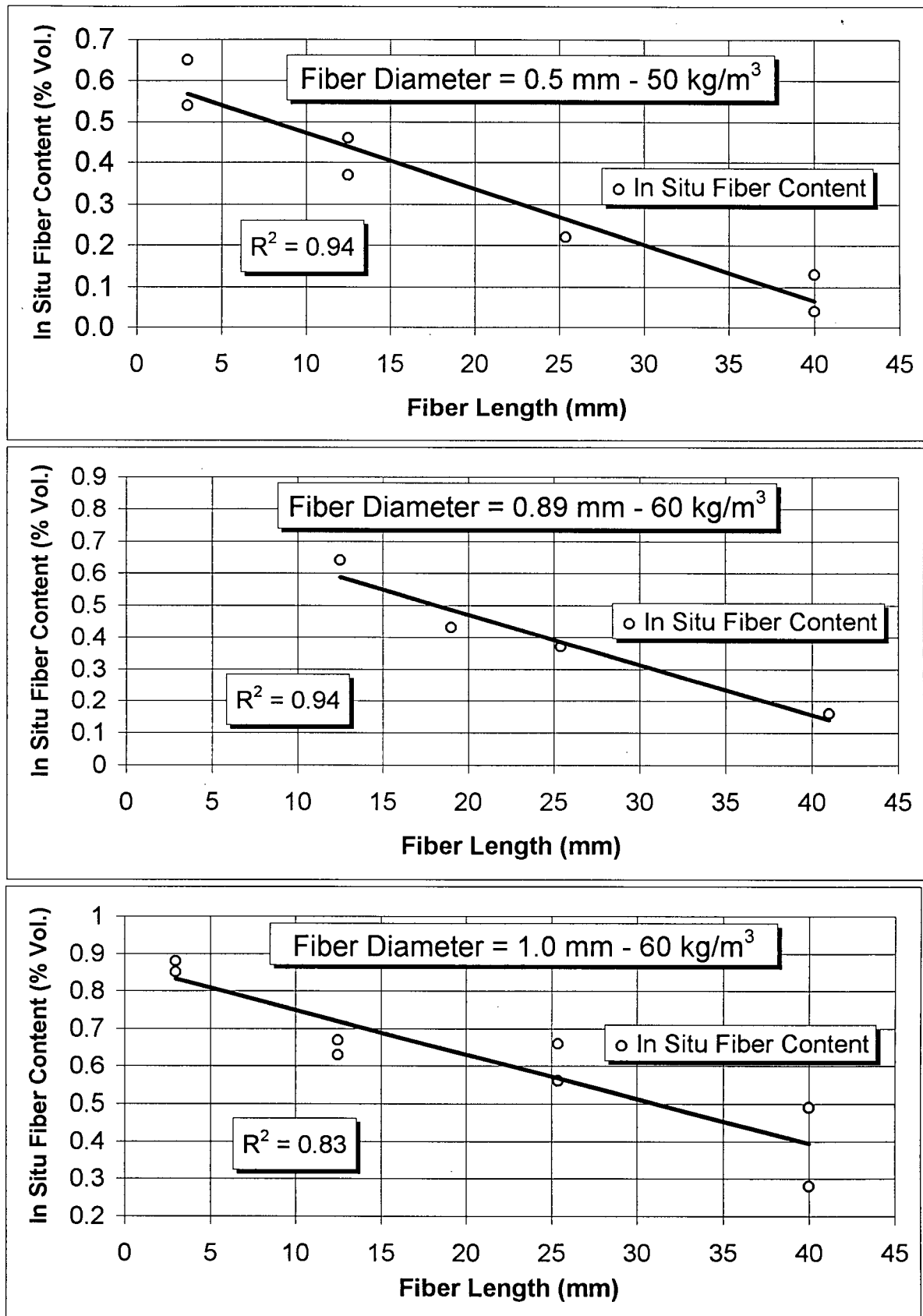
Figure 8.5 - Variation in in-situ fiber content with fiber length for three different fiber diameters.
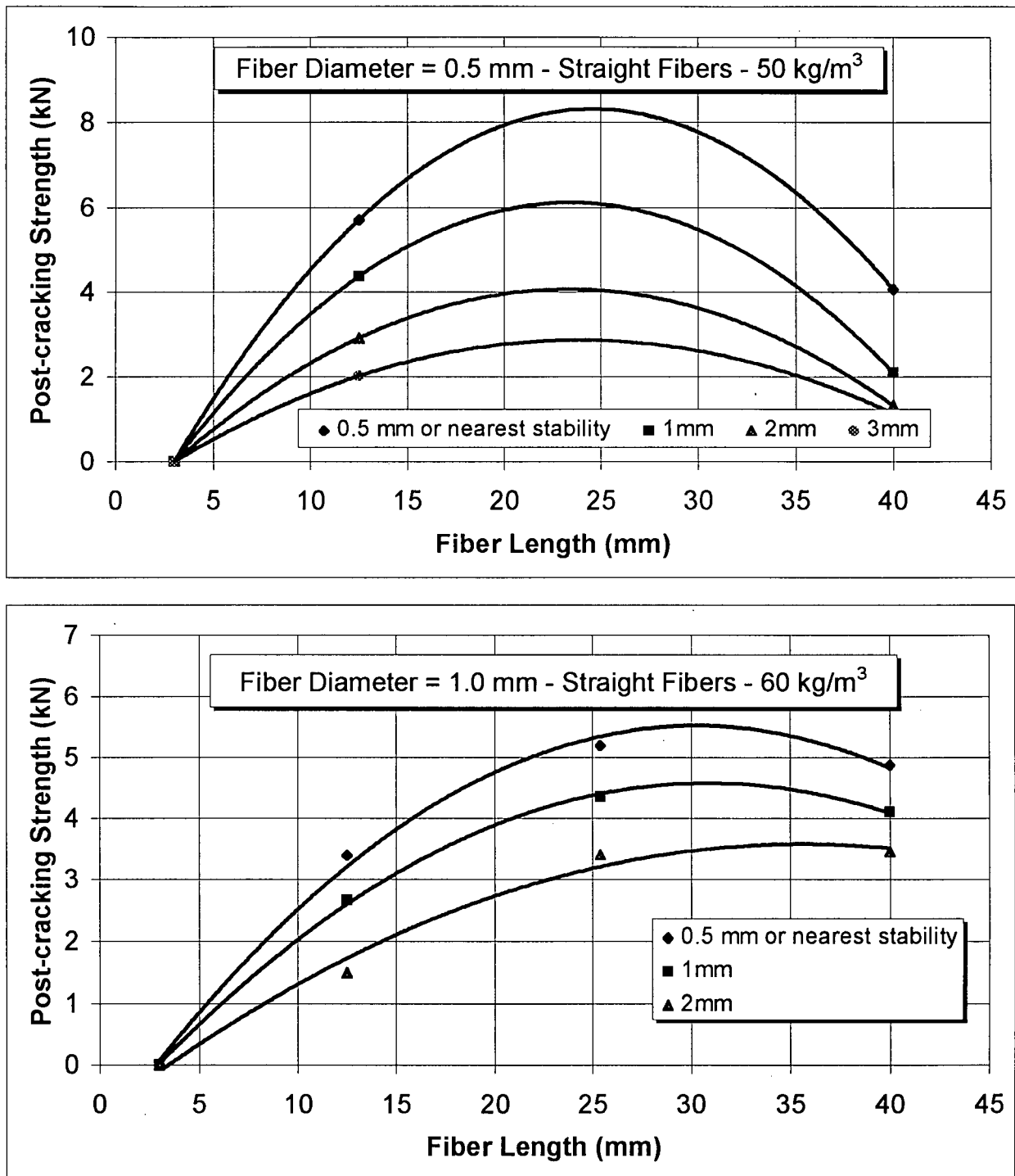
Figure 8.6 - Variation in post-cracking flexural strength with fiber length at two different fiber diameters (undeformed fibers). Each curve represents a given midspan deflection as shown in the legend.
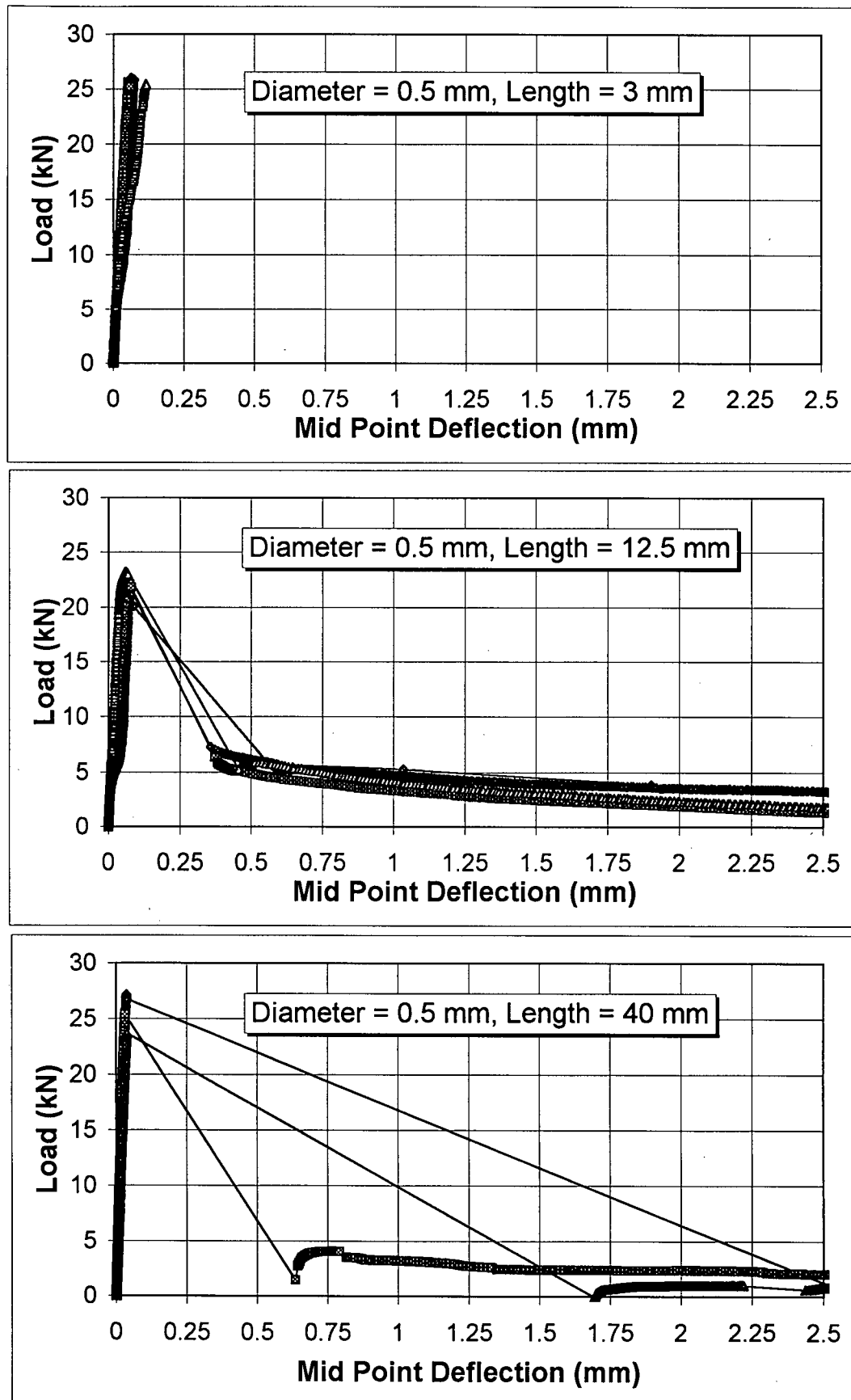
Figure 8.7 - Variation in flexural post-cracking behavior with fiber length for
0.5 mm diameter straight fiber (50kg/m^3).
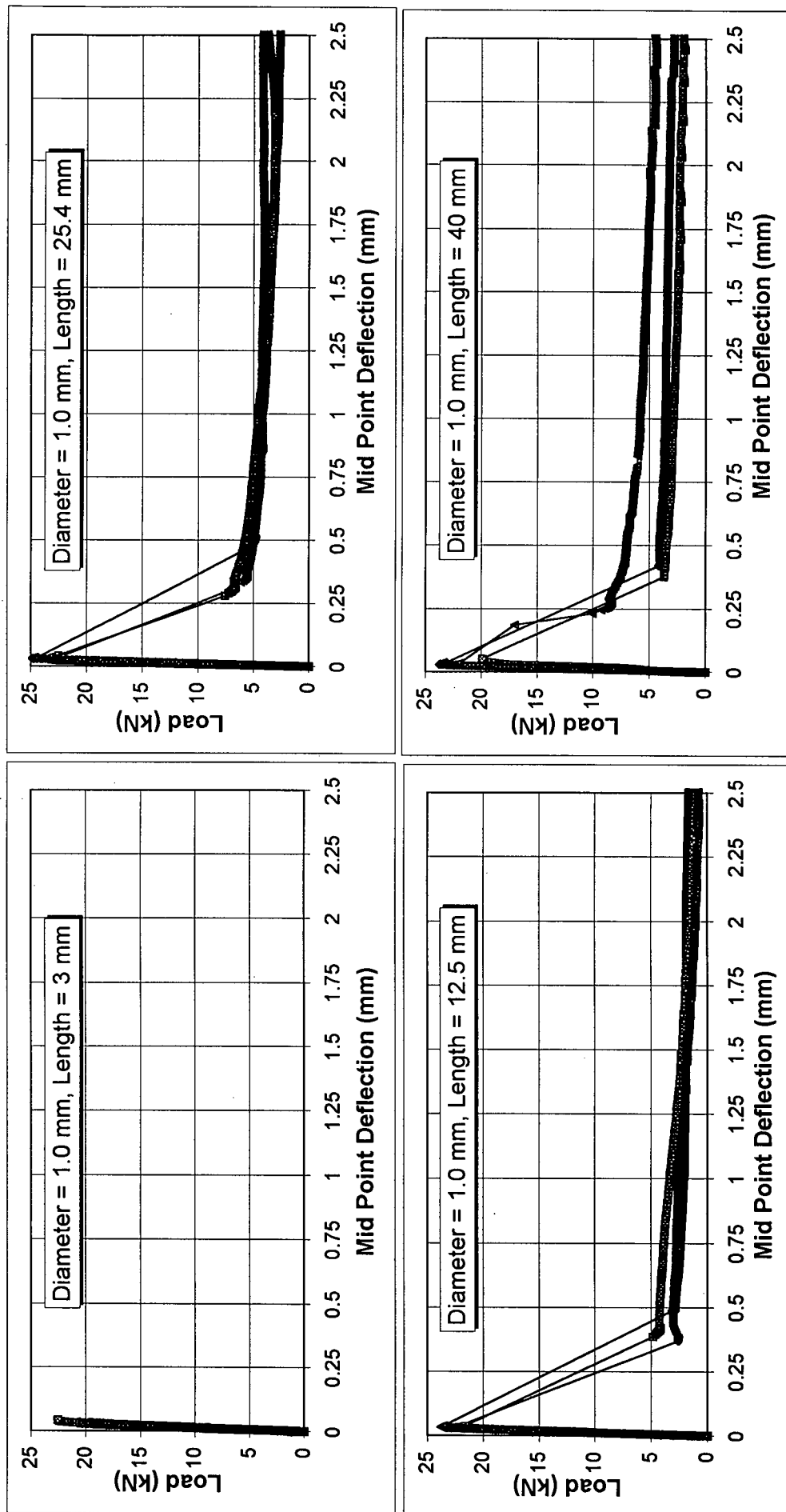
Figure 8.8 - Variation in flexural post-cracking behavior with fiber length for 1.0 mm diameter straight fiber (60kg/m³).

8.3.3 - Variation in Fiber Rebound with Fiber Diameter

In order to test the variation in fiber rebound with fiber diameter, in addition to the hooked fibers (25.4 mm long, 0.5 mm in diameter) another five undeformed fiber geometries were tested, all 25.4 mm in length, diameters of 0.61, 0.65, 0.76, 0.89 and 1.0 mm. The fiber rebound results obtained are presented in Fig. 8.9a. These data show that there is a correlation between fiber rebound and diameter ($r^2 = 0.95$), with a greater diameter leading to less fiber rebound.

As a result of the reduced fiber rebound, the data obtained for the in-situ fiber content show (Fig. 8.9b) that a greater fiber diameter tends to lead to a greater in-situ fiber content. Therefore, Fig. 8.9b shows that the in-situ fiber content doubled going from 0.5 to 1 mm diameter (the lower in-situ fiber content for the 0.89 mm diameter is due to the lower overall rebound that characterized this panel - 30% against 40% for all other cases - Table 8.2).

In Fig. 8.10, a comparison of flexural toughness results obtained for the 0.5 and 1.0 mm diameter fibers shows that, because the 1.0 mm diameter fiber resulted in double the in-situ fiber content, its post cracking strength is comparable to the 0.5 mm diameter, hooked case, despite the fact that its fibers contain no deformations (i.e. straight fiber).

8.3.4 - Variation in Fiber Rebound with the Aspect Ratio

Given that both the fiber length and diameter were found to influence fiber rebound, the hypothesis that the aspect ratio is a general parameter determining fiber rebound was tested for cases of fiber diameter equal to 0.50, 0.61, 0.65, 0.76, 0.89 and 1.0 mm at lengths of 3, 12.5, 19, 25.4 and 40 mm. The results obtained are shown in Fig. 8.11 and show that the fiber rebound linearly correlates ($r^2 = 0.92$) with a fiber aspect ratio given by the fiber length divided by the square root of the diameter.

Considering that the steel fibers commonly used in shotcrete today are usually about 0.5 mm in diameter and 25 mm in length ($l_f / \sqrt{\phi} = 36$ mm$^{-0.5}$), Fig. 8.11 shows that steel fiber rebound in dry-mix shotcrete could be reduced significantly if fibers of a lower aspect ratio were to be used.
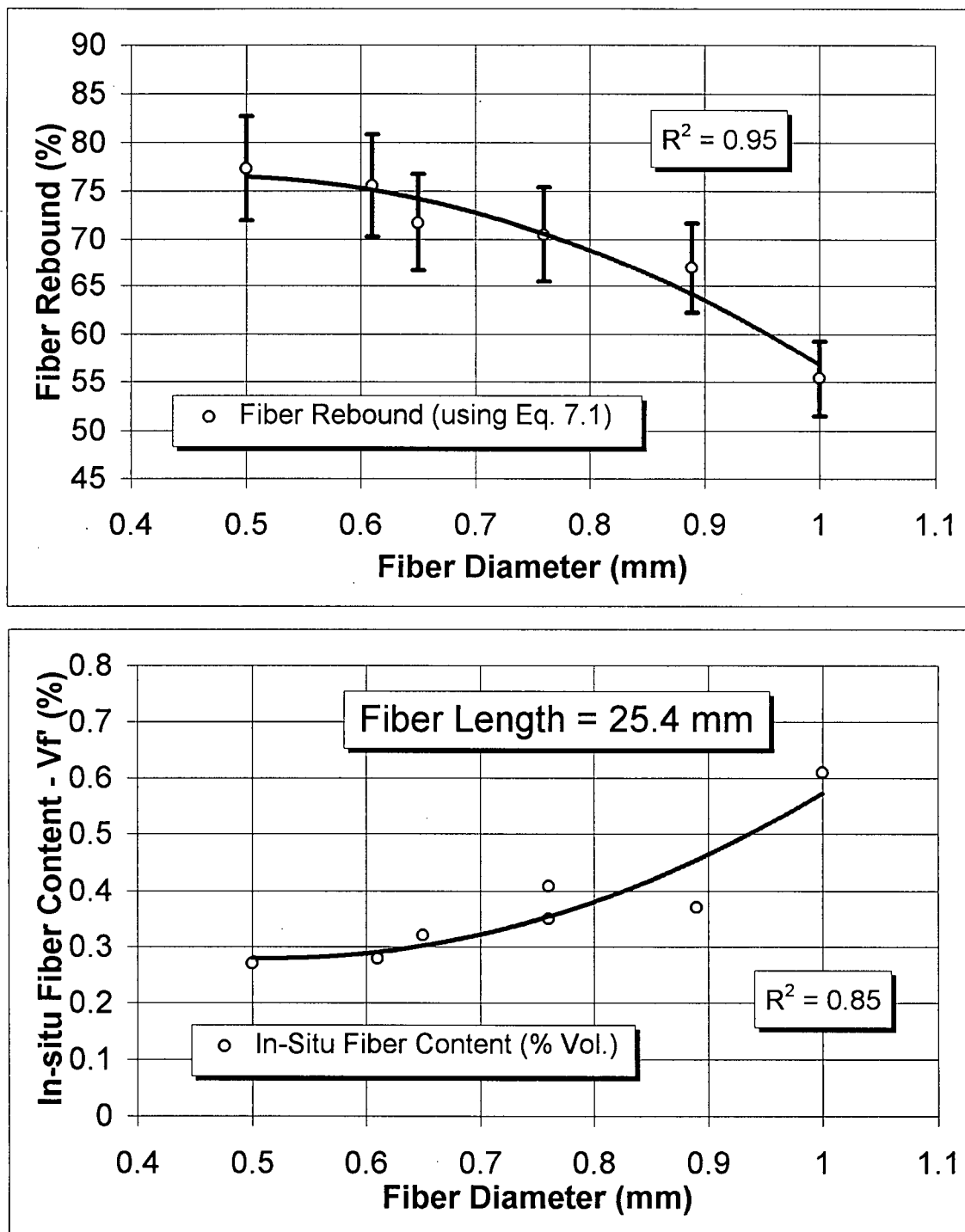
Figure 8.9 - Influence of fiber diameter on steel fiber rebound (a) and in-situ fiber content (b) for a 25.4 mm fiber length.
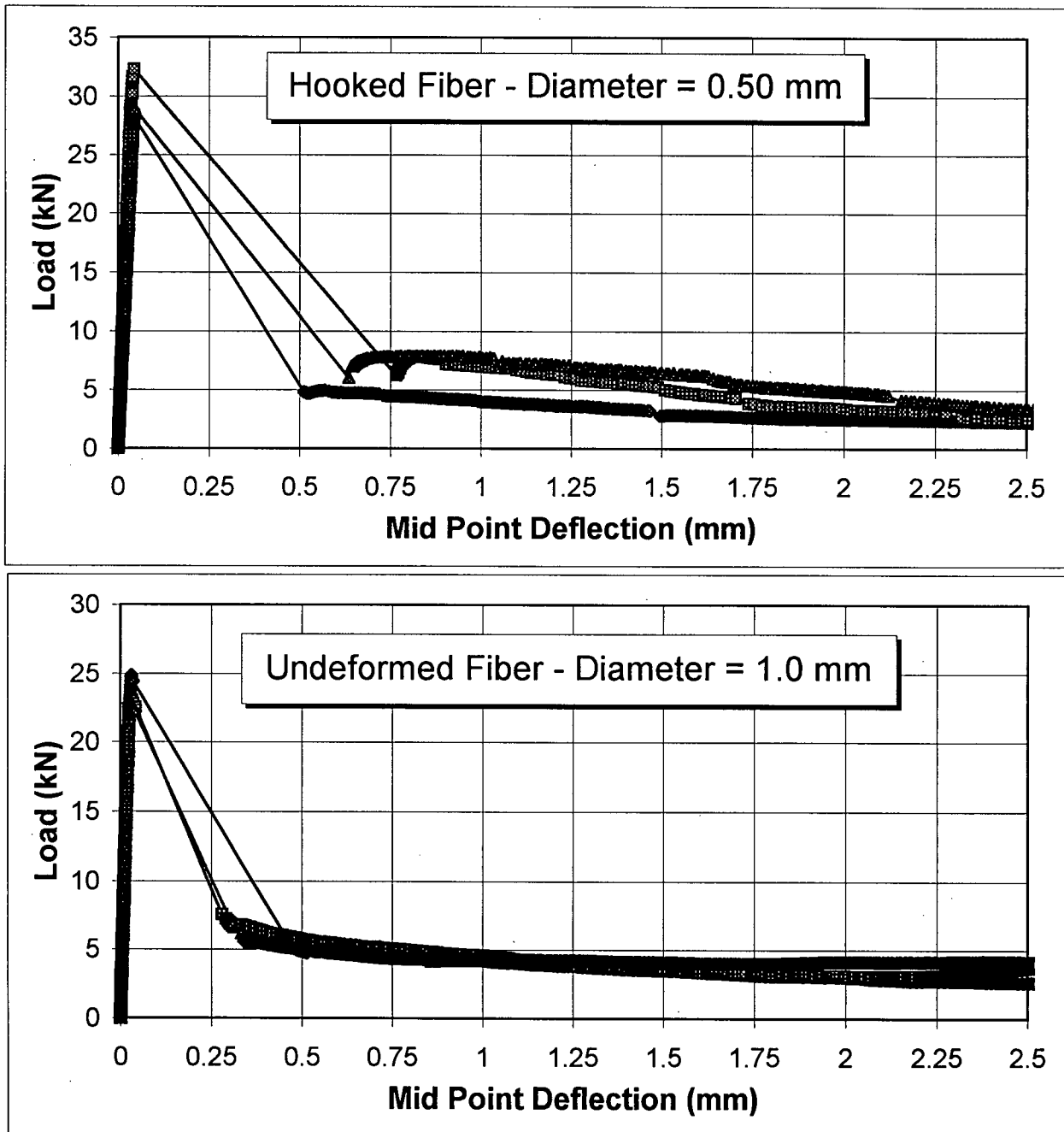
Figure 8.10 - Post-cracking flexural resistance: comparison between hooked, 0.50 mm diameter fibers and straight (undeformed), 1.0 mm diameter fibers (both at 60 kg/m^3).
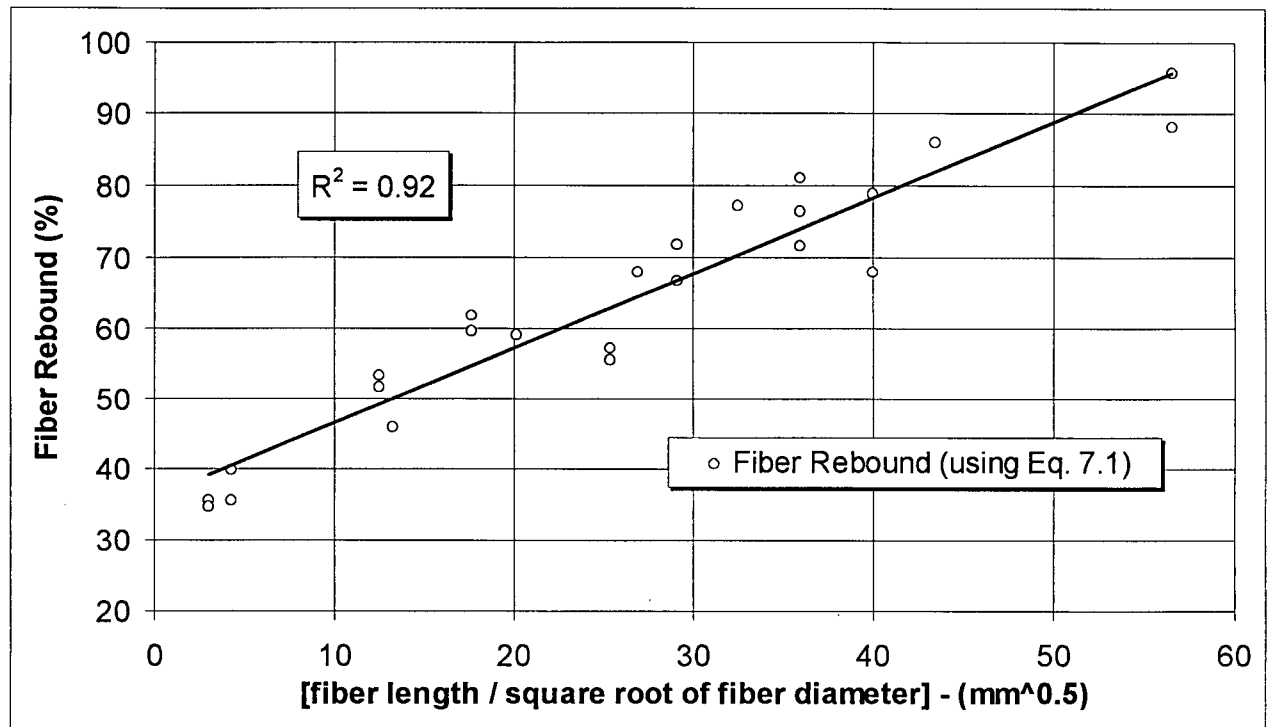
Figure 8.11 - Variation in steel fiber rebound with the aspect ratio given by the fiber length divided by the square root of the diameter (circular cross section fibers, diameters between 0.5 and 1.0 mm, lengths between 3 and 40 mm).

This concept is further explored in Chapter 10, where toughness aspects are brought into considerations to develop an optimized steel fiber geometry for dry-mix shotcrete.

8.4 - Conclusions

In this chapter, shotcrete was produced under laboratory controlled conditions of shooting consistency and air flow and careful measurements of fiber rebound were made for various steel fiber shapes and geometries. Based on the results obtained, the main conclusions to be drawn are as follows:

1) The specific projected area alone was *not* found to be a determinant of steel fiber rebound (i.e. for similar lengths, flat fibers were not found to rebound more than circular cross section fibers).

2) For a given fiber diameter, the fiber length was found to be a key parameter in determining steel fiber rebound, with shorter fibers leading to a significantly lower rebound.

3) For a given fiber length, the fiber diameter was also found to influence steel fiber rebound, with a greater diameter leading to less rebound.

4) For fibers with a circular cross section, an aspect ratio (the fiber length divided by the square root of its diameter) was found to linearly correlate to fiber rebound, indicating that more efficient fiber geometries for dry-mix shotcrete could be produced by reducing this parameter.

5) For a given fiber diameter, there is an optimum fiber length that leads to maximized dry-mix shotcrete toughness.

Chapter 9 - Predicting the Flexural Post-Cracking Performance of Steel-fiber Reinforced Concrete from the Pull-out of Single Fibers

9.1 - Introduction

It is commonly observed that, after cracking, steel fibers tend to pull out of the matrix, which is recognized as the main reinforcing mechanism in steel fiber reinforced concrete. This has led to several investigations on the pull-out of single fibers embedded in cement matrices to understand the toughening behavior of SFRC (Naaman & Shah, 1976; Gray & Johnston, 1984; Banthia & Trottier, 1995).

However, these experiments have shown that the pull-out mechanisms are influenced by factors such as the inclination angle of the fiber with respect to the loading direction, its embedment length, the fiber geometry and the strength of the matrix (Banthia & Trottier, 1995). Additional complications occur given that the toughness of SFRC is usually evaluated from flexural tests under third-point loading (Fig. 2.3) in which a combination of tensile forces from the fibers being pulled out and compressive forces in the concrete generate a bending moment that gives rise to what is commonly referred to as the flexural post-cracking reinforcing capability of the composite.

As a result, when trying to relate experimental fiber pull-out results to the flexural toughness of SFRC, some apparent inconsistencies arise: for instance, it is well known that when doubling the fiber content of a mix, in spite of the fact that roughly twice as many fibers are expected to be present at the cracked section (Eq. 9.8) the post-crack residual strength is not increased proportionally (i.e. is not doubled - Balaguru & Patel, 1992). It has also been observed that, while high-strength matrices offer an equivalent resistance to the pull-out of fibers, the flexural toughness of the composite is often inferior to that made with lower strength matrices (Balaguru & Patel, 1992 and Banthia & Trottier, 1995). Given these difficulties, while some attempts have been made to model the composite behavior using experimental results on the pull-out of aligned fibers (Jenq & Shah, 1986), no one model has been able to account for the combined influence of

fiber orientation, fiber embedment length, and the variability of the pull-out response to accurately predict the flexural toughness of fiber reinforced concrete.

From a fiber development point of view, the relevance of being able to quantitatively relate pull-out data to the expected toughness of the composite lies in the fact that this allows one to produce a limited number of steel fibers (approximately 5 units) and estimate the performance of a fiber geometry without the need to actually produce fiber reinforced concrete, for which a semi-industrial steel fiber production would be required[1].

The objective of this chapter is to develop a model, based on basic principles of mechanics, that is capable of relating data from single fiber pull-out tests to the expected flexural toughness of the composite. This model will be used in Chapter 10 as a tool for the development of a new fiber design with optimized performance for dry-mix shotcrete reinforcement.

9.2 - Model Description

In order to model the third-point flexural toughness test, one may start by considering that, while the elastic deflections of the specimen in the ASTM C 1018 test are of the order of hundredths of a millimeter (Morgan, et al., 1995), the actual region of interest in the load versus deflection diagram for calculating the ASTM or JSCE toughness indices lies in a range of deflections 10 to 100 times greater than those at first crack (up to 2 mm), indicating that rigid body motion of the two broken halves of the specimen is, by far, the dominant mechanism. Consequently, the failure mode commonly observed, characterized by a main failure crack at midspan, has clear resemblance with a common plasticity approach of a hinge - as it has been suggested before (Lim et al., 1987 and Goparalatnam, 1991). Nevertheless, the question remains on how to determine the size and position of the 'plastic hinge" formed. To overcome this problem, Lim et al (1987) have argued that the hinge should be located at the extreme top of the prism (which does not satisfy equilibrium), and Goparalatnam et al (1991) have suggested a factor (k) as a fraction of the height of the specimen, without however attempting to calculate this factor.

---

[1] A typical 20 liter laboratory batch of fiber reinforced concrete ($V_f = 0.75\%$) will require in excess of 30,000 steel fibers (0.5 mm in diameter, 25.4 mm in length).

A simple solution is, however, possible if we start by assuming a given axial compressive strain at the top-most fiber of the specimen at midspan (ε_o). The total axial shortening (Δ_o) can then be computed as (from the strain diagram in Fig. 9.1):

$$\Delta_0 = \int_0^L \varepsilon_x dx = \varepsilon_0 \cdot 2l \tag{9.1}$$

The position of the neutral axis, measured from the top of the specimen (c - center of rotation) can be calculated by satisfying the equilibrium of forces in the cracked section of the prism at midspan. The incremental rotation angle ($d\theta$ in Fig. 1) can be obtained using:

$$d\theta \cong \frac{\Delta_0}{2 \cdot c} \tag{9.2}$$

The resulting increment in the deflection ($d\delta$) and crack-mouth opening displacement (dCMOD) will be given by:

$$d\delta = d\theta \cdot \frac{3l}{2} \tag{9.3}$$

$$dCMOD = 2\left[d\theta \cdot (h - c)\right] \tag{9.4}$$

The load (P) may be obtained by satisfying the equilibrium of moments:

$$P = \frac{2 \cdot M_e}{l} \tag{9.5}$$

The equilibrating moment (M_e) can be computed from the individual moments generated by the force carried by each of the N individual fibers that are being pulled out (f_i), multiplied by their
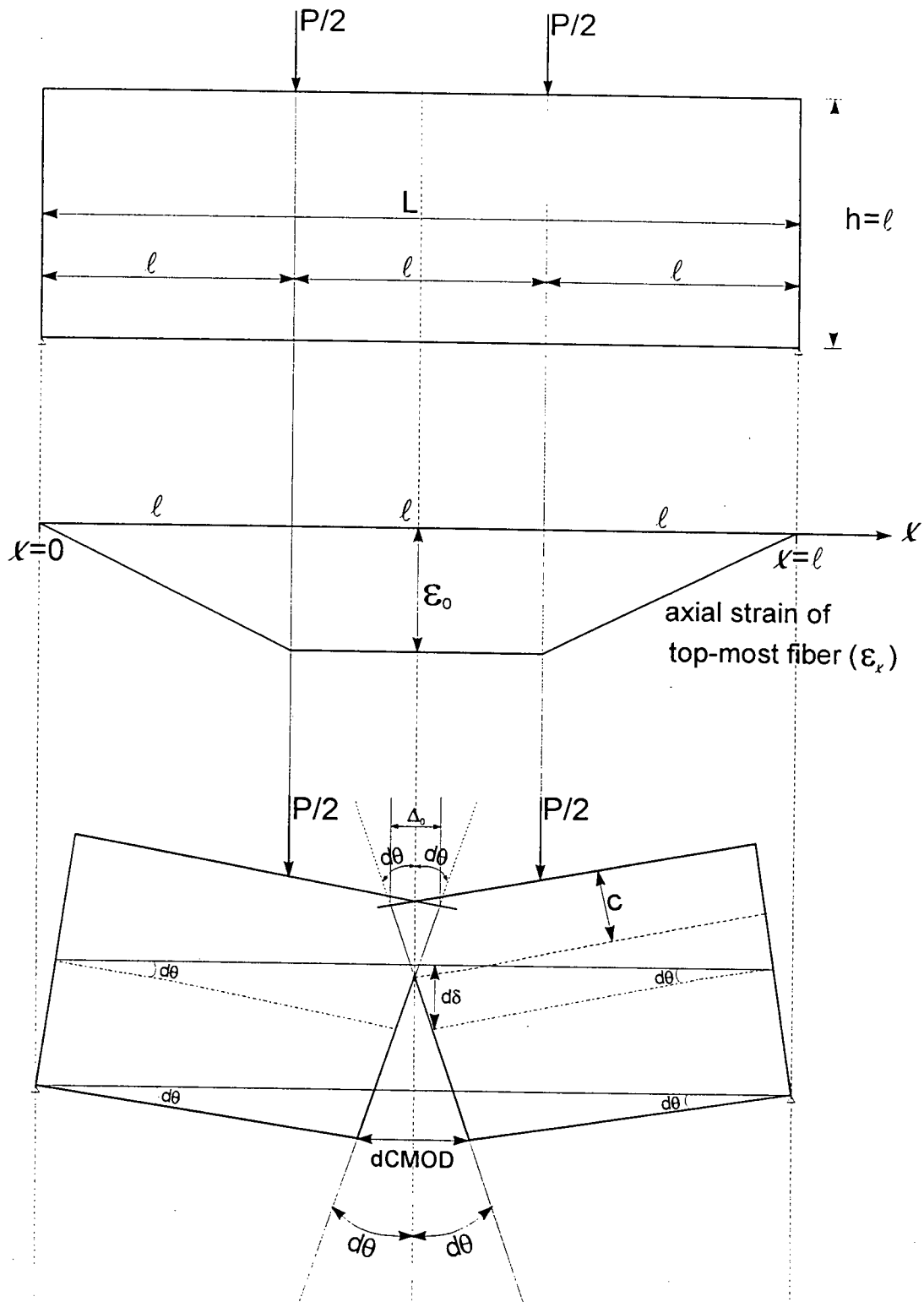
Figure 9.1 - Schematic representation of the test specimen under third point flexural loading and the failure mode assumed for calculation of the mid point deflection (δ).

positions with respect to the neutral axis (y_i), plus the moment generated by the concrete stresses $(\sigma_c$ - Fig. 2):

equilibrium of forces: $\displaystyle\int_0^{c'}\sigma_c(b\cdot dy)+\sum_1^N f_i = 0$ (9.6)

equilibrium of moments: $\displaystyle M_e = \int_0^{c'}\sigma_c(b\cdot dy)\cdot y+\sum_1^N\left(f_i\cdot y_i\right)$ (9.7)
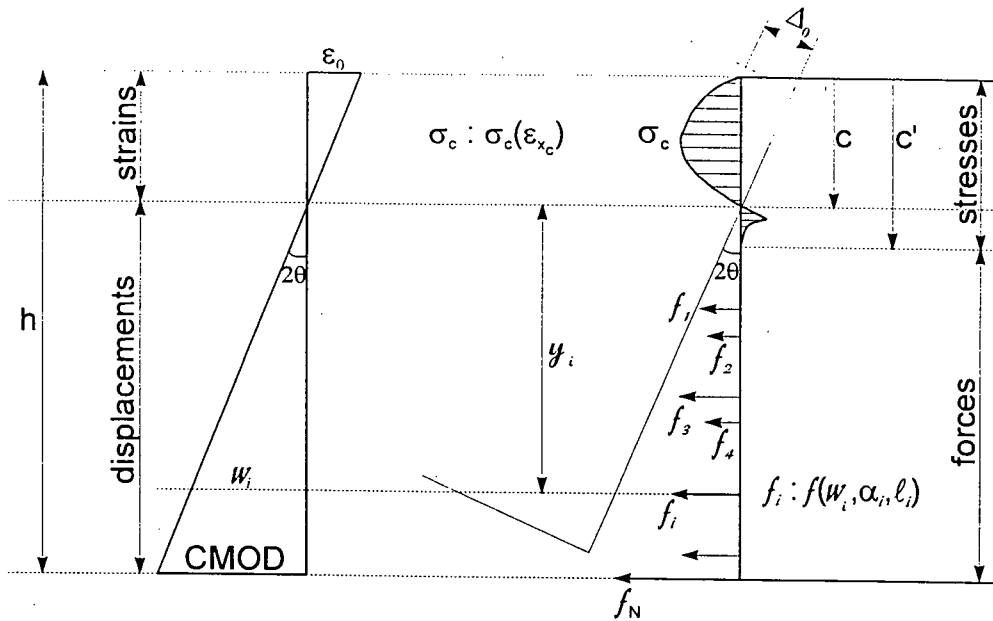
Figure 9.2 - Schematic view of the forces and stresses acting on the cracked section of the beam.

The number of fibers (N) contained in a given area can be calculated from the fiber density distribution (n) as proposed by Romualdi and Mandel (1964). Therefore, with the total length of fibers (L) and a total concrete volume (V) or the fiber cross sectional area (A_f):

$$n = \alpha \cdot \tfrac{L}{V} = \alpha \cdot V_f \cdot \frac{1}{A_f} \qquad \text{where}^3 \; \alpha = 0.50 \tag{9.8}$$

A difficulty arises, however, in that the concrete stresses are related to concrete *strains*, while pull-out forces are related to crack opening *displacement*. This may be overcome if we make the simplifying assumption of a straight crack (i.e. one with a linear profile), allowing one to relate the crack opening at the location of any fiber (w_i) to its position (y_i):

$$w_i = \left[\frac{CMOD}{(h-c)} \right] \cdot y_i \tag{9.9}$$

Notice that, since this formulation starts by imposing strains (Eq. 9.1) compatibility conditions are automatically satisfied. It is also interesting to note that the ratio between the change in *CMOD* to the change in deflection *(dCMOD/dδ)* approaches 4/3 as the neutral axis approaches the top of the prism *(c → 0)*, leading to the result observed even by the naked eye that, at the end of a flexural toughness test, the *CMOD* is greater than the mid-point deflection. From Eq. 9.3 and 9.4, and taking $l = h$ (i.e. the ASTM standard size specimen):

$$\frac{dCMOD}{d\delta} = \frac{2d\theta(h-c)}{d\theta \cdot \frac{3}{2} \cdot h} = \frac{4}{3} \tag{9.10}$$

9.3 - Material and Methods

As mentioned earlier, the model developed is based on experimentally obtained parameters of individual fiber pull-out behavior. However, because this study is concerned with predicting not only average responses, but also their confidence intervals, a large number of specimens were required to accurately characterize the distributions of the fiber pull-out force, fiber density and post-cracking flexural loads.

---

[3] The coefficient α accounts for the fiber orientation with a value of 0.50 referring to a random (3-D) distribution. For a case of dry-mix shotcrete, for which a strong tendency for bidimensional distribution occurs, a value $\alpha = 0.64$ could be used.

Consequently, only one steel-fiber type (hooked ends, approximately 25.4 mm long, 0.5 mm in diameter) was investigated. Pull-out tests of single fibers (Fig. 9. 3) were performed at full embedment length $(l_e = l_f/2)$ at inclination angles[3] with respect to the pull-out direction of 0, 22.5, 45 and 67.5 degrees. For both the 0 and 45 degree cases, 20 specimens were tested, while, for the remaining two inclination angles, 10 specimens each were tested. During the pull-out tests, simultaneous measurements of pull-out load and crack opening displacements were performed. The instrumentation included two LVDTs for displacement measurements (Fig. 9. 3) and an electronic data acquisition system.
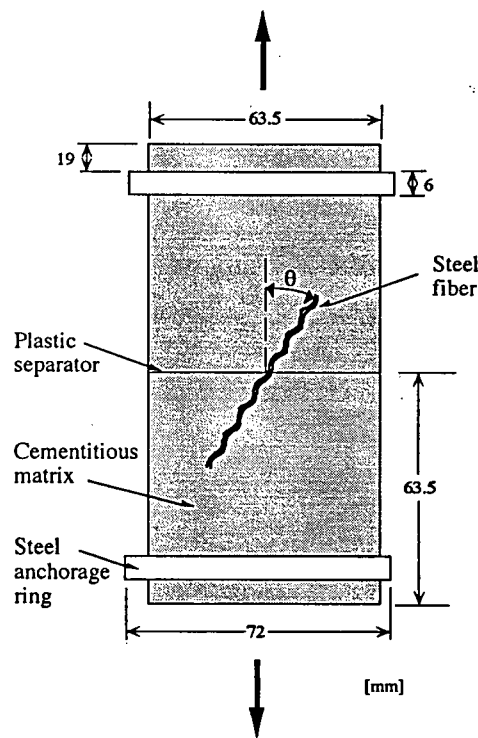
Figure 9.3 - Schematic representation of the single fiber pull-out test used.

Two fiber contents (0.75 and 1.5% by volume) were chosen for flexural toughness tests on 100 x 100 x 350 mm SFRC beams using third-point loading. Respectively, 17 and 19 specimens were tested for the two fiber contents and simultaneous measurements of load and mid-point deflection were made. In order to eliminate any extraneous deformations from the mid-point deflection

---
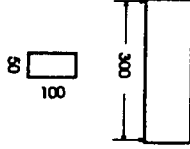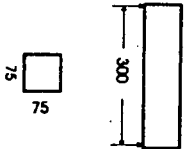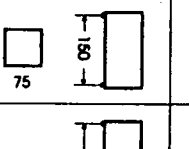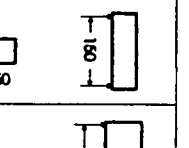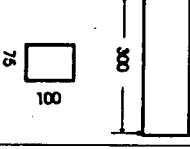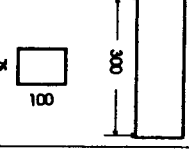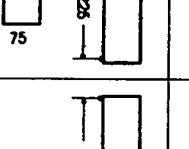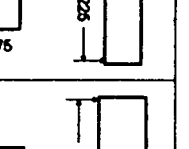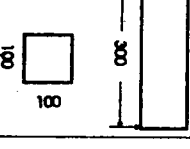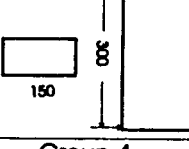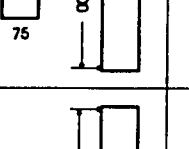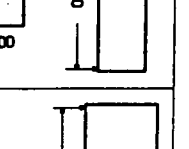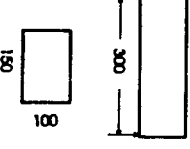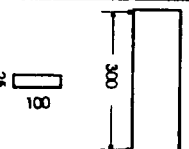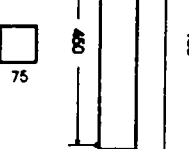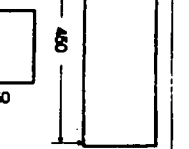
[3] Throughout this thesis, fiber inclinations are reported in terms of the angle formed between the fiber and the pull-out direction (i.e. a zero degree inclination refers to an aligned fiber).

measurements, a Japanese yoke, instrumented with two LVDTs was used (Fig. 2.3). The concrete composition (1:0.45:2.14:2.61 - cement:water:sand:coarse agg.) and testing age were kept constant for both pull-out and flexural toughness tests. This concrete developed an average 28 day compressive strength of 58 MPa.

After testing, the flexural prisms were sawn transversally and a 1 inch-thick slice was obtained from each specimen. These sections were then divided into 2x2 cm squares and the intercepting steel-fibers were visually counted to obtain the fiber density (number of fibers per unit area - Eq. 9.8). A total of 500 such squares were sampled for each mix.

In order to evaluate the model's ability to predict the influence of the changes in specimen size on the flexural toughness test, a test series, proposed[5] by Chen (1995), was repeated using a 0.75% fiber content with 5 specimens tested per size. The specimen sizes used in this series are presented in Table 9.1.

Table 9.1 - Specimen sizes tested to evaluate the model's ability to predict the size effect on flexural toughness testing of SFRC - 5 replicate specimens tested per size (from Chen, 1995).

---

[5] The test series was proposed by Chen (1995) however the data presented in this chapter refers to tests repeated by the author.

9.4 - Results and Discussion

9.4.1 - Fiber Density Distribution

The results for the number of fibers intercepting a 4 cm^2 area in a transverse section of the flexural prisms for the two fiber contents tested (0.75 and 1.5%) are given in Table 9.2. From these data, it should be noticed that, in accordance with Eq. 9.8, the average fiber density is directly proportional to the fiber content, in such a way that the 1.5% mix presents roughly twice as many fibers per unit area when compared with the 0.75% case. Moreover, the results obtained analytically are within a 2 % error with respect to the experimental data (Table 9.2) proving that Eq. 9.8 provides an accurate estimate of the actual fiber density distribution (n).

Table 9.2 - Fiber density values obtained experimentally and analytically using Eq. 9.8.

Calculation Method	Experimental		Analytical - Eq. 9.8	
Fiber Content (% vol.)	0.75%	1.50%	0.75%	1.50%
Average (fibers per 4cm^2)	7.92	15.17	7.64	15.28
Std. Dev. (fibers per 4cm^2)	6	8.9	-	-
Sample size (n)	448	493	-	-

9.4.2 - Pull-out of Single Fibers

After the pull-out test results had been individually processed, an *average* pull-out load versus displacement response was obtained using the 10 to 20 replicate specimens for each of the four fiber orientations tested. In Figs. 9.4 a to d, results of the pull-out load versus displacement plots are presented in terms of individual values as well as the average and predicted 95% confidence interval for an individual result.

For the sake of simplicity, it is assumed throughout this Chapter that the sample sizes are large enough to approximate the standard deviation and mean of the samples to those of the population $\left(\bar{x} = \mu \text{ and } S_d = \sigma \right)$ and, therefore, the 95% confidence intervals are approximated by $\mu \pm 1.96 \cdot \sigma$.
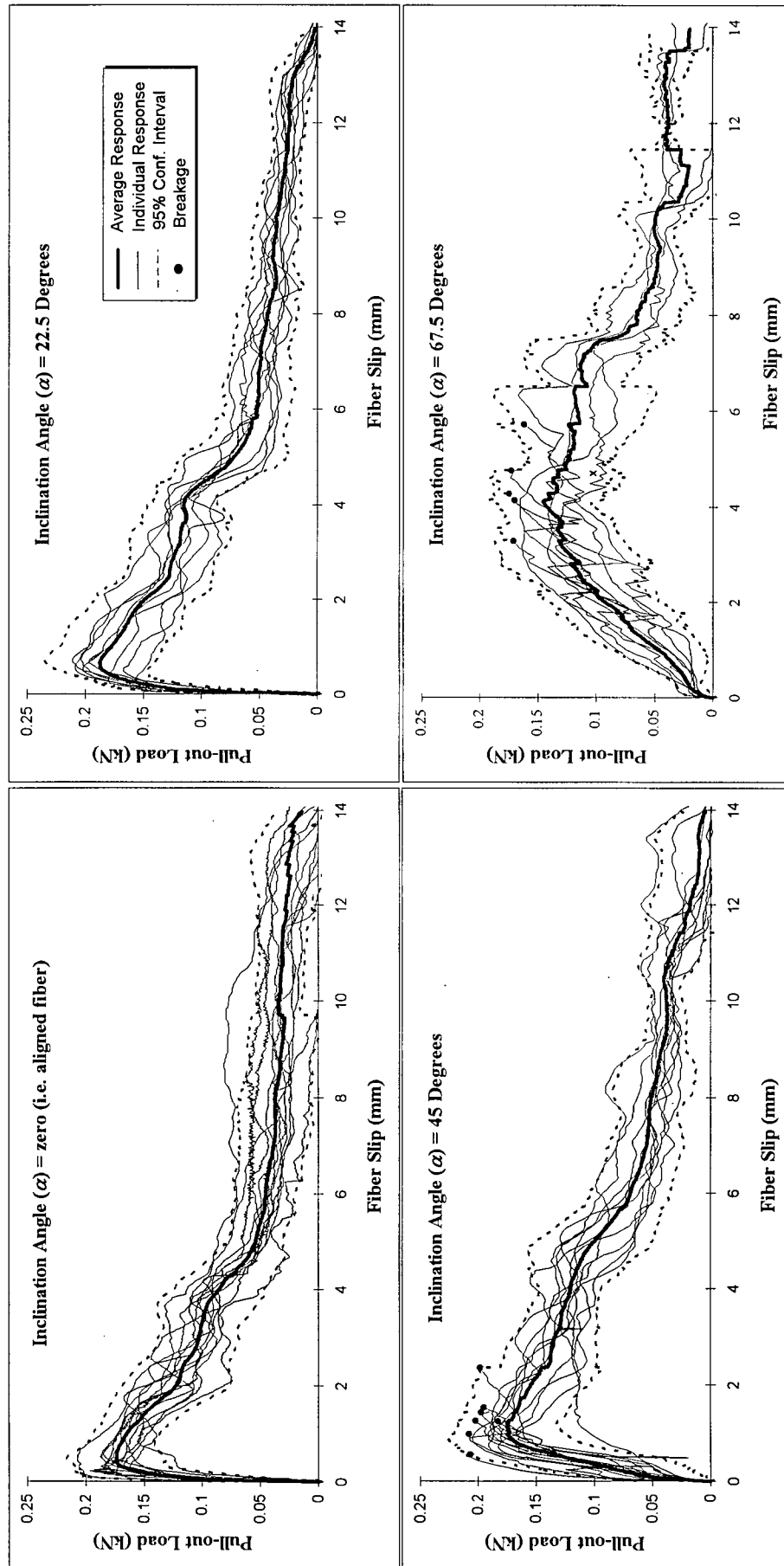
Figure 9.4a to d - Experimetal pull-out response of individual fibers inclined at zero, 22.5, 45 and 67.5 degrees - respect., a to d. Hooked fibers, legend in Fig. b.

From the average responses obtained for inclination angles of 0, 22.5, 45 and 67.5 degrees (Figs. 9.4a to d), it is clear that the fiber orientation has a definite influence on the pull-out response (as reported previously by Banthia & Trottier, 1995) with the action of the anchoring hook being mobilized only at greater displacements for the inclined fibers. It should be noticed that, for this particular fiber/matrix combination, fiber breakage occurred only for inclination angles greater than 45 degrees and at displacements greater than 1 mm (Figs. 9.4c and d).

9.4.3 - Flexural Response of SFRC Under Third-Point Loading (ASTM C 1018)

Similar to the pull-out data, the individual load versus mid-point deflection plots from the flexural tests were obtained by averaging the deflections from the two LVDTs on the yoke. After that, for a given mid-point deflection, the average and the standard deviation of the load were obtained from all replicate specimens. This procedure gave the overall mean load versus deflection diagrams presented in Figs. 9.5a and b, along with the 95% confidence interval for a predicted individual result.

Besides the expected enhanced toughening at a higher fiber content, a comparison of the two mixes at any given deflection up to 3 mm shows that, although the 1.5% mix has, on an average, twice as many fibers bridging the cracked section (Table 9.2), its residual load bearing capacity is not proportionally doubled. This is generally observed (Balaguru et al., 1992) and the reasons for this will become clearer based on the results from the model.

9.5 - Implementation of the Model[5]

In the proposed model, the height of the beam is divided into 20 layers of equal size. Concrete is assumed to behave elastically under tension, with a modulus of elasticity (E_{ct}) estimated from its cylinder compressive strength (f'_c) using the expression given by the CSA (1984) Code:

$$E_{ct} = 5500\sqrt{f'_c} \quad \text{(in MPa)} \tag{9.11}$$

---

[5] A description of the various steps taken by the computer code is given in Appendix C.
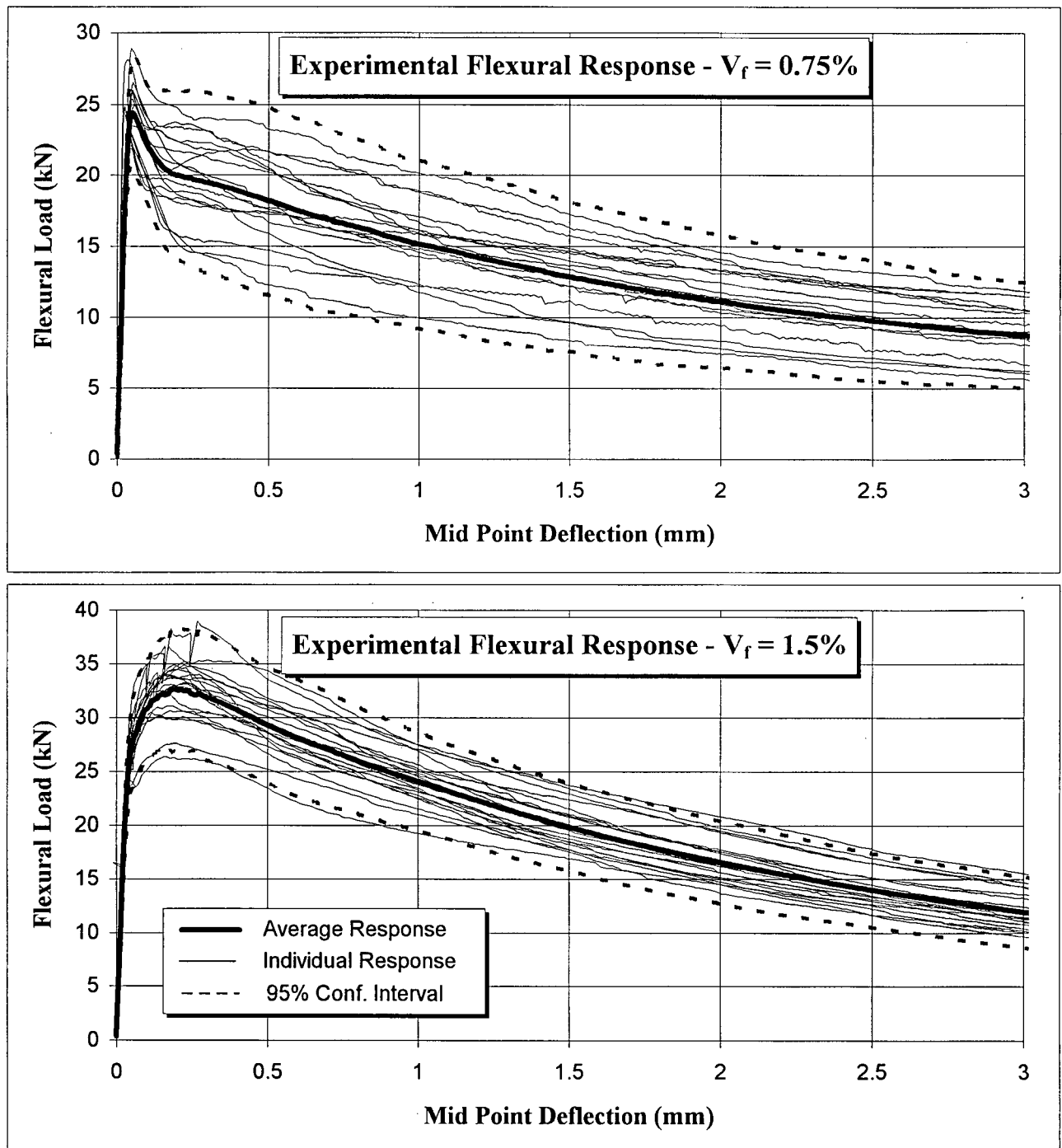
Figure 9.5a & b - Experimental flexural response of SFRC at V_f = 0.75 and 1.5% (hooked fibers).

Strain-softening of concrete under tension is assumed to occur whenever the cracking strain (ε_{cr}) is exceeded, this value being calculated as a function of the flexural tensile strength (f_{cr}) of the 0.75% beams tested:

$$\varepsilon_{cr} = f_{cr} / E_{ct} \qquad (9.12)$$

The tensile stress in the concrete under the strain-softening regime (σ_{ct}) is taken to decrease exponentially up to an additional crack opening of 0.04 mm (according to experiments reported by Goparalatnam & Shah, 1985). The expression used in this case was:

$$\frac{\sigma_{ct}}{f_{cr}} = e^{-k.w.\lambda} \qquad (w \ in \ mm, \ k = 60.787 \ and \ \lambda = 1.01) \qquad (9.13)$$

Under compression, concrete was assumed to behave according to a parabolic stress-strain relationship as proposed by the CSA (1989) code:

$$\sigma_c = f_c' \left[2\frac{\varepsilon_c}{\varepsilon_c'} - \left(\frac{\varepsilon_c}{\varepsilon_c'}\right)^2 \right] \qquad where: \ \varepsilon_c' = 2\frac{f_c'}{E_{ct}} \qquad (9.14)$$

In the model, the pull-out force of each fiber (f_i) is expressed as a function of the crack width (w_i) according to the average pull-out force versus opening width relationships obtained experimentally at the full embedment length $\left(l_e = \frac{l_f}{2}\right)$. In order for that to be possible, the Ramberg Osgood equation (Collins & Mitchell, 1987) was used to obtain an expression fitting the average numerical data for each inclination angle. The excellent fit can be noted in Fig 9.6, where the fitting constants A, B, C and E_p used for each inclination angle are also given:

$$f_i(\alpha_i, w_i) = E_p.w_i \left\{ A + \frac{1-A}{\left[1+(B.w_i)^C\right]^{\frac{1}{C}}} \right\} \qquad (9.15)$$

Inclination	A	B	C	Ep
0 Deg.	-0.015	12.1	1.2	2.5
22.5 Deg.	-0.017	9.7	1.1	2.2
45 Deg.	-0.1	1.42	4	0.27
67.5 Deg.	-0.2	0.3	4	0.047
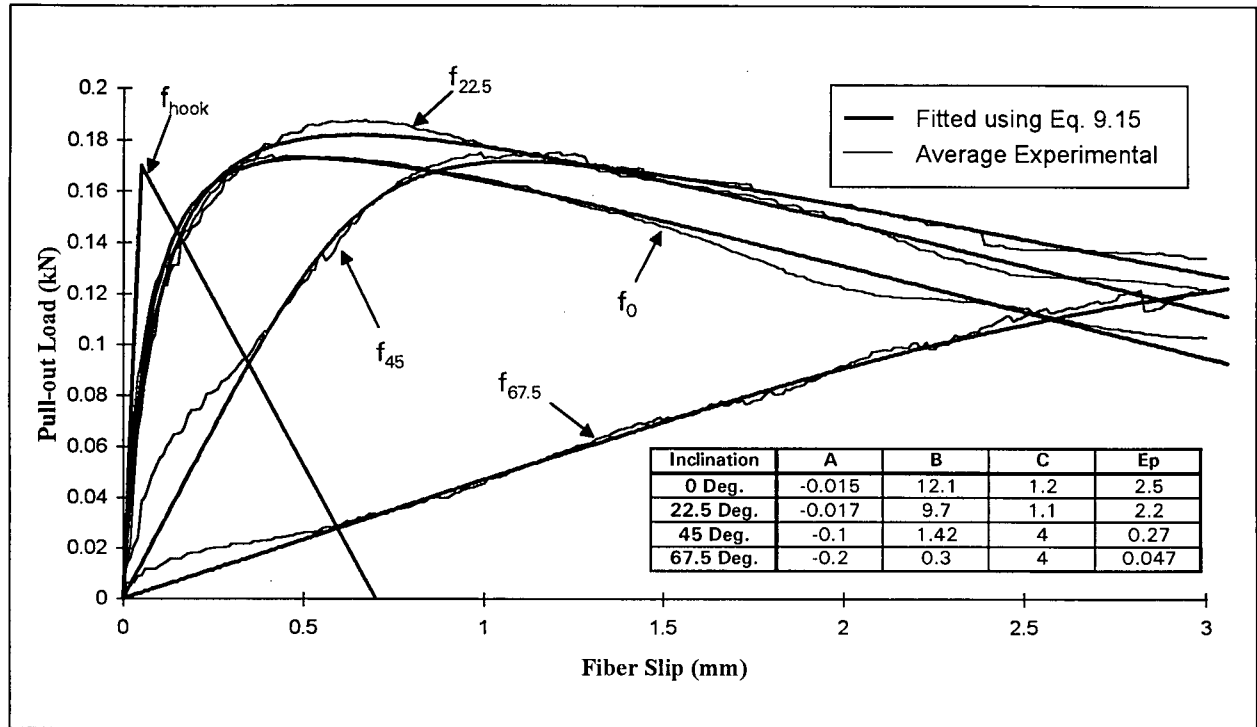
Figure 9.6 - Average experimental pull-out relationships obtained at the various inclination angles and the Ramberg-Osgood functions used to represent them in the model (hooked fiber).

The model accounts for the variation in the pull-out force with the embedment length by considering the smallest possible embedment length to have the strength of the hook for the aligned fiber (f_{hook} in Fig. 9.6). This way, the total tensile force carried by the N fibers contained in a given region (or layer - F_t) is:

$$F_t = \sum_1^N f_i \tag{9.16}$$

From the definition of the mean, the average pull-out force in the region $\left(\overline{f}\right)$ may be computed:

$$\overline{f} = \frac{\left(\sum_1^N f_i\right)}{N} \tag{9.17}$$

allowing one to write:

$$F_t = \overline{f} . N \tag{9.18}$$

When calculating the value of the average pull-out force $\left(\overline{f}\right)$, assuming a random orientation of the fibers, all possible combinations of inclinations (α) and embedment lengths $\left(l_e\right)$ are possible (i.e. obey a uniform distribution). Therefore, assuming a trapezoidal integration, the average pull-out force $\left(\overline{f}\right)$ may be numerically estimated by[6]:

$$\overline{f}(w) = \frac{\int\limits_0^{\frac{\pi}{2}}\int\limits_0^{\frac{l_f}{2}} f(l_e,\alpha).dl_e.d\alpha}{\int\limits_0^{\frac{\pi}{2}}\int\limits_0^{\frac{l_f}{2}} dl_e.d\alpha} \cong \frac{1}{2}\left\{\left[\left(\frac{f_0(w)}{2} + f_{22.5}(w) + f_{45}(w) + f_{67.5}(w) + \frac{f_{90}(w)}{2}\right)\cdot\frac{1}{4}\right] + f_{hook}(w)\right\} \qquad (9.19)$$

In order to obtain the stochastic variation (spread) of the load at a given deflection, the source-code written to find the position of equilibrium of the system was linked to the Reliability Analysis code (RELAN - item 6.4) developed at UBC (Foschi et al., 1993) allowing for the calculation not only of the most probable value (mean), but also the confidence intervals for predicted values (limits between the maximum and minimum values to be expected).

To account for the stochastic nature of the process, two main sources of variation may be recognized: the variation in the pull-out force of a single fiber and the variation in the number of fibers present at the cracked section. Thus, to estimate the variation in the post-cracking flexural load, both quantities (f_i and N) were implemented into the reliability analysis code as stochastic variables. For each of the 20 layers that the section was divided into, both the number of fibers in the layer and the pull-out force of each fiber were considered to be normally distributed, with mean and standard deviation values as determined experimentally. The average fiber density was calculated using Eq. 9.8, and for the pull-out force, the average values at any crack opening was assumed to be normally distributed and associated with a 12% coefficient of variation (an average value as shown in Fig. 9.4). Breakage of fibers with inclination greater than 45 degrees was assumed to occur beyond a crack-opening of 1 mm, at a rate of 5 out of 20 fibers per mm of opening as was observed experimentally (Fig. 9.4c and d).

---

[6] The exact solution to finding the average fiber pull-out force is given by the expression on the left hand side of Eq. 9.19. However, a closed form solution is not possible since the function $f:f(l_e, \alpha)$ is not known. Therefore a numerical solution is given by the right-hand side of the equation using the experimental pull-out data obtained.

9.6 - Analytical Results and Comparison with the Experimental Data

9.6.1 - Comparison of Mean Values

In order to evaluate the validity of the model proposed, computations were carried out for the cases of V_f = 0.75% and 1.5%. In Fig. 9.7, the analytical results are presented in terms of the mean expected residual strength, along with the average experimental data from Fig. 9.5. As it can be observed, in general, the model agrees well with the experimental data in the post-cracking region, presenting all its main features of increasing and decreasing load bearing capacity (respectively, for the 1.5 and 0.75 % cases). Moreover, while in the case of V_f = 0.75% the error in the predicted value does not exceed 20% of the experimental average, in the 1.5% case, this error lies below 6%. In terms of accumulated energy (i.e. area under the load vs. displacement diagram - not shown), the maximum errors are, respectively, 13 and 4%.
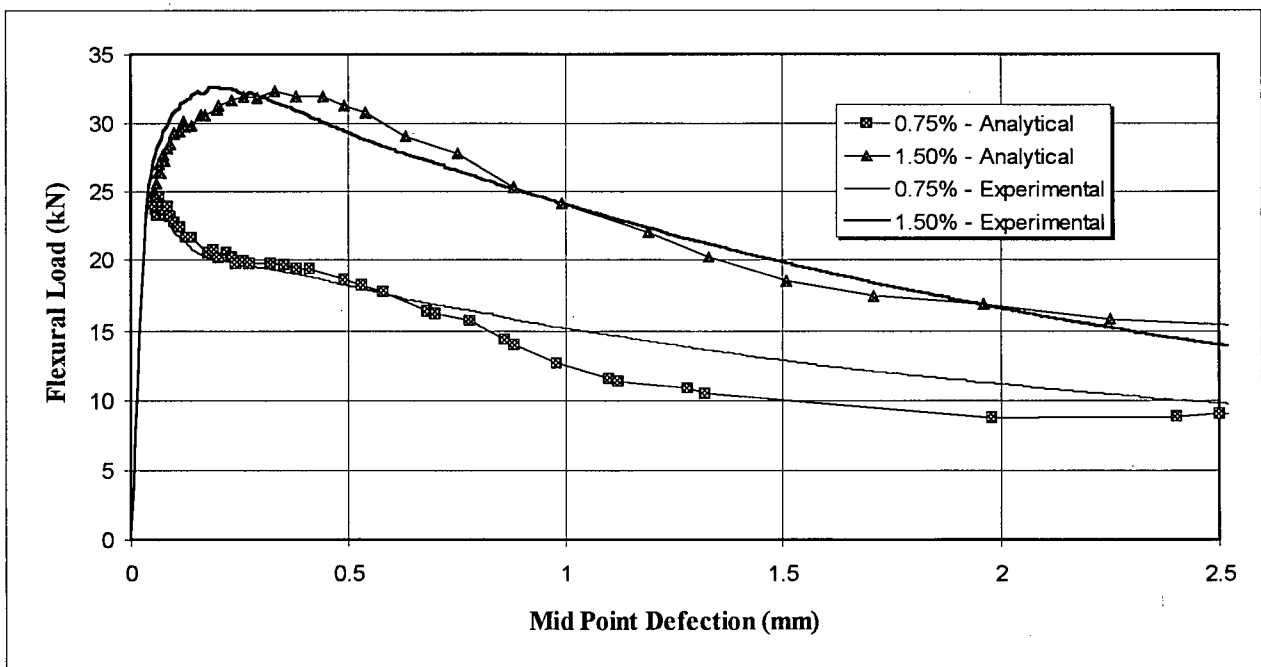
Figure 9.7 - Comparison of analytical and experimental results for the flexural response of SFRC at 0.75 and 1.5% fiber contents (hooked fibers, average response).

The analytical results also agree with the observation that, while twice as many fibers intercept the cracked-section for the V_f = 1.5% composite, its flexural reinforcing capability is not increased

proportionally. An explanation for this can be found in Fig. 9.8 in which, for both fiber contents, the position of the neutral axis is plotted, along with the accumulated energy consumed by the concrete under compression. As can be observed, for the higher fiber content, the concrete in the upper part of the specimen is more severely loaded, with a greater depth of the neutral axis and greater compressive strains (the latter not shown). As a result, greater work is done by the concrete (roughly twice as much) as opposed to that by the pull-out of fibers.

From the depth of the neutral axis vs. mid-point deflection curves presented in Fig. 9.8, it may be seen that, for a 100 mm deep beam, the compressed region of the specimen is usually less than 15 mm deep by the time a 1 mm mid-point deflection has been attained. Thus, any type of calculation of the residual-strength based on the elastic formula, which assumes a neutral axis at mid-depth (e.g. JSCE toughness factor) will grossly overestimate the "true" residual stress of the composite by approximately 100%, resulting in meaningless stress values.
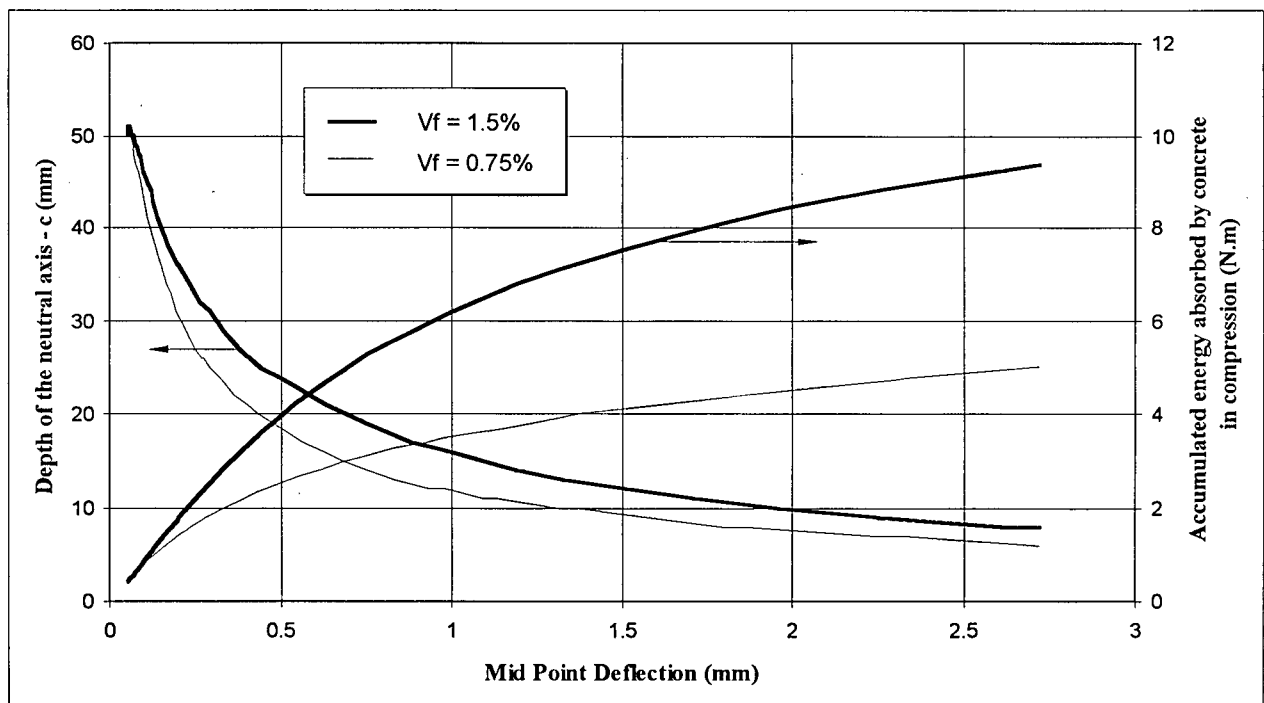
Figure 9.8 - Position of the neutral axis and energy accumulated by concrete under compression as a function of the mid-point deflection (V_f = 0.75 and 1.5%, hooked fibers).

9.6.2 - Comparison of Confidence Intervals

In order to compare the predicted and experimentally obtained variations in the flexural load at a given deflection, in Figs. 9.9a and b, the 95% confidence intervals (calculated using $1.96 \cdot \sigma$ in the experimental case) are plotted as a function of the mid-point deflection for the experimental and analytical cases. In Figs 9.9a and b, data from large sample size test series reported in the literature (Morgan et al., 1995 and Chen, 1995) for SFRC with the same fiber type and contents and a similar matrix ($f'_c = 50$ MPa) are compared with the analytical curves. Note that, in general, the model is accurate in predicting that the amplitude of the confidence interval should reach a maximum value at a deflection of approximately 0.3 mm, after which it tends to become narrower.

In terms of quantitatively predicting the variability, in the case of the composite with $V_f = 0.75\%$, the model shows good agreement with all three test series, with an average error of less than 2 kN. In the case of the composite with 1.5% fiber, the model again shows an error of less than 2 kN when compared to the experimental data by Chen (1995), but shows a greater error when compared with the test series from this study. In that sense, in dealing with a 95% confidence interval, it should be noted that experimental values below the predicted ones are always a possibility, since the analytical result should only be exceeded in 5% of the cases.

9.6.3 - Predicting the Variation in Flexural Response with Specimen Size

In order to evaluate the model's ability to predict the variation in the flexural response with the specimen size, the computer program was used[7] with specimen dimensions as shown in Table 9.1. In this Table, four series are presented (groups 1 to 4) corresponding to the evaluation of the effect of a varying size for a constant specimen width : height : span ratio (Group 1), varying span for a constant cross section (Group 2), varying height for a constant width and span (Group 3) and varying width for a constant height and span (Group 4).

---

[7] The latest (Windows based) version of the program allows the option of predicting the average pull-out force of a single fiber (Eq. 9.19) from the post-cracking residual load vs. crack opening relationship obtained from a uniaxial tension tests using SFRC. This is the procedure used in item 9.6.3.
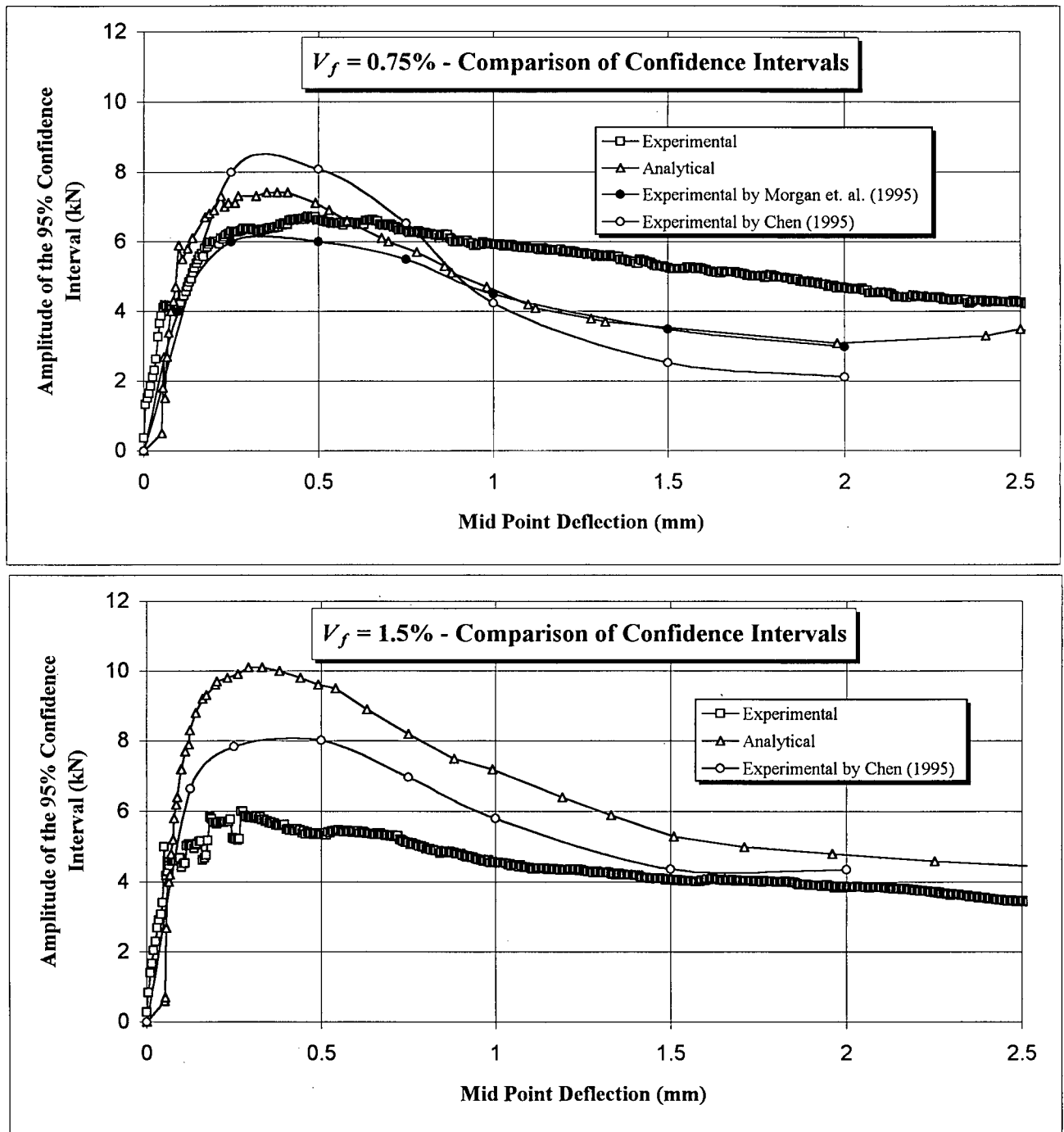
Figure 9.9a & b - Comparison of experimental and analytically predicted amplitude of the 95% confidence interval of the flexural load. SFRC, V_f = 0.75 and 1.5% (respect., a and b) hooked fibers.

Results from these tests are presented in Figs. 9.10 to 9.13 in terms of the analytically predicted and the average experimental response obtained from 5 replicate specimens for each size. These data show that, in general, the model is able to predict the influence of specimen dimensions on the flexural post-cracking behavior of fiber reinforced concrete with good accuracy, the average error of all four test series is less than 15%.

9.6.4 - Comparison of the Kinematics of the Failure Mode

In spite of the good agreement between the predicted and the average experimental results, it remains to be shown that the assumptions made in obtaining the *CMOD* from the mid-point deflection are valid, that is whether the assumed failure mode resembles the experimental reality. To this end, use was made of a test series performed by Chen (1995), in which six 75 x 75 x 250 mm SFRC prisms containing 0.75% of the same fibers used in this study ($f'c$ = 50 MPa) were tested with simultaneous measurements of mid-point deflection and *CMOD*. These data are presented in Fig. 9.14 along with results from the model up to a deflection of 1/150 of the span.

As shown previously (Eq. 9.10), as the neutral axis approaches the top of the prism, the ratio $dCMOD/d\delta$ should be size independent (provided that geometrical similarity is maintained, i.e. span = three times the height). It was also shown that, according to the rigid body mechanism assumed, a value of $dCMOD/d\delta$ = 4/3 should be reached at this point. A comparison of the data in Fig. 9.14 shows that, while, in general, the experimental results lie above the analytical, the obtained ratio $dCMOD/d\delta$ of approximately 4.5/3 is close to the theoretically predicted value of 4/3, indicating that the failure mode assumed is in good agreement with the experimental reality.
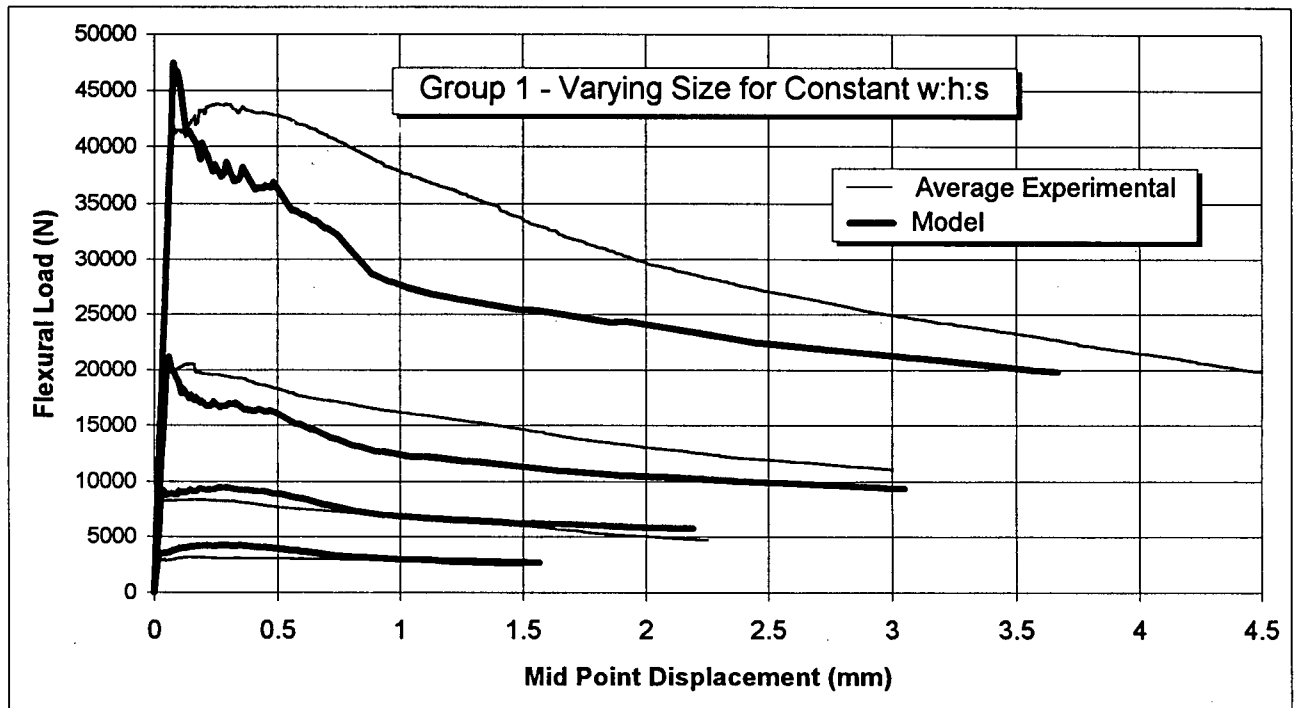
Figure 9.10 – Model predictions vs. experimental averages, square cross sections = 50, 75, 100 & 150 mm, 0.75% hooked fiber.
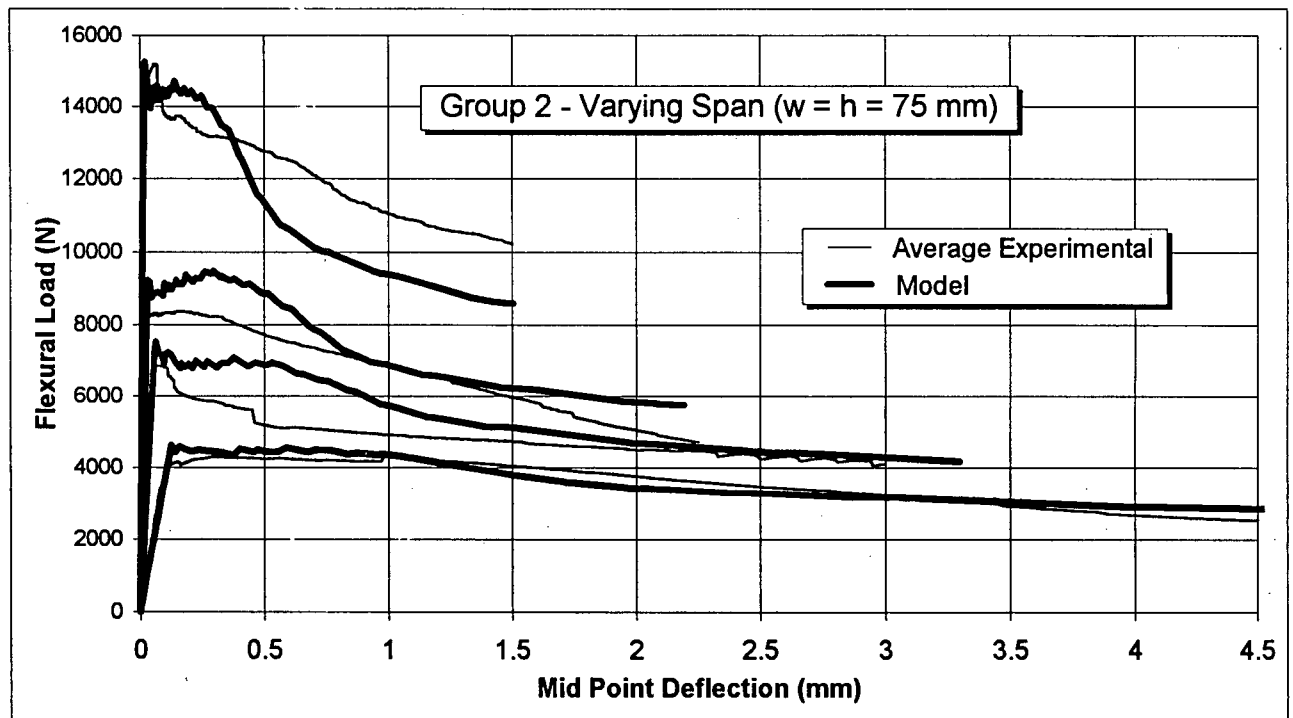
Figure 9.11 – Model predictions vs. experimental averages, span = 150, 225, 300 and 450 mm, 0.75% hooked fiber.
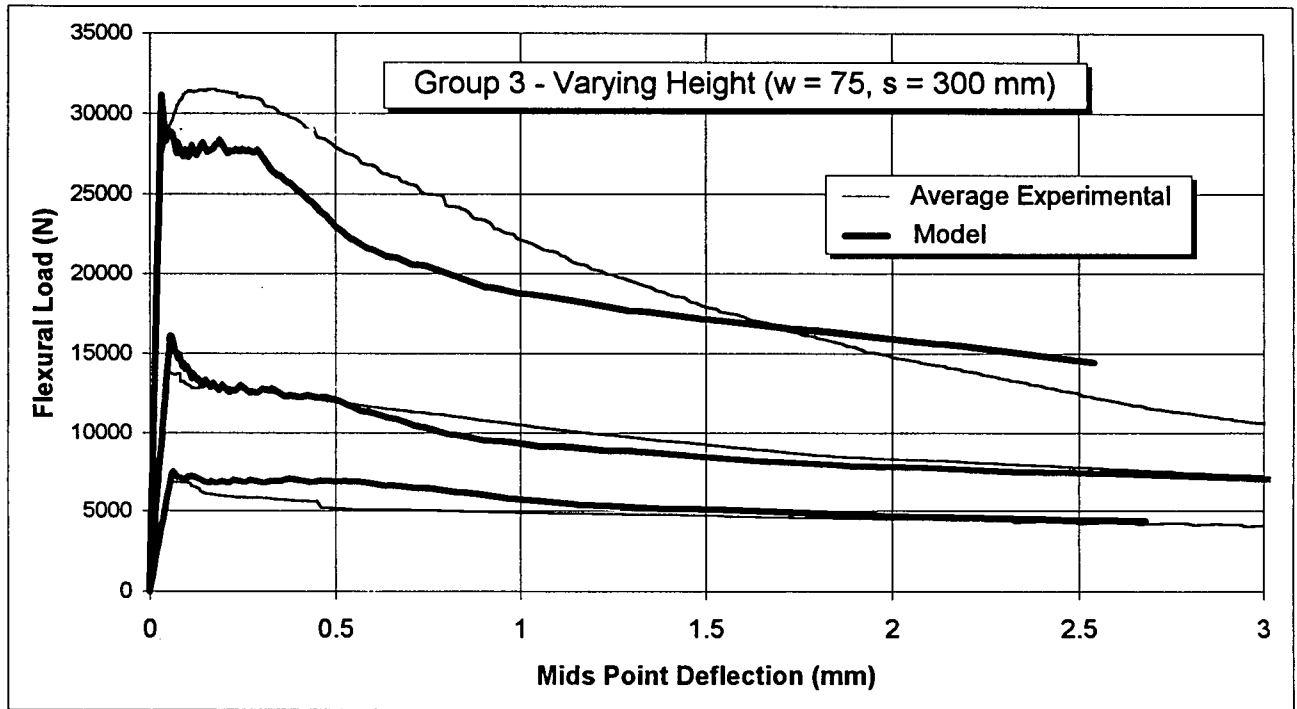
Figure 9.12 - Model predictions vs. experimental averages, height = 75, 100 and 150 mm, 0.75% hooked fiber.
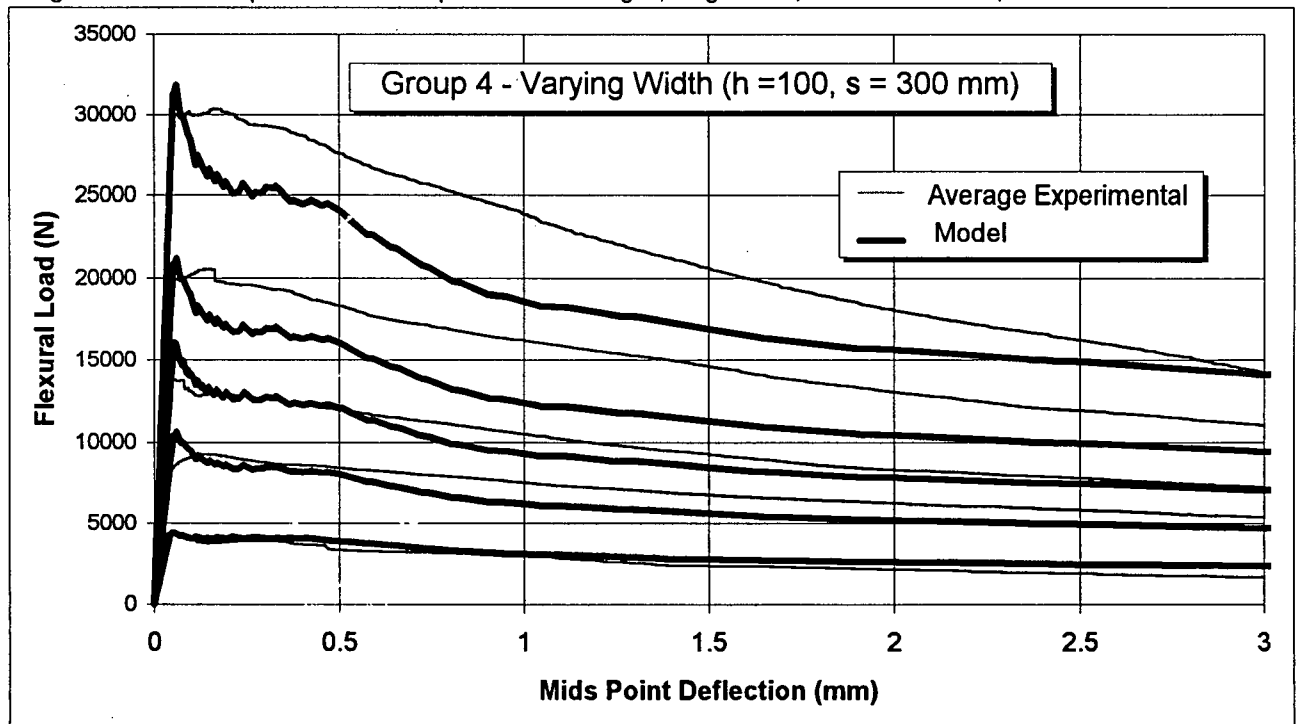
Figure 9.13 - Model predictions vs. experimental averages, width = 25, 50, 75, 100 & 150 mm, 0.75% hooked fiber.
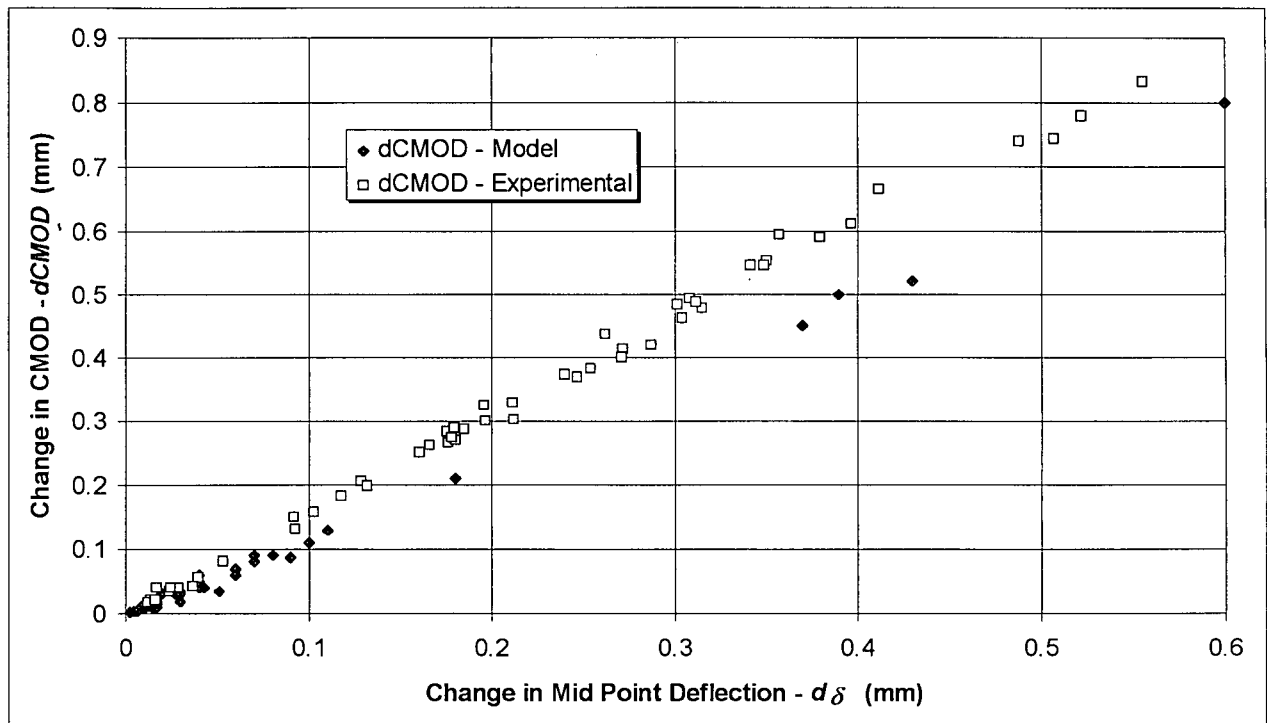
Figure 9.14 - Change in crack mouth opening displacement (*dCMOD*) as a function of the change in mid point deflection (*dδ*). SFRC, V_f = 0.75%, flexural testing under third-point loading.

9.7 - Conclusions

In this chapter, an analytical model has been proposed and shown to be capable of predicting the flexural post-cracking behavior of steel-fiber reinforced concrete based on data obtained from the pull-out of single fibers. More specific conclusions to be drawn from this chapter are:

1) The pull-out force of individual fibers can be quantitatively related to the overall toughness performance of SFRC under flexural loading if an average fiber pull-out force approach is used to account for the influence of the fiber inclination, embedment length and fiber density distribution.

2) The kinematics of the failure mode of a SFRC beam under flexural toughness testing (ASTM C 1018) can be modeled with relative accuracy by assuming a rigid-body behavior of the structure and relating the mid-point deflection to rotations about the central crack.

3) The variation in the toughness response of SFRC (spread of results) is determined by the variation in the pull-out force of a single fiber and the variation in the fiber density distribution.

Chapter 10 - Development of a New Steel Fiber For Dry-Mix Shotcrete

10.1 - Introduction and Objectives

In principle, for a given in-situ fiber content and matrix composition, steel fiber reinforced cast concrete and dry-mix shotcrete should behave similarly with respect to flexural toughness. A somewhat increased post-cracking residual load bearing capacity should be expected for dry-mix shotcrete due to the fact that its fibers tend to be oriented in a bidimensional fashion and therefore more fibers are expected at the cracked section, in the direction perpendicular to the plane of shooting (as demonstrated by Armelin & Helene, 1995).

However, a simple experiment shows that, for the hooked fibers presently being used for shotcrete reinforcement, this is not true. Therefore, if two test panels are simultaneously shot using the same mixture proportions and fiber content and the material in one of the test panels is placed in a mixer and vibrated back into the panel (i.e. identical in-situ fiber content and mix composition for the shot and shot + mixed cases) it is found that, at the age of 28 days, during flexural toughness testing, the shot + mixed case invariably leads to a greater post-cracking residual strength (as shown in Fig. 10.1 for fiber contents of 50 and 75 kg/m^3).

It may be argued that in the results presented in Fig. 10.1 the mixed shotcrete situation always led to a lower peak load in the elastic branch - undoubtedly the cause of its smaller instability region. However, it must be considered that, in both fiber contents tested, the average residual load for the mixed case was almost twice that of the shot situation. Since both cases have a similar number of fibers intercepting the cracked section (equal V'_f), it must be concluded that this is caused by greater fiber breakage in the shot case - confirmed by visual observation of the cracked section.

Although the exact causes[1] for this are not known, the fact remains that, as shown by Fig. 10.1, even for situations of equal in-situ fiber content (i.e. without bringing into consideration the fiber

---

[1] Possibly a stronger fiber-matrix interface region in the shot situation, due to its stiff rheology, leading to greater bond.

194
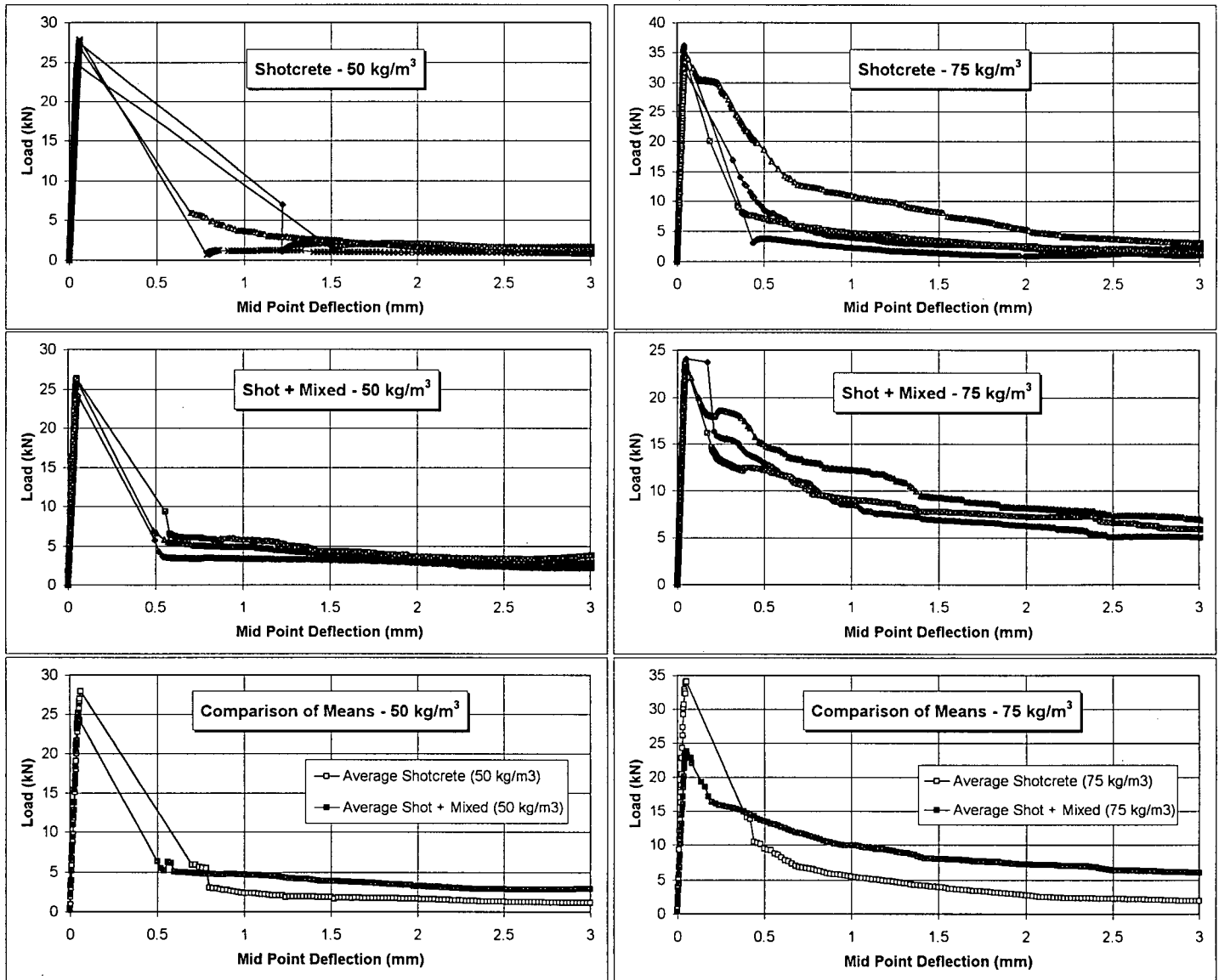
Figure 10.1 - Influence of mixing on the flexural toughness behavior of fiber reinforced dry-mix shotcrete : shot, mixed and comparison of average behavior (hooked fibers, 50 and 75 kg/m³ - respect., left and right).

rebound issue) the hooked fibers presently available in the market were developed to perform in cast-concrete and are not optimized from a dry-mix shotcrete toughness perspective.

The objective of this chapter is to introduce a new concept in fiber design and to use the fiber rebound information generated in Chapter 8, along with the model developed in Chapter 9, in order to arrive at a fiber geometry that is optimized with respect to flexural toughness performance for dry-mix shotcrete.

10.2 - Material and Methods

Single fiber pull-out experiments were conducted using the same apparatus described in Fig. 9.3 and developed by Banthia & Trottier (1995). The cementitious matrix used in these experiments was the same pre-blended, bone-dry mixture used for the shotcrete experiments at a water to cement ratio of 0.40 (an average value for the 2 MPa shooting consistency, as shown in Table 3.1). In order to arrive at the exact fiber dimensions that allowed the fiber anchoring concept devised here to be realized (item 10.3) single fibers were manually produced using a hand-press (capacity in excess of 5 kN). Once the desired fiber dimensions were determined, mass scale fiber production for the shotcrete tests was carried out using an automatic feed press, equipped with a variable length die. Steel used for manufacturing fibers had tensile strength of 1100 to 1200 MPa and circular cross section.

Shotcrete was produced and sampled using identical shooting procedures and equipment as described in items 7.2 and 8.2 at a constant fiber content of 60 kg/m^3. All flexural toughness tests were carried out at the age of 7 days - this testing age was chosen since it is commonly used for shotcrete quality control in the industry as a means of minimizing instability in the post-cracking region of the flexural toughness curve.

Cast SFRC was also tested in order to compare the reinforcing capability of the various fibers produced at an equal and controlled fiber content (fixed at 0.75% by volume - approximately 60 kg/m^3).

10.3 - The Fiber Anchorage Concept

As described in Chapter 9, fibers being pulled-out of the concrete matrix is the main mechanism that allows SFRC to have increased post-cracking resistance. As a result, fibers are usually deformed at the ends, or along their length, in order to enhance anchorage with the matrix. With respect to their pull-out load vs. displacement behavior, the fibers presently available in the market can be divided into two large groups, depending on their anchoring mechanism: "dead anchors" and "drag anchors". In the first case, the fiber is equipped with a hook at its end and its pull-out behavior is characterized by an increasing load bearing capacity up to approximately 0.5 mm (Fig. 10.2) point after which the pull-out resistance tends to drop as the hook is straightened or broken[2].
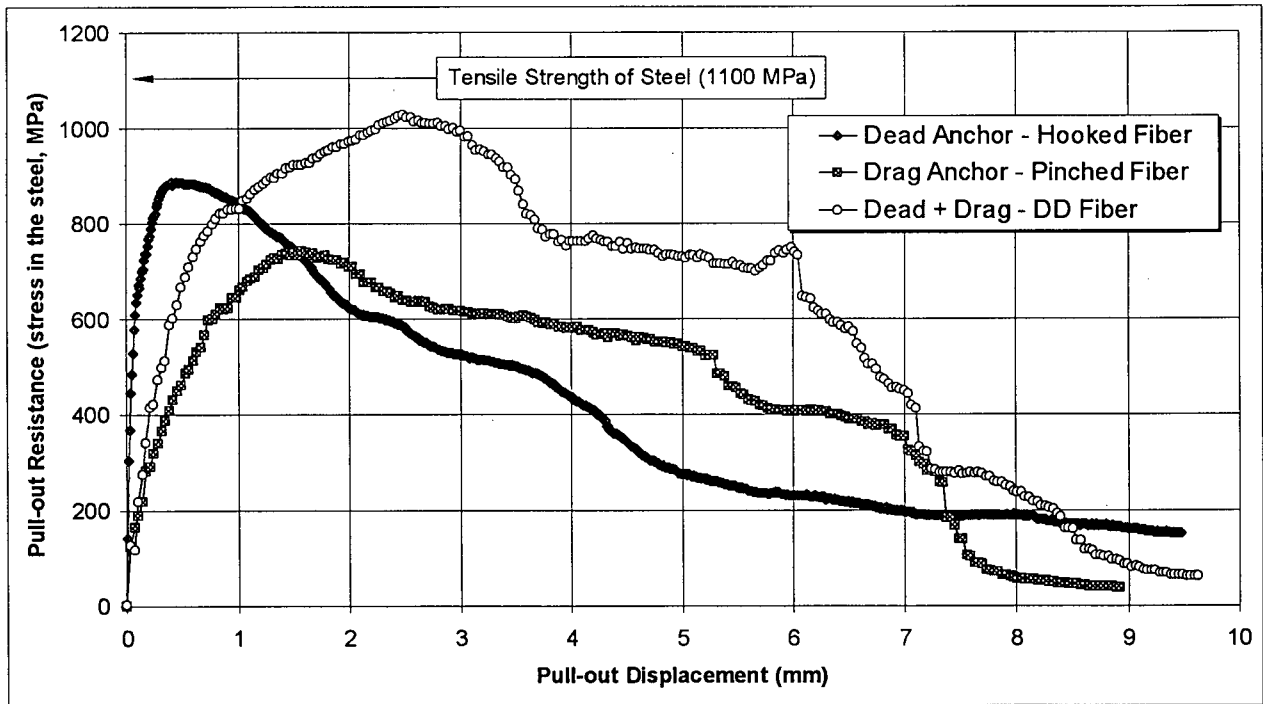
Figure 10.2 - Characteristic pull-out behavior of steel fibers with "dead", "drag" and "dead + drag" anchors. Fibers were aligned with the pull-out direction, fiber geometries in Table 10.1.

In the case of a "drag anchor", the fiber is enlarged at its ends in such a way that, during pull-out, the enlargement generates friction with the matrix and the fiber is "dragged" out of its concrete

---

[2] Twin-cone fibers can also be considered to belong to this category since their anchors tend to break during pull-out (as shown by Banthia & Trottier, 1995).

embedment. With respect to its pull-out behavior, this type of fiber usually shows a relatively lower maximum pull-out resistance when compared to the "dead anchor" case, but its effect tends to last for a greater pull-out displacement, and therefore a greater pull-out energy (the area contained by the pull-out curve[3]) is consumed by the end of the pull-out process (Fig. 10.2).

The concept involved in the development of this new fiber is to conciliate the advantages of a high maximum pull-out resistance of the "dead anchor" with the greater pull-out energy of the "drag anchor". In order to do so, a fiber design was devised in which both components are present, thus creating a "dead plus drag" (or DD) anchor (Fig. 10.3). The rationale involved is that, as the pull-out force increases, maximum pull-out resistance is developed[4], at which point the "dead" component of the anchor fails[5], leaving the "drag" component to generate frictional resistance. The result is simultaneously maximized pull-out resistance and pull-out energy (Fig. 10.2 and Table 10.1).

To determine the exact fiber dimensions that allow this concept to be realized, using the basic shape in Fig. 10.3, individual fiber pull-out tests were carried out initially using either a "dead" or a "drag anchor" of varying dimensions. The objective of this was to empirically obtain the dimensions that satisfied the conditions for which:

$$\text{Pull-out Stress }_{\text{"dead"}} + \text{Pull-out Stress }_{\text{"drag"}} \leq \text{Tensile Strength of Steel} \qquad 10.1$$

Once the exact dimensions were found (Fig. 10.4) the design for the anchor was fixed as a function of the fiber diameter (Fig. 10.3). It should be noticed that, compared to the hooked and "drag" fibers, this new anchoring concept (here named DD) led to a maximum pull-out resistance 14 to 36% greater and a 42% increase in pull-out energy (Table 10.1).

---

[3] In order to allow comparison of fibers of different diameter, in Fig. 10.2 the pull-out force is divided by the fiber cross sectional area. By doing so, the pull-out energy results in units of J/mm^2 (i.e. energy consumed per unit area of steel). The total pull-out force and energy can be estimated by multiplying this quantity by the average expected area of steel (the fiber density, Eq. 9.8, multiplied by the fiber cross sectional area and the cracked area of concrete).

[4] It is desirable to achieve a pull-out resistance as high as possible without however reaching the tensile strength of the steel, which would inevitably lead to fiber breakage.

[5] Failure of the "dead anchor" (Fig. 10.3) occurs by either breakage or lateral bending of the anchor leading to a reduction in its width.
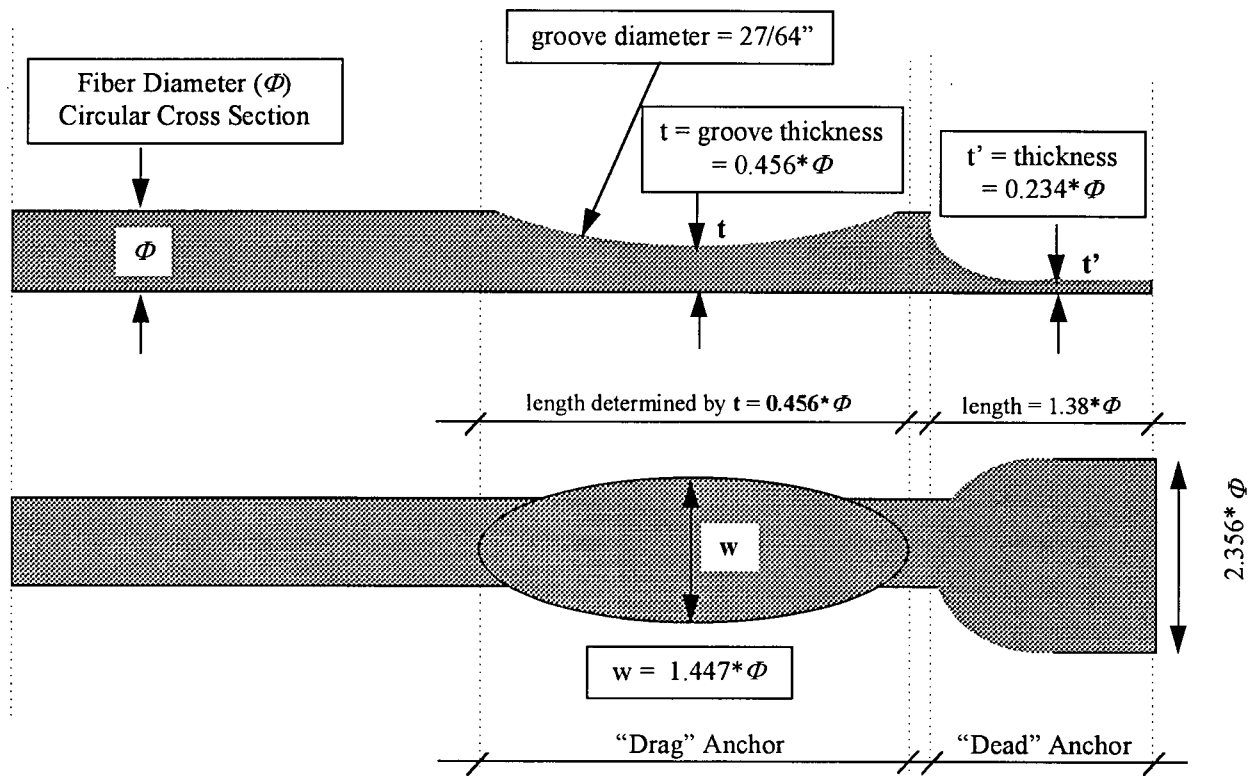
Figure 10.3 - Shape and dimensions of the fiber design that allow the DD anchoring concept to be realized.

Table 10.1 - Comparison among steel fibers with "dead", "drag" and DD anchors with respect to maximum pull-out stress and energy (from Fig. 10.2).

Anchor Type*	Shape	Dimensions* (mm)	Maximum Pull-out Resistance (MPa)	Pull-out Energy (J/mm^2)**
"Dead Anchor"		$\Phi = 0.5$, $l_f = 28$	885	3.42
"Drag Anchor"		$\Phi = 0.65$, $l_f = 30$	740	3.82
"Dead + Drag"		$\Phi = 0.89$, $l_f = 25.4$	1010	5.41

* circular cross section - "Dead", "Drag" and "Dead + Drag" anchors refer, respectively to hooked, pinched and DD fibers.

** computed up to a 7 mm pull-out displacement
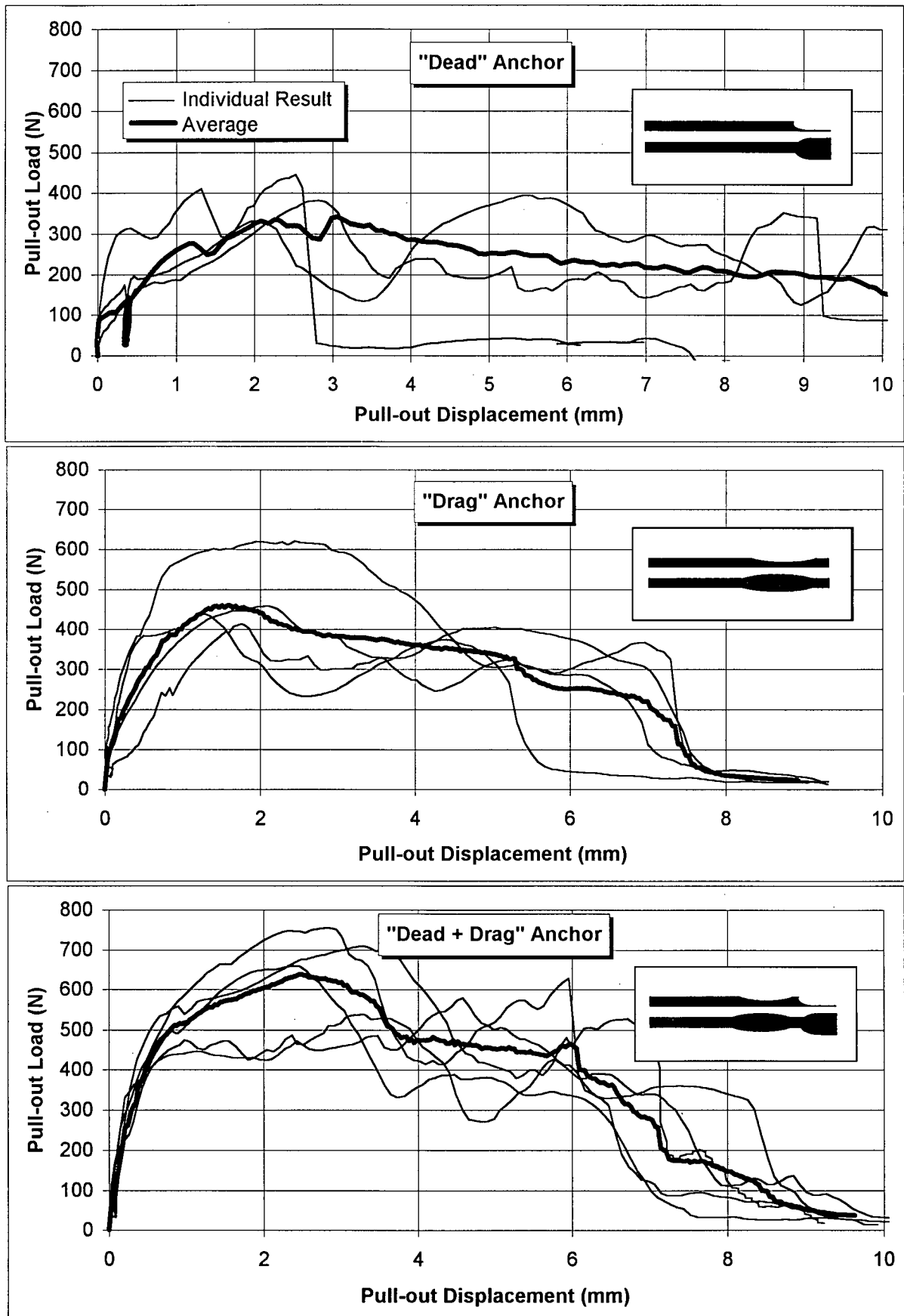
Figure 10.4 - Pull-out of "dead", "drag" and "dead + drag" anchors using the DD shape fiber diameter = 0.89 mm, dimensions as shown in Fig. 10.3.

10.4 - Length and Diameter Optimization

10.4.1 - Analytical Optimization with Respect to Length

As mentioned earlier, from basic SFRC technology, it is well known that, for a given fiber content, fibers of smaller diameter and greater length lead to increased flexural toughness performance. However, as shown in item 8.3.4, the aspect ratio, given by the quotient $\dfrac{l_f}{\sqrt{\phi}}$, is the primary determinant of fiber rebound in dry-mix shotcrete, with slender fibers tending to rebound more. Therefore, it should be expected that optimum conditions of fiber length and diameter exist, for which a compromise between fiber rebound and reinforcing capability lead to maximized shotcrete toughness performance.

In order to analytically estimate the optimum fiber length, the model described in Chapter 9 was used with the fiber pull-out relationships obtained experimentally using the DD shape (Fig. 10.3) at a fixed fiber diameter of 0.89 mm, at fiber lengths of 12.5, 19, 25.4 and 40 mm. The experimental pull-out relationships obtained for aligned and 45 degree inclined fibers[6], as well as the Ramberg-Osgood functions used to represent them in the model (Eq. 9.15) are presented in Fig. 10.5. The fitting constants as well as the assumed short fiber function are presented in Table 10.2.

For all cast concrete situations tested, the fiber content was assumed to be 0.75% by volume. For the shotcrete cases, the in-situ fiber content was estimated using Eq. 2.2 with a fiber rebound (R_f) estimated using the trendline in Fig. 8.11 and a design fiber content of 60 kg/m³. For all cases, the overall rebound (R) was assumed to be 35%[7]. The resulting estimated in-situ fiber contents assumed in the model are presented in Table 10.3.

---

[6] Because data on the pull-out behavior of only two inclination angles were available (zero and 45 degrees) in this case, the numerical solution to Eq. 9.19 was done using the same trapezoidal integration, however resulting in the expression $\overline{f}(w) = \dfrac{1}{2}\left\{\left[\left(f_0(w) + f_{45}(w) + f_{90}(w)\right)\cdot\dfrac{1}{3}\right] + f_{hook}(w)\right\}.$

[7] For example, using a design fiber content of 60 kg/m³ (0.764% vol.), for the case of a fiber having diameter = 0.89 mm and length = 25.4 mm, from Fig. 8.11, the fiber rebound is estimated at R_f = 64%. From Eq. 2.2, using V_f = 0.764%, R = 35% and R_f = 64%, the expected in-situ fiber content is estimated at V'_f = 0.42%.
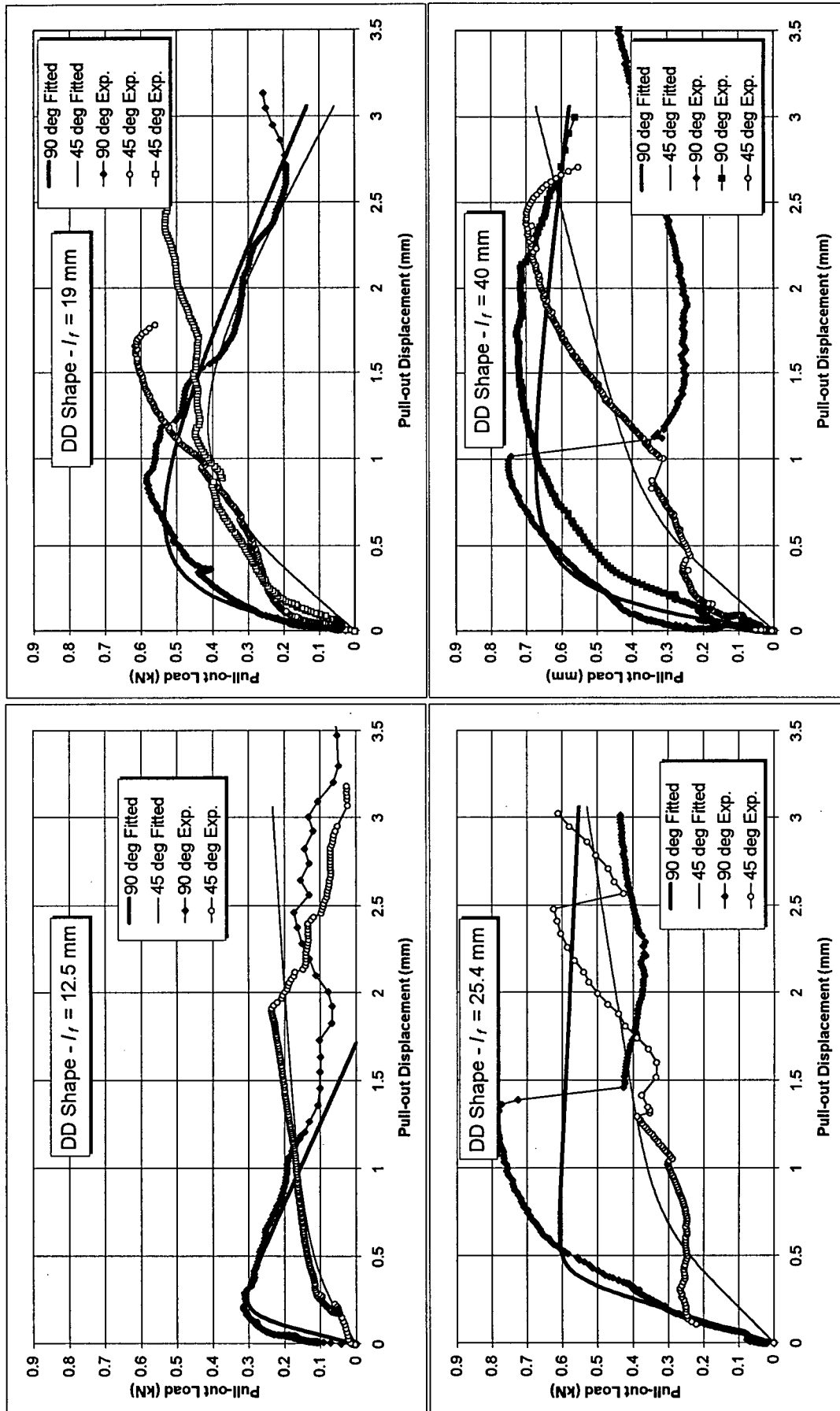
Figure 10.5 - DD fiber design (diam. = 0.89 mm, l_f = 12.5, 19, 25.4 and 40 mm) experimental pull-out behavior and fitted functions used as input for the model; constants in Table 10.2.

Table 10.2 - Fitting constants (A, B, C and E_p - Eq. 9.15) used to input the DD fiber pull-out behavior into the model - fitted curves are presented in Figs. 10.5 and 10.7.

Diameter (mm)	Length (mm)	Inclination	A	B	C	E_p	F_{short} (kN)*	w_{max} (mm)	w_{zero} (mm)
0.89	12.5	0°	-0.11	5.9	4	2	0	0	0
		45°	0.09	2	2	0.32			
	19	0°	-0.062	4.5	1.2	3.5	0.506	0.04	0.4
		45°	-0.5	0.9	2.8	0.55			
	25.4	0°	-0.015	2.6	7	1.6	0.633	0.05	0.7
		45°	0.15	1.42	4	0.5			
	40	0°	-0.02	4	1.8	3	0.746	0.06	0.7
		45°	0.22	1.42	4	0.55			
0.61	25.4	0°	-0.38	1.5	4	0.7	0.35	0.05	0.7
		45°	-1.5	0.6	6	0.25			
0.76		0°	-0.35	1.3	4	0.9	0.59	0.05	0.7
		45°	-0.9	0.9	4.5	0.55			
0.89		0°	-0.015	2.6	7	1.6	0.633	0.05	0.7
		45°	0.15	1.42	4	0.5			

* F_{short} refers to the assumed behavior for the smallest possible embedment length - F_{hook} in Fig. 9.6.
where F_{short} and w_{max} indicate maximum pull-out load and displacement and w_{zero} = end of pull-out contribution

Table 10.3 - Estimated in-situ fiber content assumed in the model for the shotcrete cases and the actual figures obtained experimentally.

Diameter (mm)	Length (mm)	Case	V_f (% Vol.)	$l_f/(\phi)$^0.5 (mm$^{-0.5}$)	Estimated			Actual Figures[e]		
					R^b (%)	R_f^c (%)	V'_f^d (% Vol.)	R (%)	R_f (%)	V'_f (% Vol.)
0.89	12.5	cast	0.75%	13.24	-	-	-	-	-	-
		shotcrete	0.75%[a]		35%	50%	0.59	32.5	46%	0.65
	19	cast	0.75%	20.14	-	-	-	-	-	-
		shotcrete	0.75%		35%	57%	0.51	31	59%	0.43
	25.4	cast	0.75%	26.92	-	-	-	-	-	-
		shotcrete	0.75%		35%	64%	0.42	35.1	68%	0.37
	40	cast	0.75%	42.40	-	-	-	-	-	-
		shotcrete	0.75%		35%	79%	0.25	31	86%	0.17
0.61	25.4	cast	0.75%	32.50	-	-	-	-	-	-
		shotcrete	0.75%		35%	69%	0.36	37.6	74%	0.28
0.76		cast	0.75%	29.10	-	-	-	-	-	-
		shotcrete	0.75%		35%	67%	0.39	41.5	67%	0.41
0.89		cast	0.75%	26.90	-	-	-	-	-	-
		shotcrete	0.75%		35%	64%	0.42	35.1	68%	0.37

a - Equivalent to approximately 60 kg/m^3
b - Assumed average overall rebound.
c - Estimated using the trendline in Fig. 8.11.
d - Estimated using Eq. 2.2
e - Experimentally obtained from actual shotcrete.

The flexural toughness results obtained using the model for the cast and shotcrete cases are presented in Fig. 10.6a to c. As shown by these Figures, the model predicts a linear growth in toughness with length for cast concrete (Figs. 10.6a and c) while an optimum fiber length of approximately 25 mm is predicted for shotcrete (Figs. 10.6b and c). Once more, this loss in toughness for the 40 mm fiber length is due to the greater fiber rebound that its high $\dfrac{l_f}{\sqrt{\phi}}$ ratio tends to generate.

10.4.2 - Analytical Optimization with Respect to Diameter

In order to analytically estimate the optimum fiber diameter, the fiber length was fixed at 25.4 mm (previously found to be an optimum value) and the model was used to test cases of fiber diameters equal to 0.61, 0.76 and 0.89 mm[8]. The experimental pull-out behavior obtained for these fibers are presented in Fig. 10.7, along with the fitted Ramberg-Osgood functions used to represent them in the model (Eq. 9.15, constants given in Table 10.2). Once more, both cast concrete ($V_f = 0.75\%$) and shotcrete were tested, with the in-situ shotcrete fiber content being estimated using Eq. 2.2 in a procedure identical to that described in 10.4.1. The estimated in-situ fiber content results used in the model are presented in Table 10.3.

The analytical results obtained on the estimated flexural toughness of cast concrete and shotcrete are presented in Figs. 10.8a to c. As these Figures show, the model predicts that, in both cast concrete and shotcrete, maximum toughness should occur for the 0.76 mm diameter case. As will be shown ahead (Fig. 10.12) the optimum fiber diameter found for the cast concrete case is incorrect since cast concrete toughness is known to decrease with an increase in fiber diameter. This is a consequence of the fact that the model underestimates the post-cracking resistance for the 0.61 mm case. The optimum point estimated for the shotcrete case will, however, be confirmed and is a consequence of the compromise point between the low fiber rebound that characterizes a greater fiber diameter and the greater toughness that a smaller diameter fiber generates.

---

[8] The diameter sizes tested were chosen as a function of the steel wire sizes commercially available.
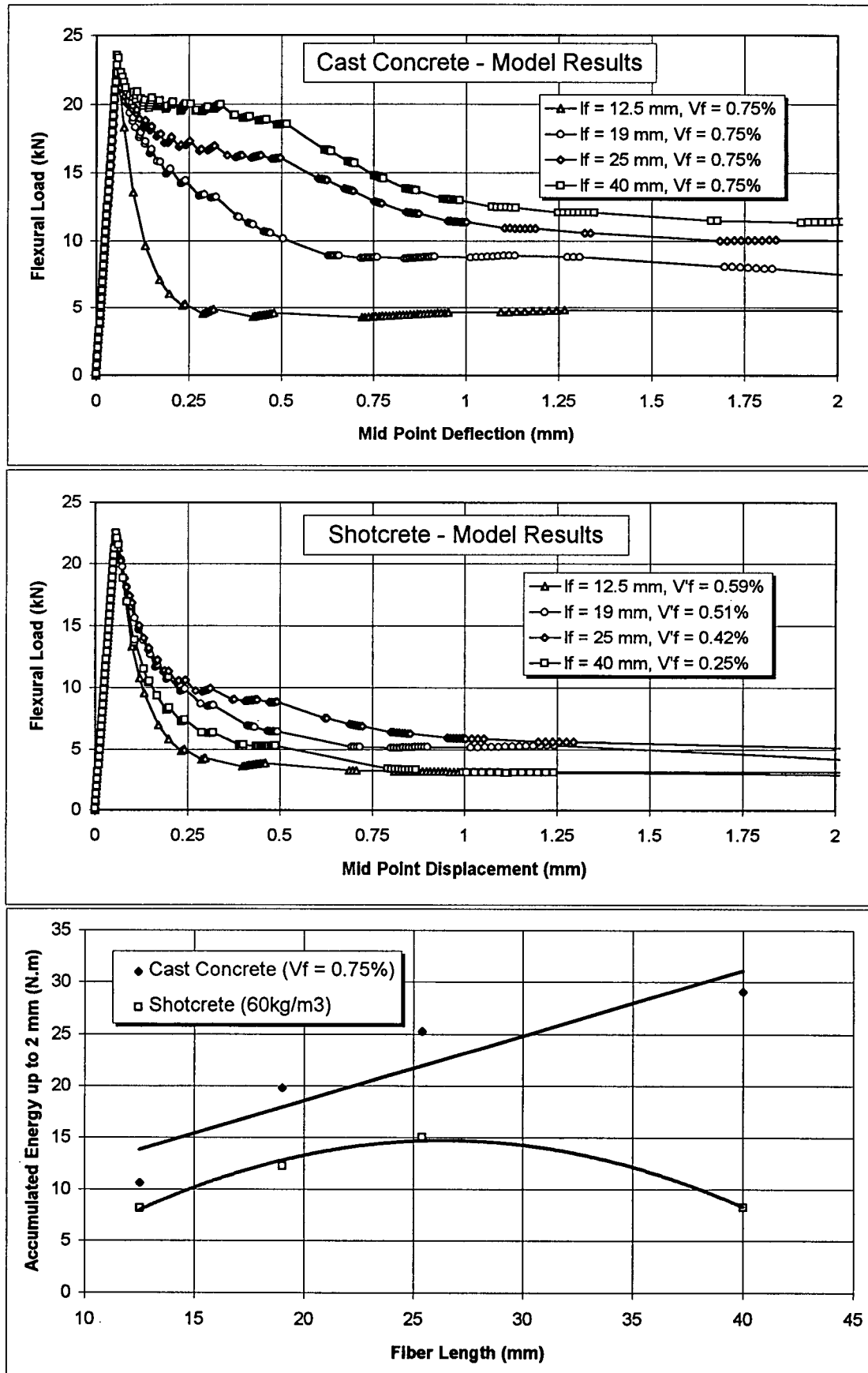
Figure 10.6 - Model results for variation in flexural toughness with fiber length. DD fiber (diam = 0.89 mm), cast concrete (Vf = 0.75%) and dry-mix shotcrete (60 kg/m3).
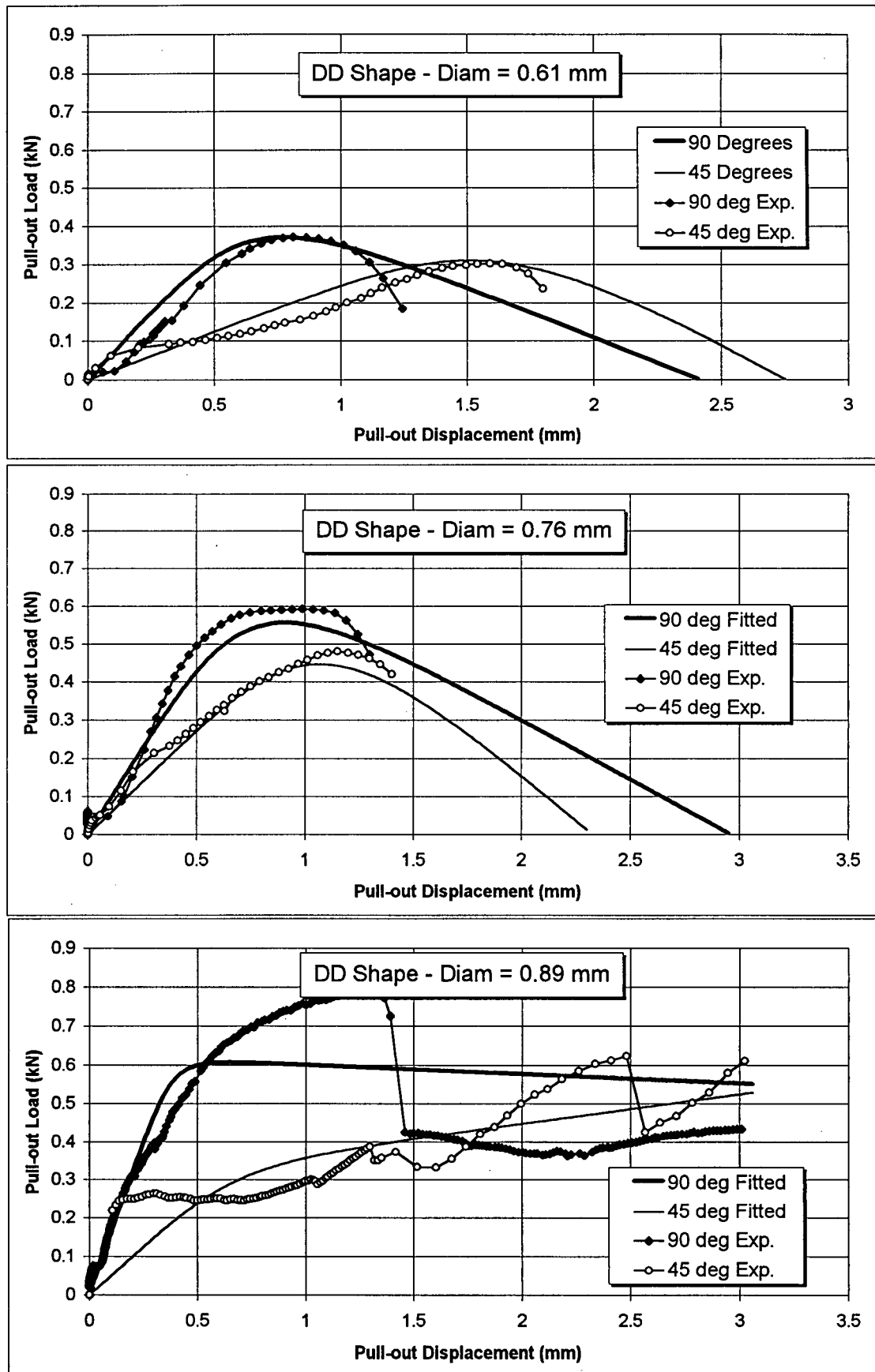
Figure 10.7 - DD fiber design (I_f = 25.4, diam. = 0.61, 0.76 and 0.89 mm) experimental pull-out behavior and fitted functions used as input for the model; fitting constants in Table 10.2.
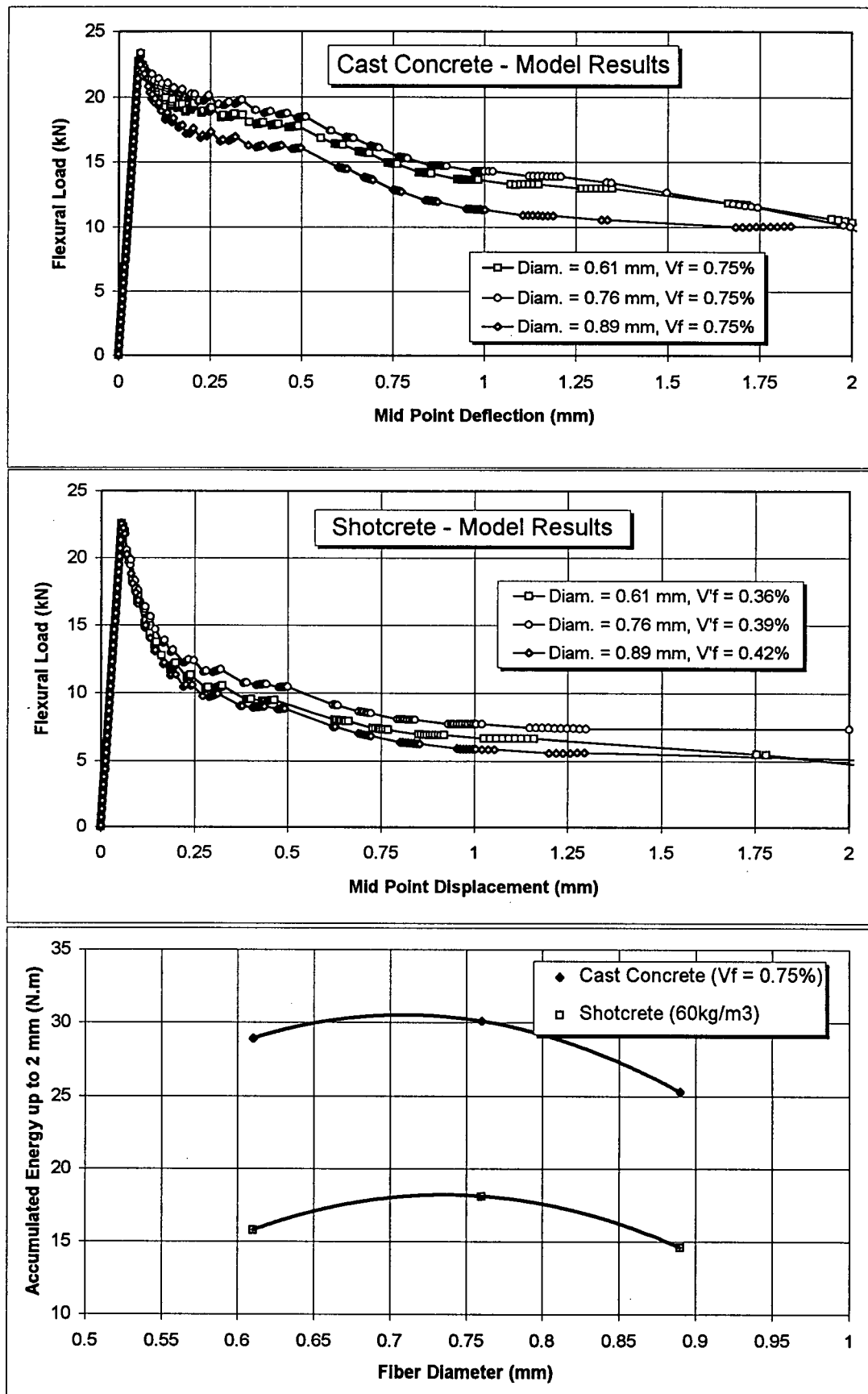
Figure 10.8 - Model results for variation in flexural toughness with fiber diameter. DD fiber (l_f = 25.4 mm) concrete (V_f = 0.75%) and dry-mix shotcrete (60 kg/m^3).

10.4.3 - Experimental Optimization with Respect to Length

The fiber optimization process was also analyzed experimentally. To investigate the variation in flexural toughness with fiber length, dry-mix shotcrete was produced at a 60 kg/m^3 fiber content using the DD fiber design (Fig. 10.3) at a fixed fiber diameter of 0.89 mm for cases of fiber length equal to 12.5, 19, 25.4 and 40 mm. For all cases (except l_f = 19 mm) cast concrete was also tested for comparative purposes and control at V_f = 0.75%.

The shotcrete experimental flexural toughness results are presented in Fig. 10.9 in terms of individual specimen responses and, in Figs. 10.10a to c, in terms of the average of all specimens. These results confirm the linear variation in toughness for the case of cast concrete (Figs. 10.10a and c) while an optimum fiber length of approximately 30 mm is found for the case of shotcrete - as predicted by the model (Fig. 10.6).

10.4.4 - Experimental Optimization with Respect to Diameter

Shotcrete was also produced using the DD fiber design (60 kg/m^3) at a fixed 25.4 mm fiber length for cases of fiber diameter equal to 0.61, 0.76 and 0.89 mm. Again, for comparative purposes and control, cast concrete was tested at V_f = 0.75% for all three fiber sizes.

The shotcrete toughness results obtained are presented in Fig. 10.11 in terms of the individual specimen responses and, in Figs. 10.12a to c, in terms of the average response. These results show that, for the case of cast concrete, the flexural toughness decreases with an increase in fiber diameter. For the shotcrete case, however, the optimum fiber diameter predicted by the model is confirmed at 0.76 mm. This should be considered, in part, a consequence of the higher fiber rebound that the smallest fiber diameter presented (Table 10.3 and in accordance with Fig. 8.9). However, it must also be considered that dry-mix shotcrete usually results in a high-strength matrix (flexural toughness cracking load in excess of 20 kN for the ASTM C 1018 test), a condition for which smaller diameter fibers are known to lead to greater fiber breakage and a consequent loss in flexural toughness performance[9].

---

[9] Even under closed-loop, strain-rate controlled conditions of flexural loading, steel fiber reinforced dry-mix shotcrete still resulted in unstable failures, illustrating its greater brittleness as compared to cast concrete.
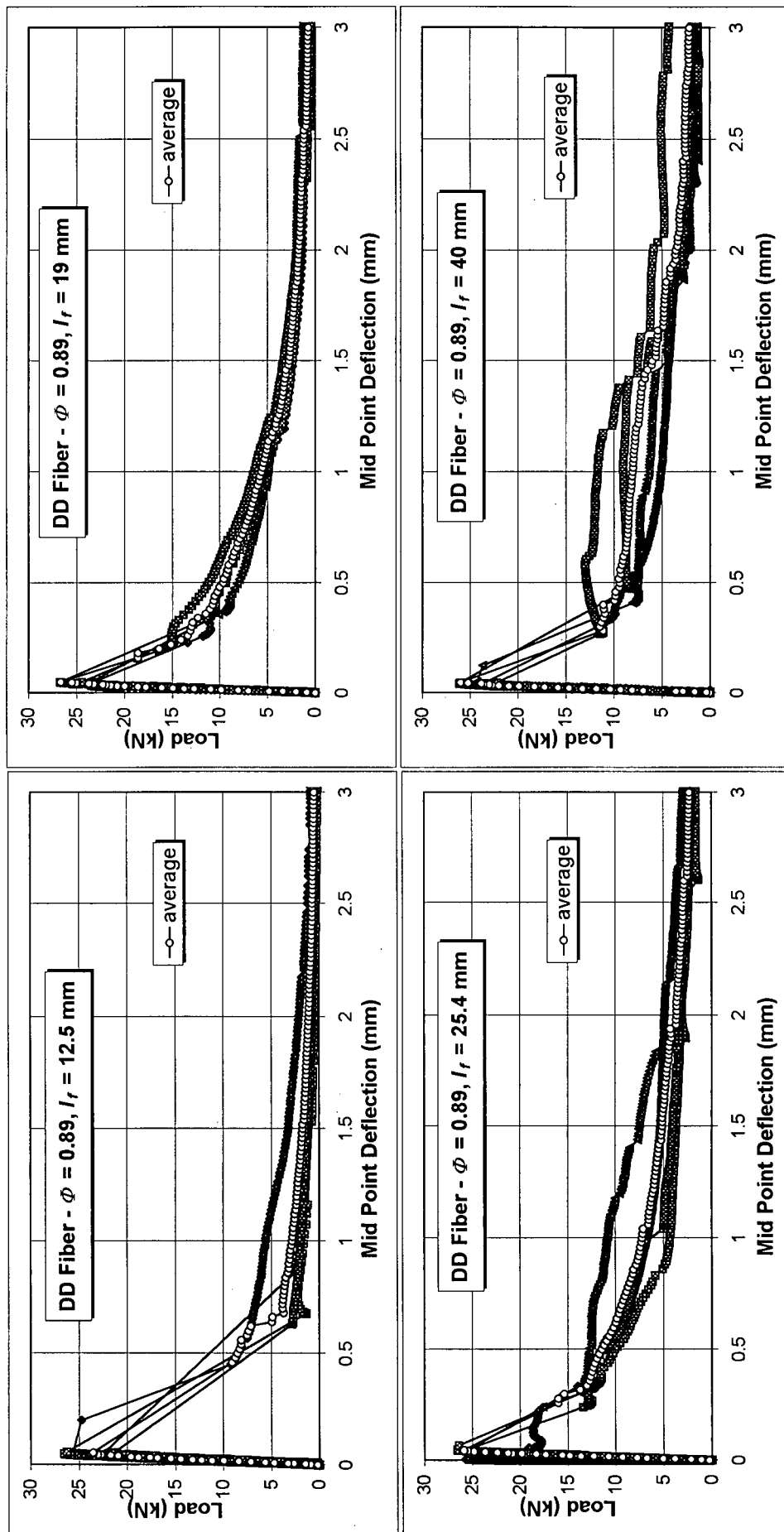
Figure 10.9 - Individual experimental results, flexural toughness of dry-mix shotcrete produced with DD fibers (60 kg/m^3); variation in fiber length.
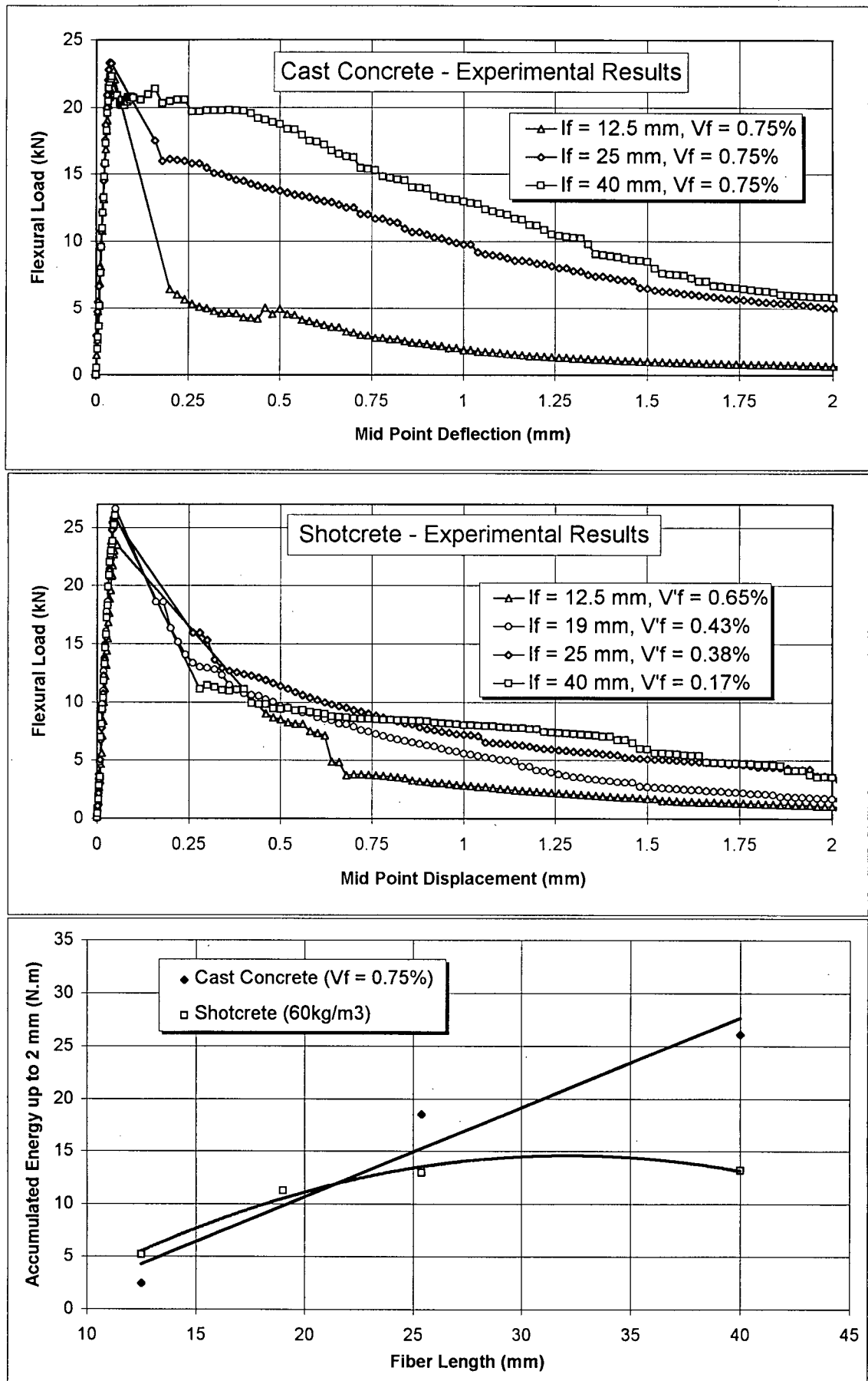
Figure 10.10 - Experimental results for variation in flexural toughness with fiber length. DD fiber (diam = 0.89 mm) cast concrete (V_f = 0.75%) and dry-mix shotcrete (60 kg/m^3).
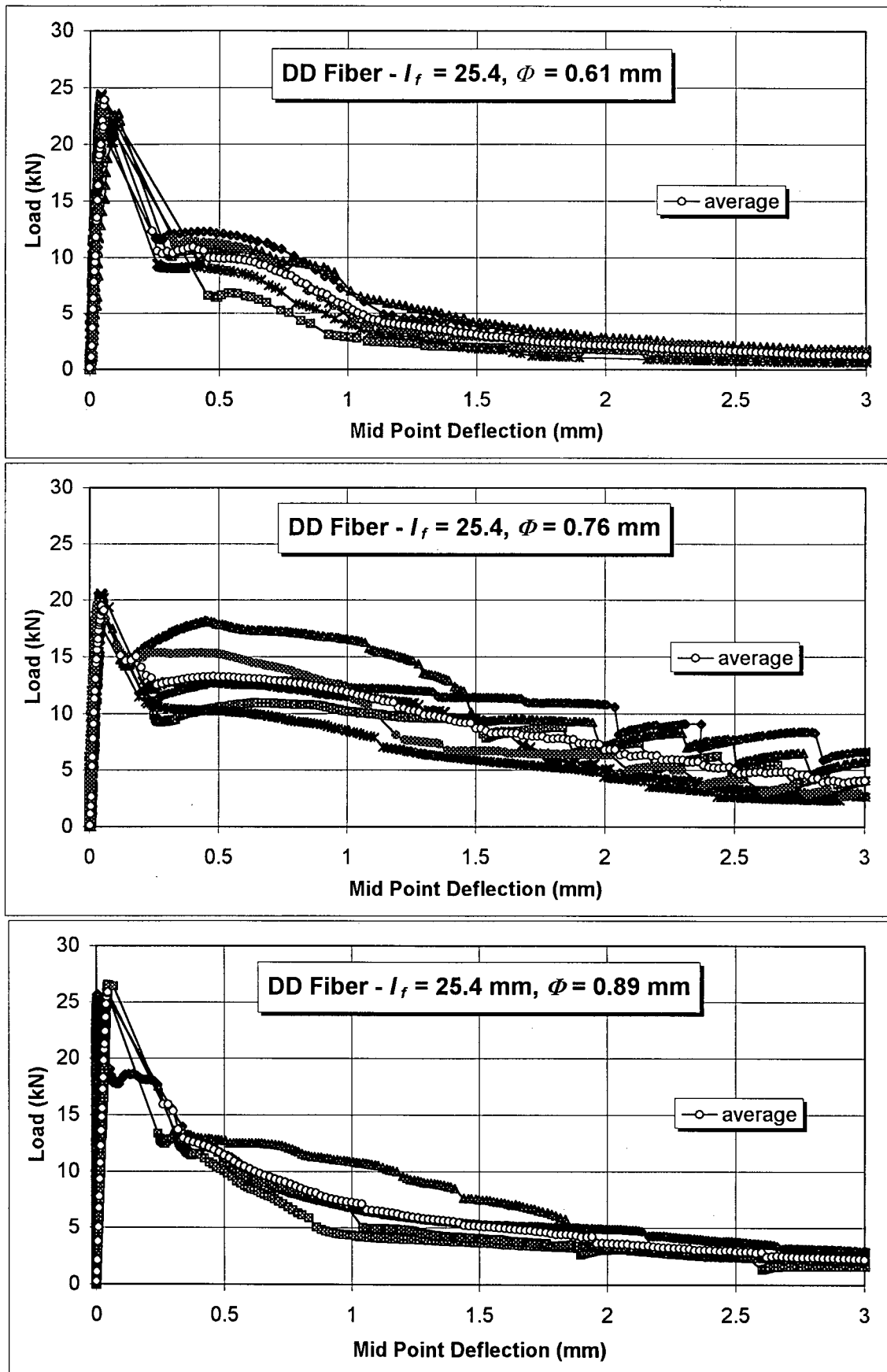
Figure 10.11 - Individual experimental results, flexural toughness of dry-mix shotcrete produced with DD fibers (60 kg/m^3); variation in fiber diameter.
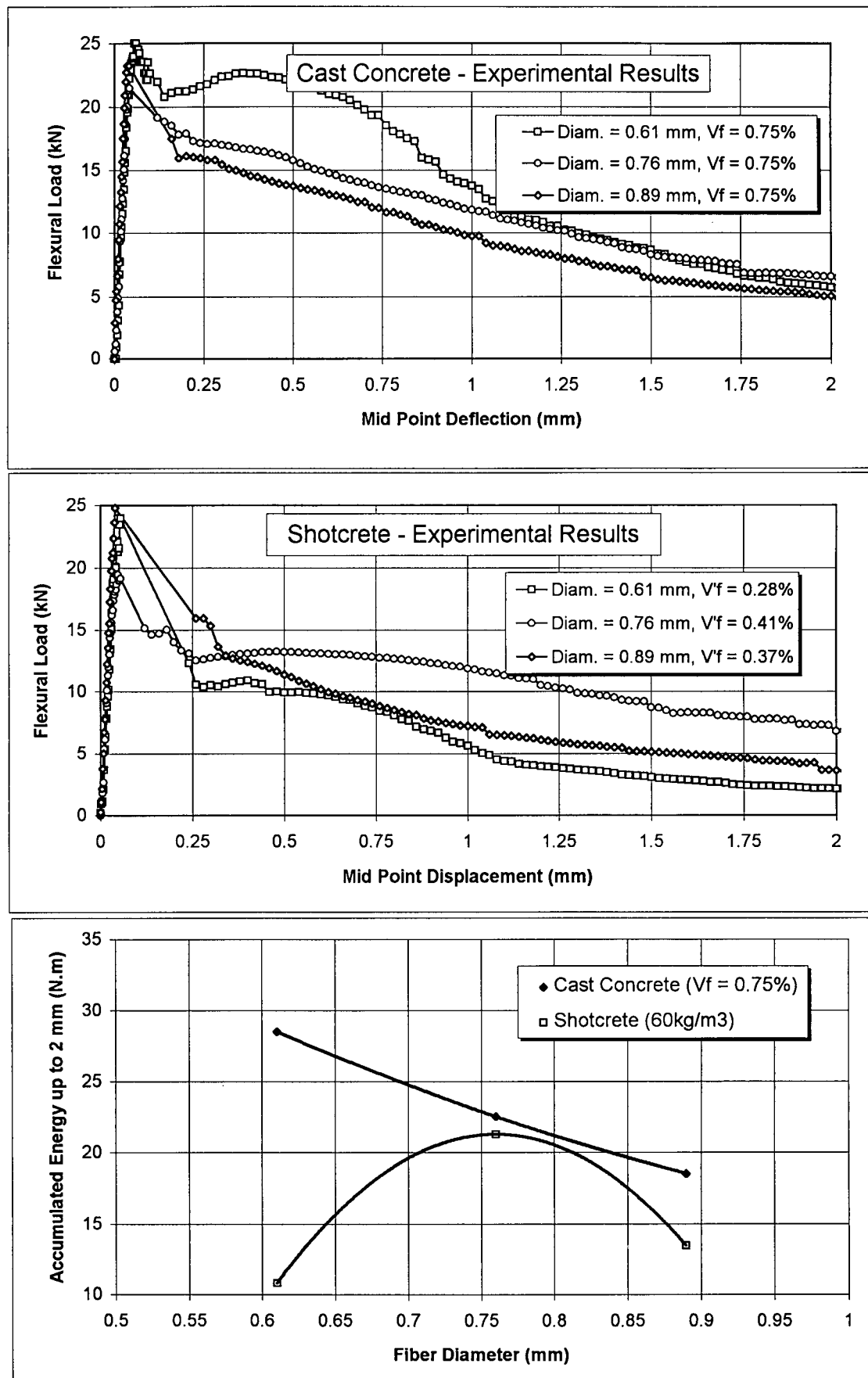
Figure 10.12 - Experimental results: variation in flexural toughness with fiber diameter. DD fiber (length = 25.4 mm) cast concrete (V_f = 0.75%) and dry-mix shotcrete (60 kg/m³).

10.5 - Prototype Testing and Performance Comparison with Market Fibers

Having arrived at the fiber design (Fig. 10.3) and optimized conditions of length and diameter, the prototype optimized DD fiber was fabricated in mass quantities (l_f = 25.4 mm, diameter = 0.737 mm) and tested in dry-mix shotcrete. Two other commercial steel fiber geometries that are often used for shotcrete reinforcement were also tested (here named hooked and pinched geometries - Table 10.1). All mixtures were produced using a 60 kg/m^3 fiber content.

The flexural toughness results obtained are presented in Fig. 10.13 in terms of individual specimen responses and, in Fig. 10.14, in terms of the average behavior. The ASTM and JSCE toughness indices[10], calculated from the average responses, are presented in Fig. 10.15 and Table 10.4. These results indicate that, when compared with the hooked fiber, the optimized fiber design proposed showed a 100% increase in ASTM indices and, on average, a 76% increase when compared with the pinched case (Table 10.4). For the JSCE indices, the optimized fiber showed an 85% performance increment with respect to the hooked case and 27% when compared to the pinched geometry.

From Table 10.4 it may be seen that one of the reasons for this improved toughness performance is the reduced fiber rebound for the optimized shape (approximately 15% lower) leading to a greater in-situ fiber content. The other reason is related to the superior pull-out performance of this fiber, as explained earlier in item 10.3.

---

[10] For all toughness calculations, the energy consumed in the unstable post-cracking branch was neglected (i.e. the area contained by the unstable branch of the diagram was not accounted for).
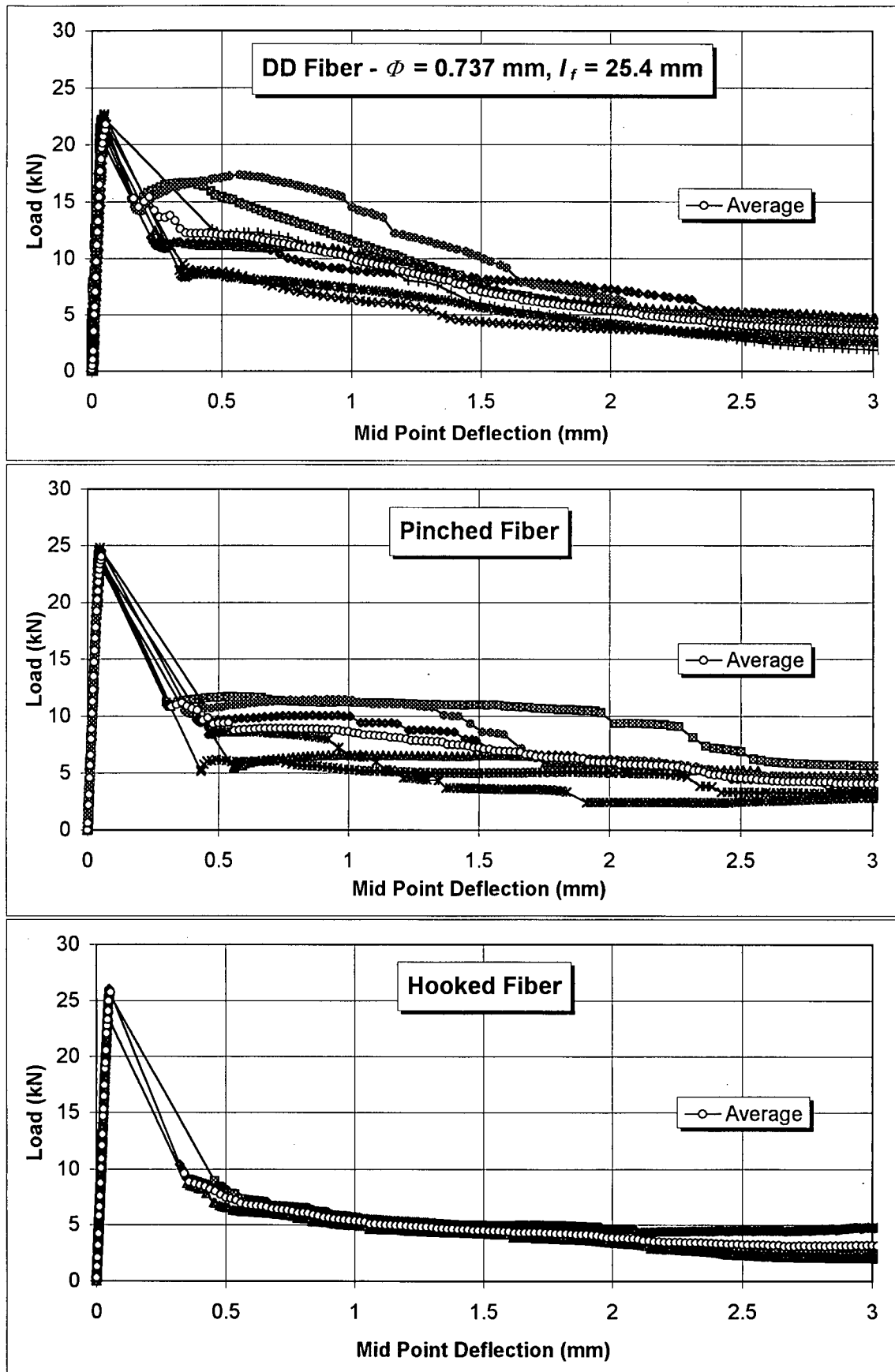
Figure 10.13 - Individual experimental results, flexural toughness of dry-mix shotcrete produced with DD fibers, pinched and hooked fibers (60 kg/m^3 for all cases).
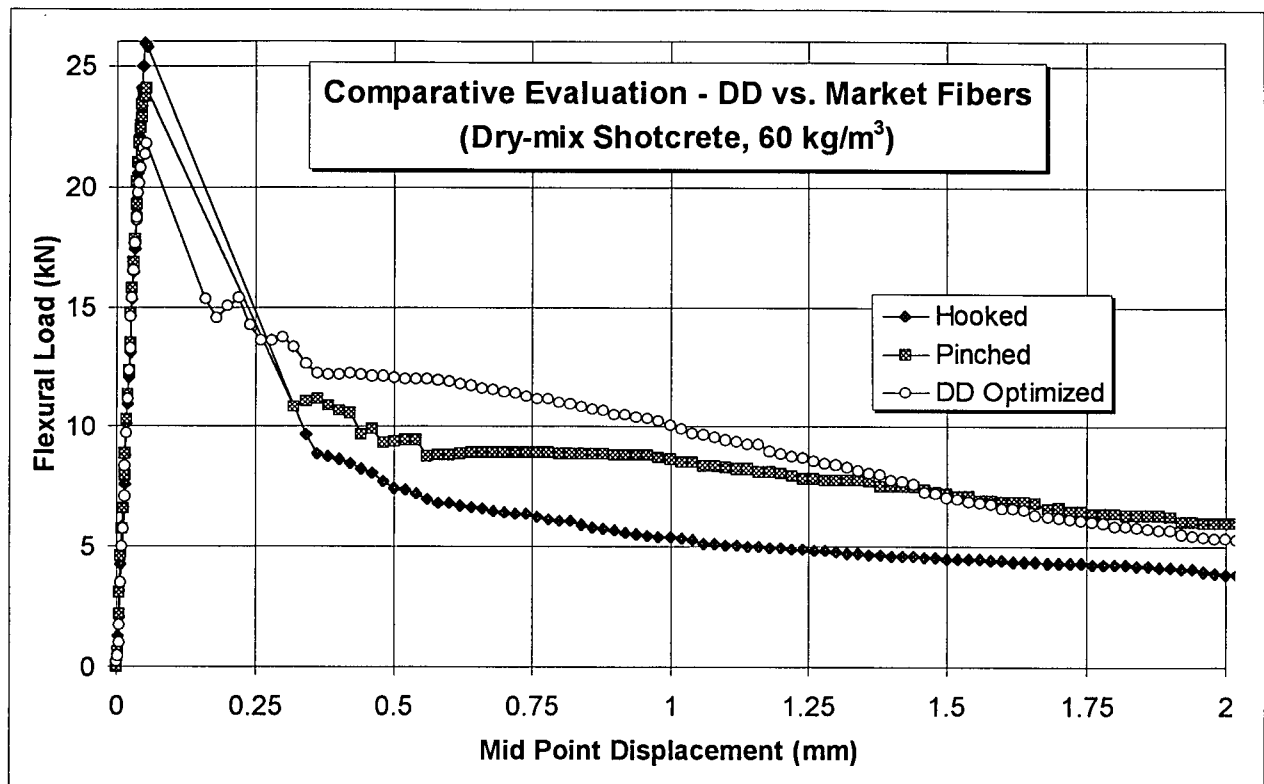
Figure 10.14 - Flexural toughness testing: comparison between the DD optimized fiber design and market fibers (dry-mix shotcrete, 60 kg/m^3 - results are average of six or more specimens).

Table 10.4 - Performance comparison: DD fiber against market leading types (average experimental results).

Criterion	Hooked	Pinched	DD
Fiber Rebound (%)	77.20	78.70	62.70
In-situ Fib. Content (%)	0.31	0.20	0.35
ASTM I5	U*	U	U
ASTM I10	U	U	3.58
ASTM I20	3.28	4.09	8.37
ASTM I30	5.43	7.28	12.83
ASTM I50	9.01	13.29	20.27
T JSCE (J)	9.82	14.25	18.15
F JSCE (MPa)	1.47	2.14	2.72

* test unstable at this midspan level.
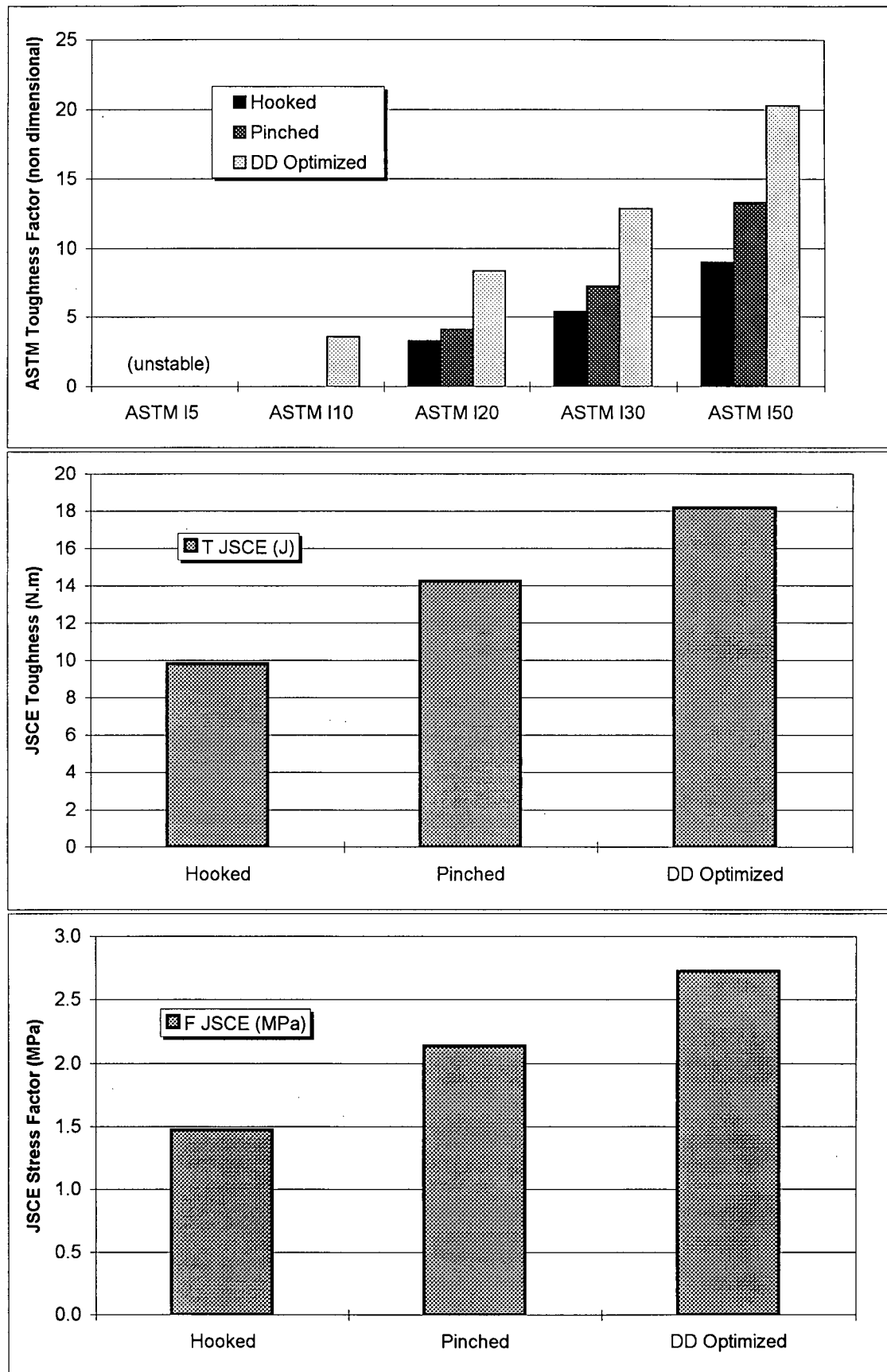
Figure 10.15 - Performance comparison with respect to ASTM and JSCE flexural toughness indices: dry-mix shotcrete with DD optimized, hooked and pinched fibers (all mixes at 60 kg/m^3).

10.6 - Conclusions

In this Chapter, the reinforcing pull-out mechanisms used by the state-of-the-art steel fibers have been analyzed and a new concept in steel fiber design has been introduced. In addition, concepts developed in Chapters 8 and 9 were used to optimize this fiber with respect to length and diameter. More specific conclusions to be drawn from this chapter are as follows:

1 - Even at an equal in-situ fiber content (i.e. not taking into account the fiber rebound aspect) fibers of a small diameter (e.g. hooked, 0.5 mm diameter fibers) tend to lose post-cracking reinforcing performance due to fiber breakage when used in dry-mix shotcrete. The same behavior is not found in dry-mix shotcrete that has been subjected to mixing.

2 - A new concept in fiber anchorage has been developed that combines the advantages of a high maximum pull-out resistance of a "dead anchor" with the high pull-out energy of a "drag anchor". This concept was realized by using two anchors to form a "dead plus drag" (or DD) anchor.

3 - Contrary to cast concrete, it has been demonstrated both analytically and experimentally that, for a given fiber design, there are optimum fiber length and diameter conditions for which maximum dry-mix shotcrete flexural toughness is obtained.

4 - Using the DD anchor concept developed here, a steel fiber geometry was optimized and experimentally shown to have lower fiber rebound and yield significantly enhanced toughness performance when compared with the two market leading fibers available today.

Chapter 11 - General Conclusions and Recommendations for Future Research

11.1 - General Conclusions

Throughout this thesis, specific conclusions have been drawn at the end of each chapter and the reader should refer to those for a more detailed account. As for general conclusions to be drawn from this research program, it may be said that:

On the mechanics involved in the rebound process: Aggregate and steel fiber rebound in dry-mix shotcrete is a phenomenon governed by the impact of particles against the existing shotcrete bedding and is therefore characterized by strain rates several orders of magnitude greater than those usually encountered in traditional cast-in-place concrete conditions and testing procedures. Because of the high strain-rates involved, it is found that additives that lead to a reduction in the fresh shotcrete *viscosity*, without significantly influencing the yield strength (e.g. silica fume), are most effective in reducing fiber and aggregate rebound.

On minimizing rebound in dry-mix shotcrete: Through an extensive experimental program, it has been shown that, besides the obvious cost implications that it has, rebound in dry-mix shotcrete can also lead to a poorer in-situ shotcrete having a high cementitious content and low fiber content. It has also been experimentally shown that rebound can be kept to a minimum by proper adjustment of the shooting consistency, aggregate gradation, cement content, addition of fines (e.g., silica fume, crushed limestone, etc.) and adequate air-flow.

On the subject of shotcrete kinematics: Because the mechanism of aggregate and fiber rebound is essentially that of an impact process, the velocity of impact is one of its main determining parameters. In that respect, the high-speed camera test have shown that the nominal air speed and particle size are the main factors that determine both aggregate and steel fiber velocity, irrespective of air pressure or hose size.

On the subject of steel fiber rebound: For a given fiber geometry, steel fiber rebound is closely related and proportional to aggregate rebound. The main parameters of fiber geometry that

determine fiber rebound are the fiber length and diameter with fiber rebound showing a linear correlation with an aspect ratio given by the fiber length divided by the square root of its diameter.

On the reinforcing mechanism of steel fibers: Fibers being pulled-out of the cementitious matrix is the main mechanism of post-cracking reinforcement that allows SFRC to have flexural toughness several times higher than its unreinforced matrix. Using this concept, a simple model, based on straightforward principles of mechanics and statistics, has been proposed, allowing prediction of the composite post-cracking strength from the experimental pull-out behavior of single fibers.

On the development of an optimized steel fiber for the reinforcement of dry-mix shotcrete: Although it is well established that the flexural post-cracking resistance of cast-in-place concrete is proportional to the length and diameter of steel fibers, in dry-mix shotcrete, slender fibers tend to rebound more, causing a loss in the in-situ fiber content. As a result, it is found that there are optimum conditions of fiber length and diameter that lead to maximized toughness performance. Based on this concept and on the introduction of a novel fiber anchoring concept, a new steel fiber design has been proposed and demonstrated to lead to improved dry-mix shotcrete reinforcing performance when compared to the two most efficient commercial fibers.

11.2 - Suggestions and Recommendations for Future Research on the Subject

Throughout the course of this research project, a number of topics have surfaced for which further work is needed. Among those are some suggestions for future research:

1 - The water flowmeter developed for this research program showed to be a reliable and inexpensive means of controlling the amount of water added during shooting, giving the nozzleman greater control and allowing mixtures to be consistently reproduced. Analogously, the in-line air flowmeter used also showed to be a practical means of controlling the shooting velocity. Both instruments could be used by the industry without any modifications needed and with guaranteed benefits in terms of a better quality in-situ shotcrete and minimized rebound.

2 - There is a general lack of standards on the procedures used to fill test panels and test for shotcrete rebound. It has been demonstrated in this study that test panels shot positioned on the floor and leaning against the wall lead to lower aggregate and fiber rebound and are, therefore, not representative of actual shotcrete. In order for shotcrete tests to be consistent and representative, it is necessary to always position test panels on the wall or overhead. Furthermore, a device for measuring the shooting consistency (e.g. penetrometer[1]) should always be used to eliminate the subjectivity in the nozzleman's judgment and guarantee reproducibility of results. For dry-mix shotcrete, results from this thesis indicate that a 2 ± 0.5 MPa penetration resistance seems to be an adequate shooting consistency to be adopted.

3 - From the general model for aggregate rebound developed, it may be said that, in order to reduce rebound, the fresh shotcrete viscosity must be reduced. However, measures that reduce viscosity and yield[2] *simultaneously* (e.g. greater water addition) are not effective since this leads to lower build-up. Therefore, measures must be sought that reduce the viscosity while keeping the yield at an acceptable level.

4 - From the shotcrete flexural toughness tests shown throughout this thesis, it becomes apparent that instability in the post-cracking region often dominates the test, with meaningless results up to a 0.5 to 1 mm mid-point deflection (strictly speaking, the most important part of the test). This is caused by the combination of a high matrix strength, and low in-situ coarse aggregate and fiber contents that usually characterize dry-mix shotcrete. In order to minimize this problem, shotcrete is often tested for its flexural toughness at 7, rather than at 28 days - a measure which merely hides the problem rather than solving it.

Therefore, it is imperative that modifications be made to the flexural toughness test to seek a more stable failure mode. In that sense, some changes that would lead to greater stability without loss in the rationale involved are:

---

[1] There are pocket-size penetrometers readily available in the market that can be used for shotcrete. One such model is produced by Soiltest, Chicago, IL.

[2] Yield and viscosity are accounted for in the model described in Chapters 5 and 6 through the static and dynamic contact stresses respectively.

- reducing the peak load without reducing the cross sectional area sampled by decreasing the specimen height and increasing its width proportionally.

- reducing the peak load by increasing the span and/or using center span loading with a notched specimen as opposed to third point loading.

5) From experiments and the model developed in Chapter 9, it has been shown that, in the flexural toughness test (ASTM C 1018) by the time a 1 mm midspan deflection has been reached, the *CMOD* is approximately 1.3 to 1.5 mm. Considering that serviceable cracks in actual structures should not exceed 1 mm in width, it becomes apparent that specifications and toughness criteria should emphasize on the energy consumed only up to a 0.5 to 0.7 mm mid point deflection.

It is expected that, with the development of more stable testing procedures, and once the flexural toughness criteria (ASTM, JSCE, etc.) and specifications shift towards emphasizing crack openings up to 1.0 mm, fibers of a shorter length (12.5 to 19 mm) which were shown here to lead to a significantly greater in-situ fiber content, will become advantageous for shotcrete, with possibilities for significant gains in shrinkage cracking control.

6) Although steel fiber reinforced shotcrete is extensively used throughout the world today, structural design procedures for shotcrete linings that are able to account for the fiber contribution in transmitting forces across a crack are still lacking, with the existing applications being governed by empirical rules or fiber manufacturer's recommendations. Therefore, research efforts emphasizing on full-scale structural elements are needed in order to develop rational design procedures that will allow for the full potential of steel fibers as a means for structural reinforcement to be developed.

References

Adebar, P., Mindess, S., St-Piere, D. and Olund, B., Shear Tests of Fiber Concrete Beams without Stirrups, ACI Structural Journal, Jan.-Feb., 1997.

American Concrete Institute, ACI 506R-90, *Guide to Shotcrete*, ACI, Detroit, 1990.

Amtsbuchler, R. and van der Westhuizen, J. L. J., *Shotcrete Tests at the Fish Ecca Tunnel*. In: Shotcrete for Underground Support V, Proceedings of the Engineering Foundation Conference, Uppsala, Sweden, 1990. Published by ASCE, New York, pp. 213-223.

Armelin, H. and Helene, P., *Physical and Mechanical Properties of Steel-Fiber Reinforced Dry-Mix Shotcrete*, ACI Materials Journal, V. 92, N. 3, May-June 1995, pp. 258-267.

ASTM C1018-89, *Standard Test Method for Flexural Toughness and First-Crack Strength of Fiber Reinforced Concrete (Using Beam with Third-Point Loading)*, 1991 Book of ASTM Standards, Part 04.02, ASTM, Philadelphia, pp. 507-513.

ASTM C 1117-89 Standard *Test Method for Time of Setting of Shotcrete Mixtures by Penetration Resistance*, ASTM Book of Standards, Philadelphia, USA, V. 04.02, pp. 579-581.

Austin, S. A., *(Shotcrete) Production and Installation. Sprayed Concrete: Properties, Design and Application* (Edited by S. A. Austin and P. J. Robins). McGraw-Hill, New York, 1995, pp. 41.

Austin, S. A., Peaston, C. H. and Robins, P. J., *Material and Fiber Losses with Fiber Reinforced Sprayed Concrete*, In: Proceedings of the Sixth International Conference on Structural Faults and Repair, V. 2 (Edited by M. C. Forde), London, 4th July, 1995.

Austrian Concrete Society, *Guideline on Shotcrete*. Austrian Concrete Society, Viena, 1990.

Balaguru, P., Ramesh, N. and Patel, M., *Flexural Toughness of Steel Fiber Reinforced Concrete*, ACI Materials Journal, V. 89, 1992, N. 6, pp. 541-546.

Banthia, N., Trottier, J. -F., Wood, D. and Beaupre, D., *Influence of Fiber Geometry in Steel-Fiber Reinforced Dry-Mix Shotcrete*, Concrete International, May 1992, pp. 24-28.

Banthia, N., Trottier, J. -F., Wood, D. and Beaupre, D., *Influence of Fiber Geometry in Steel-Fiber Reinforced Wet-Mix Shotcrete*, Concrete International, June, 1994.

Banthia, N. and Trottier, J. -F., *Concrete Reinforced with Deformed Steel Fibers, Part I: Bond-slip Mechanisms*, ACI Materials Journal, V. 91, 1995, N. 5, pp. 435-446.

Banthia, N. and Trottier, J. -F., *Concrete Reinforced with Deformed Steel Fibers, Part II: Toughness Characterization*, ACI Materials Journal, V. 92, N. 2, 1995, pp. 146-154.

Beaupre, D., *Rheology of High Performance Shotcrete*, Ph.D. Thesis, University of British Columbia, Vancouver, Canada, 1994, 250 pp.

Bishop, R. F., Hill, R. and Mott, F. R. S., *The Theory of Indentation and Hardness Tests*, The Proceedings of the Physical Society, V. 57, Part 3, N. 321, May 1945, pp. 147-159.

Blumel, O. W., Lutsch, H. and Stehno, G., *State-of-the-Art Shotcrete Technology*. Shotcrete for Underground Support III, Engineering Foundation, New York, 1978, pp. 15-26.

Campbell, K., *Restrained Plastic Shrinkage in Shotcrete Overlays*, Masters Thesis, Department of Civil Engineering, University of British Columbia, (in progress).

Canadian Standards Association, *Design of Concrete Structures for Buildings* (CAN3-A23.3-M84), Canadian Standards Association, Rexdale, Canada, 1984, 281 pp.

Chen, L., *Flexural Toughness of Fiber Reinforced Concrete*, Ph.D. Thesis, Civil Engineering Department, University of British Columbia, Vancouver, Canada, 1995, 319 pp.

Collins, M. P. and Mitchell, D., *Prestressed Concrete Basics*, Canadian Prestressed Concrete Institute (CPCI), Ottawa, 1987, pp. 82.

Foschi, R. O., Folz, B. R. and Yao, F. Z. - *RELAN: RELiability ANalysis: User's Manual*. Civil Engineering Department, University of British Columbia, Vancouver, Canada, 1993, 51 pp.

Ghio, V., *The Rheology of Fresh Concrete and its Effects on the Shotcrete Process*, Ph.D. Thesis, University of California at Berkeley, 1993, 192 pp.

Glassgold, I. L., *Shotcrete Durability: An Evaluation*. Concrete International, V. 11, N. 8, 1989, pp. 78-85.

Goldman, A. and Bentur, A., *Properties of Cementitious Systems Containing Silica Fume or Non Reactive Microfillers*, Advanced Cement Based Materials, V. 1, 1994, pp. 209-215.

Goparalatnam, V. S. and Shah, S. P., *Softening Response of Plain Concrete in Direct Tension*, ACI Journal, V. 82, N. 3, 1985, pp. 310-323.

Goparalatnam, V. S., Surendra, S. P., Gordon, B. B., Criswell, M. E., Ramakrishnan, V. and Wecharatana, M., *Fracture Toughness of Fiber Reinforced Concrete*, ACI Materials Journal, V. 88, N. 4, 1991, pp. 339-353.

Gray, R. J. and Johnston, C. D., *The Effect of Matrix Composition on Fiber/Matrix Interfacial Bond Shear Strength in Fiber Reinforced Mortar*, Cement and Concrete Research, V. 14, 1984, pp. 285-296.

Hibbeler, R. C., *Engineering Statics and Dynamics*, Macmillan Publishing Co., New York, 1974, pp. 715.

Hill, R., *The Mathematical Theory of Plasticity*, Oxford University Press, London, UK, 1950. pp. 99.

Jenq, Y. S. and Shah, S. P., *Crack Propagation in Fiber-Reinforced Concrete*, ASCE Journal of Structural Engineering, V. 112, N.1, 1986, pp. 19-34.

Johnson, K. L., *Contact Mechanics*, Cambridge University Press, Cambridge, UK, 1985, pp. 171.

Jolin, M., *Influence of Set Accelerating Admixtures on the Durability of Dry-Mix Shotcrete*. Masters Thesis, Civil Engineering Department, Universite Laval, Quebec, 1996, 170 pp. (in French).

JSCE SF 4, *Method of Test for Flexural Strength and Flexural Toughness of Fiber Reinforced Concrete*. Japan Society of Civil Engineers, JSCE Standard for Test Methods of Fiber Reinforced Concrete, 1984, pp. 45-51.

Lim, T. Y., Paramasivam, P. and Lee, S. L., *Bending Behavior of Steel-Fiber Concrete Beams*, ACI Structural Journal, N. 84, V. 6, 1987, pp. 524-536.

Little, T., *An Evaluation of Steel Fiber Reinforced Shotcrete*, 36th Canadian Geotechnical Conference, Vancouver, B.C., June 1983.

Maidl, B. R., and Sommavilla, P., *Equipment for the Production of Sprayed Concrete*, In: Sprayed Concrete: Properties, Design and Application (Edited by S. A. Austin and P. J. Robins). McGraw-Hill, New York, 1995, pp. 171.

Melbye, T., Opsahl, O. and Holtmon, J., *Shotcrete for Rock Support. Sprayed Concrete: Properties, Design and Application* (Edited by S. A. Austin and P. J. Robins). McGraw-Hill, New York, 1995, pp. 354.

Morgan, D. R. and Mowatt, D. N., *A Comparative Evaluation of Plain, Mesh and Steel Fiber Reinforced Shotcrete*. ACI SP 81, Detroit, 1984, pp. 70-74.

Morgan, D. R., *Dry-mix Silica Fume Shotcrete in Western Canada*. Concrete International, V. 10, N. 1, 1988, pp. 24-32.

Morgan, D. R., *Advances in Shotcrete Technology for Support of Underground Openings in Canada*. In: Shotcrete for Underground Support V, Proceedings of the Engineering Foundation Conference, Uppsala, Sweden, 1990. Published by ASCE, New York, pp. 359-382.

Morgan, D. R., *New Developments in Shotcrete for Repairs and Rehabilitation*. CANMET Symposium on Advances in Concrete Technology (Ed. V. M. Malhotra), Athens, Greece, 1992, pp. 699-737.

Morgan, D. R. and Pigeon, M., Proceedings for the Half-day Presentation of the Fourth Semiannual Meeting of the Network of Centers of Excellence on High Performance Concrete. Toronto, Canada, 1992, pp. 31-56.

Morgan, D. R., *Shotcrete in North America: The State-of-the-Art*. Proceedings of the Laich SA Shotcrete Colloquium, Wildegg, Switzerland, Sept. 24, 1993, pp. 47-69.

Morgan, D. R., *Special Sprayed Concretes* (In: Sprayed Concrete: Properties, Design and Application), Edited by S. A. Austin & P. J. Robins, McGraw-Hill, New York, 1995. pp. 262.

Morgan, D. R., Mindess, S. and Chen, L., *Testing and Specifying Toughness for Fiber Reinforced Concrete and Shotcrete*, In: Second University-Industry Workshop on Fiber Reinforced Concrete and Other Advanced Composites, Ed: N. Banthia and S. Mindess, Toronto, March 26-29, 1995, pp. 29-50.

Morgan, D. R., Presentation on Plastic Fiber Reinforced Wet-Mix Shotcrete at the ACI Fall Convention, New Orleans, November 1996.

Naaman, A. E., Argon, A. S. and Moavenzadeh, F., *A Fracture Model for Fiber Reinforced Cementitious Materials*, Cement and Concrete Research, V. 3, pp. 397-411, 1973.

Naaman, A. E. and Shah, S. P., *Pull-Out Mechanisms in Steel-Fiber Reinforced Concrete*, Journal of the Structural Division, ASCE, Aug. 1976, pp. 1537-1548.

Naaman, A. E. and Najm, H., *Bond-Slip Mechanisms of Steel Fibers in Concrete*, ACI Materials Journal, V. 88, 1991, N. 2, pp. 135-145.

Nishioka, K., Sumio, Y., Kameda, Y and Akihama, S., *Present Status on Applications of Steel Fiber Concrete in Japan*. The International Journal of Cement Composites, V. 2, N. 4, pp. 205-232, 1980.

Opshal, O. A., *Steel Fiber Reinforced Concrete for Rock Support*. Report for the Royal Norwegian Council for Scientiffic and Industrial Research, 1982.

Parker, H. W., *Field Oriented Investigation of Conventional and Experimental Shotcrete for Tunnels*, Ph.D. Thesis, University of Illinois at Urbana-Champaign, USA, 1976, 630 pp.

Peaston, C. H., *Production, Properties and Design of Sprayed Fiber Concrete*, Ph. D. thesis, Loughborough University of Technology, UK, 1993.

Powers, T. C., *The Properties of Fresh Concrete*, John Wiley and Sons, New York, 1968, pp. 461.

Prudencio Jr. , L. R., Armelin, H. S. and Helene, P., *Interaction Between Accelerating Admixtures and Portland Cement for Shotcrete: The Influence of the Admixture's Chemical Base and Correlation Between Paste Tests and Shotcrete Performance*. ACI Materials Journal, V. 93, N. 6, 1996, pp. 619 - 628.

Robins, P. J. and Austin, S. A., *Sprayed Steel Fiber Concrete, Part I - Production and Installation*. Concrete, V. 19, N. 3, 1985, pp. 17-19.

Romualdi, J. P. and Mandel, J. A., *Tensile Strength of Concrete as Affected by Uniformly Distributed and Closely Spaced Short-Lengths of Wire Reinforcement*. ACI Journal, V. 61, 1964, pp. 650-670.

Ryan, T. F., *Gunite: A Handbook for Engineers*. Cement and Concrete Association, Wexham Springs, 1973, 63 pp.

Schultz, R. J. - *Effects of Accelerators on Shotcrete Properties*, Shotcrete for Underground Support V, Proceedings of the Engineering Foundation Conference, Paipa, Colombia, 1982. Published by The Engineering Foundation, New York, pp. 139-153.

Stewart, E. P., *New Test Data Aid Quality Control of Gunite*. Engineering News-Record, Nov. 9, 1933, 4 pp.

Tabor, D., *A Simple Theory of Static and Dynamic Hardness*, Proceedings of the Royal Society, A192, 1948, pp. 247-274.

Telles, R., Personal Comunication during construction of the Sao Paulo Metro System, 1992.

Tattersal, G. H. and Banfill, P. F. G., *The Rheology of Fresh Concrete*, Pitman Books Ltd., London, UK, 1983, 356 pp.

Valencia, F. E., *Practical Aspects of Shotcrete Application*. Use of Shotcrete for Underground Structural Support, SP-45, ACI/ASCE, Detroit, 1974, pp. 114-129.

Vandewalle, M., Tunneling the World, Published by N. V. Bekaert S. A., 179 pp., 1990.

Ward, W. H. and Hills, D. L., *Sprayed Concrete - Tunnel Support Requirements and the Dry-mix Process*, Shotcrete for Ground Support (SP-54), ACI, Detroit, 1977, pp. 475-532.

Warner, J., *Understanding Shotcrete - The Fundamentals*. Concrete International, May and June 1995, Vol. 17 Nos. 5 and 6, pp. 59-64 and pp. 37-41.

Wolsiefer Sr., J. and Morgan, D. R., *Silica Fume in Shotcrete*, Concrete International, V. 15, N. 4, April 1993, pp. 34-39.

Appendix A - Deduction of Equations 2.1 and 2.2

Given a volume of concrete to be shot (Vol_{Total}) at a given design fiber content (V_f), a certain volume of shotcrete will be produced (Vol_s) as well as a certain volume of rebound. The in-situ fiber content of the shotcrete produced is termed V_f' and therefore:

- Total volume of fibers shot: $\quad Vol\ Fib_{Total} = Vol_{Total} \cdot V_f$

- Volume of in-situ shotcrete produced: $\quad Vol_s = (1 - R) \cdot Vol_{Total}$

- Volume of fibers in the in-situ shotcrete: $\quad Vol\ Fib_{shotcrete} = (1 - R) \cdot Vol_{Total} \cdot V_f'$

From the definition of rebound, the fiber rebound (R_f) is given by: $\quad R_f = \dfrac{\left(Vol\ Fib_{Total} - Vol\ Fib_{shotcrete}\right)}{Vol\ Fib_{Total}}$

and therefore, $\qquad R_f = 1 - \left(\dfrac{V_f'}{V_f}\right) + \left(\dfrac{V_f'}{V_f}\right) \cdot R$

Defining fiber retention (T) as: $\quad T = \dfrac{V_f'}{V_f}$

The fiber Rebound (R_f) can be calculated as: $\quad R_f = 1 - T + T \cdot R$

In terms of percentage values:
$$R_f(\%) = 100 - T(\%) + T(\%) \cdot \dfrac{R(\%)}{100}$$

Or isolating the in-situ fiber content:
$$V_f'(\%) = \dfrac{V_f \cdot \left(100 - R_f(\%)\right)}{\left(100 - R(\%)\right)}$$

Appendix B -Water Injection and Flowmeter Systems and Air Flowmeter
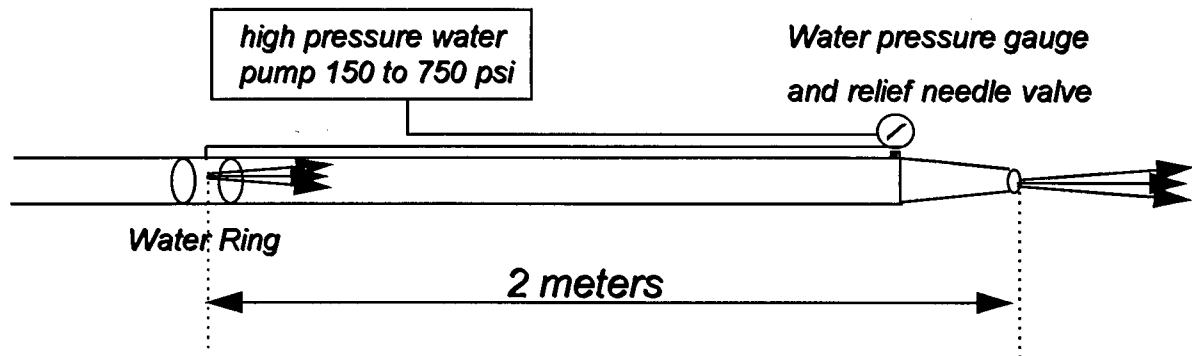
Figure B1 - Schematic representation of the water injection system and the flowmeter (pressure gauge with a relief needle valve).
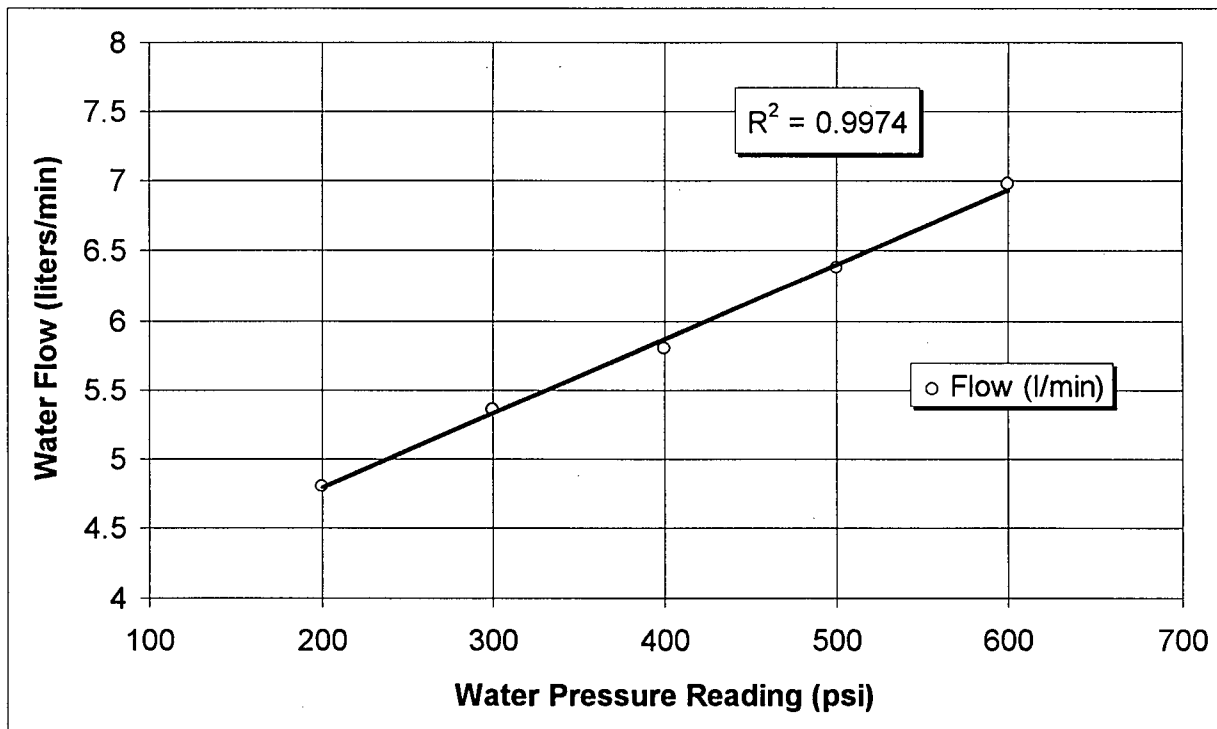
Figure B2 -Experimental calibration of the water flowmeter showing that the water pressure reading is linearly related to the water flow (145 psi = 1MPa).

Figure B3 - High pressure water injection ring.

Figure B4 - Because water is injected at a high pressure through a small orifice, a water mist is created.
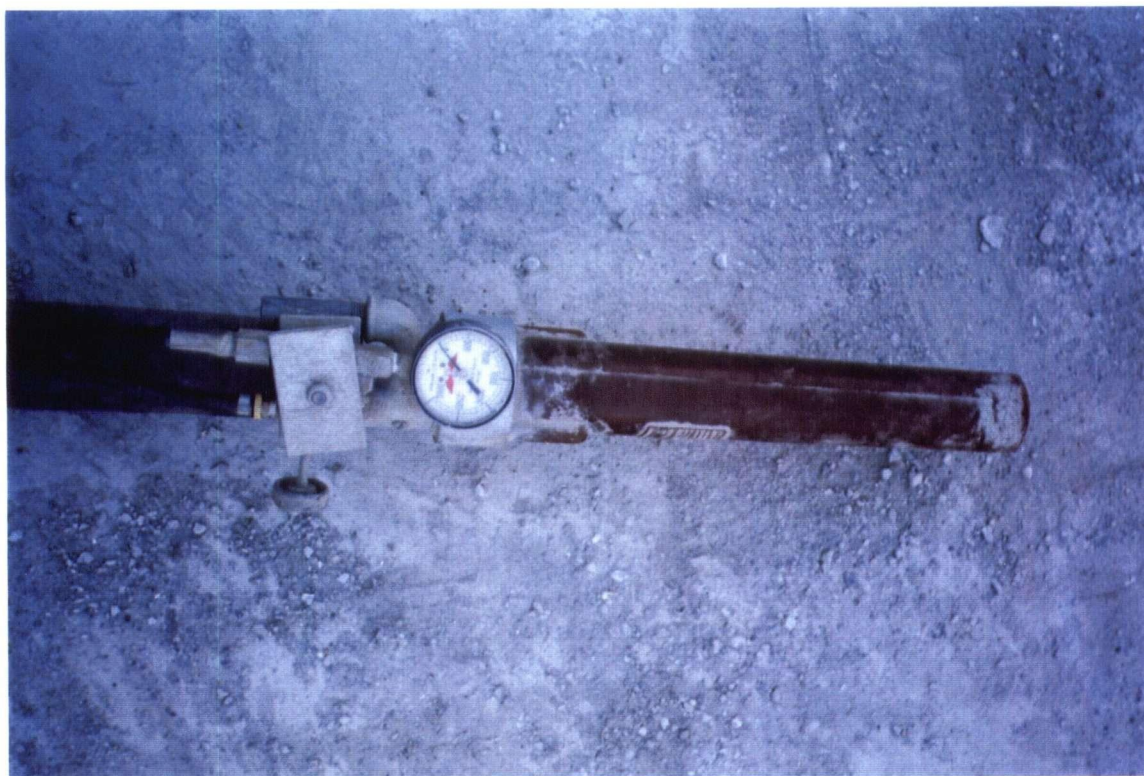
Figure B5 - Water flowmeter at the nozzle: composed of a water pressure gauge and a relief needle valve.

Figure B6 - Air flowmeter installed at the shotcrete machine's compressed air intake.

Appendix C - Steps Taken by the Computer Code to Predict the Flexural Post-cracking Behavior of Fiber Reinforced Concrete and Shotcrete.

1) From the fiber content (V_f), determine the fiber density (n) using Eq. 9.8.

2) Assume a compressive strain (ε_o) on the top most part of the beam section at midspan. Using Eq. 9.1 determine the axial shortening of the top most part of the beam (Δ_o).

3) From the concrete compressive strength, estimate the secant modulus of elasticity (E_{ct} - Eq. 9.11) and the flexural tensile strength ($f_{cr} = 0.6 \cdot \sqrt{f_c'}$, in MPa).

4) Calculate the ultimate tensile strain under flexural loading (Eq. 9.12).

5) Assuming a linear strain profile in the compressed region, iterate on the depth of the neutral axis until equilibrium of forces is attained (Eq. 9.6). In order to do so:

- Divide the section into 20 layers of equal thickness.
- Calculate the total compressive force using the parabolic stress-strain relationship given by Eq. 9.14 (integration done using stress block factors: α and β).
- In the region below the neutral axis, tensile stresses are elastically transmitted by concrete only up to the ultimate strain under flexural loading (Eq. 9.12). For strains above this value, strain softening is assumed to occur (Eq. 9.13).
- Calculate the *CMOD* assuming a linear crack profile, with zero crack opening at the neutral axis and a known axial shortening of the top of the beam (Δ_o) - Fig. 9.2.
- Assuming a linear crack profile, calculate the crack opening in the center of each of the section's layers under tension.
- From the crack opening at each layer, calculate the average fiber pull-out force in each layer (numerical integration of Eq. 9.19).
- From the average fiber pull-out force (Eq. 9.19) and fiber density (Eq. 9.8), calculate the total fiber pull-out force in each layer under tension (Eq. 9.18).

- Add all tensile forces and test for equilibrium of the midspan section (Eq. 9.6). If equilibrium is not attained, assume a neutral axis closer to the top of the specimen and repeat all calculations.

6) Having satisfied equilibrium of forces, calculate the equilibrating moment (M_e - Eq. 9.7) and the equilibrating load (P - Eq. 9.5).

7) From the increment in crack mouth opening ($dCMOD$) and knowing the depth of the neutral axis (c), calculate the increment in beam rotation ($d\theta$ - Eq. 9.4).

8) Using $d\theta$, calculate the increment in midspan deflection ($d\delta$ - Eq. 9.3).

9) Plot the values found for the midspan deflection (δ) and load (P).

10) Increase the top strain (ε_o) and return to step 1 for a new calculation.

Computer Code in Microsoft Visual Basic Language

```vb
Private Sub cmdBeginProg_Click()

    ' Disable invalid buttons for the time being
    cmdBeginProg.Enabled = False
    cmdPrevProg.Enabled = False
    cmdQuitProg.Enabled = False

    frmFinalResult.finalGraph.Cls
    frmFinalResult.AutoRedraw = True
    frmFinalResult.AutoRedraw = False


    Dim msgBreak As String

    Dim msg, FName As String
    Dim plotCrackPt, crack, ShowCrackColor, flagBreakInLayer As Integer
    Dim counter, layer, i, fileNum, j As Integer
    Dim miniA, miniB, miniC, miniD, miniE, miniF, miniG, miniH As Double
    Dim miniCWhat, miniDWhat, miniEWhat, miniGWhat As Double
    Dim pullOut(2000), deFlexC(2000) As Double
    Dim eWidthv, eF22v, eF45v, eF67v, eF90v, eFshortv, eFTensv, eResMomv, forceAvgTotv As Double
    Dim deFlexv, eTopv, delTopv, delBotv, forceCompv, resMomTotv, eFAvgv, eFAvgRealv As Double
    Dim delBotOldv, ddeFlexv, pullOutLoadv, forceTensTotv, forceSumv, DELcrkv As Double
    Dim alphav, betav, ePrimeCv, nav, ccv, cco, bmHv, dog, peak, firstCrackDefl As Double
    Dim DrawArea As Control

    Dim maxstress, factor As Double
    Dim compStress, compStressy, compStressValue, forceCompValue, posCompStress, tensArea As Double
    Dim tenStress1 As Double
    Dim posTenStress1 As Double
    Dim logStress1, logStress2, logStress3, logStress4, logStress5, logStress6, logStress7, logStress8, logStress9, logStress10 As Double
    Dim logStress11, logStress12, logStress13, logStress14, logStress15, logStress16, logStress17, logStress18, logStress19, logStress110 As Double

    Dim dAreaOAEFO, AreaOAEFO, AreaTotalOAEFO, tFJSCE, pullOutNew, pullOutOld, deflexNew, deflexOld As Double

    Dim counterBACD, counterDCEF, counterFEGH, counterHGIJ, counterJIKL, counterLK As Integer
    Dim firstCrack As Integer
    Dim firstCrackLoad, firstCrackDeflex, pullOutNow, deflexNow As Double
    Dim I1deflex, I5deflex, I10deflex, I20deflex, I30deflex, I50deflex As Double
    Dim dBaseBD, dBaseDF, dBaseFH, dBaseHJ, dBaseJL As Double
    Dim BaseTotalBD, BaseTotalDF, BaseTotalFH, BaseTotalHJ, BaseTotalJL As Double
    Dim BaseBD, BaseDF, BaseFH, BaseHJ, BaseJL As Double
    Dim dHeigthBA, dHeigthDC, dHeigthFE, dHeigthHG, dHeigthJI, dHeigthLK As Double
    Dim AreaOABO, AreaOACDBO, AreaOAEFBO, AreaOAGHBO, AreaOAIJBO, AreaOAKLBO As Double
    Dim dAreaBACD, dAreaDCEF, dAreaFEGH, dAreaHGIJ, dAreaJIKL As Double
    Dim AreaBACD, AreaDCEF, AreaFEGH, AreaHGIJ, AreaJIKL As Double
    Dim AreaTotalBACD, AreaTotalDCEF, AreaTotalFEGH, AreaTotalHGIJ, AreaTotalJIKL As Double
    Dim firstPullOutBA, firstPullOutDC, firstPullOutFE, firstPullOutHG, firstPullOutJI, firstPullOutLK As Double
    Dim firstDeflecBA, firstDeflecDC, firstDeflecFE, firstDeflecHG, firstDeflecJI, firstDeflecLK As Double
    Dim lastPullOutBA, lastPullOutDC, lastPullOutFE, lastPullOutHG, lastPullOutJI As Double
    Dim lastDeflecBA, lastDeflecDC, lastDeflecFE, lastDeflecHG, lastDeflecJI As Double
```

```
Dim sumAreaOACDBO, sumAreaOAEFBO, sumAreaOAGHBO, sumAreaOAIJBO, sumAreaOAKLBO As
Double

Dim p2x, p2y, p3x, frac22F, frac45F, frac67F, frac90F, fracshortF As Double

p2x = Val(p2xM.Text)
p2y = Val(p2yM.Text)
p3x = Val(p3xM.Text)
frac22F = Val(fracF22.Text)
frac45F = Val(fracF45.Text)
frac67F = Val(fracF67.Text)
frac90F = Val(fracF90.Text)
fracshortF = Val(fracFshort.Text)


' Initialize the variables for JSCE
tFJSCE = 0
dAreaOAEFO = 0
AreaOAEFO = 0
AreaTotalOAEFO = 0

' Initialize the variables for ASTM
counterBACD = 0
counterDCEF = 0
counterFEGH = 0
counterHGIJ = 0
counterJIKL = 0
counterLK = 0
pullOutNow = 0
deflexNow = 0
I1deflex = 0
I5deflex = 0
I10deflex = 0
I20deflex = 0
I30deflex = 0
I50deflex = 0
dBaseBD = 0
dBaseDF = 0
dBaseFH = 0
dBaseHJ = 0
dBaseJL = 0
BaseBD = 0
BaseDF = 0
BaseFH = 0
BaseHJ = 0
BaseJL = 0
BaseTotalBD = 0
BaseTotalDF = 0
BaseTotalFH = 0
BaseTotalHJ = 0
BaseTotalJL = 0
dAreaBACD = 0
dAreaDCEF = 0
dAreaFEGH = 0
dAreaHGIJ = 0
dAreaJIKL = 0
AreaOABO = 0
```

```
AreaBACD = 0
AreaDCEF = 0
AreaFEGH = 0
AreaHGIJ = 0
AreaJIKL = 0
AreaTotalBACD = 0
AreaTotalDCEF = 0
AreaTotalFEGH = 0
AreaTotalHGIJ = 0
AreaTotalJIKL = 0
AreaOACDBO = 0
AreaOAEFBO = 0
AreaOAGHBO = 0
AreaOAIJBO = 0
AreaOAKLBO = 0
firstPullOutBA = 0
firstPullOutDC = 0
firstPullOutFE = 0
firstPullOutHG = 0
firstPullOutJI = 0
firstPullOutLK = 0
firstDeflecBA = 0
firstDeflecDC = 0
firstDeflecFE = 0
firstDeflecHG = 0
firstDeflecJI = 0
firstDeflecLK = 0
lastPullOutBA = 0
lastPullOutDC = 0
lastPullOutFE = 0
lastPullOutHG = 0
lastPullOutJI = 0
lastDeflecBA = 0
lastDeflecDC = 0
lastDeflecFE = 0
lastDeflecHG = 0
lastDeflecJI = 0


' Define a constant
dog = ((Val(frmConcreteInfo.fiberLen.Text)) / ((2 / 3) * (Val(bmlength.Text))))

' Define to-be assigned color code
AXIS_COLOR = RGB(0, 0, 0)              ' black
LINE_COLOR = RGB(0, 0, 255)           ' blue
GREEN_COLOR = RGB(0, 255, 0)           ' green
MINORGRID_COLOR = RGB(255, 0, 0)        ' red
CRACK_COLOR = RGB(0, 255, 255)          ' turqoise
STRESS_COLOR = RGB(255, 0, 0)          ' blue

' Set the drawing area for the Stress Diagram
stressDiag.DrawMode = 13
stressDiag.AutoRedraw = False
stressDiag.Cls
stressDiag.AutoRedraw = True

If mnuScalePick(1).Checked = True Then
```

```
            maxstress = 15
    ElseIf mnuScalePick(2).Checked = True Then
            maxstress = 25
    ElseIf mnuScalePick(3).Checked = True Then
            maxstress = 50
    ElseIf mnuScalePick(4).Checked = True Then
            maxstress = 75
    ElseIf mnuScalePick(5).Checked = True Then
            maxstress = 100
    Else
            maxstress = 200
    End If
    stressDiag.Scale ((-1.1 * maxstress), (-0.15 * (Val(bmHeigth.Text))))-((1.1 * maxstress), (1.15 *
(Val(bmHeigth.Text))))


    ' Draws the permanent lines on the stress diagram
    ' this draws the two outer boundary lines
    stressDiag.Line (-maxstress, 0)-(-maxstress, (Val(bmHeigth.Text))), GREEN_COLOR
    stressDiag.Line (maxstress, 0)-(maxstress, (Val(bmHeigth.Text))), GREEN_COLOR
    ' this draws the midlength cross-sectional line
    stressDiag.Line (0, 0)-(0, (Val(bmHeigth.Text))), STRESS_COLOR

    stressDiag.AutoRedraw = False


    ' Set the drawing area for the upcoming Flexural Load vs. Midpoint Deflection graph
    Set DrawArea = frmFinalResult.finalGraph
    DrawArea.DrawMode = 13
    DrawArea.AutoRedraw = False
    DrawArea.Cls
    DrawArea.AutoRedraw = True


    ' The scale of the Flex. Load vs. Deflex graph can be adjusted to 6 different setting
    If mnuChoiceDim(0).Checked = True Then
        DrawArea.Scale (-0.1, 25)-(2.7, -5)
    ElseIf mnuChoiceDim(1).Checked = True Then
        DrawArea.Scale (-0.1, 45)-(2.7, -5)
    ElseIf mnuChoiceDim(2).Checked = True Then
        DrawArea.Scale (-0.1, 80)-(2.7, -5)
    ElseIf mnuChoiceDim(3).Checked = True Then
        DrawArea.Scale (-0.1, 110)-(2.7, -5)
    ElseIf mnuChoiceDim(4).Checked = True Then
        DrawArea.Scale (-0.1, 160)-(2.7, -5)
    ElseIf mnuChoiceDim(5).Checked = True Then
        DrawArea.Scale (-0.1, 210)-(2.7, -5)
    Else
        DrawArea.Scale (-0.1, 310)-(2.7, -5)
    End If


    DrawArea.Line (0, 0)-(2.5, 0), AXIS_COLOR            ' x-axis full length

    If mnuChoiceDim(0).Checked = True Then
        DrawArea.Line (0, 0)-(0, 20), AXIS_COLOR
    ElseIf mnuChoiceDim(1).Checked = True Then
        DrawArea.Line (0, 0)-(0, 40), AXIS_COLOR         ' y-axis full length
    ElseIf mnuChoiceDim(2).Checked = True Then
        DrawArea.Line (0, 0)-(0, 75), AXIS_COLOR         ' y-axis full length
    ElseIf mnuChoiceDim(3).Checked = True Then
```

```
        DrawArea.Line (0, 0)-(0, 100), AXIS_COLOR        ' y-axis full length
ElseIf mnuChoiceDim(4).Checked = True Then
        DrawArea.Line (0, 0)-(0, 150), AXIS_COLOR
ElseIf mnuChoiceDim(5).Checked = True Then
        DrawArea.Line (0, 0)-(0, 200), AXIS_COLOR
Else
        DrawArea.Line (0, 0)-(0, 300), AXIS_COLOR
End If


' Ticks for the x-axis
For miniA = 0 To 2 Step 1
        DrawArea.Line (miniA, 0)-(miniA, -3), AXIS_COLOR        ' big ticks on x-axis
Next miniA
For miniB = 0 To 2.6 Step 0.1
        DrawArea.Line (miniB, 0)-(miniB, -2), AXIS_COLOR        ' small ticks on x-axis
Next miniB


' Ticks for the y-axis
If mnuChoiceDim(0).Checked = True Then
        miniCWhat = 20
        miniDWhat = 15
ElseIf mnuChoiceDim(1).Checked = True Then
        miniCWhat = 40
        miniDWhat = 35
ElseIf mnuChoiceDim(2).Checked = True Then
        miniCWhat = 70
        miniDWhat = 75
ElseIf mnuChoiceDim(3).Checked = True Then
        miniCWhat = 100
        miniDWhat = 95
ElseIf mnuChoiceDim(4).Checked = True Then
        miniCWhat = 150
        miniDWhat = 145
ElseIf mnuChoiceDim(5).Checked = True Then
        miniCWhat = 200
        miniDWhat = 195
Else
        miniCWhat = 300
        miniDWhat = 295
End If

For miniC = 0 To miniCWhat Step 10
        DrawArea.Line (0, miniC)-(-0.07, miniC), AXIS_COLOR    ' big ticks on y-axis
Next miniC
For miniD = 5 To miniDWhat Step 10
        DrawArea.Line (0, miniD)-(-0.04, miniD), AXIS_COLOR    ' small ticks on y-axis
Next miniD


' Draws the red grid lines
If mnuChoiceDim(0).Checked = True Then
        miniEWhat = 20
ElseIf mnuChoiceDim(1).Checked = True Then
        miniEWhat = 40
ElseIf mnuChoiceDim(2).Checked = True Then
        miniEWhat = 75
```

```
ElseIf mnuChoiceDim(3).Checked = True Then
    miniEWhat = 100
ElseIf mnuChoiceDim(4).Checked = True Then
    miniEWhat = 150
ElseIf mnuChoiceDim(5).Checked = True Then
    miniEWhat = 200
Else
    miniEWhat = 300
End If

For miniE = 5 To miniEWhat Step 5
    DrawArea.Line (0, miniE)-(2.5, miniE), MINORGRID_COLOR     ' horizontal grid lines
Next miniE
For miniF = 0.1 To 2.6 Step 0.1
    DrawArea.Line (miniF, 0)-(miniF, miniEWhat), MINORGRID_COLOR   ' vertical grid lines
Next miniF


' Draws the major grid lines
If mnuChoiceDim(0).Checked = True Then
    miniGWhat = 20
ElseIf mnuChoiceDim(1).Checked = True Then
    miniGWhat = 40
ElseIf mnuChoiceDim(2).Checked = True Then
    miniGWhat = 70
ElseIf mnuChoiceDim(3).Checked = True Then
    miniGWhat = 100
ElseIf mnuChoiceDim(4).Checked = True Then
    miniGWhat = 150
ElseIf mnuChoiceDim(5).Checked = True Then
    miniGWhat = 200
Else
    miniGWhat = 300
End If

For miniG = 10 To miniGWhat Step 10
    DrawArea.Line (0, miniG)-(2.5, miniG), GREEN_COLOR       ' major hor. lines
Next miniG
For miniH = 0.5 To 2.5 Step 0.5
    DrawArea.Line (miniH, 0)-(miniH, miniGWhat), GREEN_COLOR     ' major vert. lines
Next miniH


DrawArea.PSet (0, 0), LINE_COLOR

fileNum = FreeFile
FName = fileInputForm.userNamedFile.Text & ".txt"
Open FName For Output As fileNum

' Initialize ProgressBar
ProgressBar1.Min = LBound(pullOut)
ProgressBar1.Max = UBound(pullOut)
ProgressBar1.Value = ProgressBar1.Min
boom.BackColor = &HFFFFFF

' Initialize gauge ( Flexural load )
gaugeLoad.Min = 0
```

```
gaugeLoad.Max = 50
gaugeLoad.Value = 0

' Initialize gauge elemental
gaugeF22.Value = 0
gaugeF45.Value = 0
gaugeF67.Value = 0
gaugeF90.Value = 0
gaugeFShort.Value = 0
gaugeFAvg.Value = 0

frmProgBar2.AutoRedraw = False
ShowCrackColor = 0   ' if 0 then search for cracked eWidth if true then show in the diagram
plotCrackPt = 0      ' if plotCrackPt=0 then search for the deflection value of first crack
flagBreakInLayer = 0   ' if 0 do not start the break in layer yet
crack = 0

' Loop for specified number of times (pullOut)
For counter = LBound(pullOut) To UBound(pullOut)
    howManyNow.Text = counter
    ' Put a break on every 400 data points found to prevent it from freezing the screen
    If counter = 400 Or counter = 800 Or counter = 1200 Or counter = 1600 Then
        msgBreak = "Click OK to continue."
        MsgBox msgBreak
    End If

    frmProgBar2.AutoRedraw = False
    boom.BackColor = &HFFFFFF

    ' Set approximate position of progress
    If counter <= 2000 Then
        ProgressBar1.Value = counter
    Else
        Exit For            ' For data point 1000 get out
    End If

    ' Set these variables into their new values
    eTopv = Val(eTop.Text)
    eTop.Text = Format((eTopv), "0.000000")
    ccv = Val(cC.Text)
    nav = Val(na.Text)
    bmHv = Val(bmHeigth.Text)

    ' This part here self-adjusts the starting point of the moving NA finders
    If ccv = bmHv Then
        ccv = ((Val(bmHeigth.Text)) - 1)
        cC.Text = Format((ccv), "0.00")
    Else
        If (bmHv - ccv) > 1 Then
            ccv = ((nav) + 1)
            cC.Text = Format((ccv), "0.00")
        Else
            ccv = ((Val(bmHeigth.Text)) - 1)
            cC.Text = Format((ccv), "0.00")
        End If
    End If
```

```
deFlexv = Val(deFlex.Text)
deFlex.Text = Format((deFlexv), "0.000000")
DELcrkv = Format((Val(frmConcreteInfo.DELcrack.Text)), "0.000000")
DELcrk.Text = DELcrkv

' Reset Favg(i), F(avg), Fconc(i), F(tens), Mres(i), Res.Moment and all elemental forces values back to zero
after finding a data point
eWidth.Text = Format(0, "0.000000")
eF22.Text = Format(0, "0.000000")
eF45.Text = Format(0, "0.000000")
eF67.Text = Format(0, "0.000000")
eF90.Text = Format(0, "0.000000")
eFshort.Text = Format(0, "0.000000")
eFAvgReal.Text = Format(0, "0.000000")
eFTens.Text = Format(0, "0.000000")
eResMom.Text = Format(0, "0.000000")
forceAvgTot.Text = Format(0, "0.000000")
forceTensTot.Text = Format(0, "0.000000")
forceComp.Text = Format(0, "0.000000")
forceSum.Text = Format(0, "0.000000")

' Actual calculation starts here
delTopv = ((eTopv) * (2 / 3) * (Val(bmlength.Text)))
delTop.Text = Format((delTopv), "0.000000")
ePrimeCv = ((-(2 * (Val(compStrenConc.Text))) / (5000 * (Val(compStrenConc.Text)) ^ (0.5))))
ePrimeC.Text = Format((ePrimeCv), "0.000000")
betav = ((4 - ((eTopv) / (ePrimeCv))) / (6 - (2 * (eTopv) / (ePrimeCv))))
beta.Text = Format((betav), "0.000000")
alphav = ((1 / (betav)) * (((eTopv) / (ePrimeCv)) - ((1 / 3) * ((eTopv) / (ePrimeCv)) ^ 2)))
alpha.Text = Format((alphav), "0.000000")

frmProgBar2.AutoRedraw = True

Do

    frmProgBar2.AutoRedraw = False

    ccv = Val(cC.Text)
    cC.Text = Format((ccv), "0.00")
    forceCompv = ((alphav) * (Val(compStrenConc.Text)) * (Val(bmWidth.Text)) * (ccv) * (betav))
    forceComp.Text = Format((forceCompv), "0.000000")
    forceCompValue = Format(((forceCompv) / 1000), "0.0000")
    delBotv = (Abs(((delTopv) / (ccv)) * ((Val(bmHeigth.Text)) - (ccv))))
    delBot.Text = Format((delBotv), "0.000000")
    If delBotv > (0.02 * (Val(bmlength.Text))) Then
        Exit For
    End If
    numFibPerLayerv = ((((Val(bmHeigth.Text)) - (ccv)) / 20) * (Val(bmWidth.Text)) *
(Val(noFibreUnitArea.Text)))
    numFibPerLayer.Text = Format((numFibPerLayerv), "0.000000")

    ' Reset accumulating variables back to zero before starting a new data point
    eFAvgReal.Text = Format(0, "0.000000")
    eFTens.Text = Format(0, "0.000000")
    eResMom.Text = Format(0, "0.000000")
    forceAvgTot.Text = Format(0, "0.000000")
    forceTensTot.Text = Format(0, "0.000000")
```

```
forceSum.Text = Format(0, "0.000000")

frmProgBar2.AutoRedraw = True

' Add up elemental forces and moments
For layer = 1 To 20 Step 1

    frmProgBar2.AutoRedraw = False

    layerText.Text = layer
    eWidthv = ((delBotv) / 20) * ((20 - layer) + 0.5)
    eWidth.Text = Format((eWidthv), "0.000000")
    frmProgBar2.AutoRedraw = True
    frmProgBar2.AutoRedraw = False
    crack = 0

    If eWidthv < DELcrkv Then
        crack = 0      ' crack=0 means that it had not cracked yet
    Else
        crack = 1      ' crack=1 means that it had already cracked
        If ShowCrackColor = 0 Then
          If Val(eWidth.Text) > Val(DELcrk.Text) Then
            middleSpecimenColor.BackColor = &HFF&
            firstCrack = (counter - 1)
            frmProgBar2.AutoRedraw = True
            frmProgBar2.AutoRedraw = False
            If (mnuChoiceSnd(0).Checked = True) Or (mnuChoiceSnd(1).Checked = True) Then
              For i = 1 To 100
                Beep
              Next i
            End If
            ShowCrackColor = 1
          End If
        End If
    End If


    If (Customizer.optFAvgCalc(1) = True) And (Customizer.f22available = 0) Then
        eF22v = 0
        eF22.Text = Format((eF22v), "0.000000")
        If eF22v >= 0 Then
        If (eF22v * 1000) < 1000 Then
            gaugeF22.Value = (eF22v * 1000)
        Else
            gaugeF22.Value = 1000
        End If
        End If
        frmProgBar2.AutoRedraw = True
        frmProgBar2.AutoRedraw = False
    Else
      If crack = 0 Then
        eF22v = ((Val(Ep22c.Text)) * (eWidthv * dog) * ((Val(A22c.Text)) + ((1 - (Val(A22c.Text))) / (1 +
((Val(B22c.Text)) * (eWidthv * dog)) ^ (Val(C22c.Text))) ^ (1 / (Val(C22c.Text)))))))
        eF22.Text = Format((eF22v), "0.000000")
        If eF22v >= 0 Then
        If (eF22v * 1000) < 1000 Then
            gaugeF22.Value = (eF22v * 1000)
```

```
            Else
                gaugeF22.Value = 1000
            End If
            End If
            frmProgBar2.AutoRedraw = True
            frmProgBar2.AutoRedraw = False
        Else
            eF22v = ((Val(Ep22c.Text)) * (eWidthv) * ((Val(A22c.Text)) + ((1 - (Val(A22c.Text))) / (1 +
((Val(B22c.Text)) * (eWidthv)) ^ (Val(C22c.Text))) ^ (1 / (Val(C22c.Text))))))
            eF22.Text = Format((eF22v), "0.000000")
            If eF22v >= 0 Then
            If (eF22v * 1000) < 1000 Then
                gaugeF22.Value = (eF22v * 1000)
            Else
                gaugeF22.Value = 1000
            End If
            End If
            frmProgBar2.AutoRedraw = True
            frmProgBar2.AutoRedraw = False
        End If
    End If



    If (Customizer.optFAvgCalc(1) = True) And (Customizer.f45available = 0) Then
        eF45v = 0
        eF45.Text = Format((eF45v), "0.000000")
        If eF45v >= 0 Then
        If (eF45v * 1000) < 1000 Then
            gaugeF45.Value = (eF45v * 1000)
        Else
            gaugeF45.Value = 1000
        End If
        End If
        frmProgBar2.AutoRedraw = True
        frmProgBar2.AutoRedraw = False
    Else
        If crack = 0 Then
            eF45v = ((Val(Ep45c.Text)) * (eWidthv * dog) * ((Val(A45c.Text)) + ((1 - (Val(A45c.Text))) / (1 +
((Val(B45c.Text)) * (eWidthv * dog)) ^ (Val(C45c.Text))) ^ (1 / (Val(C45c.Text))))))
            eF45.Text = Format((eF45v), "0.000000")
            If eF45v >= 0 Then
            If (eF45v * 1000) < 1000 Then
                gaugeF45.Value = (eF45v * 1000)
            Else
                gaugeF45.Value = 1000
            End If
            End If
            frmProgBar2.AutoRedraw = True
            frmProgBar2.AutoRedraw = False
        Else
            eF45v = ((Val(Ep45c.Text)) * (eWidthv) * ((Val(A45c.Text)) + ((1 - (Val(A45c.Text))) / (1 +
((Val(B45c.Text)) * (eWidthv)) ^ (Val(C45c.Text))) ^ (1 / (Val(C45c.Text))))))
            eF45.Text = Format((eF45v), "0.000000")
            If eF45v >= 0 Then
            If (eF45v * 1000) < 1000 Then
                gaugeF45.Value = (eF45v * 1000)
```

```
Else
    gaugeF45.Value = 1000
End If
End If
frmProgBar2.AutoRedraw = True
frmProgBar2.AutoRedraw = False

    If mnuFibBreakOpt(1).Checked = True Then     ' Option of introducing fiber
        If eWidthv >= 1 And eWidthv < 1.2 Then   ' breakage for 45 degrees
            eF45v = ((Val(eF45.Text)) * (16 / 17))
            eF45.Text = Format((eF45v), "0.000000")
            If eF45v >= 0 Then
            If (eF45v * 1000) < 1000 Then
                gaugeF45.Value = (eF45v * 1000)
            Else
                gaugeF45.Value = 1000
            End If
            End If
            frmProgBar2.AutoRedraw = True
            frmProgBar2.AutoRedraw = False
        End If
        If eWidthv >= 1.2 And eWidthv < 1.4 Then
            eF45v = ((Val(eF45.Text)) * (15 / 17))
            eF45.Text = Format((eF45v), "0.000000")
            If eF45v >= 0 Then
            If (eF45v * 1000) < 1000 Then
                gaugeF45.Value = (eF45v * 1000)
            Else
                gaugeF45.Value = 1000
            End If
            End If
            frmProgBar2.AutoRedraw = True
            frmProgBar2.AutoRedraw = False
        End If
        If eWidthv >= 1.4 And eWidthv < 1.6 Then
            eF45v = ((Val(eF45.Text)) * (14 / 17))
            eF45.Text = Format((eF45v), "0.000000")
            If eF45v >= 0 Then
            If (eF45v * 1000) < 1000 Then
                gaugeF45.Value = (eF45v * 1000)
            Else
                gaugeF45.Value = 1000
            End If
            End If
            frmProgBar2.AutoRedraw = True
            frmProgBar2.AutoRedraw = False
        End If
        If eWidthv >= 1.6 And eWidthv < 1.8 Then
            eF45v = ((Val(eF45.Text)) * (13 / 17))
            eF45.Text = Format((eF45v), "0.000000")
            If eF45v >= 0 Then
            If (eF45v * 1000) < 1000 Then
                gaugeF45.Value = (eF45v * 1000)
            Else
                gaugeF45.Value = 1000
            End If
            End If
```

```vb
            frmProgBar2.AutoRedraw = True
            frmProgBar2.AutoRedraw = False
          End If
          If eWidthv >= 1.8 And eWidthv < 2 Then
            eF45v = ((Val(eF45.Text)) * (12 / 17))
            eF45.Text = Format((eF45v), "0.000000")
            If eF45v >= 0 Then
            If (eF45v * 1000) < 1000 Then
               gaugeF45.Value = (eF45v * 1000)
            Else
               gaugeF45.Value = 1000
            End If
            End If
            frmProgBar2.AutoRedraw = True
            frmProgBar2.AutoRedraw = False
          End If
          If eWidthv >= 2 Then
            eF45v = ((Val(eF45.Text)) * (12 / 17))
            eF45.Text = Format((eF45v), "0.000000")
            If eF45v >= 0 Then
            If (eF45v * 1000) < 1000 Then
               gaugeF45.Value = (eF45v * 1000)
            Else
               gaugeF45.Value = 1000
            End If
            End If
            frmProgBar2.AutoRedraw = True
            frmProgBar2.AutoRedraw = False
          End If
        End If
      End If
  End If


  If (Customizer.optFAvgCalc(1) = True) And (Customizer.f67available = 0) Then
      eF67v = 0
      eF67.Text = Format((eF67v), "0.000000")
      If eF67v >= 0 Then
      If (eF67v * 1000) < 1000 Then
         gaugeF67.Value = (eF67v * 1000)
      Else
         gaugeF67.Value = 1000
      End If
      End If
      frmProgBar2.AutoRedraw = True
      frmProgBar2.AutoRedraw = False
  Else
    If crack = 0 Then
        eF67v = ((Val(Ep67c.Text)) * (eWidthv * dog) * ((Val(A67c.Text)) + ((1 - (Val(A67c.Text))) / (1 +
((Val(B67c.Text)) * (eWidthv * dog)) ^ (Val(C67c.Text))) ^ (1 / (Val(C67c.Text)))))))
        eF67.Text = Format((eF67v), "0.000000")
        If eF67v >= 0 Then
        If (eF67v * 1000) < 1000 Then
           gaugeF67.Value = (eF67v * 1000)
        Else
           gaugeF67.Value = 1000
```

```
            End If
            End If
            frmProgBar2.AutoRedraw = True
            frmProgBar2.AutoRedraw = False
        Else
            eF67v = ((Val(Ep67c.Text)) * (eWidthv) * ((Val(A67c.Text)) + ((1 - (Val(A67c.Text))) / (1 +
((Val(B67c.Text)) * (eWidthv)) ^ (Val(C67c.Text))) ^ (1 / (Val(C67c.Text))))))
            eF67.Text = Format((eF67v), "0.000000")
            If eF67v >= 0 Then
            If (eF67v * 1000) < 1000 Then
                gaugeF67.Value = (eF67v * 1000)
            Else
                gaugeF67.Value = 1000
            End If
            End If
            frmProgBar2.AutoRedraw = True
            frmProgBar2.AutoRedraw = False
        End If
    End If




        If (Customizer.optFAvgCalc(1) = True) And (Customizer.f90available = 0) Then
            eF90v = 0
            eF90.Text = Format((eF90v), "0.000000")
            If eF90v >= 0 Then
            If (eF90v * 1000) < 1000 Then
                gaugeF90.Value = (eF90v * 1000)
            Else
                gaugeF90.Value = 1000
            End If
            End If
            frmProgBar2.AutoRedraw = True
            frmProgBar2.AutoRedraw = False
        Else
          If crack = 0 Then
            eF90v = ((Val(Ep90c.Text)) * (eWidthv * dog) * ((Val(A90c.Text)) + ((1 - (Val(A90c.Text))) / (1 +
((Val(B90c.Text)) * (eWidthv * dog)) ^ (Val(C90c.Text))) ^ (1 / (Val(C90c.Text))))))
            eF90.Text = Format((eF90v), "0.000000")
          .  If eF90v >= 0 Then
            If (eF90v * 1000) < 1000 Then
                gaugeF90.Value = (eF90v * 1000)
            Else
                gaugeF90.Value = 1000
            End If
            End If
            frmProgBar2.AutoRedraw = True
            frmProgBar2.AutoRedraw = False
          Else
            eF90v = ((Val(Ep90c.Text)) * (eWidthv) * ((Val(A90c.Text)) + ((1 - (Val(A90c.Text))) / (1 +
((Val(B90c.Text)) * (eWidthv)) ^ (Val(C90c.Text))) ^ (1 / (Val(C90c.Text))))))
            eF90.Text = Format((eF90v), "0.000000")
            If eF90v >= 0 Then
            If (eF90v * 1000) < 1000 Then
                gaugeF90.Value = (eF90v * 1000)
            Else
```

```
              gaugeF90.Value = 1000
          End If
          End If
          frmProgBar2.AutoRedraw = True
          frmProgBar2.AutoRedraw = False
      End If
  End If



  If (Customizer.optFAvgCalc(1) = True) And (Customizer.fshortavailable = 0) Then
      eFshortv = 0
      eFshort.Text = Format((eFshortv), "0.000000")
      If eFshortv >= 0 Then
      If (eFshortv * 1000) < 1000 Then
          gaugeFShort.Value = (eFshortv * 1000)
      Else
          gaugeFShort.Value = 1000
      End If
      End If
      frmProgBar2.AutoRedraw = True
      frmProgBar2.AutoRedraw = False
  Else
      If crack = 0 Then
          If eWidthv <= Val(p2xM.Text) Then
              eFshortv = (((p2y) / (p2x)) * (eWidthv * dog))
              eFshort.Text = Format((eFshortv), "0.000000")
              If eFshortv >= 0 Then
              If (eFshortv * 1000) < 1000 Then
                  gaugeFShort.Value = (eFshortv * 1000)
              Else
                  gaugeFShort.Value = 1000
              End If
              End If
              frmProgBar2.AutoRedraw = True
              frmProgBar2.AutoRedraw = False
          End If
          If eWidthv > Val(p2xM.Text) Then
              If eWidthv > Val(p3xM.Text) Then
                  eFshortv = 0
                  eFshort.Text = Format((eFshortv), "0.000000")
                  If eFshortv >= 0 Then
                  If (eFshortv * 1000) < 1000 Then
                      gaugeFShort.Value = (eFshortv * 1000)
                  Else
                      gaugeFShort.Value = 1000
                  End If
                  End If
                  frmProgBar2.AutoRedraw = True
                  frmProgBar2.AutoRedraw = False
              Else
                  eFshortv = (-(((p2y) / ((p3x) - (p2x))) * ((eWidthv * dog) - (p2x))) + (p2y))
                  eFshort.Text = Format((eFshortv), "0.000000")
                  If eFshortv >= 0 Then
                  If (eFshortv * 1000) < 1000 Then
                      gaugeFShort.Value = (eFshortv * 1000)
                  Else
```

```
                    gaugeFShort.Value = 1000
                End If
            End If
            frmProgBar2.AutoRedraw = True
            frmProgBar2.AutoRedraw = False
        End If
    End If
Else
    If eWidthv <= Val(p2xM.Text) Then
        eFshortv = (((p2y) / (p2x)) * (eWidthv))
        eFshort.Text = Format((eFshortv), "0.000000")
        If eFshortv >= 0 Then
        If (eFshortv * 1000) < 1000 Then
            gaugeFShort.Value = (eFshortv * 1000)
        Else
            gaugeFShort.Value = 1000
        End If
        End If
        frmProgBar2.AutoRedraw = True
        frmProgBar2.AutoRedraw = False
    End If
    If eWidthv > Val(p2xM.Text) Then
        If eWidthv > Val(p3xM.Text) Then
            eFshortv = 0
            eFshort.Text = Format((eFshortv), "0.000000")
            If eFshortv >= 0 Then
            If (eFshortv * 1000) < 1000 Then
                gaugeFShort.Value = (eFshortv * 1000)
            Else
                gaugeFShort.Value = 1000
            End If
            End If
            frmProgBar2.AutoRedraw = True
            frmProgBar2.AutoRedraw = False
        Else
            eFshortv = (-(((p2y) / ((p3x) - (p2x))) * (eWidthv - (p2x))) + (p2y))
            eFshort.Text = Format((eFshortv), "0.000000")
            If eFshortv >= 0 Then
            If (eFshortv * 1000) < 1000 Then
                gaugeFShort.Value = (eFshortv * 1000)
            Else
                gaugeFShort.Value = 1000
            End If
            End If
            frmProgBar2.AutoRedraw = True
            frmProgBar2.AutoRedraw = False
        End If
    End If
End If
End If


        ' FAvg is transformed from kN to Newtons
        eFAvgv = ((1000 * (((((frac22F) * (eF22v)) + ((frac45F) * (eF45v)) + ((frac67F) * (eF67v)) + ((frac90F)
* (eF90v)))) + ((fracshortF) * (eFshortv)))) * (numFibPerLayerv))
        eFAvgRealv = ((((((frac22F) * (eF22v)) + ((frac45F) * (eF45v)) + ((frac67F) * (eF67v)) + ((frac90F) *
(eF90v)))) + ((fracshortF) * (eFshortv))))
```

```
eFAvgReal.Text = Format((eFAvgRealv), "0.000000")
If eFAvgRealv >= 0 Then
If (eFAvgRealv * 1000) < 1000 Then
    gaugeFAvg.Value = (eFAvgRealv * 1000)
Else
    gaugeFAvg.Value = 1000
End If
End If
frmProgBar2.AutoRedraw = True
frmProgBar2.AutoRedraw = False


If crack = 0 Then
    eFTensv = (((Val(bmHeigth.Text)) - ccv) / 20) * (Val(bmWidth.Text)) * ((eWidthv / (((2 / 3) *
(Val(bmlength.Text))))) * (Val(frmConcreteInfo.elasModConc.Text)))
    eWidth.Text = Format((eWidthv), "0.000000")
    eFTens.Text = Format((eFTensv), "0.000000")
    frmProgBar2.AutoRedraw = True
    frmProgBar2.AutoRedraw = False
Else
    eFTensv = ((((bmHeigth.Text) - ccv) / 20) * (bmWidth.Text) * ((frmConcreteInfo.flexStrnConc.Text)
/ ((2.71828182845) ^ ((60.7874) * (eWidthv) * (1.01)))))
    ' eFTensv = (0.759 * 0.00034418 * ((eWidthv) ^ (-3)) * (((Val(bmHeigth.Text)) - ccv) / 20) *
(Val(bmWidth.Text)))
    eWidth.Text = Format((eWidthv), "0.000000")
    eFTens.Text = Format((eFTensv), "0.000000")
    frmProgBar2.AutoRedraw = True
    frmProgBar2.AutoRedraw = False
End If


' Draws the Stress Diagram
compStress = ((forceCompv) / ((ccv) * (Val(bmWidth.Text))))
compStressValue = Format((compStress), "0.0000")
posCompStress = (betav * ccv) / 2

If middleSpecimenColor.BackColor = &HFF8080 Then
  If layer = 1 Then
    tensArea = (((Val(bmHeigth.Text)) - ccv) / 20) * (Val(bmWidth.Text))
    compStressy = ((eFAvgv + eFTensv) / (tensArea))
  End If
  For j = 0 To 10
    If j = 0 Then
      factor = 1
      posCompStress = 0
    ElseIf j = 1 Then
      factor = (9 / 10)
      posCompStress = (ccv / 10) * 1
    ElseIf j = 2 Then
      factor = (8 / 10)
      posCompStress = (ccv / 10) * 2
    ElseIf j = 3 Then
      factor = (7 / 10)
      posCompStress = (ccv / 10) * 3
    ElseIf j = 4 Then
      factor = (6 / 10)
      posCompStress = (ccv / 10) * 4
    ElseIf j = 5 Then
```

```
      factor = (5 / 10)
      posCompStress = (ccv / 10) * 5
   ElseIf j = 6 Then
      factor = (4 / 10)
      posCompStress = (ccv / 10) * 6
   ElseIf j = 7 Then
      factor = (3 / 10)
      posCompStress = (ccv / 10) * 7
   ElseIf j = 8 Then
      factor = (2 / 10)
      posCompStress = (ccv / 10) * 8
   ElseIf j = 9 Then
      factor = (1 / 10)
      posCompStress = (ccv / 10) * 9
   ElseIf j = 10 Then
      factor = 0
      posCompStress = (ccv / 10) * 10
   End If

  If compStress <= maxstress Then
      stressDiag.Line (0, posCompStress)-(-(factor * compStressy), posCompStress), STRESS_COLOR
      stressDiag.AutoRedraw = True
      stressDiag.AutoRedraw = False
  Else
      stressDiag.Line (0, posCompStress)-(-maxstress, posCompStress), STRESS_COLOR
      stressDiag.AutoRedraw = True
      stressDiag.AutoRedraw = False
  End If
Next j

Else

For j = 0 To 10
   If j = 0 Then
      factor = 0
      posCompStress = 0
   ElseIf j = 1 Then
      factor = (4 / 10)
      posCompStress = (ccv / 10) * 1
   ElseIf j = 2 Then
      factor = (6.5 / 10)
      posCompStress = (ccv / 10) * 2
   ElseIf j = 3 Then
      factor = (9 / 10)
      posCompStress = (ccv / 10) * 3
   ElseIf j = 4 Then
      factor = (9.5 / 10)
      posCompStress = (ccv / 10) * 4
   ElseIf j = 5 Then
      factor = 1
      posCompStress = (ccv / 10) * 5
   ElseIf j = 6 Then
      factor = (9.5 / 10)
      posCompStress = (ccv / 10) * 6
   ElseIf j = 7 Then
      factor = (9 / 10)
      posCompStress = (ccv / 10) * 7
```

```
    ElseIf j = 8 Then
        factor = (6.5 / 10)
        posCompStress = (ccv / 10) * 8
    ElseIf j = 9 Then
        factor = (4 / 10)
        posCompStress = (ccv / 10) * 9
    ElseIf j = 10 Then
        factor = (2 / 10)
        posCompStress = (ccv / 10) * 10
    End If


    If compStress <= maxstress Then
        stressDiag.Line (0, posCompStress)-(-(factor * compStress), posCompStress), STRESS_COLOR
        stressDiag.AutoRedraw = True
        stressDiag.AutoRedraw = False
    Else
        stressDiag.Line (0, posCompStress)-(-maxstress, posCompStress), STRESS_COLOR
        stressDiag.AutoRedraw = True
        stressDiag.AutoRedraw = False
    End If
 Next j
End If


tensArea = (((Val(bmHeigth.Text)) - ccv) / 20) * (Val(bmWidth.Text))
tenStress1 = ((eFAvgv + eFTensv) / (tensArea))
posTenStress1 = (ccv + ((((Val(bmHeigth.Text)) - ccv) / 20) * ((20 - layer) + 0.5)))
If tenstress <= maxstress Then
    stressDiag.Line (0, posTenStress1)-(tenStress1, posTenStress1), STRESS_COLOR
    stressDiag.AutoRedraw = True
    stressDiag.AutoRedraw = False
Else
    stressDiag.Line (0, posTenStress1)-(maxstress, posTenStress1), STRESS_COLOR
    stressDiag.AutoRedraw = True
    stressDiag.AutoRedraw = False
End If

If layer = 1 Then
    logStress1 = Format(tenStress1, "0.0000")
ElseIf layer = 2 Then
    logStress2 = Format(tenStress1, "0.0000")
ElseIf layer = 3 Then
    logStress3 = Format(tenStress1, "0.0000")
ElseIf layer = 4 Then
    logStress4 = Format(tenStress1, "0.0000")
ElseIf layer = 5 Then
    logStress5 = Format(tenStress1, "0.0000")
ElseIf layer = 6 Then
    logStress6 = Format(tenStress1, "0.0000")
ElseIf layer = 7 Then
    logStress7 = Format(tenStress1, "0.0000")
ElseIf layer = 8 Then
    logStress8 = Format(tenStress1, "0.0000")
ElseIf layer = 9 Then
    logStress9 = Format(tenStress1, "0.0000")
ElseIf layer = 10 Then
    logStress10 = Format(tenStress1, "0.0000")
```

```
ElseIf layer = 11 Then
    logStress11 = Format(tenStress1, "0.0000")
ElseIf layer = 12 Then
    logStress12 = Format(tenStress1, "0.0000")
ElseIf layer = 13 Then
    logStress13 = Format(tenStress1, "0.0000")
ElseIf layer = 14 Then
    logStress14 = Format(tenStress1, "0.0000")
ElseIf layer = 15 Then
    logStress15 = Format(tenStress1, "0.0000")
ElseIf layer = 16 Then
    logStress16 = Format(tenStress1, "0.0000")
ElseIf layer = 17 Then
    logStress17 = Format(tenStress1, "0.0000")
ElseIf layer = 18 Then
    logStress18 = Format(tenStress1, "0.0000")
ElseIf layer = 19 Then
    logStress19 = Format(tenStress1, "0.0000")
Else
    logStress20 = Format(tenStress1, "0.0000")
End If


        eResMomv = ((Val(eResMom.Text)) + ((eFAvgv) + (eFTensv)) * ((((Val(bmHeigth.Text)) - ccv) / 20) *
((20 - layer) + 0.5)))
        eResMom.Text = Format((eResMomv), "0.000000")
        forceAvgTotv = ((Val(forceAvgTot.Text)) + (eFAvgv))
        forceAvgTot.Text = Format((forceAvgTotv), "0.000000")
        forceTensTotv = ((forceTensTot.Text) + (eFTensv))
        forceTensTot.Text = Format((forceTensTotv), "0.000000")
        forceSumv = ((forceAvgTotv) + (forceTensTotv))
        forceSum.Text = Format((forceSumv), "0.000000")


        frmProgBar2.AutoRedraw = True

        If mnuModeStyle(2).Checked = True Then
            If flagBreakInLayer = 1 Then
                msg = "Click OK to continue."
                MsgBox msg
            End If
        End If

        ' If the layer reaches 20 clear the stress diagram and draw on the new page
        If layer = 20 Then
            stressDiag.Cls
            stressDiag.AutoRedraw = True
            stressDiag.AutoRedraw = False
            ' Draws the permanent lines on the stress diagram
            ' this draws the two outer boundary lines
            stressDiag.Line (-maxstress, 0)-(-maxstress, (Val(bmHeigth.Text))), GREEN_COLOR
            stressDiag.Line (maxstress, 0)-(maxstress, (Val(bmHeigth.Text))), GREEN_COLOR
            ' this draws the midlength cross-sectional line
            stressDiag.Line (0, 0)-(0, (Val(bmHeigth.Text))), STRESS_COLOR
            stressDiag.AutoRedraw = True
            stressDiag.AutoRedraw = False
        End If
```

```
Next layer

If Val(forceSumv) >= Val(forceCompv) Then


        frmProgBar2.AutoRedraw = False

        flagBreakInLayer = 1
        resMomTot.Text = Format(0, "0.000000")
        resMomTotv = ((Val(eResMom.Text)) + ((forceCompv) * (ccv - (betav * ccv / 2))))
        resMomTot.Text = Format((resMomTotv), "0.000000")
        nav = Val(cC.Text)
        na.Text = Format((nav), "0.00")
        boom.BackColor = &HFF00&

        ' Pull-out load converted into kN and stored in an array
        pullOutLoadv = (2 * 0.001 * (resMomTotv) / ((Val(bmlength.Text)) / 3))
        pullOutLoad.Text = Format((pullOutLoadv), "0.000000")
        pullOut(counter) = pullOutLoadv
        showFlexLoad.Text = Format(pullOutLoadv, "0.00")
        If (Val(pullOutLoadv)) < 0 Then
            msg = "Instability in the test run has occurred."
            MsgBox msg
            Exit For
        End If

        If pullOutLoadv < 50 Then
            loadOverFlow.BackColor = &HFFFFFF       ' load less then 50 kN
            gaugeLoad.Value = pullOutLoadv
            frmProgBar2.AutoRedraw = True
            frmProgBar2.AutoRedraw = False
        Else
            gaugeLoad.Value = 50
            loadOverFlow.BackColor = &HFF          ' load more than 50 kN
frmProgBar2.AutoRedraw = True
            frmProgBar2.AutoRedraw = True
            frmProgBar2.AutoRedraw = False
        End If

        ddelBotv = ((Val(delBot.Text)) - (Val(delBotOld.Text)))
        ddelBot.Text = Format((ddelBotv), "0.000000")
        frmProgBar2.AutoRedraw = True
        frmProgBar2.AutoRedraw = False
        ddeFlexv = (((ddelBotv) / 2) / ((Val(bmHeigth.Text)) - (cco))) * ((Val(bmlength.Text)) / 2))
        ddeFlex.Text = Format((ddeFlexv), "0.000000")
        frmProgBar2.AutoRedraw = True
        frmProgBar2.AutoRedraw = False
        deFlexv = ((Val(deFlex.Text)) + (ddeFlexv))
        deFlex.Text = Format((deFlexv), "0.000000")
        deFlexC(counter) = deFlexv
        cco = ccv
        delBotOldv = Val(delBot.Text)
        delBotOld.Text = Format((delBotOldv), "0.000000")
        delBot.Text = Format((delBotv), "0.000000")
        frmProgBar2.AutoRedraw = True
        frmProgBar2.AutoRedraw = False
```

```
If deFlexv > (0.011 * (Val(bmlength.Text))) Then
    Exit For
End If


' This line of code draws the graph on the next screen
If deFlexv <= 2.6 Then
    DrawArea.Line -(deFlexv, pullOutLoadv), LINE_COLOR ' Draws the line
End If



' This part of the code writes the output file in a tab-delimited format

If fileInputForm.OptM1Output(0) = True Then
    If counter = 0 Then Print #fileNum, "FIBRAPACK "
    If counter = 0 Then Print #fileNum, "Beam length : " & bmlength.Text & " mm"
    If counter = 0 Then Print #fileNum, "Beam width :  " & bmWidth.Text & " mm"
    If counter = 0 Then Print #fileNum, "Beam depth :  " & bmHeigth.Text & " mm"
    If counter = 0 Then Print #fileNum, "Fiber volume : " & volumeFiber.Text & " %"
    If counter = 0 Then Print #fileNum, "Fiber length : " & frmConcreteInfo.fiberLen.Text & " mm"
    If counter = 0 Then Print #fileNum, "Fiber description : " & frmConcreteInfo.comment.Text
    If counter = 0 Then Print #fileNum, "Compressive strength : " & compStrenConc.Text & " MPa"
    If counter = 0 Then Print #fileNum, "Tensile strength : " & frmConcreteInfo.flexStrnConc.Text & " MPa"
    If counter = 0 Then Print #fileNum, "Favg = " & fracF22.Text & " F22 + " & fracF45.Text & " F45 + " & fracF67.Text & " F67 + " & fracF90.Text & " F90 + " & fracFshort.Text & " Fshort"
    If counter = 0 Then Print #fileNum, Chr$(9) & "A" & Chr$(9) & "B" & Chr$(9) & "C" & Chr$(9) & "Ep" & Chr$(9) & Chr$(9) & "Fshort"
    If counter = 0 Then Print #fileNum, "22" & Chr$(9) & A22c.Text & Chr$(9) & B22c.Text & Chr$(9) & C22c.Text & Chr$(9) & Ep22c.Text & Chr$(9) & Chr$(9) & "point1" & Chr$(9) & p1xM.Text & Chr$(9) & p1yM.Text
    If counter = 0 Then Print #fileNum, "45" & Chr$(9) & A45c.Text & Chr$(9) & B45c.Text & Chr$(9) & C45c.Text & Chr$(9) & Ep45c.Text & Chr$(9) & Chr$(9) & "point2" & Chr$(9) & p2xM.Text & Chr$(9) & p2yM.Text
    If counter = 0 Then Print #fileNum, "67" & Chr$(9) & A67c.Text & Chr$(9) & B67c.Text & Chr$(9) & C67c.Text & Chr$(9) & Ep67c.Text & Chr$(9) & Chr$(9) & "point3" & Chr$(9) & p3xM.Text & Chr$(9) & p3yM.Text
    If counter = 0 Then Print #fileNum, "90" & Chr$(9) & A90c.Text & Chr$(9) & B90c.Text & Chr$(9) & C90c.Text & Chr$(9) & Ep90c.Text
    If counter = 0 Then Print #fileNum, "------------------------------------------------------------------------------"
    If counter = 0 Then Print #fileNum, "Deflec (mm)" & Chr$(9) & "Load (kN)" & Chr$(9) & "TopStrain (mm/mm)" & Chr$(9) & "NA (mm)" & Chr$(9) & "CMOD (mm)" & Chr$(9) & "CompF (N)" & Chr$(9) & "CompStress (MPa)" & Chr$(9) & "Stress1 (MPa)" & Chr$(9) & "Stress2 (MPa)" & Chr$(9) & "Stress3 (MPa)" & Chr$(9) & "Stress4 (MPa)" & Chr$(9) & "Stress5 (MPa)" & Chr$(9) & "Stress6 (MPa)" & Chr$(9) & "Stress7 (MPa)" & Chr$(9) & "Stress8 (MPa)" & Chr$(9) & "Stress9 (MPa)" & Chr$(9) & "Stress10 (MPa)" & Chr$(9) & "Stress11 (MPa)" & Chr$(9) & "Stress12 (MPa)" & Chr$(9) & "Stress12 (MPa)" & Chr$(9) & "Stress14 (MPa)" & Chr$(9) & "Stress15 (MPa)" & Chr$(9) & "Stress16 (MPa)" & Chr$(9) & "Stress17 (MPa)" & Chr$(9) & "Stress18 (MPa)" & Chr$(9) & "Stress19 (MPa)" & Chr$(9) & "Stress20 (MPa)"
    If counter = 0 Then Print #fileNum, "0.0000" & Chr$(9) & "0.0000" & Chr$(9) & "0.0000" & Chr$(9) & na.Text & Chr$(9) & "0.0000" & Chr$(9) & "0.0000" & Chr$(9) & "0.0000" & Chr$(9) & "0.0000" & Chr$(9) & "0.0000" & Chr$(9) & "0.0000" & Chr$(9) & "0.0000" & Chr$(9) & "0.0000" & Chr$(9) & "0.0000" & Chr$(9) & "0.0000" & Chr$(9) & "0.0000" & Chr$(9) & "0.0000" & Chr$(9) & "0.0000" & Chr$(9) & "0.0000" & Chr$(9) & "0.0000" & Chr$(9) & "0.0000" & Chr$(9) & "0.0000" & Chr$(9) & "0.0000" & Chr$(9) & "0.0000" & Chr$(9) & "0.0000"
    Print #fileNum, deFlex.Text & Chr$(9) & pullOutLoad.Text & Chr$(9) & eTop.Text & Chr$(9) & na.Text & Chr$(9) & delBot.Text & Chr$(9) & forceCompValue & Chr$(9) & compStressValue & Chr$(9) &
```

```
logStress1 & Chr$(9) & logStress2 & Chr$(9) & logStress3 & Chr$(9) & logStress4 & Chr$(9) & logStress5 &
Chr$(9) & logStress6 & Chr$(9) & logStress7 & Chr$(9) & logStress8 & Chr$(9) & logStress9 & Chr$(9) &
logStress10 & Chr$(9) & logStress11 & Chr$(9) & logStress12 & Chr$(9) & logStress13 & Chr$(9) & logStress14
& Chr$(9) & logStress15 & Chr$(9) & logStress16 & Chr$(9) & logStress17 & Chr$(9) & logStress18 & Chr$(9)
& logStress19 & Chr$(9) & logStress20
        End If

        If fileInputForm.OptM1Output(1) = True Then
            If counter = 0 Then Print #fileNum, "FIBRAPACK "
            If counter = 0 Then Print #fileNum, "Fiber description : " & frmConcreteInfo.comment.Text
            If counter = 0 Then Print #fileNum, "---------------------------------------------------------------------------
--"
            If counter = 0 Then Print #fileNum, "Deflec (mm)" & Chr$(9) & "Load (kN)"
            If counter = 0 Then Print #fileNum, "0.0000" & Chr$(9) & "0.0000"
            Print #fileNum, deFlex.Text & Chr$(9) & pullOutLoad.Text
        End If


        ' Calculates the JSCE indices
        If counter = 0 Then
            pullOutNew = 0
            pullOutOld = 0
            deflexNew = 0
            deflexOld = 0
        Else
            pullOutNew = pullOut(counter)
            pullOutOld = pullOut(counter - 1)
            deflexNew = deFlexC(counter)
            deflexOld = deFlexC(counter - 1)
        End If


        If deFlexv <= ((Val(bmlength.Text)) / 150) Then
            dAreaOAEFO = (((pullOutNew + pullOutOld) / 2) * (deflexNew - deflexOld))
            AreaTotalOAEFO = AreaOAEFO + dAreaOAEFO
            AreaOAEFO = AreaTotalOAEFO
            frmJSCE.toughnessjsce.Text = Format(AreaOAEFO, "0.000")
            tFJSCE = (((AreaOAEFO * 1000) * (Val(bmlength.Text))) / ((Val(bmWidth.Text)) *
(Val(bmHeigth.Text)) * (Val(bmHeigth.Text)) * ((Val(bmlength.Text)) / 150)))
            frmJSCE.toughnessfactorjsce.Text = Format(tFJSCE, "0.000")
            frmJSCE.AutoRedraw = True
            frmJSCE.AutoRedraw = False
        End If

        ' Pull-Out load and Deflection at first crack
        firstCrackLoad = pullOut(firstCrack)
        firstCrackDeflex = deFlexC(firstCrack)
        whereFirstCrack.Text = Format(firstCrackDeflex, "0.000")
        frmFirstCrackDeflec.showValueFirstCrack.Text = Format(firstCrackDeflex, "0.0000")
        If deFlexv = firstCrackDeflex And deFlexv <> 0 Then
            DrawArea.Line (firstCrackDeflex, 0)-(firstCrackDeflex, miniEWhat), AXIS_COLOR
            DrawArea.PSet (deFlexv, pullOutLoadv), LINE_COLOR
        End If

        ' Calculates the ASTM Indices
        I1deflex = firstCrackDeflex
        I5deflex = (3 * firstCrackDeflex)
```

```
I10deflex = (5.5 * firstCrackDeflex)
I20deflex = (10.5 * firstCrackDeflex)
I30deflex = (15.5 * firstCrackDeflex)
I50deflex = (25.5 * firstCrackDeflex)

AreaOABO = ((1 / 2) * (firstCrackLoad * firstCrackDeflex))
calcASTM.areaOABOText.Text = Format(AreaOABO, "0.000")
calcASTM.AutoRedraw = True
calcASTM.AutoRedraw = False

' Area calculation for section BACD
If deFlexv >= I1deflex And deFlexv < I5deflex Then
    pullOutNow = pullOut(counter)
    deflexNow = deFlexC(counter)
    calcASTM.cntBA.Text = counterBACD
    If counterBACD = 0 Then
        firstPullOutBA = pullOut(counter)
        calcASTM.firstPullOutBAText.Text = Format(firstPullOutBA, "0.000")
        firstDeflecBA = deFlexC(counter)
        calcASTM.firstDeflecBAText.Text = Format(firstDeflecBA, "0.000")
        dBaseBD = ((deFlexC(counter)) - (firstCrackDeflex))
        dHeigthBA = (((pullOut(counter)) + firstCrackLoad) / 2)
    Else
        dBaseBD = ((deFlexC(counter)) - (deFlexC(counter - 1)))
        dHeigthBA = (((pullOut(counter)) + (pullOut(counter - 1))) / 2)
    End If
    BaseTotalBD = BaseBD + dBaseBD
    BaseBD = BaseTotalBD
    dAreaBACD = ((dHeigthBA) * (dBaseBD))
    AreaTotalBACD = AreaBACD + dAreaBACD
    AreaBACD = AreaTotalBACD
    calcASTM.areaBACDText.Text = Format(AreaBACD, "0.000")
    lastPullOutBA = pullOutNow
    lastDeflecBA = deflexNow
    counterBACD = (calcASTM.cntBA.Text) + 1
    calcASTM.AutoRedraw = True
    calcASTM.AutoRedraw = False
End If

' Area calculation for section DCEF
If deFlexv >= I5deflex And deFlexv < I10deflex Then
    pullOutNow = pullOut(counter)
    deflexNow = deFlexC(counter)
    calcASTM.cntDC.Text = counterDCEF
    If counterDCEF = 0 Then
        firstPullOutDC = pullOut(counter)
        calcASTM.firstPullOutDCText.Text = Format(firstPullOutDC, "0.000")
        firstDeflecDC = deFlexC(counter)
        calcASTM.firstDeflecDCText.Text = Format(firstDeflecDC, "0.000")
        dBaseDF = ((deFlexC(counter)) - (I5deflex))
        If pullOut(counter) < lastPullOutBA Then
            dHeigthDC = (pullOut(counter))
        Else
            dHeigthDC = (((pullOut(counter)) + lastPullOutBA) / 2)
        End If
    Else
        dBaseDF = ((deFlexC(counter)) - (deFlexC(counter - 1)))
```

```
            dHeigthDC = (((pullOut(counter)) + (pullOut(counter - 1))) / 2)
        End If
        BaseTotalDF = BaseDF + dBaseDF
        BaseDF = BaseTotalDF
        dAreaDCEF = ((dHeigthDC) * (dBaseDF))
        AreaTotalDCEF = AreaDCEF + dAreaDCEF
        AreaDCEF = AreaTotalDCEF
        calcASTM.areaDCEFText.Text = Format(AreaDCEF, "0.000")
        lastPullOutDC = pullOutNow
        lastDeflecDC = deflexNow
        counterDCEF = (calcASTM.cntDC.Text) + 1
        calcASTM.AutoRedraw = True
        calcASTM.AutoRedraw = False
End If

' Area calculation for section FEGH
If deFlexv >= I10deflex And deFlexv < I20deflex Then
    pullOutNow = pullOut(counter)
    deflexNow = deFlexC(counter)
    calcASTM.cntFE.Text = counterFEGH
    If counterFEGH = 0 Then
        firstPullOutFE = pullOut(counter)
        calcASTM.firstPullOutFEText.Text = Format(firstPullOutFE, "0.000")
        firstDeflecFE = deFlexC(counter)
        calcASTM.firstDeflecFEText.Text = Format(firstDeflecFE, "0.000")
        dBaseFH = ((deFlexC(counter)) - (I10deflex))
        If pullOut(counter) < lastPullOutDC Then
            dHeigthFE = (pullOut(counter))
        Else
            dHeigthFE = (((pullOut(counter)) + lastPullOutDC) / 2)
        End If
    Else
        dBaseFH = ((deFlexC(counter)) - (deFlexC(counter - 1)))
        dHeigthFE = (((pullOut(counter)) + (pullOut(counter - 1))) / 2)
    End If
    BaseTotalFH = BaseFH + dBaseFH
    BaseFH = BaseTotalFH
    dAreaFEGH = ((dHeigthFE) * (dBaseFH))
    AreaTotalFEGH = AreaFEGH + dAreaFEGH
    AreaFEGH = AreaTotalFEGH
    calcASTM.areaFEGHText.Text = Format(AreaFEGH, "0.000")
    lastPullOutFE = pullOutNow
    lastDeflecFE = deflexNow
    counterFEGH = (calcASTM.cntFE.Text) + 1
    calcASTM.AutoRedraw = True
    calcASTM.AutoRedraw = False
End If

' Area calculation for section HGIJ
If deFlexv >= I20deflex And deFlexv < I30deflex Then
    pullOutNow = pullOut(counter)
    deflexNow = deFlexC(counter)
    calcASTM.cntHG.Text = counterHGIJ
    If counterHGIJ = 0 Then
        firstPullOutHG = pullOut(counter)
        calcASTM.firstPullOutHGText.Text = Format(firstPullOutHG, "0.000")
        firstDeflecHG = deFlexC(counter)
```

```
            calcASTM.firstDeflecHGText.Text = Format(firstDeflecHG, "0.000")
            dBaseHJ = ((deFlexC(counter)) - (I20deflex))
            If pullOut(counter) < lastPullOutFE Then
                dHeigthHG = (pullOut(counter))
            Else
                dHeigthHG = (((pullOut(counter)) + lastPullOutFE) / 2)
            End If
        Else
            dBaseHJ = ((deFlexC(counter)) - (deFlexC(counter - 1)))
            dHeigthHG = (((pullOut(counter)) + (pullOut(counter - 1))) / 2)
        End If
        BaseTotalHJ = BaseHJ + dBaseHJ
        BaseHJ = BaseTotalHJ
        dAreaHGIJ = ((dHeigthHG) * (dBaseHJ))
        AreaTotalHGIJ = AreaHGIJ + dAreaHGIJ
        AreaHGIJ = AreaTotalHGIJ
        calcASTM.areaHGIJText.Text = Format(AreaHGIJ, "0.000")
        lastPullOutHG = pullOutNow
        lastDeflecHG = deflexNow
        counterHGIJ = (calcASTM.cntHG.Text) + 1
        calcASTM.AutoRedraw = True
        calcASTM.AutoRedraw = False
End If

' Area calculation for section JIKL
If deFlexv >= I30deflex And deFlexv < I50deflex Then
    pullOutNow = pullOut(counter)
    deflexNow = deFlexC(counter)
    calcASTM.cntJI.Text = counterJIKL
    If counterJIKL = 0 Then
        firstPullOutJI = pullOut(counter)
        calcASTM.firstPullOutJIText.Text = Format(firstPullOutJI, "0.000")
        firstDeflecJI = deFlexC(counter)
        calcASTM.firstDeflecJIText.Text = Format(firstDeflecJI, "0.000")
        dBaseJL = ((deFlexC(counter)) - (I30deflex))
        If pullOut(counter) < lastPullOutHG Then
            dHeigthJI = (pullOut(counter))
        Else
            dHeigthJI = (((pullOut(counter)) + lastPullOutHG) / 2)
        End If
    Else
        dBaseJL = ((deFlexC(counter)) - (deFlexC(counter - 1)))
        dHeigthJI = (((pullOut(counter)) + (pullOut(counter - 1))) / 2)
    End If
    BaseTotalJL = BaseJL + dBaseJL
    BaseJL = BaseTotalJL
    dAreaJIKL = ((dHeigthJI) * (dBaseJL))
    AreaTotalJIKL = AreaJIKL + dAreaJIKL
    AreaJIKL = AreaTotalJIKL
    calcASTM.areaJIKLText.Text = Format(AreaJIKL, "0.000")
    lastPullOutJI = pullOutNow
    lastDeflecJI = deflexNow
    counterJIKL = (calcASTM.cntJI.Text) + 1
    calcASTM.AutoRedraw = True
    calcASTM.AutoRedraw = False
End If
```

```
' Last part of calculation
If deFlexv >= I50deflex Then
    If counterLK = 0 Then
        firstPullOutLK = pullOut(counter)
        calcASTM.firstPullOutLKText.Text = Format(firstPullOutLK, "0.000")
        firstDeflecLK = deFlexC(counter)
        calcASTM.firstDeflecLKText.Text = Format(firstDeflecLK, "0.000")
        counterLK = 1
    End If
    calcASTM.AutoRedraw = True
    calcASTM.AutoRedraw = False
End If


' Changes the increment in top strain
If deFlexv < 0.1 Then
    eTopv = ((Val(eTop.Text)) - 0.000005)                ' orig - 0.000005
    eTop.Text = Format((eTopv), "0.000000")
ElseIf deFlexv > 0.1 Then
    If deFlexv < 1 Then
        eTopv = ((Val(eTop.Text)) - 0.000005)
        eTop.Text = Format((eTopv), "0.000000")
    Else
        eTopv = ((Val(eTop.Text)) - 0.00001)             ' orig - 0.00002
        eTop.Text = Format((eTopv), "0.000000")
    End If
End If


If mnuChoiceSnd(1).Checked = True Then
    For i = 1 To 2
        Beep
    Next i
End If



boom.BackColor = &HFF0000

' See whether the user wants to stop when a data point is found
If mnuModeStyle(0).Checked = True Then
    msg = "Click OK to Proceed."
    MsgBox msg
End If

frmProgBar2.AutoRedraw = True

' Get out of the loop after a successful search of a data point
    Exit Do

End If

' There is no point to continue after cc passed 0 mm
If Val(cC.Text) = 1 Then
    Exit For
End If

frmProgBar2.AutoRedraw = False

ccv = ((Val(cC.Text)) - 1)
```

```
        cC.Text = Format(((ccv), "0.00")

        frmProgBar2.AutoRedraw = True

    Loop Until Val(forceSumv) >= Val(forceCompv)

  Next counter


  ' Do the error correction for the area calculation
  If BaseBD <> (2 * firstCrackDeflex) Then
      If lastPullOutBA < firstPullOutDC Then
          AreaBACD = ((Val(calcASTM.areaBACDText.Text)) + (((lastPullOutBA + firstPullOutDC) / 2) *
(I5deflex - lastDeflecBA)))
      Else
          AreaBACD = ((Val(calcASTM.areaBACDText.Text)) + ((firstPullOutDC) * (I5deflex - lastDeflecBA)))
      End If
      calcASTM.areaBACDText.Text = Format(AreaBACD, "0.000")
      calcASTM.AutoRedraw = True
      calcASTM.AutoRedraw = False
  End If


  If BaseDF <> (4.5 * firstCrackDeflex) Then
      If lastPullOutDC < firstPullOutFE Then
          AreaDCEF = ((Val(calcASTM.areaDCEFText.Text)) + (((lastPullOutDC + firstPullOutFE) / 2) *
(I10deflex - lastDeflecDC)))
      Else
          AreaDCEF = ((Val(calcASTM.areaDCEFText.Text)) + ((firstPullOutFE) * (I10deflex - lastDeflecDC)))
      End If
      calcASTM.areaDCEFText.Text = Format(AreaDCEF, "0.000")
      calcASTM.AutoRedraw = True
      calcASTM.AutoRedraw = False
  End If


  If BaseFH <> (9.5 * firstCrackDeflex) Then
      If lastPullOutFE < firstPullOutHG Then
          AreaFEGH = ((Val(calcASTM.areaFEGHText.Text)) + (((lastPullOutFE + firstPullOutHG) / 2) *
(I20deflex - lastDeflecFE)))
      Else
          AreaFEGH = ((Val(calcASTM.areaFEGHText.Text)) + ((firstPullOutHG) * (I20deflex - lastDeflecFE)))
      End If
      calcASTM.areaFEGHText.Text = Format(AreaFEGH, "0.000")
      calcASTM.AutoRedraw = True
      calcASTM.AutoRedraw = False
  End If

  If BaseHJ <> (14.5 * firstCrackDeflex) Then
      If lastPullOutHG < firstPullOutJI Then
          AreaHGIJ = ((Val(calcASTM.areaHGIJText.Text)) + (((lastPullOutHG + firstPullOutJI) / 2) * (I30deflex -
lastDeflecHG)))
      Else
          AreaHGIJ = ((Val(calcASTM.areaHGIJText.Text)) + ((firstPullOutJI) * (I30deflex - lastDeflecHG)))
      End If
      calcASTM.areaHGIJText.Text = Format(AreaHGIJ, "0.000")
      calcASTM.AutoRedraw = True
      calcASTM.AutoRedraw = False
  End If
```

```
    If BaseJL <> (24.5 * firstCrackDeflex) Then
        If lastPullOutJI < firstPullOutLK Then
            AreaJIKL = ((Val(calcASTM.areaJIKLText.Text)) + (((lastPullOutJI + firstPullOutLK) / 2) * (I50deflex -
lastDeflecJI)))
        Else
            AreaJIKL = ((Val(calcASTM.areaJIKLText.Text)) + ((firstPullOutLK) * (I50deflex - lastDeflecJI)))
        End If
        calcASTM.areaJIKLText.Text = Format(AreaJIKL, "0.000")
        calcASTM.AutoRedraw = True
        calcASTM.AutoRedraw = False
    End If


    sumAreaOACDBO = ((AreaOABO) + (AreaBACD))
    sumAreaOAEFBO = ((AreaOABO) + (AreaBACD) + (AreaDCEF))
    sumAreaOAGHBO = ((AreaOABO) + (AreaBACD) + (AreaDCEF) + (AreaFEGH))
    sumAreaOAIJBO = ((AreaOABO) + (AreaBACD) + (AreaDCEF) + (AreaFEGH) + (AreaHGIJ))
    sumAreaOAKLBO = ((AreaOABO) + (AreaBACD) + (AreaDCEF) + (AreaFEGH) + (AreaHGIJ) +
(AreaJIKL))

    frmASTM.ASTMI5.Text = Format((sumAreaOACDBO / AreaOABO), "0.000")
    frmASTM.ASTMI10.Text = Format((sumAreaOAEFBO / AreaOABO), "0.000")
    frmASTM.ASTMI20.Text = Format((sumAreaOAGHBO / AreaOABO), "0.000")
    frmASTM.ASTMI30.Text = Format((sumAreaOAIJBO / AreaOABO), "0.000")
    frmASTM.ASTMI50.Text = Format((sumAreaOAKLBO / AreaOABO), "0.000")
    frmASTM.AutoRedraw = True
    frmASTM.AutoRedraw = False

    ' Write the ASTM Indices and JSCE Indices on the file
    Print #fileNum, "---------------------------------------------------------------------------------"
    Print #fileNum, "d1st : " & whereFirstCrack.Text
    Print #fileNum, "I5 : " & frmASTM.ASTMI5.Text
    Print #fileNum, "I10 : " & frmASTM.ASTMI10.Text
    Print #fileNum, "I20 : " & frmASTM.ASTMI20.Text
    Print #fileNum, "I30 : " & frmASTM.ASTMI30.Text
    Print #fileNum, "I50 : " & frmASTM.ASTMI50.Text
    Print #fileNum, "T JSCE : " & frmJSCE.toughnessjsce.Text
    Print #fileNum, "F JSCE : " & frmJSCE.toughnessfactorjsce.Text


    boom.BackColor = &HFFFFFF
    Call clean_it_up
    cmdNextProg.Enabled = True
    cmdQuitProg.Enabled = True
    cmdNextProg.SetFocus
    Close

    For i = 1 To 20
        Beep
    Next i

End Sub
```

Appendix D - Practical Guidelines for Low Rebound Mix Design and Shooting Technique

As a general guideline to design a dry-mix shotcrete mixture for minimized overall and fiber rebound, the following steps and figures may be used:

1) Aggregate Gradation

Whenever possible, an ACI N° 2 gradation curve (containing up to 5% of 9.5 mm aggregates) should be used. A N° 1 gradation (containing only sand) can be used and should lead to lower overall rebound values, however it tends to lead to greater difficulty in handling the shotcrete machine, greater shrinkage cracking and lower compaction.

Table D1 - Recommended limits for an ACI N° 2 aggregate gradation curve

Sieve Size (mm)	9.5	4.8	2.4	1.2	0.6	0.3	0.15
Minimum Passing (%)	90	70	50	35	20	8	2
Maximum Passing (%)	100	85	70	55	35	20	10

2) Cement Content

The cement content, calculated as a weight percentage of the total dry mix, is the primary determinant of overall rebound and fiber rebound. As a rule of thumb, without silica fume addition, the following overall and fiber rebound figures should be expected as a function of the cement content chosen:

Table D2 - Expected overall and fiber rebounds as a function of the cement content (no silica fume addition, ACI N° 2 gradation curve, steel fibers: 0.5 mm diameter, 30 mm in length).

Cement Content (% by weight)	Cement Content kg/m^3	Expected Overall Rebound (%)	Expected Fiber Rebound (%)
16.8%	350	45%	75%
19.0%	400	41%	73%
21.6%	450	37%	71%
24.2%	500	34%	69%
27.0%	550	30%	67%

3) Silica Fume Content

Whenever available, undensified silica fume should be used in order to minimize the overall and fiber rebound. In this case, the silica fume addition, calculated as a substitution rate of the total cementitious content will lead to a reduction in the overall and fiber rebounds of approximately:

Table D3 - Expected decrease in the overall and fiber rebounds as a function of the silica fume content in mass substitution to cement (ACI N° 2 gradation curve, steel fibers: 0.5 mm diameter, 30 mm in length).

Silica Fume Content (% cement subst.)	Reduction in Overall Rebound (%)	Reduction in Fiber Rebound (%)
0%	0%	0%
4%	-5%	-4%
8%	-9%	-8%
12%	-13%	-12%
16%	-15%	-16%

In practice, the cementitious content employed by the industry is usually around 20% at a silica fume content of 8 to 12% by weight substitution of cement. Higher cementitious contents tend to increase the cost and lead to excessive shrinkage cracking.

Example: Assuming a 21.6% cementitious content (450 kg/m^3) with a 12% silica fume content, the expected overall rebound should be:

$$37\% \text{ (from Table D2) - 13\% (from Table D3)} = 24\%$$

The expected fiber rebound (for a standard hooked 0.5 mm diameter and 30 mm long steel fiber) should be:

$$71\% \text{ (from Table D2) - 12\% (from Table D3)} = 59\%$$

4) Accelerator Admixture Content

Accelerator admixtures (liquid or powder) have not been found to affect the overall rebound of dry-mix shotcrete, but are primary determinants of the maximum overhead build up. The dosage used by the industry is usually 2 to 4% for carbonate and aluminate based compositions and 4 to 6% for calcium aluminate cement based admixtures.

5) Shooting Consistency:

For minimized rebound, enough shooting water should be used to maintain the 'wettest stable consistency'. In addition to minimized overall and fiber rebound this also leads to maximized strength and compaction.

6) Air Flow

As shown in Chapter 3.3.2.1, there is an ideal air flow value that tends to lead to minimized rebound and maximized physical properties. In practice, shotcrete machines are not equipped with air flowmeters but only pressure gauges. This ideal air flow, however, can be obtained with good accuracy by visual tuning, and the pressure reading can be used as an indicator for quality control procedures.

As a general guide and based on the results obtained in this thesis, the following air flow conditions should be used to determine the minimum air compressor capacity:

Table D4 - Approximate air flow values for minimized overall rebound as a function of hose diameter and length (1 in = 25.4 mm, 1 ft = 305 mm, 100 cfm = 0.047 m³/s).

Hose Internal Diameter (in)	Air Flow (cfm)		
	Distance = 50 ft.	Distance = 500 ft.	Distance = 1000 ft.
1.5"	170	200/230	230/250
2.0"	300	350/400	400/450
2.5"	470	550/620	620/700